Thèse n° 9893

Investigating Scrape-Off Layer transport in alternative divertor geometries on the TCV tokamak

Présentée le 24 janvier 2020

à la Faculté des sciences de base
SPC - Physique du Tokamak TCV
Programme doctoral en physique

pour l'obtention du grade de Docteur ès Sciences

par

Roberto MAURIZIO

Acceptée sur proposition du jury

Prof. C. Hébert, présidente du jury
Dr. B. P. Duval, Dr H. Reimerdes, directeurs de thèse
Prof. B. Lipschultz, rapporteur
Dr B. Sieglin, rapporteur
Dr J. Loizu, rapporteur

École
polytechnique
fédérale
de Lausanne

2020

Nature has a great simplicity and, therefore, a great beauty.
— Richard Feynman, The Character of Physical Law

Abstract

Thermonuclear fusion is a potentially clean and limitless energy source that can substantially change the current global electricity generation mix, which is highly dependent on limited fossil fuels. This thesis contributes to the development of fusion energy with experiments on the TCV tokamak, addressing power exhaust in the divertor, which remains a major issue for a fusion tokamak reactor. A large fraction of the heating power needed to keep the plasma at the parameters required for fusion reactions, is continuously transported by the plasma across closed magnetic surfaces into a thin layer with open field lines surrounding the plasma, the Scrape-Off Layer (SOL), where it follows magnetic field lines towards the divertor targets. Unmitigated target peak heat fluxes in a fusion reactor are projected to greatly exceed available material limits. While acceptable target conditions may be possible by operating the divertor in a detached regime, a degradation of core plasma performance may ensue. A unification of a performant core and a detached divertor may be possible using alternative magnetic configurations to the standard Single-Null (SN). This thesis assesses the power exhaust properties over an unprecedented range of alternative magnetic configurations with the goals of both reducing the power exhaust challenge through divertor geometry modifications and improving the current understanding of SOL transport physics. TCV's infrared thermography systems are extensively used to measure divertor target heat fluxes, fitted to extract the SOL heat power width $\lambda_{q,u}$ and the spreading factor S_u.

Power sharing between divertor targets significantly varies with the plasma and/or divertor geometry, mostly interpreted as the effect of parallel electron heat conduction. The $\lambda_{q,u}$ is found sensitive to properties of the plasma core, shape of the plasma and the divertor, and is consistent with empirical cross-machine scalings. The dependence on plasma current can be mostly understood with a model based on the competition between parallel and perpendicular diffusive transport. Poloidal asymmetries and field direction effects indicate that more physics is needed. The S_u scales with the inverse of the target flux expansion. In the Low-Field-Side Snowflake Minus configuration, the secondary x-point enhances cross-field transport in the divertor, consistently with turbulence simulations. At the L- to H-mode transition, cross-field transport reduces in the main and divertor SOL, suggesting that the edge transport barrier propagates into the SOL. The upstream $\lambda_{q,u}$ between Type-I ELMs agrees with cross-machine scaling predictions only with the toroidal magnetic field as regression parameter, revealing that this field dependence is vital. A comparison of the ELM power deposition duration

in TCV and JET supports the hypothesis of it increasing with the parallel connection length, and the ELM peak parallel energy fluence is consistent with a cross-machine scaling, supporting current extrapolations to ITER. Divertor geometry variations reveal that the ELM power width scales with the inverse of the target flux expansion.
These results provide unique input for testing models required to reliably extrapolate to the divertor of a fusion reactor, and may have significant implications in the optimization of its magnetic configuration.

Keywords: nuclear fusion, tokamak, TCV, plasma, power exhaust, divertor, Scrape-Off Layer width, infrared thermography.

Résumé

La fusion thermonucléaire est une source d'énergie potentiellement propre et illimitée, qui peut modifier de manière substantielle la composition actuelle de la production d'électricité dans le monde, fortement dépendante de combustibles fossiles limités. Cette thèse contribue au développement de l'énergie de fusion grâce à des expériences sur le tokamak TCV, qui traitent de l'échappement de puissance dans le divergeur, qui reste un problème majeur pour un réacteur à fusion. Une grande partie de la puissance de chauffage, nécessaire pour maintenir le plasma aux paramètres requis pour les réactions de fusion, est transportée en continu par le plasma à travers des surfaces magnétiques fermées dans une couche mince entourée par de lignes de champ ouvertes entourant le plasma, le *Scrape-Off Layer* (SOL), où elle suit les lignes de champ magnétique vers les cibles du divergeur. Les flux thermiques non atténués sur ces cibles dans un réacteur à fusion devraient dépasser largement les limites des matériaux disponibles. Bien que des conditions acceptables aux cibles puissent être possibles en faisant fonctionner le divergeur en régime détaché, une dégradation des performances du plasma du coeur peut en résulter. L'unification d'un coeur performant et d'un divergeur détaché peut être possible en utilisant des configurations magnétiques alternatives au standard *Single-Null* (SN). Cette thèse évalue les propriétés de l'échappement de puissance sur une gamme sans précédent de configurations magnétiques alternatives dans le but de réduire le problème de l'échappement de puissance par des modifications de la géométrie du divergeur et d'améliorer la compréhension actuelle de la physique du transport dans le SOL. Les systèmes de thermographie infrarouge de TCV sont largement utilisés pour mesurer les flux de chaleur sur les cibles du divergeur, à partir desquels on estime la largeur de puissance thermique du SOL (*SOL power width*) $\lambda_{q,u}$ et le facteur d'étalement (*spreading factor*) S_u.

Le partage de puissance entre les cibles du divergeur varie de manière significative avec la géométrie du plasma et/ou du divergeur, principalement interprété comme l'effet de la conduction thermique parallèle par les électrons. Le $\lambda_{q,u}$ se révèle sensible aux propriétés du plasma du coeur, à la forme du plasma et du divergeur, et est compatible avec lois d'échelle empiriques entre machines. La dépendance au courant de plasma peut être généralement comprise avec un modèle basé sur la compétition entre transport diffusif parallèle et perpendiculaire. Des asymétries poloïdales et des effets de direction de champ indiquent qu'il faut davantage de physique. Le S_u évolue avec l'inverse de l'expansion du flux au cible. Dans la configuration *Low-Field-Side Snowflake Minus*, le point-x secondaire augmente le transport perpendiculaire aux lignes de champ dans le divergeur, conformément aux simulations numériques de turbulence. À la transition entre mode L et mode H, le transport perpendiculaire aux lignes de champ réduit dans le SOL principal et dans le SOL du divergeur, ce qui suggère que la barrière de transport de bord se propage dans le SOL. Le $\lambda_{q,u}$ *upstream* entre ELMs de type I est cohérent avec les prédictions de lois d'échelle empiriques sur plusieurs machines seulement avec le champ magnétique toroïdal comme un paramètre de régression, révélant que cette dépendance de champ est vitale. Une comparaison du temps de dépôt de la puissance d'un ELM dans TCV et JET confirme l'hypothèse d'une augmentation avec la longueur de connexion parallèle, et le sommet du profile de fluence d'énergie parallèle d'un ELM est compatible avec une loi d'échelle entre machines, soutenant les extrapolations actuelles à ITER. Les variations de la géométrie du divergeur révèlent que la largeur de puissance d'un ELM est proportionnelle à l'inverse de l'expansion du flux au cible.

Ces résultats fournissent des informations uniques pour tester les modèles requis pour une extrapolation fiable au divergeur d'un réacteur à fusion et peuvent avoir des implications importantes pour l'optimisation de sa configuration magnétique.

Mots-clés : fusion nucléaire, tokamak, TCV, plasma, échappement de puissance, divergeur, largeur du Scrape-Off Layer, thermographie infrarouge.

Sinossi

La fusione termonucleare è una fonte di energia potenzialmente pulita e senza limiti che può cambiare sostanzialmente l'attuale mix globale di generazione d'elettricità, fortemente dipendente dai combustibili fossili. Questa tesi contribuisce allo sviluppo dell'energia da fusione con esperimenti sul tokamak TCV, affrontando lo scarico di potenza nel divertore che rimane un grosso problema per un reattore tokamak a fusione. Gran parte della potenza di riscaldamento, necessaria per mantenere il plasma ai parametri richiesti per le reazioni di fusione, è continuamente trasportata dal plasma attraverso superfici magnetiche chiuse in uno strato sottile con linee di campo aperte che circondano il plasma, lo *Scrape-Off Layer* (SOL), dove segue le linee del campo magnetico verso i bersagli del divertore. Si prevede che i flussi di calore non mitigati su tali bersagli in un reattore a fusione supereranno largamente i limiti dei materiali disponibili. Sebbene condizioni accettabili sui bersagli potrebbero essere possibili operando il divertore nel regime distaccato (*detached*), una degradazione delle prestazioni del cuore del plasma può derivarne. L'unificazione di un nucleo performante e un divertore distaccato potrebbe essere possibile utilizzando configurazioni magnetiche alternative allo standard *Single-Null* (SN). Questa tesi studia le proprietà dello scarico di potenza per una gamma senza precedenti di configurazioni magnetiche alternative, con l'obiettivo sia di ridurre la sfida dello scarico di potenza attraverso modifiche della geometria del divertore, sia di migliorare l'attuale comprensione della fisica del trasporto nel SOL. I sistemi di termografia a infrarosso di TCV sono ampiamente utilizzati per misurare i flussi di calore sui bersagli del divertore, dai quali si estrae la larghezza della potenza termica del SOL (*SOL power width*) $\lambda_{q,u}$ e il fattore di diffusione (*spreading factor*) S_u.

La ripartizione della potenza tra i bersagli del divertore varia in modo significativo con la geometria del plasma e/o del divertore, il che è per lo più interpretato come l'effetto della conduzione elettronica parallela del calore. La $\lambda_{q,u}$ è sensibile alle proprietà del nucleo del plasma, alla forma del plasma e del divertore, ed è coerente con regressioni multi-macchina. La sua dipendenza dalla corrente del plasma può essere principalmente compresa con un modello basato sulla competizione tra trasporto diffusivo parallelo e perpendicolare. Le asimmetrie poloidali e gli effetti della direzione del campo indicano che è necessaria più fisica. Il S_u scala con l'inverso dell'espansione di flusso ai bersagli. Nella configurazione *Low-Field-Side Snowflake Minus*, il punto-x secondario aumenta il trasporto perpendicolare alle linee di campo nel divertore, coerentemente con simulazioni numeriche turbolente. Nella transizione da modo L a modo H, il trasporto perpendicolare alle linee di campo si riduce nel SOL principale e nel SOL del divertore, suggerendo che la barriera di trasporto di bordo si propaga nel SOL. La $\lambda_{q,u}$ *upstream* tra ELMs di tipo I concorda con le previsioni di regressioni multi-macchina solamente se il campo magnetico toroidale è un parametro di regressione, rivelando che questa dipendenza dal campo è vitale. Un confronto tra la durata della deposizione della potenza ELM in TCV e JET supporta l'ipotesi che questa aumenti con la lunghezza di connessione parallela, e il picco del profilo di fluenza di energia ELM parallela è coerente con una regressione multi-macchina, supportando le attuali estrapolazioni ad ITER. Variazioni della geometria del divertore rivelano che la larghezza della potenza ELM scala con l'inverso dell'espansione di flusso ai bersagli.

Questi risultati forniscono input unici per testare i modelli necessari per estrapolazioni affidabili al divertore di un reattore a fusione, e possono avere implicazioni significative nell'ottimizzazione della sua configurazione magnetica.

Parole chiave: fusione nucleare, tokamak, TCV, plasma, scarico di potenza, divertore, larghezza dello Scrape-Off Layer, termografia a infrarosso.

Contents

List of Symbols

Acronyms

Alcator C-Mod	Alto Campo Toro C-Mod (tokamak in Cambridge, MA, USA)
ASDEX	Axially Symmetric Divertor Experiment (tokamak in Munich, DE)
DIII-D	Doublet III - D (tokamak in San Diego, CA, USA)
DML	Diamagnetic Loop
EPFL	École Polytechnique Fédérale de Lausanne (CH)
ELM	Edge-Localised Mode
HFS	High-Field Side
HIR	Horizontal Infrared system
ISP	Inner Strike-Point
ITER	International Thermonuclear Experimental Reactor (Cadarache, FR)
JET	Joint European Tokamak (Culham, UK)
LFS	Low-Field Side
LP	Langmuir Probe
MHD	Magnetohydrodynamics
OMP	Outer Mid-Plane - "upstream" location
OSP	Outer Strike-Point
RCP	Fast Reciprocating Probe
SF	Snowflake configuration
SN	Single-Null configuration
SOL	Scrape-Off Layer
SX	Super-X configuration
TC	Thermocouple
TCV	Tokamak á Configuration Variable (Lausanne, CH)
TIR	Tangential Infrared system
TS	Thomson Scattering
VIR	Vertical Infrared system
XPT	X-Point Target configuration
2PM	Two-Point Model

Physical constants

k_B	Boltzmann constant

h	Planck constant
μ_0	permeability of free space
m_p	mass of the proton
e	charge of the electron
κ_0^e	Spitzer-Härm electron heat conduction constant

Plasma and divertor geometry

$R_{\mathrm{max}} = R_u$	plasma largest radius (OMP)
R_{min}	plasma smallest radius
R_{up}	plasma top radius
R_{down}	plasma bottom radius
a	plasma minor radius
R_{geo}	plasma geometric radius
ϵ	plasma inverse aspect ratio
κ	plasma elongation
δ_{upper}	plasma upper triangularity
δ_{lower}	plasma lower triangularity
$s_{\|}$	SOL parallel coordinate
$L_{\|}$	SOL parallel connection length
$L_{\|,\mathrm{div}}$	divertor SOL parallel connection length
$f_{x,t}$	divertor target flux expansion
$\beta_{\mathrm{pol},t}$	poloidal angle between strike-line and divertor target
γ	field line incidence angle at divertor target

Magnetic fields

$B_{\mathrm{tot},u}$	total magnetic field at OMP
$B_{p,u}$	poloidal magnetic field at OMP
$B_{\phi,u}$	toroidal magnetic field at the OMP
B_{tot}	total magnetic field at R_{geo}
B_{ϕ}	toroidal magnetic field at R_{geo}
$B_{\phi,v}$	vacuum toroidal magnetic field at R_{geo}
$\langle B_p \rangle$	poloidal magnetic field averaged around the plasma
$B_{\mathrm{tot},t}$	total magnetic field at target
$B_{p,t}$	poloidal magnetic field at target
$B_{\phi,t}$	toroidal magnetic field at target

Plasma parameters

I_{P}	plasma current
ϕ_{dia}	plasma toroidal flux (Diamagnetic loop)
$\mathrm{W}_{\mathrm{MHD}}$	plasma stored energy
β_p	poloidal beta (ratio of kinetic to magnetic pressure)

ρ	density
c_p	specific heat capacity
k	thermal conductivity
D	thermal diffusivity

Stationary power exhaust

P_{SOL}	power entering the SOL
P_{in}	power to the inner divertor
P_{out}	power to the outer divertor
c_{div}	fraction of P_{SOL} to that divertor
$q_{\perp,t}$	perpendicular heat flux, at target
$q_{p,t}$	poloidal heat flux, at target
$q_{\parallel,t}$	parallel heat flux, at target
$q_{p,u}$	poloidal heat flux, upstream
$q_{\parallel,u}$	parallel heat flux, upstream
A_{wet}	heat wetted area, at target
$\lambda^*_{\mathrm{int},t}$	SOL integral power width, at target
$\lambda^*_{q,t}$	SOL power width, at target
S^*_t	SOL divertor spreading factor, at target
$\lambda_{\mathrm{int},u}$	SOL integral power width, upstream
$\lambda_{q,u}$	SOL power width, upstream
S_u	SOL divertor spreading factor, upstream
$\lambda^{\mathrm{RCP}}_{T,u}$	SOL temperature fall-off length, upstream, from RCP
$\lambda^{\mathrm{TS}}_{T,u}$	SOL temperature fall-off length, upstream, from TS
$\lambda^{\mathrm{Spitzer}}_{q,u}$	SOL power width, upstream, using Spitzer approximation

ELM power exhaust

$\Delta \mathrm{W}_{\mathrm{MHD}}$	variation of plasma stored energy during the ELM
ΔE_{ELM}	relative ELM size [%]
$E^{\mathrm{ISP}}_{\mathrm{ELM}}$	ELM energy deposited at inner target
$E^{\mathrm{OSP}}_{\mathrm{ELM}}$	ELM energy deposited at outer target
$\tau^{\mathrm{IR}}_{\mathrm{ELM}}$	ELM energy pulse duration, at divertor target
$\tau^{\mathrm{D}\alpha}_{\mathrm{ELM}}$	ELM-induced D_α spike duration
$\tau_{\parallel,\mathrm{ion}}$	pedestal ion transit time in the SOL
$\varepsilon^{\mathrm{peak}}_{\perp,t}$	peak ELM perpendicular energy fluence, at target
$\varepsilon^{\mathrm{peak}}_{\parallel,t}$	peak ELM parallel energy fluence, at target
$\varepsilon^{\mathrm{peak}}_{\parallel,u}$	peak ELM parallel energy fluence, mapped upstream
$\lambda^{\mathrm{ELM}}_{\mathrm{int},u}$	ELM integral power width
$\lambda^{\mathrm{ELM}}_{q,u}$	ELM power width
S^{ELM}_u	ELM divertor spreading factor

1 Introduction

Energy use is a fundamental enabler for an improved quality of life, yet historically energy generation has come at an extreme cost to the environment. Thermonuclear fusion energy can change such a trade-off between living standards and environment. This doctoral thesis contributes to the fusion research efforts. After briefly describing the challenges of the current world energy supply scheme in section 1.1, the concept of thermonuclear fusion is outlined in section 1.2 and one approach to safely realize it on earth, the tokamak concept, is explained in section 1.3. The power exhaust issue and the thesis main objectives are described in section 1.5. The thesis structure is outlined in section 1.6.

1.1 The world growing energy demand

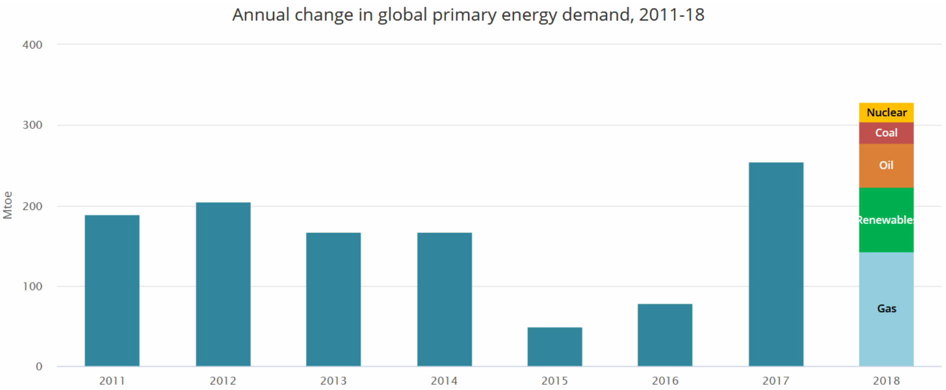

Figure 1.1 – Annual change of global primary energy demand, in Megatoes, from 2011 to 2018 (one toe, or "tonne of oil equivalent", is a unit of energy equal to 41.868 gigajoules). In 2018, most of the energy growth is met by fossil fuels (gas, oil, coal) [1]. *IEA, All rights reserved.*

A recent study [1] from the International Energy Agency (IEA) shows that the global energy demand grew by 2.3% in 2018, nearly twice the average rate of growth since 2010, when the global economy started recovering from the financial crisis. The energy demand is driven by a strong global economy and increased heating and cooling needs, as average winter and summer temperatures, in some regions, exceeded historical records in 2018.

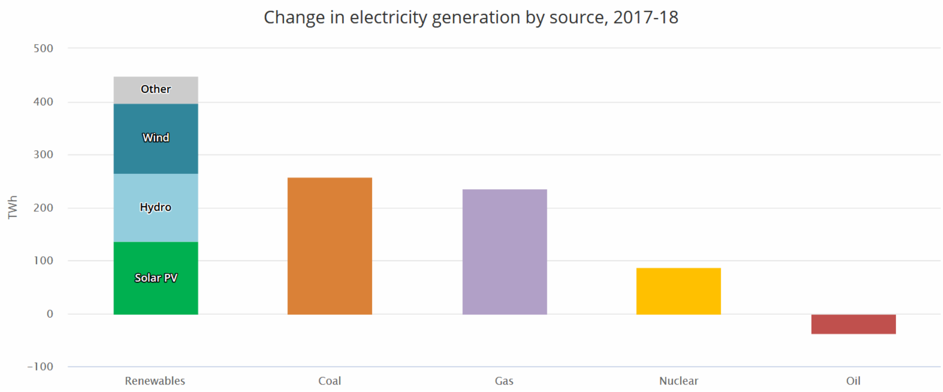

Figure 1.2 – Change in electricity production by source, between 2017 and 2018. Although most of the growth is met by renewables, the contribution of fossil fuels is also important, driving up CO2 emissions [1]. *IEA, All rights reserved.*

This growth in global energy demand was mostly (70%) met by fossil fuels, principally natural gas, as the growth of renewable energy sources, such as solar and wind is, unfortunately, not fast enough to meet the energy demand. Natural gas is the fuel choice of the year, followed by renewables, oil, coil and nuclear, see figure 1.1. As a result, global energy-related CO2 emissions rose by 1.7% in 2018, hitting a new record of 33 Gigatonnes in 2018. A third of this comes from coal power plants alone.

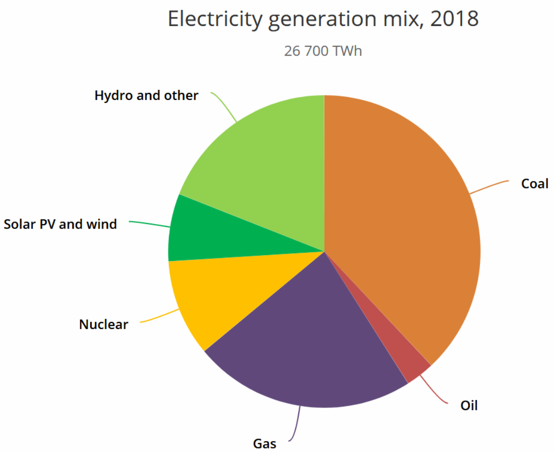

Figure 1.3 – Electricity generation mix in 2018, showing that fossil fuels (coal, oil, gas) provide the great majority of the electricity [1]. *IEA, All rights reserved.*

Interestingly, half of the energy demand growth is due to higher electricity needs, with the demand of global electricity increasing by 4% in 2018 to more than 23000 TWh. Although renewables and nuclear power met the majority of demand growth, electricity generation from gas and coal power plants also increased considerably, figure 1.2, driving up CO2 emissions.

The current electricity generation mix is highly dependent on fossil fuels, figure 1.3, and therefore an inevitable source of CO2 emissions. This mix could drastically change with the arrival of nuclear fusion power plants, based on a potentially clean and virtually limitless energy source. Fusion, the nuclear reaction that powers the stars, offers the prospect of a zero-carbon energy source but it also presents many, so-far insurmountable, physical and engineering challenges. The next sections describe the characteristics of thermonuclear fusion reactions and one particular concept being implemented to realize it as a safe and viable energy source, the "tokamak" device.

1.2 Thermonuclear fusion

Nuclear fusion is a nuclear reaction. A nuclear reaction transmutes atoms of one element into atoms of another by rearranging, and sometimes altering, the elementary particles composing their nuclei, i.e. protons and neutrons (often known as nucleons). The energy released during the reaction corresponds to the increase in the binding energy of the nuclei between initial and final states or, equivalently, the decrease in total nuclear mass. This energy is normally converted into kinetic energy of the reaction products and/or photons.

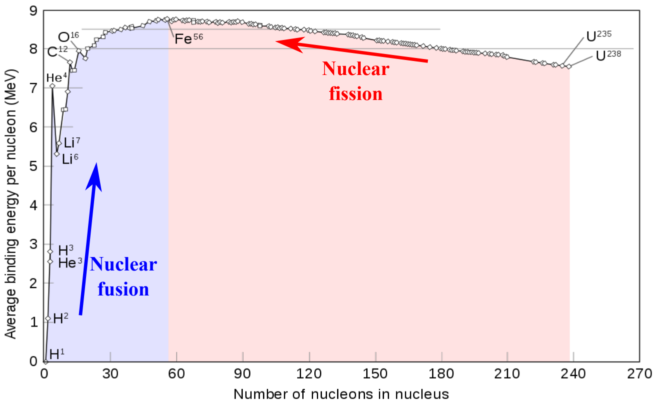

Figure 1.4 – Average binding energy per nucleon as a function of the number of nucleons in the nucleus. A reaction that increases the binding energy can occur by either the merging of light elements (blue arrow) or the fission of heavy elements (red arrow). *Adapted from Wikipedia.*

As shown in figure 1.4, the binding energy per nucleon is less than maximum for both light and heavy elements, maximizing at an intermediate value corresponding to iron (mass number A $\approx$ 56, the number of nucleons). The shape of the binding energy curve is the result of the competition between the strong short-range nuclear force and the weaker long-range Coulomb force, and implies that there are just two types of nuclear reactions that release energy. These are (1) splitting heavy elements apart ($A > 56$), known as *nuclear fission*, and (2) fusing light elements ($A < 56$), known an *nuclear fusion*.

For two light elements to undergo a nuclear fusion reaction, their nuclei must be in very close proximity to each other, i.e. at a distance of the order of their nuclear diameters. However, at such a distances, the positively charged nuclei experience a strong repulsive Coulomb force. With a sufficiently high kinetic energy, this repulsive Coulomb force can be overcome and the two nuclei can fuse. This reaction is known as *nuclear fusion*.

At the temperatures required for light nuclei to attain these kinetic energies, matter is in a state of *plasma*. The plasma is the fourth state of matter (after the solid, liquid and gas sequence) and the most common state of matter in the universe. A plasma is an electrically neutral medium of unbound positive (nuclei) and negative (electrons) charges, making it highly electrically conductive. Although these particles are unbound, they still interact through electro-magnetic forces, so that plasmas often exhibit collective behaviours and can, under certain conditions, be described as a fluid.

To reach fusion temperatures (∼100 million degrees), the plasma must be confined in a volume and heated. In nature (stars), the source of confinement is generally gravitational. Plasmas created in a laboratory, in contrast, have an insufficient mass and must be otherwise confined. Aside from gravitation, another confinement strategy applied to plasmas is using strong magnetic fields (*magnetic confinement*).

The magnetic confinement approach is used in several configurations, with the most promising being the tokamak, described in the next section, and the stellarator. These devices exploit the fact that, in a magnetic field, charged particles experience a Lorentz force, which causes them to follow the magnetic field lines. Using the Lorentz force, the simplest form of magnetic confinement is a solenoid, where plasma particles will spiral around and along the field lines. This device prevents an overall lateral motion, but the field line ends remain problematic. A solution is to bend the solenoid into a loop, thereby forming a torus.

1.3 The tokamak concept

The tokamak is a device which uses strong magnetic fields to confine a hot plasma in the shape of a torus. First developed by soviet research in the late 1960s, the tokamak configuration is, currently, the leading candidate for a future nuclear fusion reactor.

Magnetic field structure A set of coils, around the entire vacuum vessel, creates a strong magnetic field around the torus, known as the *toroidal magnetic field*, see figure 1.5. The toroidal field alone is, however, not sufficient for the confinement of a plasma. For geometrical reasons, the field on the outside of the torus is weaker than on the inside. This asymmetry causes electrons and ions to drift in opposite vertical directions, which creates a charge separation and therefore a vertical electric field. In the presence of both an electric field $\vec{E}$ and a magnetic field $\vec{B}$, plasma particles experience an $\vec{E} \times \vec{B}$ drift

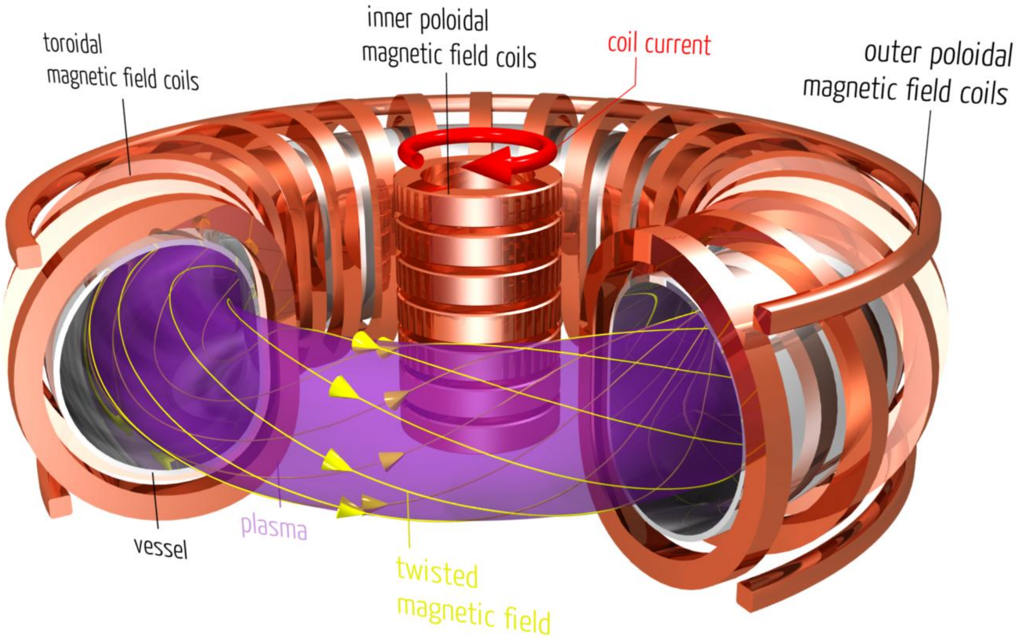

Figure 1.5 – Schematic view of a tokamak, showing the toroidal and poloidal magnetic field coils (in orange), the vessel (in light grey), the plasma (in purple) and the helical magnetic field lines (in yellow). *Source: "The long way to steady state fusion plasmas - the superconducting stellarator device Wendelstein 7-X" by Prof. T. Klinger, Swiss Nuclear Forum, EPFL - Lausanne, Switzerland, 18 February 2016.*

in the radial direction, which causes the entire plasma to hit the outer vessel wall. The solution is to add a *poloidal* component to the magnetic field, which shapes the field lines so that they twist around the plasma like the stripes of a candy-cane. In such a field, a plasma particle finds itself in the outside region, where it drifts away from a field line, for instance radially outwards, then it follows magnetic field lines and finds itself in the inside region, where it drifts towards the same field line. This cancellation is perfect as this helical field configuration was found to significantly improve particle confinement. A poloidal field is created by a set of inner and outer magnetic field coils, see figure 1.5, with the outer coils used exclusively for shaping the helical field lines and therefore controlling plasma shape and position. The principal poloidal field is, however, generated by the plasma current flowing in the toroidal direction.

Plasma current A plasma current flow around the torus is usually sustained, in present-day tokamaks, inductively, using the inner poloidal magnetic field coils, which act as a primary transformer circuit, while the plasma is the secondary transformer circuit. This scheme exploits Faraday's law of induction, where a time-varying magnetic field flux across a closed surface induces an electric field around it. In the tokamak, the current in the inner magnetic field coils is ramped up so that the poloidal field flux inside the plasma steadily varies with time. The resulting toroidal electric field drives an electrical current through the plasma. As the current in the primary transformer coils cannot be ramped indefinitely, such an inductive plasma current can only be sustained for a limited time. This limitation is incompatible with the required steady-state operation of a future fusion reactor. Intensive research is, therefore, directed towards studying alternative, non-inductive and long-living scenarios, with the plasma current driven by a combination of the self-generated bootstrap current and auxiliary heating systems[2, 3].

Auxiliary heating systems To reach fusion conditions, the plasma must attain temperatures of hundreds of millions degrees. As the plasma has a finite electrical resistivity, the toroidal current heats the plasma through the Joule effect (Ohmic heating), with a higher plasma current producing higher plasma temperatures. However, Ohmic heating becomes less effective at these higher temperatures because the electric resistivity of the plasma decreases with higher temperature, as $T_e^{-3/2}$. Auxiliary heating systems are, therefore, crucial not only for sustaining the plasma current in steady state conditions, but also to reach the temperatures required to ignite the fusion reactions. Such systems include neutral beam heating, where a high-energy beam of neutral deuterium atoms is injected into the plasma, and radio frequency heating, where high-frequency electromagnetic waves are launched and absorbed by the plasma.

1.4 The nuclear fusion power plant

A future nuclear fusion power plant based on the tokamak concept will initially employ fusion between deuterium and tritium (D-T),

$$D + T \rightarrow \alpha + n + 17.6 \text{ MeV} \tag{1.1}$$

because the D-T reaction has the largest cross section amongst the possible nuclear fusion reactions and is, thus, the easiest to initiate. While deuterium is abundant in nature, tritium is extremely rare, with a short lifetime, and must be produced. The solution is to breed tritium directly inside the reactor by irradiating a lithium-bearing layer surrounding the vessel first-wall, termed *blanket*, with the neutrons, created by the fusion reactions. The tritium breeding reactions are

$$_3\mathrm{Li}^6 + n(\mathrm{slow}) \rightarrow \alpha + T + 4.8 \text{ MeV} \tag{1.2}$$

$$_3\mathrm{Li}^7 + n(\mathrm{fast}) \rightarrow \alpha + T + n - 2.5 \text{ MeV} \tag{1.3}$$

where α is an He-4 nucleus, T the tritium nucleus. Although the largest fraction of natural lithium is $_3\mathrm{Li}^7$ ($\approx$93%), the $_3\mathrm{Li}^6$ reaction is easier to initiate and, therefore, dominates the breeding of tritium [2]. The known reserves of lithium are sufficiently large to last thousands of years. Only a small quantity of tritium is required to create the initial plasma, before D-T fusion is ignited.

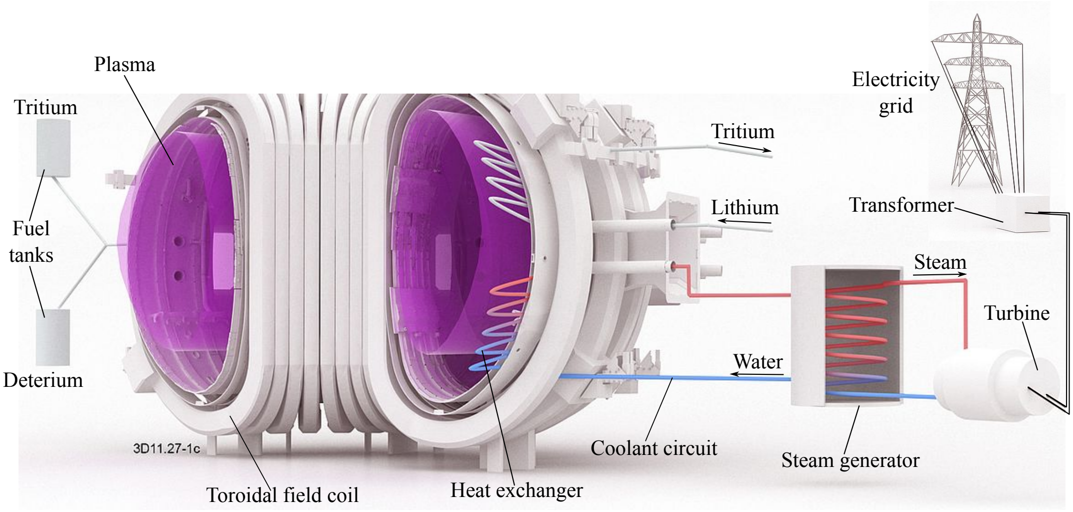

Figure 1.6 – Schematic view of a nuclear fusion reactor based on the tokamak concept. Note that the blanket is replaced by the sketch of a heat exchanger. Indeed, one of the functions of the blanket is to transform the kinetic energy of fusion-produced fast neutrons into heat, which is removed by a set of cooling tubes and transported to an external steam generator. This generator is coupled to a turbine to convert this heat into electricity. *Adapted from https://www.euro-fusion.org/programme/demo/.*

The reactor blanket functions also as a heat exchanger, see figure 1.6. The fusion-produced fast neutrons that penetrate the blanket are slowed down (moderated) to thermal energy levels, to increase their cross-section with ${}_3\mathrm{Li}^6$. The energy resulting from the slowing down heats the blanket. Embedded in the blanket is a set of cooling tubes that extract this heat, ultimately converting it into electricity through a thermal conversion system (e.g. a steam generator coupled to a turbine).

A future nuclear fusion reactor aims at conditions where the plasma temperature is maintained by compensating the energy losses solely with alpha heating, without a need of auxiliary heating. By analogy with the burning of fossil fuels, this is called *ignition*. The condition for ignition is [3]

$$n\ \tau_E > \frac{12}{\langle\sigma v\rangle}\frac{T}{E_\alpha} \tag{1.4}$$

with n and T the plasma density and temperature, τ_E the energy confinement time, $\langle\sigma v\rangle$ the velocity averaged cross section of D-T fusion and $E_\alpha = 3.5$ MeV the alpha particle energy. Taking into account the temperature dependence of $\langle\sigma v\rangle$, it can be shown that the ignition condition can be approximated by

$$n\ T\ \tau_E > 3\cdot 10^{21}\ \mathrm{m^{-3}\ keV\ s} \tag{1.5}$$

which illustrates the interplay between density, temperature and energy confinement time.

1.5 The power exhaust issue: motivation for this thesis

Although the magnetic field confines the plasma, collisions and turbulence transport particles radially towards the first-wall. To create a separation between the hot confined plasma and the inevitable plasma-wall interaction, a future fusion reactor will likely be based on a diverted magnetic configuration. Here, a null in the poloidal field in the poloidal cross section, termed *x-point*, leads to a separation in closed and open field line regions. The closed field line region, containing the hot fusion plasma, is surrounded by the open field line region, termed *Scrape-Off Layer* (SOL). The SOL receives the leaking, but still charged, plasma particles, referred to as *exhaust particles*, and directs them towards dedicated wall elements, known as *divertor plates*, designed to sustain high heat fluxes and located at a distance from the hot plasma.

At the divertor plates the heat flux must remain below the technologically acceptable maximum for actively cooled surfaces, which is of the order of 5 MW m^{-2}, increasing to 20 MW m^{-2} for transients [4]. Also, to avoid excessive sputtering and erosion of the surface, the electron temperature at the target must remain below 5 eV. The limit on the perpendicular heat flux translates to a maximum parallel (to the field lines) target heat flux of

$$q_{\parallel,t}^{\max} = \frac{q_{\perp,t}^{\max}}{\sin\gamma} = \frac{5\ \mathrm{MW/m^2}}{\sin 3^\circ} \sim 100\ \mathrm{MW/m^2}$$

where γ is the field line grazing angle at the target. The value of 3° is the minimum acceptable angle due to engineering constrains in ITER [5], and a typical value for most projected fusion reactors.

The parallel target heat flux predicted for a future nuclear fusion experiment is, however, considerably higher than this material limit. Without power losses from the SOL to the targets, the $q_{\parallel,t}$ of a tokamak would be

$$q_{\parallel,t} = \frac{c_{\mathrm{div}} P_{\mathrm{sep}}}{2\pi R_t \lambda_{q,u}} \frac{B_{\mathrm{tot},u}}{B_{p,u}} \tag{1.6}$$

where c_{div} is the fraction of the power crossing the separatrix P_{sep} that is directed towards the considered divertor target, R_t the target major radius, $\lambda_{q,u}$ the characteristic heat exhaust channel width and $B_{\mathrm{tot},u}$ and $B_{p,u}$ the total and poloidal fields at the plasma outboard mid-plane. Using equation 1.6 with the current parameters of the EU DEMO project [6] yields an unmitigated parallel heat flux of

$$q_{\parallel,t}^{\mathrm{DEMO}} \sim 6\ \mathrm{GW\ m^{-2}}$$

i.e. 60 times larger than the material limit. The heat flux must, therefore, be strongly mitigated in the divertor before reaching the targets. Mitigation can be achieved through seeded impurity radiation, which uniformly distributes the power over the entire tokamak walls and does not, thus, create high deposited peak heat fluxes. However, the absolute power and the radiation fraction required from a fusion reactor are significantly high ($\sim$ 95% in DEMO [7]) and, to date, largely exceed any value demonstrated in present day devices. This problem is known as the *power exhaust issue*.

Operating the divertor in a (partially) *detached regime* could simultaneously reduce target parallel heat fluxes below the technological limit and target temperature below 5 eV. This is the reference regime for ITER [4] and, most likely, also for DEMO. Experiments show, however, that accessing a detached state can result in a plasma with significantly degraded core performance, which would lead to unacceptably low fusion power in a reactor. A successful unification of a performant core and a detached divertor may be more easily obtainable using magnetic configurations alternative to the conventional Single-Null (SN) configuration, which is, to date, the most widely explored configuration in present-day tokamaks and that adopted for ITER. Experimentally assessing the potential power exhaust benefits of alternative divertor concepts is, therefore, important to the fusion community.

This thesis experimentally assesses the power exhaust properties of an unprecedented range of alternative magnetic configurations, generated in the Tokamak à Configuration Variable (TCV) at the Swiss Plasma Center of the École Polytechnique Fédérale de Lausanne (EPFL), Switzerland. It represents, in this field of research, the first systematic study of the impact of magnetic geometry changes on SOL power exhaust. The main objectives of this work are to

- reduce the power exhaust challenge with magnetic divertor geometry, i.e. experimentally determine which modifications to the magnetic divertor geometry modify the target heat deposition area. A broader deposition area is expected to allow access to the detached regime with better core performance.
- improve the current understanding of SOL heat and particle physics. Testing existing models and regressions in diverse operational scenarios and divertor shapes will increase the confidence in current extrapolations to a future fusion reactor.

To achieve these goals, a large experimental database is created from a wide range of experiments, where divertor heat loads are characterized as a function of (1) magnetic geometry (from conventional and alternative concepts), (2) plasma confinement mode (low/high confinement) and (3) divertor operational regime (attached/detached). Current SOL transport models and scaling laws are tested against TCV results and, where they are unable to explain the measurements, alternative transport models are formulated.

1.6 Outline of this thesis

This thesis is structured as follows:

- Chapter 2 introduces the TCV tokamak, outlining its unique plasma and magnetic divertor shaping capabilities and describing the diagnostics used in this thesis.
- Chapter 3 presents the major improvements to the TCV infrared (IR) thermography systems performed as part of the thesis work. These include a new control software for the IR cameras, improvements to the data analysis routines and the commissioning of a new IR system.
- Chapter 4 introduces the definitions and nomenclatures that are used, in this thesis, to describe the Scrape-Off Layer and divertor geometry. Important analytic relations, based on the SOL field line geometry, are also derived. Finally, the alternative divertor concepts, that are studied in this thesis, are presented, together with their potential power exhaust benefits.
- Chapter 5 reviews and extends current SOL heat transport models that, in the next chapters, are used to interpret the experimental measurements. These include models for transport in the SOL surrounding the confined plasma and/or the SOL in the divertor region (i.e. between x-point and divertor target), based on a number of heat transport processes (diffusion, convection, conduction, particle drifts).
- Chapter 6 studies the power sharing between divertors and target heat deposition area as a function of the divertor and core plasma geometry, for plasmas in the low-confinement mode (L-mode), with divertors in the attached, high-recycling regime.
    - In section 6.1, the study focusses on the Single-Null configuration, the most common in current tokamaks, and the varied quantities are four divertor geometry parameters (divertor leg length, target flux expansion, plasma triangularity, target radius) and two core plasma parameters (plasma current and magnetic field direction). Several, partly unexpected, effects of plasma shape and divertor geometry on the SOL heat flux channel width are observed. These are compared to the transport models presented in chapter 5 and to prominent multi-machine scaling laws. Potential implications of these results for the design of the magnetic divertor in a future fusion reactor are discussed.
    - In section 6.2, an alternative divertor geometry, the Snowflake (SF) configuration, is probed and its power exhaust studied as a function of the x-point separation, the relative positioning of primary and secondary x-points and the magnetic field direction. Again, the effects of divertor geometry changes on the SF power exhaust are interpreted with models discussed in chapter 5, and

  potential implications of these findings for the design of the magnetic divertor in a future fusion reactor are discussed.
  - In section 6.3, with a fixed Single-Null shape, the divertor operational regime is manipulated to perform a gradual transition to the detached state, through either impurity seeding or divertor fueling. The resulting changes in target heat loads, and the difference between the two detachment schemes, are discussed.

- Chapter 7 studies the power exhaust of plasmas in the high-confinement mode (H-mode), again with both divertors in the attached, high-recycling regime. ELMy H-mode and ELM-free H-mode, are considered. The L-H transition is analysed in section 7.1, exploring its effect on target heat loads for a standard Single-Null configuration. This study then extends to ELMy H-mode plasmas, discussing separately target heat loads in-between ELMs, section 7.2, and during the ELM event, section 7.3. Finally, potential implications of these findings for the design of the magnetic divertor in a future fusion reactor are discussed.

- Chapter 8 summarizes the main results and conclusions of this thesis.

2 The TCV tokamak

This chapter introduces the TCV tokamak, first outlining its unique plasma and magnetic divertor shaping capabilities in section 2.1, then describing the main diagnostics used for this work in section 2.2.

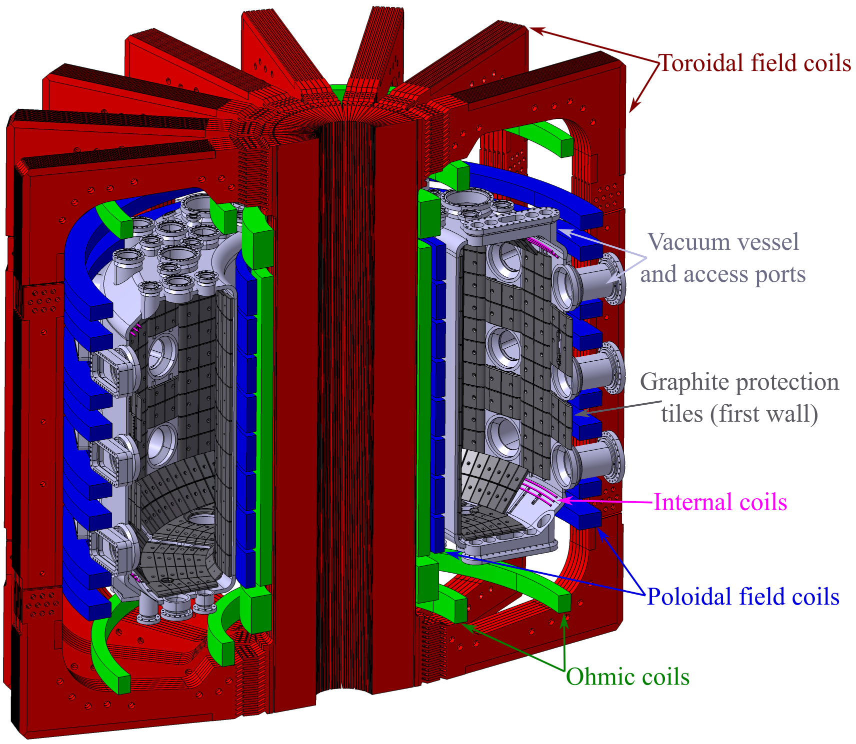

Figure 2.1 – Schematic drawing of a section of TCV, showing the Ohmic transformer in green, the poloidal field coils in blue, the internal coils in purple, the toroidal field coils in red and the vacuum vessel in grey. The vessel is almost entirely covered by graphite protection tiles, shown in dark grey (*CAD picture courtesy of M. Touissant*). The Ohmic coil in the central column is not shown.

The Tokamak à Configuration Variable (TCV) [8], figure 2.1, is a medium sized, highly elongated tokamak, capable of producing limited and diverted plasma configurations. It is located at the Swiss Plasma Center (SPC), embedded within the Swiss Federal Institute of Technology of Lausanne (École Polytechnique Fédérale de Lausanne), in Switzerland and produced its first plasma in November 1992. TCV features a major radius R_{geo} of 0.88 m, a minor radius a of 0.25 m, a vacuum toroidal field $B_{\phi,v}$ up to 1.4 T and a plasma current I_{P} up to 1 MA. The main goal of TCV is to investigate effects of the magnetic configuration on tokamak physics. For this reason, the machine was designed such that it can produce diverse plasma shapes without requiring hardware modifications. The system of magnetic field coils, shown in figure 2.1, features an OH transformer and sixteen independently powered shaping coils, located between the vacuum vessel and the toroidal field coils. Internal coils are used to control axisymmetric plasma instabilities (tokamak plasmas are vertically unstable) with high growth rates.

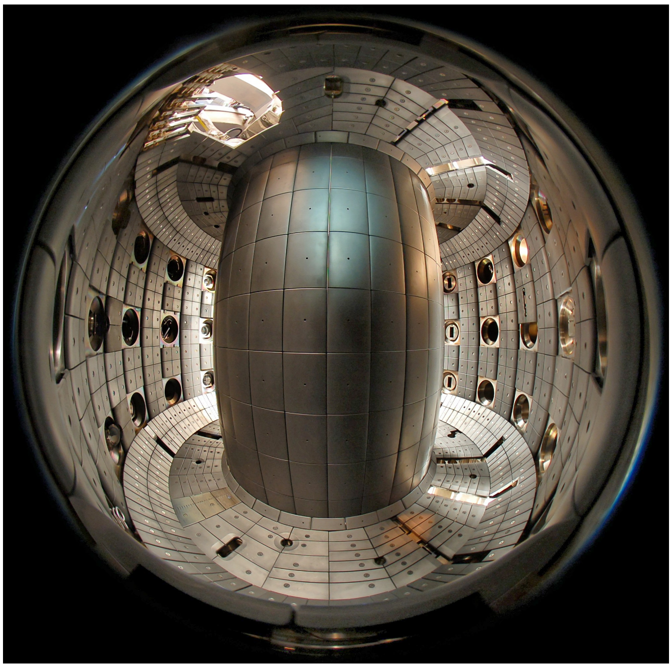

Figure 2.2 – Photograph of the inside of TCV, showing the graphite protection tiles that cover almost the entire vacuum vessel.

Over 95% of the vessel wall is covered by graphite protection tiles, see figure 2.2. These tiles protect the vacuum vessel from the plasma and permit a wide range of possible locations for the contact point between plasma and walls. Using carbon as tile material has several advantages, such as simple manufacturing and attractive thermal properties. For instance, carbon has a high thermal conductivity and, at very high temperature, sublimes instead of melting, which is the case for tungsten, the material used in other tokamaks. The sublimed carbon can radiate a lot of power in the region of the tile surface, making the wall robust to accidental plasma contact.

2.1 Plasma and divertor shaping capabilities

The magnetic configuration of a TCV discharge is prepared using the free-boundary equilibrium code FBTE [9], which computes the poloidal field coil currents required for a desired magnetic configuration. After the experiment, the actual magnetic configuration is reconstructed using the equilibrium code LIUQE [10], which employs magnetic measurements from a large array of pick-up coils and flux loops as inversion constraints. TCV plasmas and magnetic fields are described using a cylindrical coordinate system defined by the right-handed orthonormal triplet (R, φ, Z) [11]. The radius R is positive towards the outside of TCV and zero on TCV's vertical axis, the Z axis points towards the top of the machine and is zero at the equatorial plane and the toroidal angle φ is positive counter-clockwise seen from the top.

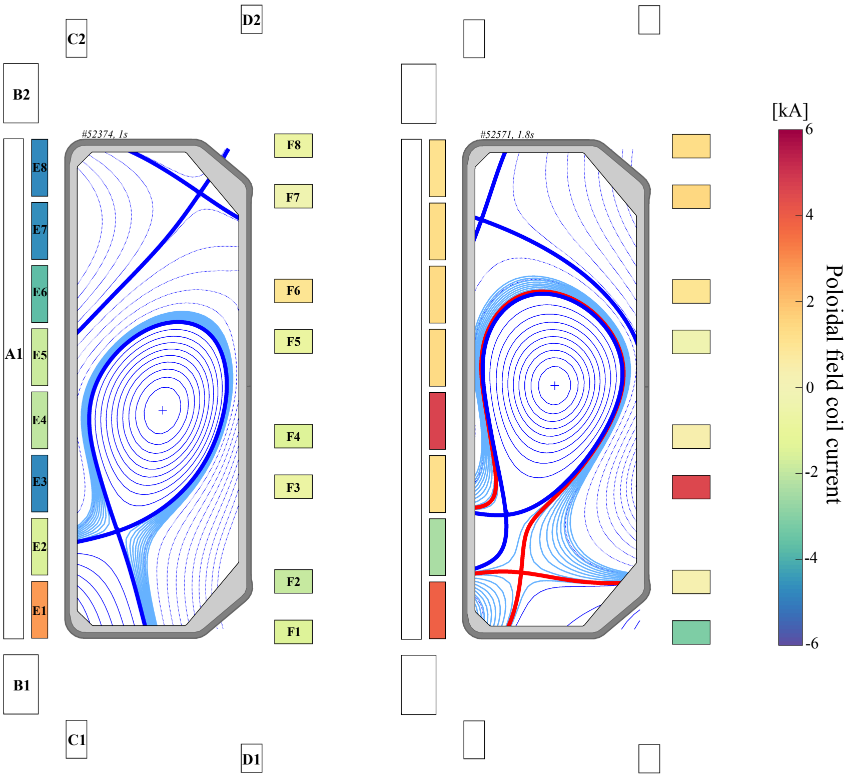

a)
Single-Null configuration
with negative upper triangularity

b)
Snowflake Minus configuration

Figure 2.3 – Example of two unconventional plasma and divertor shapes that can be generated in TCV, both studied in this work, (a) a Single-Null configuration where the upper half of the plasma has an unconventional inverse-D shape (negative plasma upper triangularity) and (b) a Snowflake Minus magnetic configuration. The names and positions of the poloidal field coils, as well as the currents, are indicated.

With 16 independently powered poloidal-field coils, TCV benefits from unique plasma and magnetic divertor shaping capabilities. The plasma shape above and below the magnetic axis can be different, as demonstrated in figure 2.3a, where the upper half of the plasma has an unconventional inverse-D shape, while the lower half has a standard D-shape, similar to that in other tokamaks. The poloidal field coil systems allows, also, complex control of the magnetic fields in the divertor region, generating innovative magnetic divertor concepts, such as the so-called Snowflake Minus configuration, shown in figure 2.3b.

2.2 Diagnostics used in this thesis

The main diagnostic systems considered in this work are described in the following sections. They include three infrared thermography systems (section 2.2.1), Langmuir probes (section 2.2.2), a fast reciprocating probe (section 2.2.3), a Thomson scattering system (section 2.2.4), bolometers (section 2.2.5) and thermocouples (section 2.2.6).

2.2.1 Infrared Thermography system

An infrared thermography system is used to simultaneously measure the divertor heat loads at each strike point for a wide range of magnetic divertor configurations. The TCV infrared (IR) thermography system towards the end of this thesis consists of three IR sub-systems, vertical (section 2.2.1.1), horizontal (section 2.2.1.2) and tangential (section 2.2.1.3). The principles of IR thermography are explained in section 2.2.1.4. Each IR camera is temperature calibrated in-situ using thermocouples (section 2.2.6) and heating elements embedded in graphite protection tiles in the field of view of each system. The inversion of target temperature measurements into heat flux, by modelling the temperature evolution in the graphite tile, is described in section A.4. Some improvements made to the TCV IR thermography system as part of this thesis work, in terms of control software and data analysis tools, is described in chapter 3.

2.2.1.1 Vertical Infrared System (VIR)

The Vertical InfraRed system (VIR) is mounted on the top of TCV and images the vessel floor through a relay optic, figure 2.4a-b, covering the outer strike point (OSP) of a typical diverted plasma configuration, figure 2.4c. Until early 2017, the camera was a *Thermosensorik CMT256 M HS*, sensitive in the wavelength range [1.5 to 5.1] μm and operated with a filter limiting the sensitivity from [4.5 to 5.1] μm. Typical frame rate and spatial resolution were 400 Hz and $\approx$ 2.5 mm in full-frame mode, respectively. A frame rate of up to 15 kHz was possible for a sub-frame. The VIR system now uses an *IRCAM Equus 81k M MWIR* camera, sensitive in the wavelength range [3.7 to 4.8] μm, with no filter installed. Typical frame rate and spatial resolution are 200 Hz and $\approx$ 2 mm in full-frame mode, respectively. The frame rate can now be increased up to 30 kHz

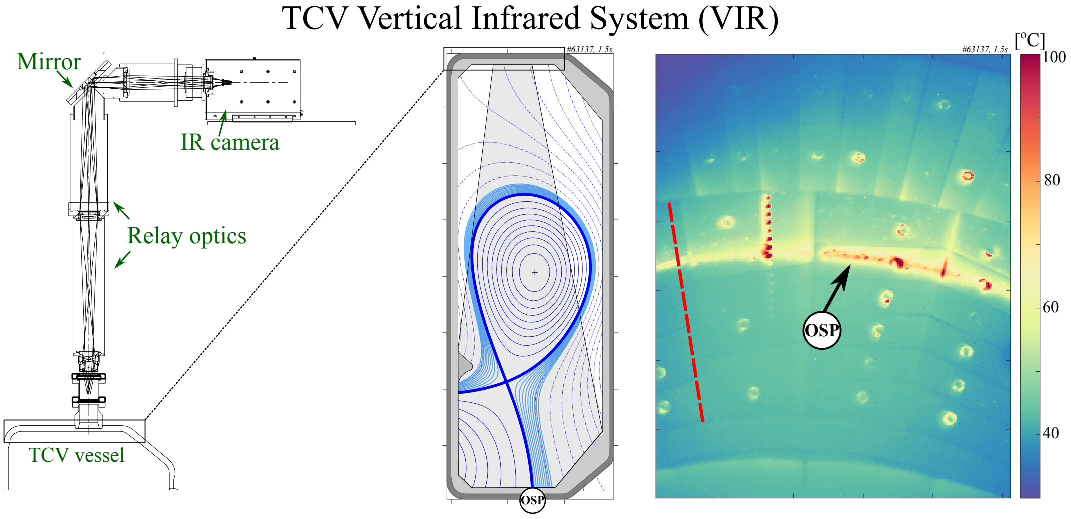

a) b) c)

Figure 2.4 – (a) Schematic drawing of the VIR system, showing the position of the IR camera, mirror and relay optics, above the TCV vessel. (b) Poloidal cross section of TCV vessel, showing the VIR camera field-of-view and a standard Single-Null configuration. (c) Full-frame temperature-calibrated image from the VIR system, showing the thermal footprint of the outer strike point (OSP) of the same Single-Null. The red dashed line indicates the part of the image typically used for data analysis.

for a sub-frame.

2.2.1.2 Horizontal Infrared System (HIR)

The Horizontal InfraRed system (HIR) is mounted on a lateral port, alternatively on a lower or a mid plane port, figure 2.5a, and images a portion of the central column covering the inner strike point (ISP) of a typical diverted plasma configuration, figures 2.5b-c. As the VIR system, the HIR system also uses an *IRCAM Equus 81k M MWIR* camera. While the camera is sensitive in the wavelength range [3.7 to 4.8] μm, a long-wavelength pass filter typically reduces the range to [4.1 to 4.8] μm. Typical frame rate and spatial resolution are 200 Hz and $\approx$ 0.8 mm in full frame, using a 25 mm focal-length lens. The HIR field-of-view can be doubled with a 12.5 mm focal-length lens, with a corresponding factor of 2 reduction in the spatial resolution. The frame rate can be increased up to 30 kHz for a sub-frame.

The HIR system shows toroidal temperature gradients on the inner column protection tiles of TCV, figure 2.5c. These temperature gradients are due to the decrease of the curvature radius of the tile surface towards the tile edges leading to higher grazing angle of the magnetic field lines, a larger perpendicular heat flux and, consequently, a higher temperature [12]. The surface curvature radius decreases only near the tile edges and does not change significantly up to 3 cm from the central screw. The area used for the

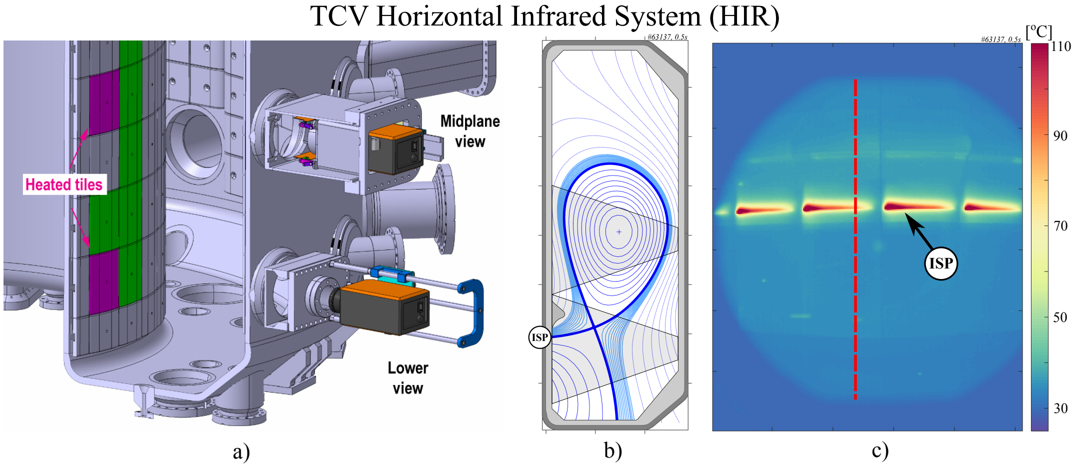

Figure 2.5 – (a) Schematic drawing of the HIR system, showing the two employed lateral ports and the heated tiles used for the in-site calibration to temperature. (b) Poloidal cross section of TCV vessel, showing the HIR camera field-of-views and a standard Single-Null configuration. (c) Full-frame temperature-calibrated image from the HIR system, showing the thermal footprint of the inner strike point (ISP) of the same Single-Null. The red dashed line indicates the part of the image typically used for data analysis. *CAD picture courtesy of M. Touissant.*

analysis is typically located ≈ 1.6 cm to the right of the screw.

2.2.1.3 Tangential Infrared System (TIR)

The Tangential InfraRed system (TIR) is mounted on a lower lateral port and uses a system of two mirrors to image a field-of-view tangential to the torus, figure 2.6a. The plasma-facing mirror is movable to protect both the mirror and the IR camera detector from glow discharge cleaning and wall boronisations. The TIR system images a portion of the floor tilted tiles and vessel outer wall, covering the outer strike point (OSP) of a Super-X magnetic configuration, figures 2.6b-c. As for the VIR and HIR systems, the TIR uses a *IRCAM Equus 81k M MWIR* camera, sensitive in the wavelength range [3.7 to 4.8] μm with no filter applied. Typical frame rate and spatial resolution are 200 Hz and ≈ 1.3 mm in full frame, using a 50 mm focal-length lens.

The TIR system, operational since June 2019, is part of the 2017-2020 TCV divertor upgrade [13]. The main element of this upgrade is the installation of an in-vessel structure to form a more closed divertor chamber, which promises access to divertor regimes with high neutral density and impurity compression in the divertor. The in-vessel structure features a HFS (inner) baffle, a LFS (outer) baffle and LFS port-protection tiles. Since the LFS baffles protrude significantly into the vacuum vessel, they hide the floor tilted tiles in the VIR field-of-view. The TIR system design can image these tiles and, in addition, the outer wall port protection tiles.

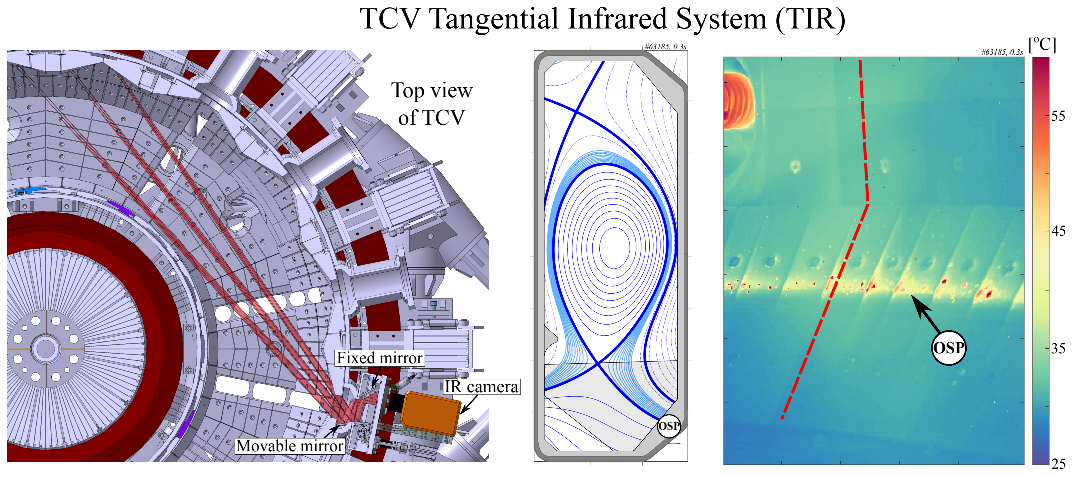

a) b) c)

Figure 2.6 – (a) Schematic drawing of the TIR system, showing the position of the IR camera and the two mirrors, as well as the field-of-view from above. (b) Poloidal cross section of TCV vessel, showing the HIR camera field-of-views and a Super-X configuration. (c) Full-frame temperature-calibrated image from the TIR system, showing the thermal footprint of the outer strike point (OSP) of the same Super-X. The red dashed line indicates a possible line to use for data analysis. *CAD image courtesy of J.-D. Landis.*

2.2.1.4 Principle of IR thermography

Any object emits electromagnetic waves as a result of random movements of its atoms and molecules. The emitted radiation consists of a continuous spectrum of frequencies/wavelengths, depending on various properties of the surface, particularly its temperature. For an object that is a perfect absorber and emitter at all wavelengths, this spectrum is determined by its temperature alone, i.e. not by the body-shape or composition. This idealized object is known as a *black body* (BB), and its spectrum, in thermal equilibrium, is described by Planck's law [14],

$$I_{\mathrm{BB}}(\lambda, T) = \frac{2hc^2}{\lambda^5} \frac{1}{\exp\left(\frac{hc}{\lambda k_B T}\right) - 1} \qquad \left[\frac{W}{sr \cdot m^3}\right] \tag{2.1}$$

where I_{BB} is the black body spectral radiance, h is the Planck constant and k_B the Boltzmann constant. For a real object, its spectral radiance $I(\lambda, T)$ is a fraction of that of the black body, $I(\lambda, T) = \varepsilon(\lambda, T) \cdot I_{\mathrm{BB}}(\lambda, T)$ with $\varepsilon(\lambda, T)$ known as *emissivity*. As Planck's law directly relates the object temperature T to its spectral radiance at a certain wavelength λ, by measuring the radiation emitted by the object at any wavelength it is possible to estimate its temperature. This is the principle of thermography.

Thermography is typically used to measure surface temperatures between 0 and ≈ 3000°C. For this range of temperatures, most of the radiation is emitted with wavelengths between ≈ 1 and ≈ 10 μm, i.e. in the infrared spectral range. Thus, thermography instruments use radiation detectors that are sensitive to infrared wavelengths, which rules out the use of standard visible wavelength sensitive silicon photodetectors.

Most modern thermal cameras feature an array (typically rectangular) of radiation-sensing pixels at the focal plane of a lens, known as Focal Plane Array (FPA), which is cooled to minimise the signal due to its own thermal emission. The IRCAM Equus cameras of the TCV thermography system, for instance, use a Stirling engine cryocooler. Typical materials used for cooled infrared detection include photodetectors based on narrow gap semiconductors, such as indium-antimonide, indium-arsenide, mercury-cadmium-telluride (used in TCV's cameras), lead-sulfide and lead-selenide. The concentration of chemical compounds in the alloy is chosen to tune the optical absorption of the material to the desired infrared wavelengths.

2.2.2 Langmuir probes

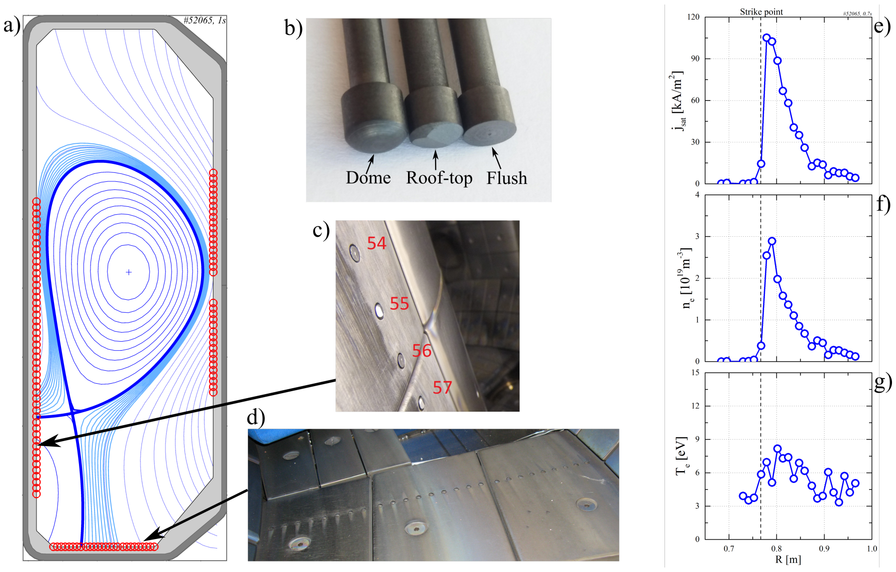

Figure 2.7 – (a) Poloidal cross section of the TCV vessel, showing the location of the wall-embedded Langmuir probes (setup prior the 2019 divertor upgrade) and a standard Single-Null configuration. (b) Picture of probe tip types used in TCV. (c-d) Picture showing the inner column and flat floor probe arrays. (e-f-g) Profiles of ion saturation current, electron density and temperature measured by the Langmuir probes at the outer divertor target of the SN configuration shown in (a). *LP images courtesy of H. De Oliveira*

A Langmuir probe system [15] is used to measure plasma density and temperature at the divertor plates. The TCV Langmuir Probe system setup described here is that prior to the 2019 divertor upgrade. It consists of 114 wall-embedded Langmuir probes (LPs), distributed poloidally around the vessel as shown in figure 2.7a. The probe tips, made of graphite and with a diameter of 4 mm, are dome-shaped for the floor probes, roof-top shaped or flush for the inner column and outer wall probes, see figure 2.7b.

A Langmuir probe is an electrode that, inserted into a plasma, collects a current I that is function of the voltage V applied to the probe and the plasma properties (electron temperature, density and plasma potential). During the experiment, the voltage applied to each Langmuir probe is often swept, using a triangular wave, between -100 V and 80 V at a typical frequency of 330 Hz. The I-V characteristic, for each probe, is then interpolated with the 4-parameter model function [15]

$$I(V) = I_{\text{sat}} \left(1 + \alpha_{\text{sheath}} (V - V_{\text{fl}}) - e^{\frac{V - V_{\text{fl}}}{T_e}} \right) \tag{2.2}$$

where V is the probe potential, I_{sat} the ion saturation current, α_{sheath} the sheath expansion factor and V_{fl} the probe floating potential. The α_{sheath} accounts for the formation of a Debye sheath over the probe head, which can significantly increment the charge collection area, causing an imperfect saturation of the ion current at negative applied voltages. The fit with equation 2.2 yields estimates of the plasma ion saturation current, figure 2.7e, the sheath expansion factor, the floating potential and the electron temperature, figure 2.7g, at the location of each probe. Then, the Bohm criterion

$$I_{\text{sat}} = e n_e c_s A_s \tag{2.3}$$

where c_s is the ion sound speed at the sheath entrance and A_s the probe collection area, yields an estimate of the electron density, figure 2.7f.

2.2.3 Fast Reciprocating Probe

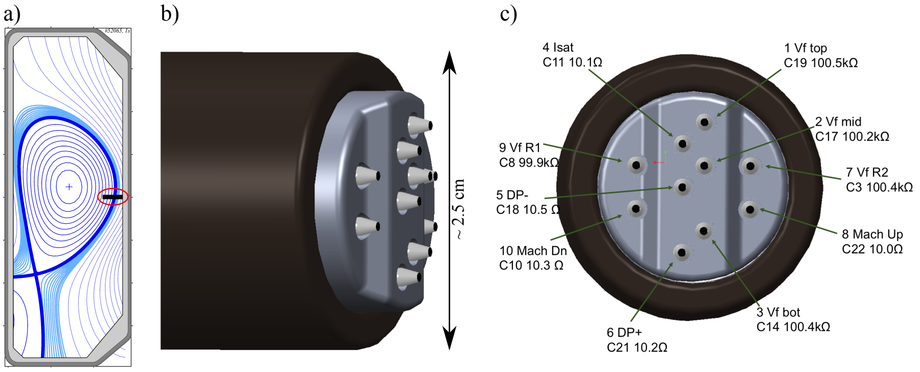

Figure 2.8 – (a) Poloidal cross section of TCV vessel, showing the location of the fast-reciprocating probe and its typical plunge depth. (b) Lateral view of the probe heat. (c) Front view of the probe head, showing the 10 electrodes and their function. *Probe pictures courtesy of C. K. Tsui.*

A fast reciprocating probe (RCP) [16, 17] is used to measure electron density and temperature at the plasma edge and in the Scrape-Off Layer (SOL). The probe is mounted at the outboard mid-plane, figure 2.8a-b, and features 10 electrodes, figure 2.8c. It is electrically isolated to keep its voltage at the floating potential of the plasma.

The working principle of a fast reciprocating probe is that of a Langmuir probe. Some of the 10 electrodes are used to measure the ion saturation current and the plasma floating potential at several positions. A double probe, consisting of two electrodes whose voltage difference is swept between ± 300 V at 1 kHz, providing I-V characteristics every 0.5 ms, yields estimates for the electron temperature T_e, electron density n_e and ion saturation current density j_{sat} in the SOL. The double probe I-V fitting function is [18, 19]

$$I(V) = j_{\text{sat}}\, A_{\text{coll}}\, \tanh\left(\frac{V - V_{\text{off}}}{2k_B T_e/e}\right) + I_{\text{off}} \tag{2.4}$$

with V_{off} and I_{off} fitted offsets and A_{coll} the probe collection area. The expression for A_{coll} accounts for the formation of a Debye sheath on the electrode, which increments its collection area $A_{\text{coll}} = A_0 + l_p\, l_{\text{sheath}}$, with A_0 the surface area of the electrode, l_p the effective perimeter of the electrode (defined in [18]) and l_{sheath} the sheath thickness

$$l_{\text{sheath}} = \lambda_{\text{Debye}} \left(\frac{\Delta V_{\text{sheath}}}{k_B T_e/e}\right)^{3/4} \tag{2.5}$$

with λ_{Debye} the Debye length and ΔV_{sheath} the potential drop across the sheath.

2.2.4 Thomson Scattering system

A Thomson Scattering system (TS) is used to measure spatial profiles of electron temperature and density in the plasma core, edge and SOL. The TS system of TCV [20, 21] uses a laser at $\lambda = 1.06\ \mu m$, injected vertically through the plasma at R = 0.9 m, corresponding to the centre of TCV vessel, and several wide-angle camera lenses, installed on three lateral ports, which collect the scattered light from the plasma. Currently, the system monitors 109 positions (small volumes) along the laser path, ranging from z = -69 cm to z = 55 cm, see figure 2.9a. The spatial resolution, defined as the vertical extent of the integrated emitting volume into one spectrometer, is 12 mm for most of the chords. Spatial channels with higher resolution (and, consequently, a lower sensitivity) of 6 mm monitor the region between z = -25.7 cm and z = -33.5 cm, measuring the plasma edge and pedestal (indicated by the black rectangle in figure 2.9a). Recently installed channels, with a lower spatial resolution of ∼ 17 mm, cover the divertor region for z < -36.9 cm, where the plasma temperature is much lower than in the confined and near-confined regions. The scattered light is analysed using filter polychromators equipped with 4/5 spectral channels. The observed Doppler broadening of the spectrum of the scattered light yields an estimate of the plasma electron temperature, while the electron density is obtained from the scattered power. Typical spatial profiles of plasma electron density and temperature for a Single-Null TCV plasma are shown in figures 2.9b and 2.9c.

The principle of a TS system is that an electromagnetic wave, sent into a plasma, is scattered by the plasma electrons. When an incident electromagnetic wave impinges on a

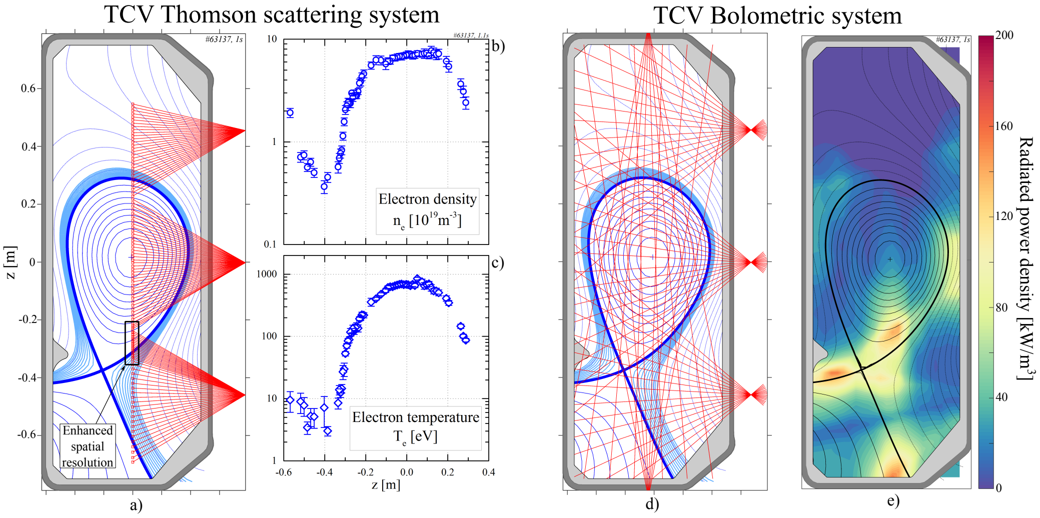

Figure 2.9 – (a) Poloidal cross section of TCV vessel, showing the lines-of-sight of the Thomson scattering system, each monitoring a small volume along the path of the laser, for a Single-Null configuration. (b-c) Electron density and temperature, obtained from the TS system, as a function of the vertical coordinate along the laser path. (d-e) Poloidal cross section of TCV vessel, showing the lines-of-sight of the Bolometric system, for a Single-Null configuration. (e) 2-D map of radiated power density obtained from a tomographic inversion of the bolometric measurements.

free charged particle (e.g. a free electron), the particle is accelerated by the wave electric and magnetic fields, and emits electromagnetic radiation in all directions [19]. The finite velocity of the particle alters the frequency of the scattered light ω_s, so the scattered light is Doppler-shifted compared to that of the incident wave ω_i

$$\omega_s = \omega_i + (\vec{k}_s - \vec{k}_i) \cdot \vec{v}_e \tag{2.6}$$

where $\vec{k}_i$ and $\vec{k}_s$ are the wave-vectors of the incident and scatter light, $\vec{v}_e$ ia the charged particle velocity. This description of the particle-wave interaction is purely classical, and neglects quantum-mechanical effects, and is nearly correct if the incident photon energy is much smaller than the scattering particle energy, $\hbar\omega_i \ll m_e c^2$, with $\hbar$ the reduced Planck constant (defined as $\hbar = h/(2\pi)$ with $h = 6.626 \cdot 10^{34}$J s the Planck constant). This classical limit of scattering by free charges is referred to as Thomson scattering. Plasma applications of electromagnetic scattering by free charges use monochromatic lasers with a wavelength in the visible range or longer, so that the associated photons are much less energetic than plasma electrons ($\sim$ 1 eV compared to $\sim$ 500 eV) and this classical description holds for divertor plasma conditions.

2.2.5 Bolometers

A bolometric system is used to measure the radiative emission from the plasma and reconstruct its 2-D spatial distribution. The bolometric system of TCV features 8 pinhole cameras installed at one toroidal location, at the vessel top, at the vessel bottom and six laterally on the LFS of the tokamak, for a total of 64 lines of sight, see figure 2.9d. Each camera features eight 4-μm thick gold foil absorbers with local thermometers, sensitive to photons and neutrals with energies from $\sim$ 1 eV to $\sim$ 10 keV. The small foil thickness results into small thermal mass of the foil, increasing the temporal response and signal to noise ratio, i.e. the rapidity and strength of the foil temperature change for a given amount of incident heat. A tomographic inversion of the line-integrated power measured along the 64 lines of sight is performed to obtain a 2-D map of the radiation emissivity, such that shown in figure 2.9e, with spatial and temporal resolutions of $\sim$ 4 cm and 10 ms respectively.

The working principle of a metal foil bolometer is that a change of foil temperature, caused by some absorbed power, results into a change of its resistance, which can be measured as a variation of voltage. In a tokamak, this power originates mainly from radiation, but may also be due to energetic neutrals generated through change-exchange reactions in the plasma. Using the bolometer bridge voltage $\theta(t)$ measurement, the instantaneous absorbed power $P(t)$ is calculated by solving the differential equation

$$P(t) = C_{\text{eff}}\left(\frac{\mathrm{d}\theta(t)}{\mathrm{d}t} + \frac{\theta(t)}{\tau_{\text{eff}}}\right) \tag{2.7}$$

with C_{eff} and τ_{eff} the bolometer effective heat capacity and time constant respectively [22].

2.2.6 Thermocouples

A thermocouple system is used to compute the total, cumulatively absorbed heat by the graphite protection tiles during a plasma shot, using tile calorimetry. This estimate can be used to cross-check the IR thermography measurements, e.g. the choice of the α parameter value (discussed in section 3.2.3). Some of the thermocouples are also used when performing the in-situ calibration of the IR cameras to measure the tile temperature. The TCV thermocouple system described here is that prior to the 2019 divertor upgrade, as used in this thesis. A range of graphite protection tiles are equipped with thermocouples, located below the surface of the tiles, at a depth between 3 and 15 mm. As shown in figure 2.10, the system features 15 thermocouples on the flat floor and LFS tilted tiles (sectors 8 to 8b), monitoring the temperature in the region of the outer strike point of a Single-Null divertor, and 18 thermocouples on the central column (14 in sector 6b, 4 in sector 14b), monitoring the temperature in the region of the inner strike point of the same SN. The thermocouples are of type-K, with a sensitivity of approximately 41 μV/°C. The two thermoelectric wires are made of NiCr (Nichrome, an alloy of nickel and chromium) and NiAl (Nickel-aluminide, an alloy of nickel and aluminium) that can work up to $\sim$ 1200 °C.

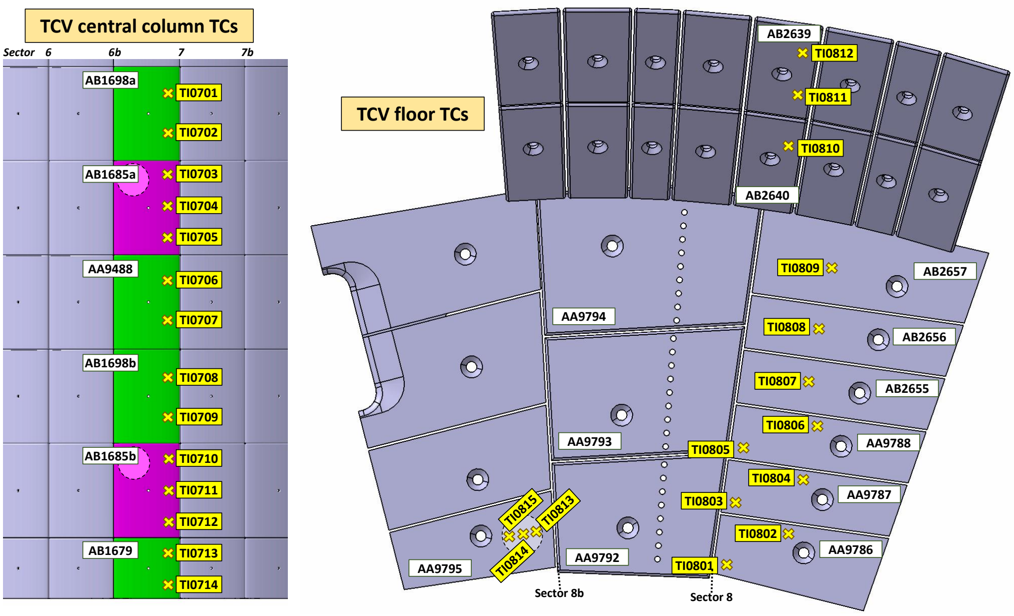

Figure 2.10 – Schematic drawing of TCV thermocouple system before the 2019 divertor upgrade. The thermocouples are indicated by yellow crosses. 14 thermocouples monitor the temperature of the inner column in sector 6b (left) and another 15 thermocouples measure the temperature of the flat floor and tilted tiles in sectors 8-8b (right). Dashed white circles indicate the heated elements, embedded in some tiles, used during the in-situ calibration of the IR cameras.

A thermocouple is an electrical device consisting of two junctions between two different conductors, that produces a temperature-dependent voltage as a result of the Seebeck effect, see figure 2.11. A first junction is placed at the object of interest, at the unknown temperature T_{sense}, and another is kept at a constant reference temperature T_{ref} (typically room temperature). The voltage produced by the thermocouple is proportional to the temperature difference between the junctions. Knowledge of the Seeback coefficients for the two conductors and of the reference temperature is used to translate the voltage into an estimate of T_{sense}.

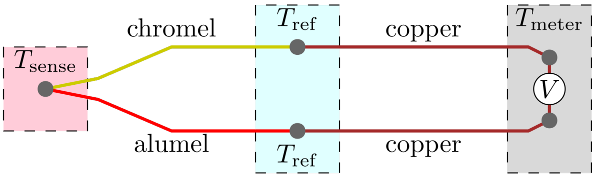

Figure 2.11 – Schematic drawing of a thermocouple, with thermoelectric wires made of chromel and alumel. There are two junctions between these conductors, the first at the unknow temperature T_{sense}, the other at the known (and constant) T_{ref}. Because of the Seebeck effect, a voltage difference exists between the endings of the two wires, and is proportional to temperature difference. *Source of the image: Wikipedia*

The procedure to estimate the tile absorbed heat is here described. After the end of the plasma discharge, once the tile has reached an internal thermal equilibrium (uniform temperature), the time evolution of its temperature T is determined by heat conduction from the tile through the screw that attaches the tile to the vacuum vessel,

$$m_{\text{tile}}\ c_{p,\text{tile}}(T)\ \frac{\mathrm{d}T}{\mathrm{d}t} = -k_{\text{screw}}\ A_{\text{screw}} \nabla T = -k_{\text{screw}}\ (A_{\text{screw}}/l_{\text{screw}})\ (T - T_{\text{vessel}}) \tag{2.8}$$

where m_{tile} and $c_{p,\text{tile}}(T)$ are the tile mass and heat capacity, k_{screw} is the conductivity of the screw, A_{screw} the contact area between tile and screw, l_{screw} the screw length and T_{vessel} the temperature of the vessel, which, due to the large thermal mass of the vessel, can be considered constant. Radiative cooling is neglected compared to conduction because of the relatively low tile temperatures achieved in TCV experiments (normally < 300 °C). As the tiles are in vacuum, heat convection is inexistent. Neglecting the dependence of $c_{p,\text{tile}}$ on temperature generates the analytical solution of equation 2.8,

$$T(t) = T_{\text{vessel}} + (T_{\text{equil}} - T_{\text{vessel}})\ e^{-(t-t_{\text{equil}})/\tau} \tag{2.9}$$

$$\tau = \frac{m_{\text{tile}} c_{p,\text{tile}} l_{\text{screw}}}{k_{\text{screw}} A_{\text{screw}}} \tag{2.10}$$

where $T_{\text{equil}} = T(t_{\text{equil}})$ is the tile temperature when it has reached internal thermal equilibrium. Following the procedure described in [23], this expression is used to fit the measured $T(t)$ evolution for $t > 100$ s, the typical time for internal thermalisation of a TCV tile [24]. This curve is then extrapolated to the time of the end of the discharge t_{end}, to estimate an equivalent homogeneous tile temperature $T_{\text{end}} = T(t_{\text{end}})$, see figure 2.12a. Finally, the total absorbed heat is computed, for each tile, as

$$Q_{\text{tile}} = \int_{T_{\text{begin}}}^{T_{\text{end}}} c_{p,\text{tile}}(T)\mathrm{d}T \tag{2.11}$$

with T_{begin} being the tile temperature before the discharge. Typical profiles of the deposited energy are shown in figures 2.12b and 2.12c for the inner and outer strike point zones of a standard lower Single-Null configuration, figure 2.12d.

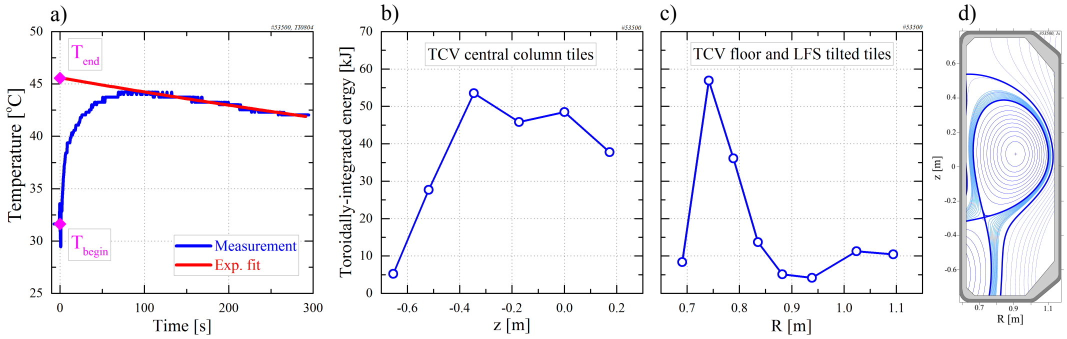

Figure 2.12 – (a) Temperature measurement of a thermocouple located on a floor tile near the outer strike point of the standard SN configuration of fig. (d). The estimated temperature before (T_{begin}) and after (T_{end}) the plasma discharge are also shown, and the exponential fit with equation 2.9 for t > 100 s. (b-c) Profile of total deposited heat after the plasma discharge, along TCV central column (b) and flat floor and tilted tiles (c), with each point corresponding to a tile equipped with thermocouples. (d) Poloidal cross section of TCV with magnetic equilibrium of this plasma discharge.

3 Improvements to the Infrared system

From 2015, the year when this thesis commenced, TCV has operated as one of the three national tokamak devices as a European facility within the medium-size tokamak work package (WPMST1) of the EUROfusion consortium. Due to its unique versatility in plasma and divertor shaping, TCV is the European reference tokamak in investigating alternative magnetic divertor configurations. The number of power exhaust experiments on TCV has significantly increased since 2015 and, with this, the requirements from boundary diagnostics such as the Infrared (IR) Thermography system. This motivated major improvements to the software that controls the IR cameras, as well as upgrades to the routines that process IR data. As part of the TCV divertor upgrade (2019-2020) a new tangential IR system was commissioned.

This chapter presents the major improvements to the TCV Infrared system performed as part of the thesis. In section 3.1, the new control software for the IR cameras and its integration in the TCV shot cycle is presented. Then, section 3.2 describes the improvements to the IR data analysis routines. Finally, the design and commissioning of a new Tangential IR system is described in section 3.3.

3.1 Automation of the IR camera control

At the start of the thesis, TCV featured two IR systems, the VIR and HIR, described in sections 2.2.1.1 and 2.2.1.2, respectively. The VIR camera was controlled by proprietary software, installed on a Windows PC located in the TCV control room. The HIR camera was controlled by proprietary software, installed on a Windows PC, located near the torus and accessed via a remote desktop connection from the TCV control room. During the plasma shot, each IR camera receives a trigger signal from a trigger box, located near the IR PC. Before the experiment, the IR operator manually selected the IR camera setup and the characteristics of the trigger signal (e.g. frequency of acquisition) for each system by inserting values into VISTA control channels, after which the camera is armed and awaits the trigger. Following the plasma shot, the IR operator manually saved the IR video of each system to a local disk. Operating the IR cameras remained a manual task even after replacing the Thermosensorik camera of the VIR system with an IRCAM model identical to the HIR camera, such that both devices could be controlled by the same computer.

This manual operation increased the risk of errors when setting the camera and trigger parameters and, furthermore, made it impractical to alternate between different experiments. The next sections describe the steps undertaken to implement a fully automated IR camera control system. These include a realization of a new software and communication system (section 3.1.1), a Graphical-User-Interface application (section 3.1.2) and a routine to integrate the systems into the TCV shot cycle (section 3.1.3).

3.1.1 New control software and communication system

To automate the IR camera control, API (Application-Programming-Interface) routines were procured from the IR camera manufacturer and used to write a new, command-line program in C++. The command-line software, *ircam_run.exe*, runs on each IR PC and the input/output communication is handled by MDS events, as sketched in figure 3.1. The MDS events, used for communications, are part of MDSplus, the set of software tools for data acquisition and storage, used on TCV as well as in many other plasma research centres. A MDS event can be generated from any computer on the TCV network and is broadcast to all connected devices. Each event carries a name, which is "ircamera" for IR control, followed by a data string.

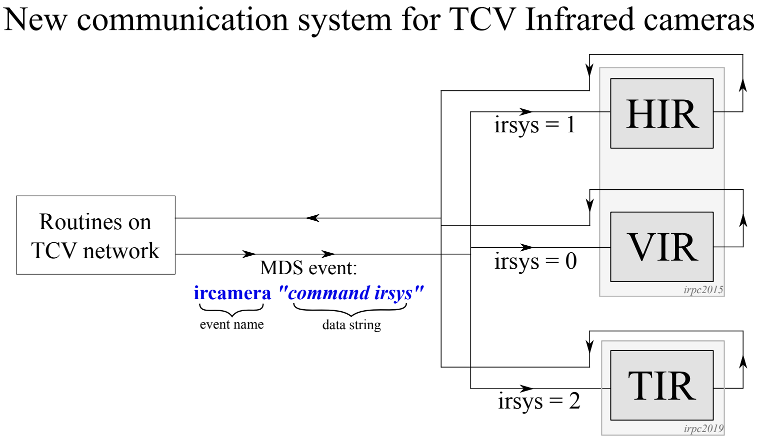

Figure 3.1 – New communication system for TCV IR cameras. Matlab routines, running on the *lac* cluster, communicate with the IR control software, which runs on each IR PC, generating MDS events with the event name "ircamera", followed by a data string containing details about the required task and the considered IR system.

To control the IR cameras, dedicated routines running on the TCV network generate

MDS events with the event name "ircamera", followed by a data string, figure 3.1. The command-line software *ircam_run.exe*, running on each IR PC, compares this data string to a pre-defined list, shown in table 3.1, and then executes any recognized task. The data string contains a numeric tag, *irsys*, which identifies the IR system to control (0=VIR, 1=HIR, 2=TIR). Once the task is completed, the command-line software generates a MDS event identical to that received. This is used as a confirmation mechanism for the calling routine, indicating that *ircam_run.exe* has completed the required task. Some information can be passed back to the calling routine by appending string characters to the MDS event data string, after *irsys*.

data string	task
start	Start camera control software on IR PCs
initialize *irsys*	Initialize camera
save *irsys*	Save video and metadata to disk
rec_on *irsys*	Start recording thread
ref_off *irsys*	Stop recording thread
arm *irsys*	Set camera to external trigger mode
disarm *irsys*	Set camera to internal trigger mode
take_NUC *irsys*	Take NUC image
deinitialize *irsys*	De-initialize camera
quit	Close camera control software on IR PCs
live *irsys*	Show live image on IR PC
setup *irsys*	Retrieve current setup of the camera
set_whlt *irsys w h l t*	Set a sub-window for the camera detector (w = width, h = height, l = left, t = top)
set_intt *irsys intt*	Set camera integration time

Table 3.1 – Commands that are accepted by the IR camera control software *ircam_run.exe*, with description of the task executed. The tag *irsys* identifies the IR system to control, with 0=VIR, 1=HIR and 2=TIR.

3.1.2 Development of a GUI application

A Graphical-User-Interface (GUI) application was also developed to facilitate the interface between the IR operator and the IR systems, see figure 3.2. This is used to set the IR camera and/or external trigger setup, check data after each shot and monitor the status of the cameras.

A radio-button panel, located on the top-left corner of the GUI window, selects IR systems. Buttons initiate calls to Matlab routines, running on the *lac* linux cluster. As an example, clicking the "setup_ir" button calls the "setup_ir.m" routine, that is used to change the setup of the IR cameras and of the trigger signal. As shown in figure 3.2, the IR operator can either specify the setup for each camera and trigger signal by providing a data table (top-right corner of the GUI window) or load the setup used in an prior plasma shot (top-center of the GUI window). In both cases, a sequence of MDS events, described in section 3.1.1, is generated to change the setup of the selected IR cameras (such as integration time, size and position of the sub-frame). In addition to communicating with the IR cameras, the routine also changes values of VISTA control channels that determine the times of the trigger signals.

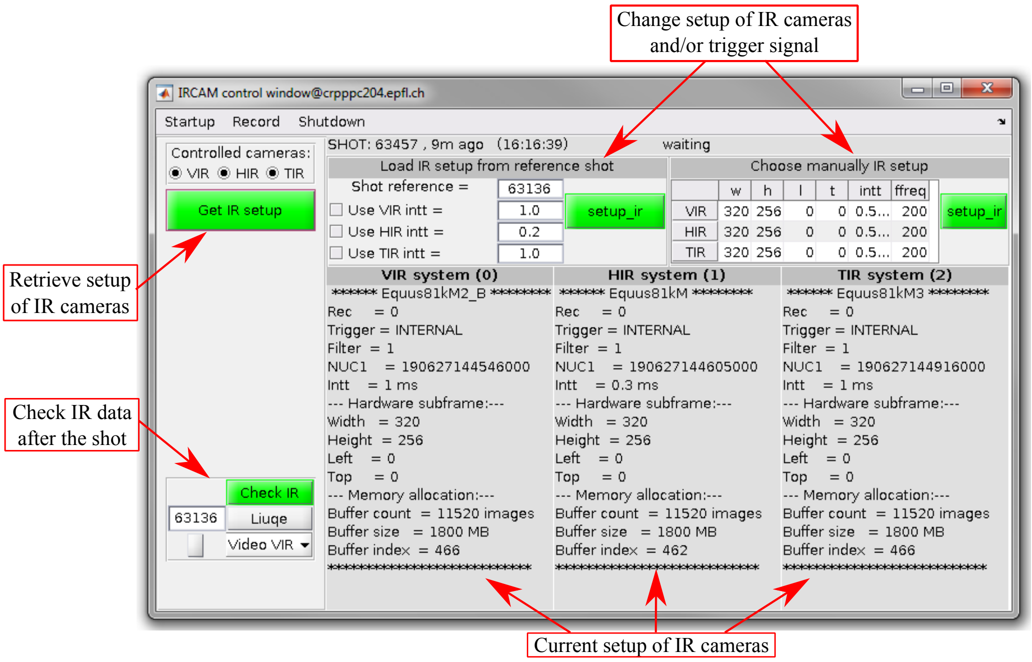

Change setup of IR cameras and/or trigger signal

Retrieve setup of IR cameras

Check IR data after the shot

Current setup of IR cameras

SHOT: 63457 , 9m ago (16:16:39) waiting

Controlled cameras: ● VIR ● HIR ● TIR

Load IR setup from reference shot

Shot reference = 63136

☐ Use VIR intt = 1.0

☐ Use HIR intt = 0.2

☐ Use TIR intt = 1.0

Choose manually IR setup

	w	h	l	t	intt	ffreq
VIR	320	256	0	0	0.5...	200
HIR	320	256	0	0	0.5...	200
TIR	320	256	0	0	0.5...	200

63136

VIR system (0)

```
****** Equus81kM2_B ********
Rec     = 0
Trigger = INTERNAL
Filter  = 1
NUC1    = 190627144546000
Intt    = 1 ms
--- Hardware subframe:---
Width   = 320
Height  = 256
Left    = 0
Top     = 0
--- Memory allocation:---
Buffer count  = 11520 images
Buffer size   = 1800 MB
Buffer index  = 466
****************************
```

HIR system (1)

```
****** Equus81kM ********
Rec     = 0
Trigger = INTERNAL
Filter  = 1
NUC1    = 190627144605000
Intt    = 0.3 ms
--- Hardware subframe:---
Width   = 320
Height  = 256
Left    = 0
Top     = 0
--- Memory allocation:---
Buffer count  = 11520 images
Buffer size   = 1800 MB
Buffer index  = 462
****************************
```

TIR system (2)

```
****** Equus81kM3 ********
Rec     = 0
Trigger = INTERNAL
Filter  = 1
NUC1    = 190627144916000
Intt    = 1 ms
--- Hardware subframe:---
Width   = 320
Height  = 256
Left    = 0
Top     = 0
--- Memory allocation:---
Buffer count  = 11520 images
Buffer size   = 1800 MB
Buffer index  = 466
****************************
```

Figure 3.2 – A Graphical-User-Interface (GUI) provides an intuitive interface between the IR operator and the three IR systems.

As the IR images are triggered externally, the compatibility of the requested frame rate and the camera settings is not guaranteed. The requested frame rate f_{trigger} is compatible with the camera settings only if the time interval between trigger pulses, equal to $1/f_{\mathrm{trigger}}$, is longer than that required to acquire an image $\Delta t_{\mathrm{frame}}$. Frame acquisition is a three-step process. The detector is reset ($\Delta t_{\mathrm{reset}}$), it collects new photons (Δt_{int}), the signal is read out ($\Delta t_{\mathrm{readout}}$). According to the documentation provided by the IR camera manufacturer[1], the time required for the acquisition of a single frame is:

$$\Delta t_{\mathrm{frame}}[\mathrm{s}] = \Delta t_{\mathrm{reset}} + \Delta t_{\mathrm{int}} + \Delta t_{\mathrm{readout}} = \frac{20}{f_{\mathrm{clk}}[\mathrm{Hz}]} + \Delta t_{\mathrm{int}}[\mathrm{s}] + \frac{N_{\mathrm{px}}}{4 f_{\mathrm{clk}}[\mathrm{Hz}]} \tag{3.1}$$

where f_{clk} is the master clock frequency, Δt_{int} the integration time of the detector and N_{px} the number of pixels in use. The typical master clock frequency is $f_{\mathrm{clk}} = 6.75$ MHz, so that $\Delta t_{\mathrm{reset}}$ is of the order of 3 μs. This relation was verified experimentally, both using the entire detector surface (i.e. full-frame mode) and a part of it (i.e. sub-frame mode), as shown in figure 3.3. In full-frame mode, figure 3.3a, the read-out phase dominates the

---

[1] Document "CameraLinkProtocolDescription_IRCAM_Equus81kM_HighMagneticFields.pdf", page 2, section "Timing of the detector"

frame-acquisition process due to the large number of pixels, with $\Delta t_{\mathrm{readout}}$ of the order of 3 ms and Δt_{int} typically below 1 ms.
To assure compatibility of the requested frame rate f_{trigger} and the camera settings, the routine "setup_ir.m" checks whether $1/f_{\mathrm{trigger}}$ exceeds the projected $\Delta t_{\mathrm{frame}}$, computed from equation 3.1, by at least 10% and, where necessary, reduces the value of f_{trigger} accordingly.

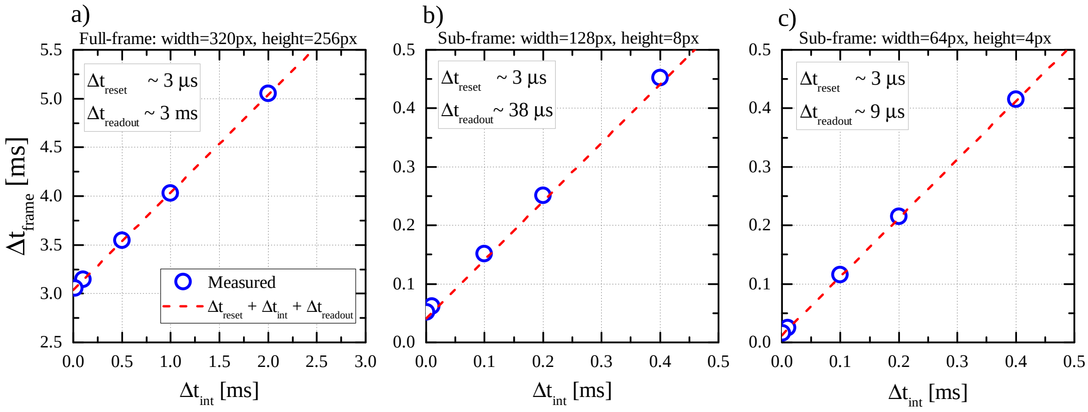

Figure 3.3 – Measured IR camera frame acquisition time as a function of integration time, with detector in full-frame mode (a), sub-frame mode with size 128x8 pixels (b) and 64x4 pixels (c). The master clock frequency is $f_{\mathrm{clk}} = 6.75$ MHz

3.1.3 Integration into the TCV shot cycle

The MDS event-based IR control routines, section 3.1.1, integrate the IR thermography system into the TCV shot cycle. The matlab routine *ircamera_cycle.m*, running on the *lac* cluster, and sketched in figure 3.4, interfaces the IR control software to the TCV shot cycle. This synchronization is based on MDS events with the name "tcvsm".
At the start of the pre-shot phase, the TCV computers generate such an event with the data string "init_done", prompting *ircamera_cycle.m* to arm the IR cameras. After the end of the shot, a "tcvsm" event with the data string "store_start" prompts *ircamera_cycle.m* to disarm the cameras and save the data. Should the TCV shot be aborted, a "tcvsm" event with the data string "abort" is generated, that prompts disarming the cameras without saving any data. All MDS event communications from the *lac* machines wait for the feedback from the IR camera software.

3.2 Upgrade of IR data analysis techniques

The existing IR data analysis routines were also improved during this thesis. The standard data analysis procedure, which is outlined in figure 3.5, is performed on the *lac* linux cluster, in Matlab.

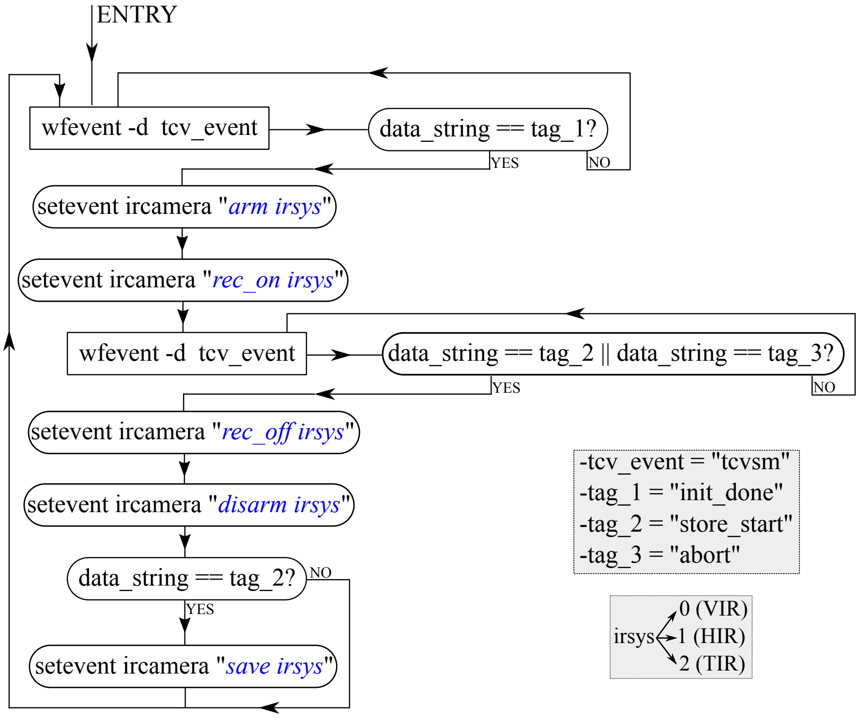

Figure 3.4 – Scheme of the matlab routine *ircamera_cycle.m*, which interfaces the IR control software to the TCV shot cycle. MDS events with event name "tcvsm", generated by the TCV computers at different stages of the cycle, cause the client software to perform designated actions on the IR cameras. The word "setevent" starts the MDS command syntax which generates a new event. The word "wfevent" starts the MDS command syntax which waits for an event.

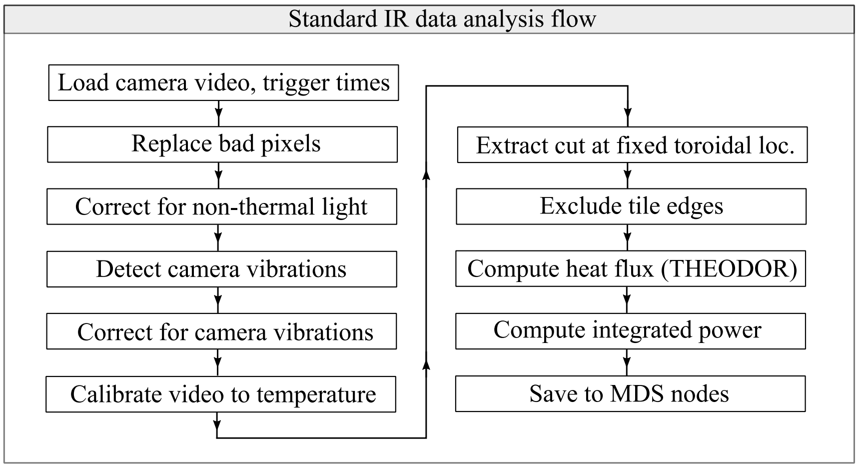

Figure 3.5 – Main steps of the standard IR data analysis process.

Once the IR video is loaded into computer memory, the detector settings and external trigger setup are retrieved, and a background image is subsequently subtracted from the raw video (Non-Uniformity-Correction). Bad pixels, identified as those whose signal is constantly null or equal to the maximum, are overwritten with an average of the eight (good) surrounding pixels. The IR video is then corrected for non-thermal light and for camera vibrations, as described in detail in sections 3.2.1 and 3.2.2, and calibrated to provide temperatures. A temperature profile at a fixed toroidal location (a radial cut for the vessel floor and a vertical cut for the inner wall, see figures 2.4 and 2.5) is selected for each video frame and tile edges, where present, are excluded. The temporal evolution of the temperature, together with the thermal properties of the tiles, are input to the THEODOR code [25] (outlined in section A.4), which returns the heat flux incident to the surface coherent with the image. The total power to the target is then computed by spatially integrating the heat flux profile. The resulting data (temperature, heat flux, power, thermal characteristics of the tile, location of the measurements, etc...) are stored into dedicated MDS "results" nodes.

3.2.1 Correction for non-thermal radiation

Under some experimental conditions, the VIR video shows an increase of the signal during the discharge from regions of the vessel wall that are not directly exposed to plasma heat flux that should, therefore, retain a constant temperature. This signal is classified as *non-thermal radiation* since it does not correspond to an increase of the target temperature. Such non-thermal signal contaminates the thermal image, and may originate from reflections inside the vessel and/or the optical tube of the VIR relay optic, as well as from Bremsstrahlung photons from the plasma. Bremsstrahlung radiation is mainly produced, by the plasma, by the acceleration of electrons through Coulomb interactions with ions [2].

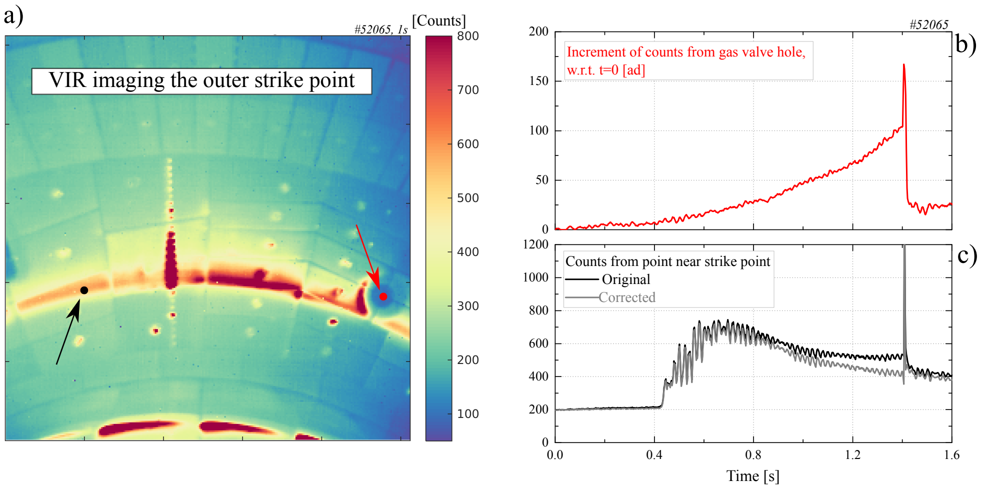

Figure 3.6 – Example of the non-thermal radiation correction.(a) VIR image of the vessel floor, with arrows indicating the gas valve hole (red) and a point near the strike line (black). (b) Increment of counts from gas valve as a function of time. (c) Counts from a point near the strike line, before and after subtracting the increment from the gas valve orifice.

A simple estimate of this non-thermal radiation is the increment of signal from the gas valve orifice located on TCV floor and imaged by the VIR system, figure 3.6a. Since the heat flux deposited on the orifice base is negligible, the orifice temperature and, thus, the IR counts should not change with time. To correct the IR video for the non-thermal light, the observed increment of the signal from the gas valve hole, figure 3.6b, is subtracted from the entire image, figure 3.6c.

The non-thermal radiation is often negligible for experiments with low plasma density, and the divertor in the attached regime, but steadily increases with increasing plasma density. Figure 3.6 shows a plasma density ramp, where radiation from the gas valve orifice steadily increases in time, finally becoming a non-negligible fraction of the total IR signal. This observation suggests that most of the non-thermal radiation may be Bremsstrahlung radiation, as it scales with the square of the plasma density [2].

3.2.2 Correction for camera vibrations

The thermal image of the VIR and TIR systems suffers from vibrations during the plasma shot. For the VIR, these are likely caused by vibrations of the mirror of the optical system between the IR camera and the torus ceiling, see figure 2.4a. For the TIR, such a movement may be caused by vibrations of the movable mirror, see figure 2.6a. The HIR system, however, is not affected by vibrations as it images the inner column directly. An algorithm based on phase correlation was developed to measure the relative movement between successive frames of an IR video.

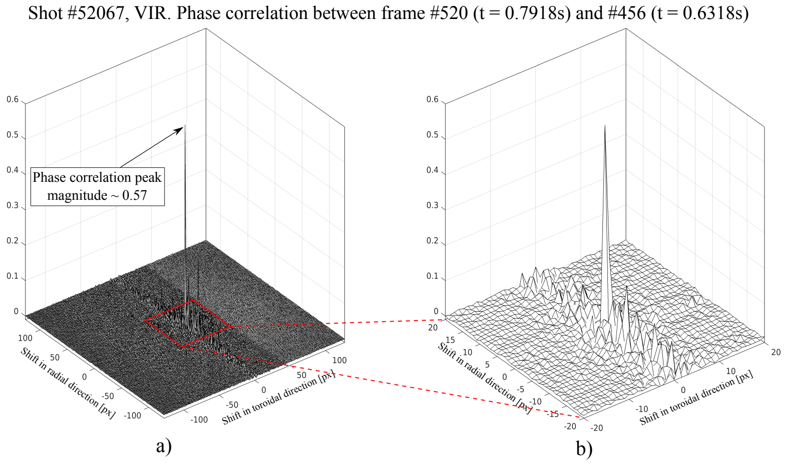
Shot #52067, VIR. Phase correlation between frame #520 (t = 0.7918s) and #456 (t = 0.6318s)

Phase correlation peak magnitude ~ 0.57

a) b)

Figure 3.7 – Example of the application of the phase correlation method to detect the displacement between two IR images. The inverse Fourier transform of equation 3.4, where $\hat{f}_1$ and $\hat{f}_2$ are the Fourier transforms of the two images, resembles a Dirac delta function (a). The peak location, better visible in the detail (b), yields the image displacement at the pixel resolution.

Phase correlation method The phase correlation method[26, 27] uses the Fourier shift theorem to translate a spatial shift between two images into a phase shift between their spatial Fourier transforms. With $f_1(x,y)$ and $f_2(x,y)$ representing two images, a spatial translation is related by

$$f_2(x,y) = f_1(x-dx, y-dy) \tag{3.2}$$

The Fourier shift theorem states that their spatial Fourier transforms $\hat{f}_1(u,v)$ and $\hat{f}_2(u,v)$ will have identical magnitudes with a phase shift

$$\hat{f}_2(u,v) = \hat{f}_1(u,v)e^{-i(u\cdot dx+v\cdot dy)} \tag{3.3}$$

This phase difference can be computed using the normalized cross power spectrum

$$e^{-i(u\cdot dx+v\cdot dy)} = \frac{\hat{f}_2(u,v)\hat{f}_1^*(u,v)}{|\hat{f}_1(u,v)\hat{f}_1^*(u,v)|} \tag{3.4}$$

where * indicates the complex conjugate. This phase difference is also the Fourier transform of the shifted Dirac delta function. Therefore, computing the inverse Fourier transform of equation 3.4 yields a 2D Dirac delta function, in real space (x,y), whose peak coordinates are (dx,dy), i.e. the shift between the two images. The peak location (dx,dy) is, thus, the image displacement at the pixel resolution, as shown in figure 3.7.

Extension to sub-pixel resolution Since the thermal images are finite size discretized arrays, the discrete Fourier transform is employed, where the Dirac delta function becomes a Dirichlet kernel [27], whose peak is found at the closest integer displacement. To obtain sub-pixel resolution, once (dx,dy) is known, the region around the peak can be interpolated by 2-D sinc function, which closely approximates the Dirichlet kernel [27], so the coordinates of its peak are the displacement at the sub-pixel resolution. Using a 1-D parabola to interpolate the region around the peak, separately along the x and y directions, was found to provide almost identical peak location and, importantly, to drastically reduce the computation time. This is the approach chosen to process the IR data.

The displacement detection procedure is iteratively run on each video frame, using a frame preceding the appearance of image vibrations, typically that at the start of the video, as the reference image. The same reference image is used until the phase correlation strength, given by the peak magnitude, descends below a threshold (typically 0.3). The last analysed frame then becomes the new reference image, and the algorithm continues until the end of the video.

A typical output of the vibration detection algorithm applied to VIR data acquired at 400 Hz, shown in figure 3.8, indicates an image oscillation in both directions with a frequency

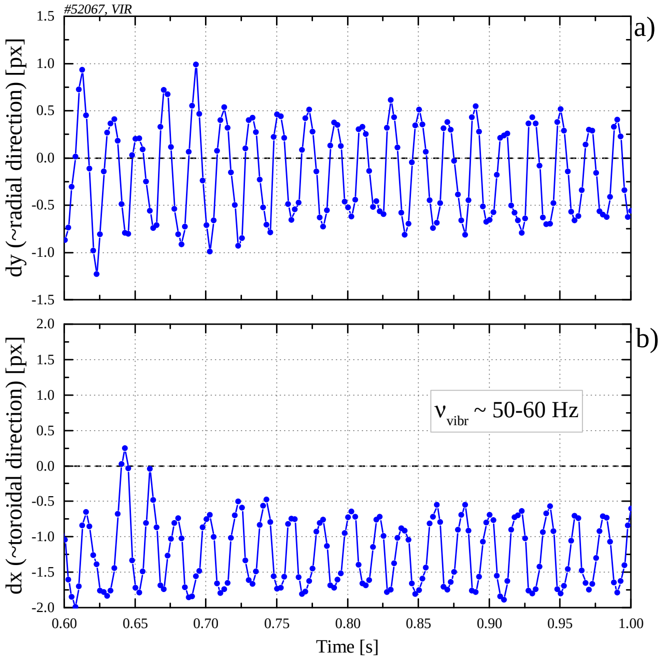

Figure 3.8 – Output of the vibration detection algorithm, applied to a VIR video acquired at 400 Hz. The algorithm shows that the image oscillates in both directions with a frequency of $\sim$ 50 Hz and a typical amplitude of the order of 1 pixel or less.

of $\sim$ 50 Hz and a typical peak-to-peak amplitude of the order of 1 pixel, corresponding to $\approx$ 2 mm. The 50 Hz value resembles the frequency of the TCV poloidal field coils power supply, which is located in proximity of the VIR optical system.

3.2.3 Estimate of the surface layer heat transmission factor

As previously outlined, the temporal evolution of the target temperature is input to the THEODOR code [25], which returns the heat flux onto the surface, see section A.4 for details. To compute the heat flux onto the divertor tiles, the THEODOR code requires a value, or a spatial profile, of the surface layer heat transmission factor α, as described in section A.4. This thermal parameter accounts for the presence of a layer of deposited material on the tile surface. A value

$$\alpha_{\mathrm{TCV}} = 160\ \mathrm{kW/m^2K} \tag{3.5}$$

was chosen to match the calorimetric measurements based on thermocouples and to satisfy the condition of a null heat flux following discharge termination. While the total energy reconstructed by the THEODOR code is independent of the choice of α, it greatly affects the deduced time evolution of the deposited power. If the value of α is too low, the code underestimates the power deposited during the discharge but indicates power deposition after the discharge terminates. Conversely, if α is too big, the code overestimates the power deposited during the discharge, compensated by a negative power deposition after the discharge terminates.

For plasma shots with relatively slow thermal transients, i.e. L-mode and ELM-free plasmas, using the same value of α across the entire target surface is a reasonable choice, as it is observed to lead to negligible negative heat fluxes. For plasma shots with fast thermal transients, such as ELMy H-mode plasma, however, the constant α value of L-mode and ELM-free plasmas leads to high negative heat fluxes after each ELM event. Lowering the value of α everywhere reduces these negative heat fluxes but creates unphysical, positive heat loads after the discharge, at locations where the previous α did not lead to negative heat fluxes.

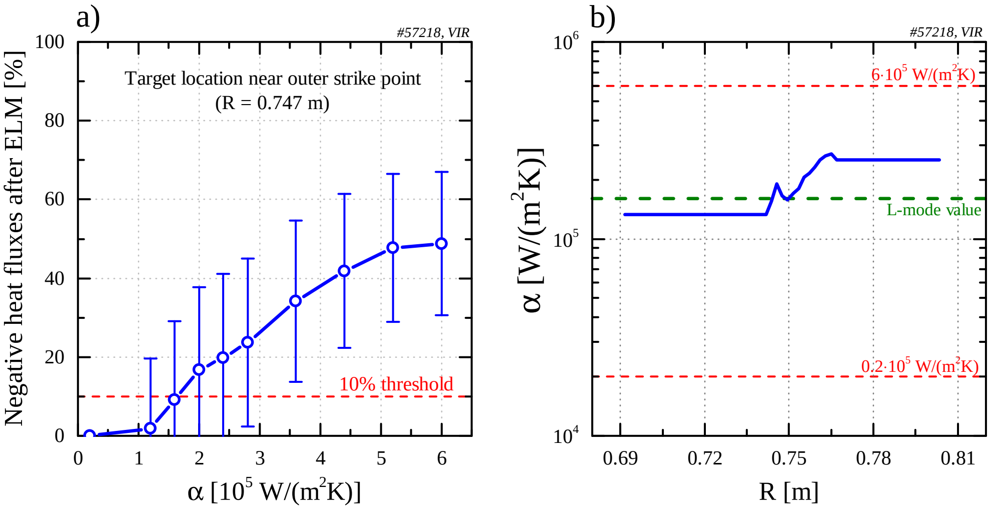

Figure 3.9 – Output of the algorithm that computes the surface layer heat transmission factor α profile, applied to the VIR video of the outer strike point of SN ELMy H-mode plasma.(a) Fraction of negative heat fluxes after each ELM as a function of the value (spatially-constant) of α, for a target location near to the strike point. The optimal value for α is defined as that corresponding to negative heat fluxes being 10% of the total power load. (b) Resulting spatial profile of α, around the outer strike point. In red, the tested range of α.

One explanation is that the surface layer is spatially-changing at the divertor target. This spatial profile for α is estimated, for each ELMy H-mode plasma shot, by a new algorithm. The algorithm first uses the THEODOR code to compute the heat flux matrix for several values of α, in the range 0.2 to $6 \cdot 10^2$ kW/(m^2 K), with α constant on the target. Then, at each location on the target and for each value of α, the percentage of negative heat fluxes after the ELM event is computed (ELM cycle interval: 0 to 50%), figure 3.9a. The optimal value of α is defined as the value with negative heat fluxes being 10% of the total power load. This procedure is only performed close to the strike point region, where significant heat flux is deposited by the ELM. The obtained spatial profile for α, see for instance figure 3.9b for the outer strike point, is then used by the THEODOR code, which finally computes a modified heat flux matrix.

Using a profile for α, rather than a constant value, significantly improves target heat flux reconstruction between and during ELMs, as it reduces the strength of negative heat fluxes in the after-ELM phase, everywhere on the target, to low levels (10%), without creating unphysical positive heat loads after the end of the discharge.

A physical interpretation of a spatially-changing α is challenging since the composition of the surface layer and, therefore, its thermal properties are not known. With α defined as the ratio between layer conductivity and thickness, equation A.33, a spatially-changing α may indicate that the layer thickness changes along the target. This is quite reasonable as, during a plasma shot, the strike-points stay for much of the discharge at a relatively fixed region and, thus, the target erosion and re-deposition associated with ELM events may be non uniform across the targets.

3.3 Commissioning of the Tangential IR system

As described in section 2.2.1.3, the 2017-2020 TCV divertor upgrade includes the addition of a third tangentially viewing infrared system (TIR), to image the floor tilted tiles and the outer wall port protection tiles. This section describes the commissioning of this system.

3.3.1 Optics of tangential view

A standard diagnostic port located in sector 12 was chosen to host the TIR system, and a tangential view of the vessel is created using a set of two flat mirrors, see figure 3.10a. These mirrors, shown in the inset of figure 3.10b, were designed by direct inspiration from TCV's Charge-Exchange diagnostic (CXRS [28]).

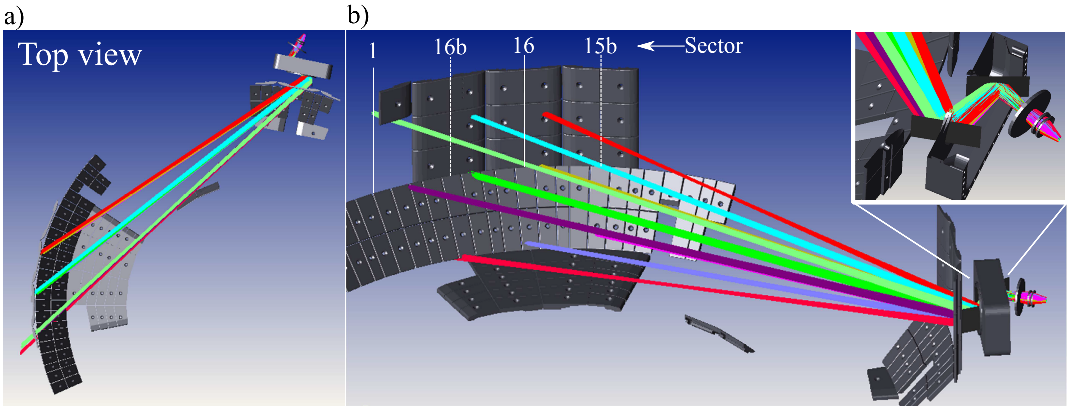

Figure 3.10 – Conceptual design of the optics for the TIR system. (a) Top view of the TIR field-of-view. (b) TIR field-of-view seen from the side, with indicated the vessel sectors. The inlet shows the two-mirror setup, with one fixed and the other movable. *Courtesy of Y. Andrebe*

The focal length of the camera lens was chosen to provide a field-of-view spanning, in the vertical direction, from the start of the LFS tilted tiles to the start of the LFS baffle tip (not shown in the picture). With a 50 mm focal length lens, the expected TIR field-of-view, shown in figure 3.10b, is wide enough to image both the tilted tiles and the outer wall tiles. Therefore, a 50 mm focal length lens was purchased. The actual TIR field-of-view, shown in figure 2.6, is in good agreement with these expectations.

3.3.2 Calibration with black body source

To calibrate the TIR camera, one of the port protection tiles in the field-of-view of the camera is equipped with a heating element and thermocouples, for an in-situ calibration, similar to the HIR and VIR systems. The first experimental campaign with the TIR system was performed without the port protection tiles. The camera was calibrated using a compact black-body source, with emissivity $\varepsilon_{\mathrm{BB}} = 1$, capable of temperatures up to $\approx$ 1000°C.

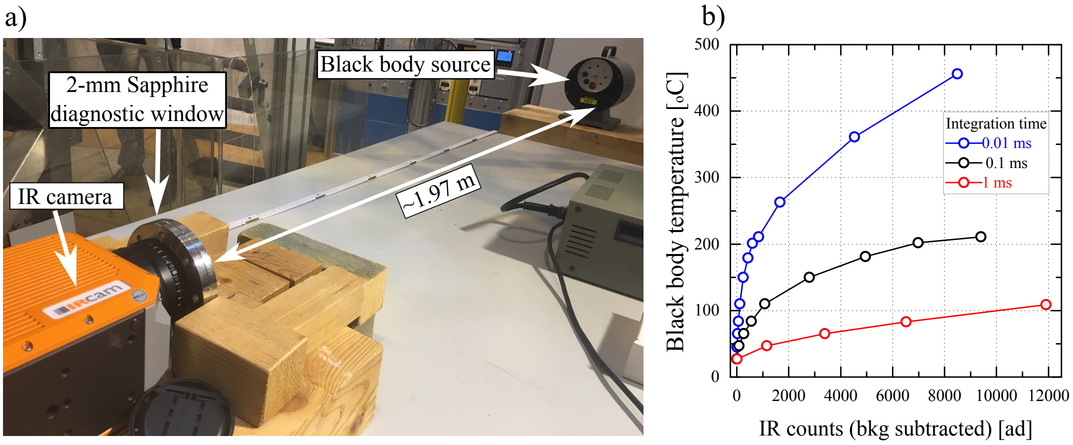

Figure 3.11 – (a) Setup for the calibration of the TIR camera with a black body source, featuring a 2-mm Sapphire diagnostic window and a distance, between lens and target, of $\approx$ 2 m. (b) Calibration curve for the black-body, i.e. temperature as a function of IR counts, for three values of the camera detector integration time.

As shown in figure 3.11a, the black body source is placed at 1.97 m from the camera, which is the length of the optical path between the TIR diagnostic port and the tile at the center of the TIR field-of-view. A 2-mm thick Sapphire window, identical to that installed in the TIR diagnostic port, is placed in front of the camera lens. The calibration curves of the black body source for three different integration times are shown in figure 3.11b. The corresponding calibration curves for the carbon tiles are obtained by rescaling the IR counts with the ratio $\varepsilon_{\mathrm{tile}}/\varepsilon_{\mathrm{BB}}$, where $\varepsilon_{\mathrm{tile}} = 0.73$ is the emissivity of the graphite tiles [29], $\varepsilon_{\mathrm{BB}} = 1$ that of the black body source.

3.3.3 Target temperature from TIR compared to VIR

To check the TIR calibration, the temperature of a LFS tilted tile measured by the TIR system, figure 3.12c, is compared to that measured by the VIR system, figure 3.12b, at another toroidal location but for the same plasma shot and time.

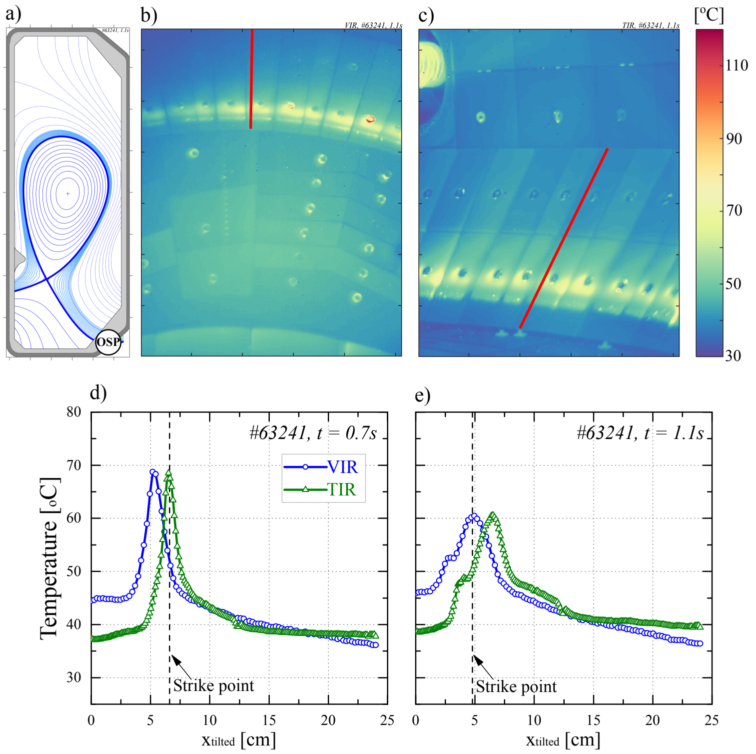

Figure 3.12 – (a) Reconstructed equilibrium for the VIR-TIR comparison. (b) Thermal image of the VIR system. (c) Thermal image of the TIR system, at the same time. (d-e) Profile of temperature on the tilted tiles at 0.7s and 1.1s, as measured by the VIR (blue) and TIR (green) systems, along the red lines shown in figures (b-c). A shift of ∼ 1.5 cm between the measurements of the two systems is visible.

A point on the tilted tiles is described through the coordinate x_{tilted}, defined as the distance from the lower edge of the tilted tiles, at constant toroidal angle. To compute the values of x_{tilted}, two points in the image, corresponding to the lower and upper edges of the tilted tiles, are manually selected, at fixed toroidal position. The distance between these two points, in pixels, corresponds to a distance of 24 cm. This yields the conversion factor between pixels and real-space distance, which is used to compute the value of x_{tilted} at each location on the tilted tile. The comparison between VIR and TIR is possible since in the first experimental campaign with the TIR system, the TCV vessel did not include the outer baffle, see figure 3.12a. With the outer baffles installed, the floor tilted tiles are no longer in the field-of-view of the VIR system.

The temperature profile measured by the TIR agrees, in absolute values, with that measured by the VIR during the entire plasma shot, see figures 3.12d-e, but there is a relative shift of ~ 1.5 cm between the two profiles. The spatial mapping of the tilted tile view has a typical uncertainty of ~ 2 pixels, which is the precision of the localisation of the lower and upper tile edges. This corresponds to 2.4 mm for the TIR (resolution: 1.2 mm) and 5 mm for the VIR (resolution: 2.5 mm), which is insufficient to explain the observed shift between the VIR and TIR profiles. The analysed tiles for the VIR and TIR system are located at different toroidal locations (sector 8 and 16 respectively, i.e. they are diametrically opposite), so the shift may result from error fields in the tokamak [30], that lead to toroidal asymmetries of the magnetic configuration and, thus, of the outer strike point position. These error fields could also explain the observed displacement of the peak heat flux from the computed strike point position when the strike point is placed on the LFS tilted tile, see section 6.2.2. However, no quantitative analysis has been carried out to assess whether the known error field is sufficient to explain the observed shifts.

Following the TIR calibration, the commissioning of the TIR system can be considered complete. Future improvements to the TIR system include (1) the use of the heated element and thermocouples embedded in one of the port protection tiles to perform an in-situ calibration of the camera, similarly to the HIR and VIR systems, and (2) the installation of a sliding shutter in front of the window, used for the NUC correction instead of the mirrors in closed position.

4 The Scrape-Off Layer and divertor geometry

This chapter reviews the magnetic field structure in a tokamak and introduces the definitions and nomenclatures that are used, in the next chapters, to describe the Scrape-Off Layer and divertor geometry. After outlining the two configurations where the plasma can be operated (limited and diverted), the main geometrical features of the plasma are introduced in section 4.1, and those of the SOL and divertor region in section 4.2. Section 4.3 presents the derivation of analytic relations, based on the SOL field line geometry, which serve to map target measurements (e.g. heat flux) to an upstream location. In section 4.4, the plasma wetted area, at the target, is defined and related to SOL and divertor geometry. Finally, section 4.5 presents the conventional and alternative magnetic divertor configurations that are experimentally studied in this thesis.

In a tokamak, the magnetic field is composed of a toroidal and a poloidal component that shape the field lines so that they twist within the plasma. These magnetic field lines lie on nested poloidal flux surfaces [31]. Magnetic field lines that lie on flux surfaces that do not intersect a solid surface are termed *closed*, while the rest are termed *open*. Starting from the plasma core and moving outwards, flux surfaces and magnetic field lines are closed until a last surface, termed the *Last-Closed-Flux-Surface* (LCFS). Surfaces radially further out are open with the magnetic field lines intercepting solid surfaces. The region radially outward of the LCFS is called the *Scrape-Off Layer* (SOL). The plasma can be operated either in a *limiter* or in a *divertor* configuration.

- In the limiter configuration, shown in figure 4.1a, the LCFS is tangent to the wall. As a result, the plasma on closed flux surfaces is in the immediate vicinity of the vessel wall.
- In the divertor (or diverted) configuration, shown in figure 4.1b, the LCFS is determined by a null-point in the poloidal field. The null-point, also termed *x-point*, is created using at least one external poloidal field coil. The associated magnetic flux surface, termed *separatrix*, coincides with the LCFS, separating the main plasma from the SOL. In a divertor configuration, SOL magnetic field lines intercept the

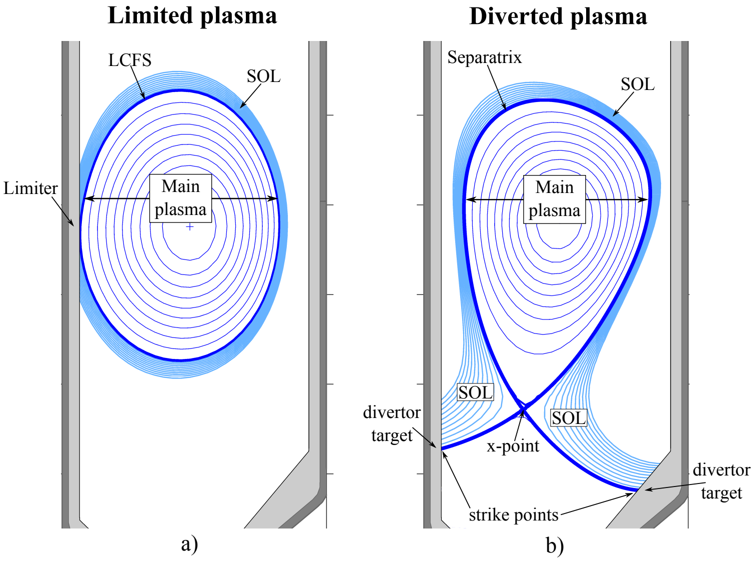

Figure 4.1 – Poloidal cross-section of the TCV tokamak showing a limited (a) and a diverted (b) configuration.

> walls in dedicated areas, termed *divertor targets*, that must be capable of handling significant plasma heat loads. Each location where the separatrix intercepts the divertor target is termed *strike point*, and the SOL field line structure extending between x-point and strike point is termed a *divertor leg*. The region between the two divertor legs, see figure 4.1b, is termed the *private flux region*. The SOL is also occasionally referred to as *common flux region*.

This thesis focuses exclusively on plasmas operated in the divertor configuration, thus complementing a recent thesis that investigated SOL physics in limited TCV plasmas [32].

4.1 The geometry of the plasma

In both the limiter and the divertor configuration, the LCFS determines the confined plasma shape. The most basic parameters that describe the geometry of the LCFS and, hence, of the plasma are:

$$a = \frac{R_{\text{max}} - R_{\text{min}}}{2} \qquad \text{minor radius} \qquad (4.1)$$

$$R_{\text{geo}} = \frac{R_{\text{max}} + R_{\text{min}}}{2} \qquad \text{major radius} \qquad (4.2)$$

$$\delta_{\text{upper}} = \frac{R_{\text{geo}} - R_{\text{up}}}{a} \qquad \text{upper triangularity} \qquad (4.3)$$

$$\delta_{\text{lower}} = \frac{R_{\text{geo}} - R_{\text{down}}}{a} \qquad \text{lower triangularity} \qquad (4.4)$$

$$\kappa = \frac{R_{\text{up}} - R_{\text{down}}}{R_{\text{max}} - R_{\text{min}}} \qquad \text{elongation} \qquad (4.5)$$

$$\epsilon = \frac{a}{R_{\text{geo}}} \qquad \text{plasma inverse aspect ratio} \qquad (4.6)$$

where the various radii are defined in figure 4.2a.

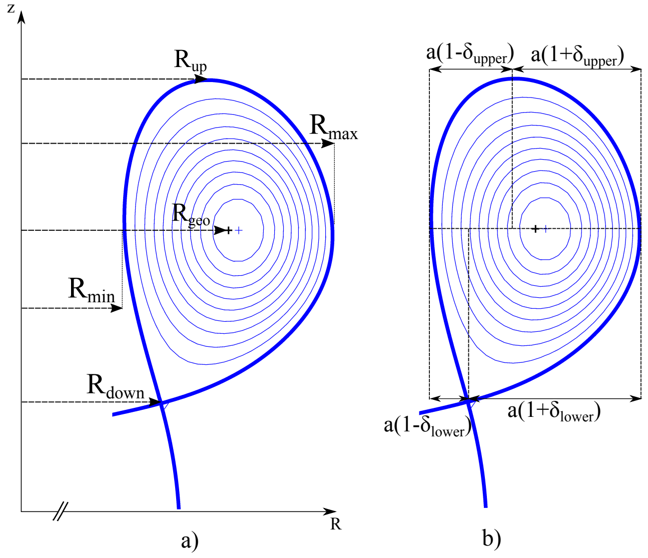

Figure 4.2 – (a) Radii commonly used to parametrise the plasma shape. (b) Radial distance between the plasma top (or bottom) and the inner (or outer) most point, as a function of lower and upper plasma triangularity.

The radial distance between plasma top (or bottom) and the inner (or outer) most point, shown in 4.2b, are functions of the plasma lower and upper triangularity:

$$R_{\text{up}} - R_{\text{min}} = a(1 - \delta_{\text{upper}}), \qquad R_{\text{max}} - R_{\text{up}} = a(1 + \delta_{\text{upper}}) \qquad (4.7)$$

$$R_{\text{down}} - R_{\text{min}} = a(1 - \delta_{\text{lower}}), \qquad R_{\text{max}} - R_{\text{down}} = a(1 + \delta_{\text{lower}}) \qquad (4.8)$$

Once the plasma current is fixed, plasma shaping affects the poloidal field strength at plasma edge, which is an important quantity for the physics of heat exhaust and plasma stability. Assuming elliptic flux surfaces, and high aspect ratio, Ampere's law yields the poloidally-averaged poloidal magnetic field strength at the plasma edge

$$\langle B_p \rangle = \frac{\mu_0 I_P}{2\pi a \sqrt{\frac{1+\kappa^2}{2}}} \tag{4.9}$$

where μ_0 is the permeability of free space and I_P the plasma current.

4.2 The geometry of the SOL in the divertor configuration

In the Scrape-Off Layer, flux surfaces are open and magnetic field lines intercept the wall at the divertor targets. Each poloidal flux surface in the SOL can be labelled with a scalar coordinate $\mathrm{d}r_u$, defined as the distance between the flux surface and the separatrix, evaluated at the outboard mid-plane, see figure 4.3. The outboard mid-plane is, by definition, at the same vertical position as the magnetic axis. Alternatively, a flux surface can be labelled by the normalized poloidal flux coordinate

$$\rho_\psi = \sqrt{(\psi - \psi_0)/(\psi_\mathrm{LCFS} - \psi_0)} \qquad \text{Normalized poloidal flux} \tag{4.10}$$

where ψ, ψ_0 and ψ_LCFS are the poloidal flux values on that surface, at the magnetic axis and at the magnetic separatrix, respectively.

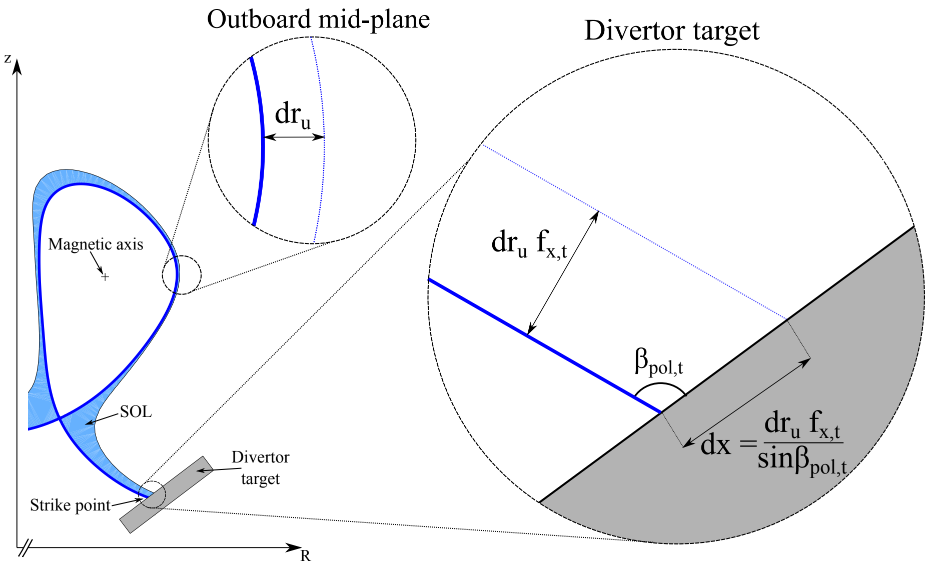

Figure 4.3 – Description of the SOL scalar coordinate $\mathrm{d}r_u$, defined at the outboard mid-plane, and its relation to the SOL scalar coordinate dx, defined at the divertor target.

The separation between SOL flux surfaces varies when moving poloidally around the confined plasma or along the divertor leg. The ratio of this distance evaluated at the divertor target and at the outboard mid-plane is termed *target poloidal flux expansion*[1]

$$f_{x,t} := \frac{\mathrm{d}r_t}{\mathrm{d}r_u} \qquad \text{Target poloidal flux expansion} \tag{4.11}$$

and is practically computed as

$$f_{x,t} = \frac{R_u B_{p,u}}{R_t B_{p,t}} \tag{4.12}$$

where R_u and $B_{p,u}$ are major radius and poloidal magnetic field at the outboard mid-plane, whereas R_t and $B_{p,t}$ are evaluated at the target. In this thesis work, $f_{x,t}$ is only referred to as *target flux expansion.*

Considering that the divertor plate can be tilted with respect to the separatrix, as shown in figure 4.3, yields

$$\mathrm{d}r_u = dx \cdot \frac{\sin\beta_{\mathrm{pol},t}}{f_{x,t}} \qquad \text{SOL coordinate} \tag{4.13}$$

with dx the distance between flux surfaces evaluated along the target, and $\beta_{\mathrm{pol},t}$ the angle, in the poloidal plane, between divertor plate and separatrix. Note that a more tilted divertor plate, relative to the horizontal, corresponds to a smaller value of $\beta_{\mathrm{pol},t}$. Such a small value of $\beta_{\mathrm{pol},t}$ is characteristic for vertical targets and such an arrangement of the plates is often referred to as a *closed* divertor. The definition of $\mathrm{d}r_u$, equation 4.13, can be extended into the private flux region, where $\mathrm{d}r_u$ becomes negative, even though the location at the target is no longer directly magnetically connected to the outboard mid-plane.

The geometrical relation 4.13 holds when the distance dx is sufficiently small to neglect variations of $\beta_{\mathrm{pol},t}$ and $f_{x,t}$ along the target. In the more general case, one should use

$$\mathrm{d}r_u = \int_{x_0}^{x} \frac{\sin\beta_{\mathrm{pol},t}(x')}{f_{x,t}(x')} dx' \tag{4.14}$$

where x is the coordinate along the target and x_0 the position of the separatrix at the target (i.e. the position of the strike point).

In the Scrape-Off Layer, the length of a magnetic field line connecting the outer mid-plane to the divertor target is termed the *parallel connection length*, and is computed with

$$L_{\|}(\mathrm{d}r_u) = \int \mathrm{d}s_{\|} = \int \mathrm{d}s_p \frac{B_{\mathrm{tot}}(\mathrm{d}r_u, s_p)}{B_p(\mathrm{d}r_u, s_p)} \qquad \text{Parallel connection length} \tag{4.15}$$

where $\mathrm{d}r_u$ is the position of the field line at the outboard mid-plane, $s_{\|}$ is a coordinate

---

[1] Note that there is also the *total flux expansion*, which represents the increase of the flux tube cross-sectional area and scales as $\propto 1/B_{\mathrm{tot}}$.

parallel to the SOL field line ($s_\parallel = 0$ at the outboard mid-plane, $s_\parallel = L_\parallel$ at the divertor plate) and s_p its projection into the poloidal plane.

4.3 Mapping of target quantities to an upstream location

To compare target heat loads of different divertor geometries, the heat flux profile measured at the divertor target is mapped, along magnetic field lines, to the corresponding *upstream location*, i.e. on the outer (outboard) mid-plane (OMP). Note that the upstream-mapped profile is not the profile upstream, as this mapping does not account for SOL power losses or any cross-field heat spreading between the upstream location and the target. This section describes two ways to perform this mapping, which are shown to be equivalent.

Mapping upstream with poloidal tilting angle of target At the target, the heat flux perpendicular to the (toroidally symmetric) plate $q_{\perp,t}$ and the poloidal component of the heat flux $q_{p,t}$ are related by

$$q_{\perp,t} = q_{p,t} \sin \beta_{\mathrm{pol},t} \tag{4.16}$$

It is assumed that upstream plasma heat somehow diffuses from the main plasma into the SOL, and then follows open field lines towards the targets without further cross-field transport and in the absence of heat sinks or sources. Under these assumptions, the power entering a flux tube of radial extent $\mathrm{d}r_u$ at the upstream location is equal to the power that exits the same flux tube at the target,

$$2\pi R_u \mathrm{d}r_u q_{p,u} = 2\pi R_t \mathrm{d}r_u f_{x,t} q_{p,t} \tag{4.17}$$

where $q_{p,u}$ is the poloidal component of the heat flux at the upstream location. This relation yields

$$q_{p,u} = q_{p,t} \frac{R_t}{R_u} f_{x,t} \tag{4.18}$$

At the upstream location, the heat flux parallel to the magnetic field $q_{\parallel,u}$ and that parallel to the poloidal component of the field $q_{p,u}$ are related by

$$q_{\parallel,u} = q_{p,u} \frac{B_{\mathrm{tot},u}}{B_{p,u}} \tag{4.19}$$

Finally, combining equations 4.16-4.18-4.19 yields a relation between the heat flux onto the target and the upstream parallel heat flux

$$\boxed{q_{\perp,t} = q_{\|,u} \frac{B_{p,u}}{B_{\text{tot},u}} \frac{R_u}{R_t} \frac{\sin \beta_{\text{pol},t}}{f_{x,t}}} \tag{4.20}$$

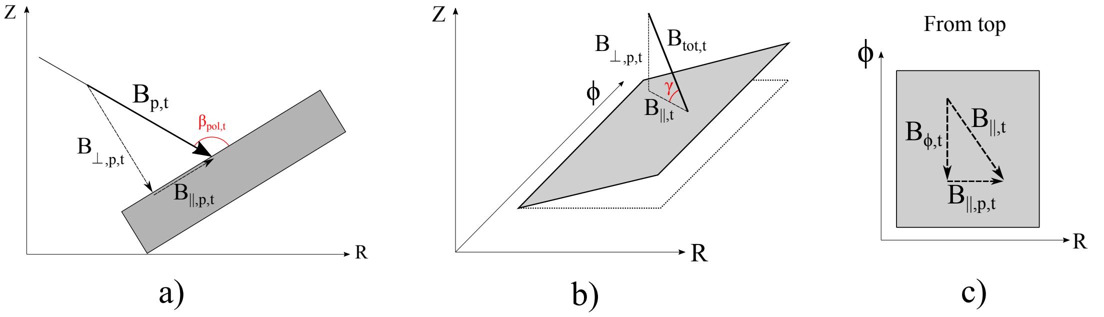

Figure 4.4 – (a) Poloidal magnetic field projected perpendicularly and parallel to the divertor plate. (b) Total field components, at the target, perpendicular and parallel to the divertor plate. (c) Top view (perpendicularly to the tilted plate surface) of the case shown in (b).

Relation between $\boldsymbol{\beta_{\text{pol},t}}$, $\boldsymbol{f_{x,t}}$ and $\boldsymbol{\gamma}$ An important observation for power exhaust is that $\beta_{\text{pol},t}$ and $f_{x,t}$ are naturally coupled through the field line incidence angle at the target γ. The poloidal field at the target $B_{p,t}$ can be projected perpendicularly and parallel to the target plate, figure 4.4a,

$$B_{\perp,p,t} = B_{p,t} |\sin(\pi - \beta_{\text{pol},t})| = B_{p,t} \sin \beta_{\text{pol},t} \tag{4.21}$$

$$B_{\|,p,t} = B_{p,t} |\cos(\pi - \beta_{\text{pol},t})| = B_{p,t} \cos \beta_{\text{pol},t} \tag{4.22}$$

In order to obtain an expression for the field line grazing angle γ, shown in figure 4.4b, an expression for $B_{\|,t}$ is obtained by observing the system from above, see figure 4.4c,

$$B_{\|,t} = \sqrt{B_{\phi,t}^2 + B_{\|,p,t}^2} \tag{4.23}$$

Therefore, the incidence angle γ is given by:

$$\begin{aligned}\tan\gamma &= \frac{B_{\perp,p,t}}{B_{\parallel,t}} = \frac{B_{p,t}\sin\beta_{\mathrm{pol},t}}{\sqrt{B_{\phi,t}^2 + B_{\parallel,p,t}^2}} = \frac{B_{p,t}\sin\beta_{\mathrm{pol},t}}{\sqrt{B_{\phi,t}^2 + B_{p,t}^2\cos^2\beta_{\mathrm{pol},t}}}\\ &= \frac{R_u}{R_t}\frac{B_{p,u}}{f_{x,t}}\frac{\sin\beta_{\mathrm{pol},t}}{B_{\phi,t}\sqrt{1+(\frac{B_{p,t}}{B_{\phi,t}})^2\cos^2\beta_{\mathrm{pol},t}}}\\ &= \frac{B_{\phi,t}}{B_{\phi,u}}\frac{B_{p,u}}{f_{x,t}}\frac{\sin\beta_{\mathrm{pol},t}}{B_{\phi,t}\sqrt{1+(\frac{B_{p,t}}{B_{\phi,t}})^2\cos^2\beta_{\mathrm{pol},t}}}\\ &\approx \frac{B_{p,u}\sin\beta_{\mathrm{pol},t}}{B_{\mathrm{tot},u}f_{x,t}}\end{aligned}$$

using the definition of $f_{x,t}$ and, in the last passage, the approximations $B_{\mathrm{tot},u} \approx B_{\phi,u}$ and $B_{p,t} \ll B_{\phi,t}$. Finally, one obtains

$$\boxed{\frac{\sin\beta_{\mathrm{pol},t}}{f_{x,t}} \approx \frac{B_{\mathrm{tot},u}}{B_{p,u}}\tan\gamma} \tag{4.24}$$

This relation shows that a particular value of γ can be equally achieved by changing the poloidal tilt of the divertor plate or the target flux expansion.

Mapping upstream with field line grazing angle at target An alternative mapping of the target heat fluxes to the upstream location is to use the field line grazing angle γ. The heat flux parallel to field lines at the target $q_{\parallel,t}$ is computed by considering the field line grazing angle γ

$$q_{\parallel,t} = q_{\perp,t}/\sin\gamma \tag{4.25}$$

which is then projected upstream

$$q_{\parallel,u} = q_{\parallel,t}\cdot\frac{B_{\mathrm{tot},u}}{B_{\mathrm{tot},t}} \approx q_{\parallel,t}\cdot\frac{R_t}{R_u} \tag{4.26}$$

where the ratio $B_{\mathrm{tot},u}/B_{\mathrm{tot},t}$ corresponds to the flux tube cross-sectional area variation between upstream location and target, also referred to as *total* flux expansion. This area scales as $\propto B_{\mathrm{tot}}^{-1} \sim R$. Combining these relations yields

$$\boxed{q_{\perp,t} \approx q_{\parallel,u}\sin\gamma\frac{R_u}{R_t}} \tag{4.27}$$

Relation 4.27 is actually equivalent to equation 4.20. Using equation 4.21 and the definition of $f_{x,t}$, one obtains

$$\sin\gamma = \frac{B_{\perp,p,t}}{B_{\text{tot},t}} = \frac{B_{p,t}\sin\beta_{\text{pol},t}}{B_{\text{tot},t}} = \frac{R_u}{R_t}\frac{B_{p,u}}{f_{x,t}}\frac{\sin\beta_{\text{pol},t}}{B_{\text{tot},t}} \tag{4.28}$$

$$\approx \frac{B_{p,u}}{f_{x,t}}\frac{\sin\beta_{\text{pol},t}}{B_{\text{tot},u}} \tag{4.29}$$

which is substituted into equation 4.27, yielding

$$q_{\perp,t} \approx q_{\parallel,u}\frac{R_u}{R_t}\frac{B_{p,u}}{f_{x,t}}\frac{\sin\beta_{\text{pol},t}}{B_{\text{tot},u}} \approx q_{\parallel,u}\frac{B_{p,u}}{B_{\text{tot},u}}\frac{\sin\beta_{\text{pol},t}}{f_{x,t}} \tag{4.30}$$

4.4 Heat wetted area at target

In a diverted plasma configuration, the *plasma-wetted (or heat-wetted) area* is the surface area, on the divertor targets, over which the SOL exhaust power is deposited. This quantity is of capital importance for the structural integrity of the divertor plates. A small wetted area is often problematic, as it translates into intense plasma-solid interactions, causing localized over-heating and, in the worst case, damage to the divertor plate. A larger wetted area, on the contrary, reduces peak heat fluxes at the target and, thereby, the risk of damaging the surface.

The heat wetted area at the target is formally defined as the ratio of deposited power and peak heat flux

$$A_{\text{wet}} := \frac{P}{q_{\perp,t}^{\text{peak}}} \qquad \text{Heat wetted area} \tag{4.31}$$

When the SOL heat flux profile along the target is described by an exponential with fall-off length $\lambda_{q,t}^*$, the deposited power is

$$P = 2\pi R_t \cdot \int q_{\perp,t}\,dx = 2\pi R_t \cdot q_{\perp,t}^{\text{peak}}\lambda_{q,t}^* \tag{4.32}$$

where R_t is the target radius and the integration is performed along the target surface. The heat wetted area therefore becomes

$$A_{\text{wet}} = 2\pi R_t \cdot \lambda_{q,t}^* \qquad \text{Heat wetted area (exponential)} \tag{4.33}$$

where R_t is the target radius. The $\lambda_{q,t}^*$ is the SOL heat channel width at the target surface, and includes the effect of target tilt. Using equation 4.13, $\lambda_{q,t}^*$ can be related to the SOL heat channel width upstream $\lambda_{q,u}$

$$\lambda_{q,t}^* = \lambda_{q,u} \cdot \frac{f_{x,t}}{\sin\beta_{\text{pol},t}} \tag{4.34}$$

which, substituted into relation 4.33, finally yields

$$\boxed{A_{\text{wet}} = 2\pi R_t \cdot \lambda_{q,u} \cdot \frac{f_{x,t}}{\sin \beta_{\text{pol},t}}} \tag{4.35}$$

The width $\lambda_{q,u}$ is determined by the competition of heat transport parallel to SOL field lines and perpendicularly to them. The value of $\lambda_{q,u}$ is experimentally seen to vary with plasma conditions (e.g. plasma current) and shape of the divertor, as shown in the following chapters, and is an important quantity in power exhaust physics as it is directly related to the target peak heat flux $q_{\perp,t}^{\text{peak}}$. Using equations 4.31-4.35 and assuming fixed exhaust power yields

$$q_{\perp,t}^{\text{peak}} \propto A_{\text{wet}}^{-1} \propto \lambda_{q,u}^{-1} \tag{4.36}$$

as neither R_t, nor $f_{x,t}$ or $\sin \beta_{\text{pol},t}$ (linked through the grazing angle γ, equation 4.24), can be arbitrarily increased or decreased.

Effect of divertor heat spreading Experimentally, some spreading of the SOL heat flux perpendicularly to flux surfaces, i.e. in the *cross-field* direction, is observed in the divertor leg. This process broadens the SOL heat channel width at the target and, therefore, the heat wetted area. To account for this process, it is convenient to define an integral SOL width $\lambda_{\text{int},t}^*$ at the target [33]

$$\lambda_{\text{int},t}^* = \frac{\int q_{\perp,t} \, dx}{q_{\perp,t}^{\text{peak}}} \qquad \text{Integral SOL width (at target)} \tag{4.37}$$

This quantity replaces $\lambda_{q,t}^*$ in the expression of the wetted area

$$A_{\text{wet}} = 2\pi R_t \cdot \lambda_{\text{int},t}^* \tag{4.38}$$

and, using equation 4.13, can be mapped upstream to a width $\lambda_{\text{int},u}$

$$\lambda_{\text{int},t}^* = \lambda_{\text{int},u} \cdot \frac{f_{x,t}}{\sin \beta_{\text{pol},t}} \tag{4.39}$$

The expression for the wetted area including divertor heat spreading is

$$\boxed{A_{\text{wet}} = 2\pi R_t \cdot \lambda_{\text{int},u} \cdot \frac{f_{x,t}}{\sin \beta_{\text{pol},t}}} \tag{4.40}$$

Using equation 4.24, the heat wetted area can be expressed in terms of γ, the magnetic field line incidence angle at the target,

$$A_{\text{wet}} \approx 2\pi \frac{B_{p,u}}{B_{\text{tot},u}} \cdot R_t (\tan \gamma)^{-1} \cdot \lambda_{\text{int},u} \tag{4.41}$$

Integral SOL power width upstream A useful expression to compute the SOL $\lambda_{\mathrm{int},u}$ from experimental data is obtained by combining the definition of $\lambda^*_{\mathrm{int},t}$, equation 4.37, with equation 4.39,

$$\boxed{\lambda_{\mathrm{int},u} = \frac{\int q_{\perp,t}\ dx}{q^{\mathrm{peak}}_{\perp,t}} \cdot \frac{\sin\beta_{\mathrm{pol},t}}{f_{x,t}}} \tag{4.42}$$

which can be conveniently expressed in terms of $q_{\|,u}$, the SOL parallel heat flux mapped to the upstream location, by using equation 4.20,

$$\lambda_{\mathrm{int},u} = \frac{\int q_{\|,u}\ \mathrm{d}r_u}{q^{\mathrm{peak}}_{\|,u}} \tag{4.43}$$

Wetted area at fixed grazing angle To reduce the risk of damaging the divertor target surface in a future nuclear fusion reactor based upon the tokamak concept, the plasma should be operated in a way that maximises the heat wetted area at the target. An obvious way to increase the wetted area is by lowering the field line grazing angle at the target γ, see equation 4.41, which is achieved either by increasing $f_{x,t}$ or by lowering $\beta_{\mathrm{pol},t}$, see equation 4.40. The effectiveness of this strategy is, however, limited, as engineering constraints on divertor component positioning pose a lower limit of $\sim$ 3° for γ [5]. With γ equal to its minimum acceptable value, and $B_{p,u}$ and $B_{\mathrm{tot},u}$ determined by the core scenario, the wetted area, equation 4.41, becomes proportional to target radius R_t and integral SOL width $\lambda_{\mathrm{int},u}$

$$A_{\mathrm{wet}} \propto R_t\ \lambda_{\mathrm{int},u} \tag{4.44}$$

This shows that a further increase in the wetted area can be achieved exclusively by a larger R_t or by increasing $\lambda_{\mathrm{int},u}$.

In addition, rearranging equation 4.24 shows that target flux expansion (here denoted as 'optimized', $f^{\mathrm{opt}}_{x,t}$) and tile tilting angle are functionally dependent,

$$f^{\mathrm{opt}}_{x,t} \approx \frac{B_{p,u}}{B_{\mathrm{tot},u}} (\tan\gamma_{\mathrm{min}})^{-1} \cdot \sin\beta_{\mathrm{pol},t} \qquad \text{Optimized } f_{x,t} \tag{4.45}$$

so that $f^{\mathrm{opt}}_{x,t} \propto \sin\beta_{\mathrm{pol},t}$ at fixed poloidal and total field upstream. For the same γ_{min}, configurations with higher target flux expansion require a larger poloidal target angle, i.e. closer to perpendicular, as shown in figure 4.5. When the plate is perpendicular to the field lines, the optimized flux expansion attains its highest value. If the target flux expansion is increased above this limit, the field line grazing angle drops below the technologically acceptable limit.

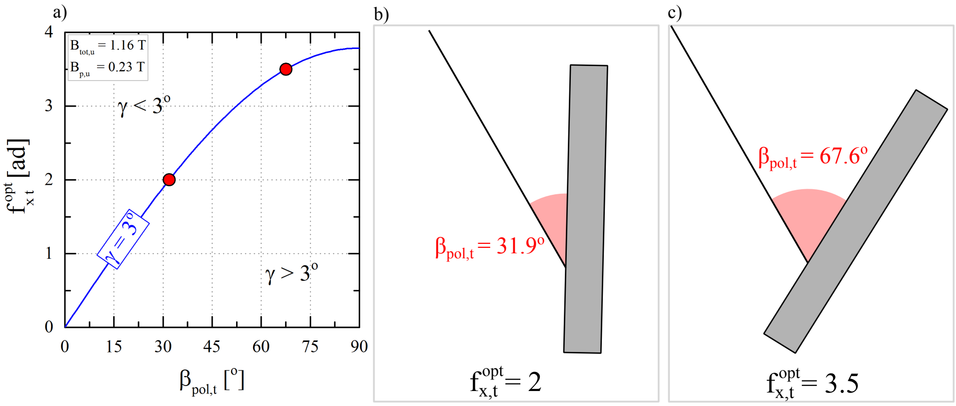

Figure 4.5 – (a) At fixed values of $B_{\text{tot},u} = 1.16$ T, $B_{p,u} = 0.23$ T, functional dependence between optimized target flux expansion, i.e. that achieves $\gamma = \gamma_{\text{min}} = 3°$, and poloidal tilting angle of the divertor tile. (b-c) The configurations indicated by red points in figure (a), corresponding to $f_{x,t}^{\text{opt}}$ of 2 and 3.5 respectively. Note that for $\beta_{\text{pol},t} > 90°$, $f_{x,t}(\theta) = f_{x,t}(\pi - \theta)$, equation 4.45.

4.5 Conventional and alternative divertor configurations

This thesis explores the multidimensional space of divertor configurations accessible in the TCV tokamak. This section presents the conventional and alternative divertor configurations studied in this thesis, introducing the terminology and outlining power exhaust benefits expected from each concept.

4.5.1 The Single-Null divertor

The most common magnetic divertor configuration in present-day tokamaks is the Single-Null (SN). The standard Single-Null divertor configuration, shown in figure 4.6a, features a first-order poloidal field null, or x-point. The two strike points are referred to as *inner strike point* (ISP), at higher toroidal field, and *outer strike point* (OSP), at lower toroidal field. From this SN configuration, a substantial increase in either the divertor leg length, the outer target flux expansion or the outer target radius results in three alternative divertor configurations.

4.5.1.1 The Long-Legged SN

The Long-Legged SN divertor arises from an increase of the poloidal length of the outer divertor leg L_{div}, figure 4.6b. A long divertor leg is potentially beneficial for power exhaust as it is expected to decrease target peak heat fluxes and to lower the upstream density required to achieve divertor detachment $n_{e,u}^{\text{det}}$ (see equation 5.53), i.e. to facilitate detachment onset. The long leg increases the field line connection length in the SOL, $L_{\parallel}$, which in turn reduces $n_{e,u}^{\text{det}}$, as $n_{e,u}^{\text{det}} \propto L_{\parallel}^{-2/7}$ (see equation 5.53). In addition, the

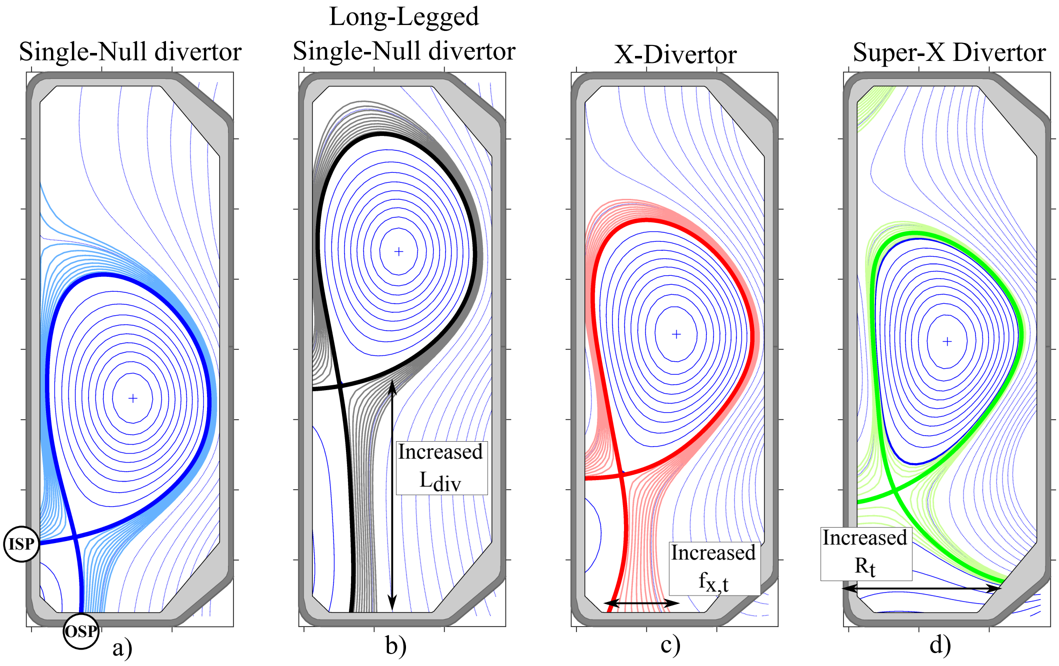

Figure 4.6 – (a) Standard Single-Null divertor with its inner (ISP) and outer (OSP) strike points. (b) Long-Legged Single-Null divertor, which increases the outer divertor leg length. (c) X-Divertor configuration, which flares the outer target flux expansion. (d) Super-X divertor configuration, which increases the outer strike point radius.

increased $L_{\parallel}$ is expected to increase the amount of cross-field spreading of the SOL heat flux in the divertor leg, broadening the heat wetted area at the target A_{wet}, and to enhance volumetric radiative losses in the SOL. Both effects further reduce $n_{e,u}^{\mathrm{det}}$, as $n_{e,u}^{\mathrm{det}} \propto (1 - f_{\mathrm{rad}})A_{\mathrm{wet}}^{-1}$ (see equation 5.53), and the target peak heat fluxes.

4.5.1.2 The X-Divertor

The X-Divertor [34, 35] (XD) introduces a flaring of magnetic flux surfaces near the targets by increasing the target flux expansion $f_{x,t}$. This corresponds to a decrease of the poloidal field at the target, equation 4.12. The TCV experiments discussed in this work achieve the X-Divertor geometry only at the outer divertor target, see figure 4.6c. This configuration has several potential benefits for power exhaust. Firstly, the flux flaring at the target is expected to counteract the movement of the contact area between SOL plasma and recycling neutrals, leading to a more robust detachment [36]. Compared to the standard SN, the detachment front should be more reluctant to move close to the x-point since, as the front moves closer, the contact area between SOL plasma and recycling neutrals is reduced. This decreases the ionization rate in the divertor and, thus, increases the plasma temperature, pushing the ionization front towards the target. Secondly, the large $f_{x,t}$ increases the field line length in the SOL $L_{\parallel}$. This, as discussed for the long-legged SN using equation 5.53, reduces the density threshold for detachment, $n_{e,u}^{\text{det}} \propto L_{\parallel}^{-2/7}$, and may enhance volumetric radiation and cross-field heat flux spreading in the divertor leg, further reducing the density threshold for detachment, $n_{e,u}^{\text{det}} \propto (1 - f_{\text{rad}}) A_{\text{wet}}^{-1}$, and lower target peak heat fluxes.

4.5.1.3 The Super-X Divertor

The Super-X Divertor [37] (SX) increases the radius R_t of the outer strike point, figure 4.6d. This configuration is potentially beneficial for power exhaust since it increases the heat wetted area (see equation 4.35) and the SOL volume, which are both proportional to R_t provided that the *poloidal* flux expansion is kept constant. The higher SOL volume may translate to increased volumetric radiative losses. Both the larger wetted area and volumetric losses lower target peak heat fluxes and the density threshold for divertor detachment, $n_{e,u}^{\text{det}} \propto (1 - f_{\text{rad}}) A_{\text{wet}}^{-1}$, equation 5.53. In addition, the geometrical dependence $q_{\parallel} \sim R^{-1}$ (see equation 4.26) creates a gradient of $q_{\parallel}$ along SOL field lines that could facilitate detachment and stabilize the cold front position [38, 39]. As the cold detachment front moves towards the x-point, the SOL parallel heat flux $q_{\parallel}$ augments, increasing plasma temperature and that would push the cold front back towards the target.

4.5.2 The Snowflake Divertor

The Snowflake divertor configuration [40] (SF), shown in figure 4.7a, features a second-order poloidal field null, where both the poloidal magnetic field and its first spatial derivatives are null. In the proximity of a second-order null, the magnetic separatrix has a characteristic hexagonal structure, see figure 4.7a, evocative of a snowflake, with two branches enclosing the plasma and the others connecting to four separate strike points at the vessel wall.

Snowflake Divertor variants Since an exact SF resides only at a single point in operational space, any experimental SF configuration will, in reality, feature two nearby first-order nulls. Note that while a small separation is unavoidable, a larger separation may be intentionally chosen. An experimental SF, therefore, features always a *primary x-point*, associated with the *primary separatrix* enclosing the plasma (shown in blue in figures 4.7b-c-d), and a *secondary x-point*, associated with a *secondary separatrix* (shown in red in figures 4.7b-c-d). Placing the secondary x-point in the private flux region of the main separatrix creates a *Snowflake Plus* (SF+) configuration, figure 4.7d, whereas placing it in the common flux region of the main separatrix creates a *Snowflake Minus* (SF-) configuration, figures 4.7b-c. This latter configuration has two variants, the Low-Field Side (LFS) and the High-Field Side (HFS) Snowflake Minus, for which the secondary x-point is located in the LFS or in the HFS SOL, respectively.

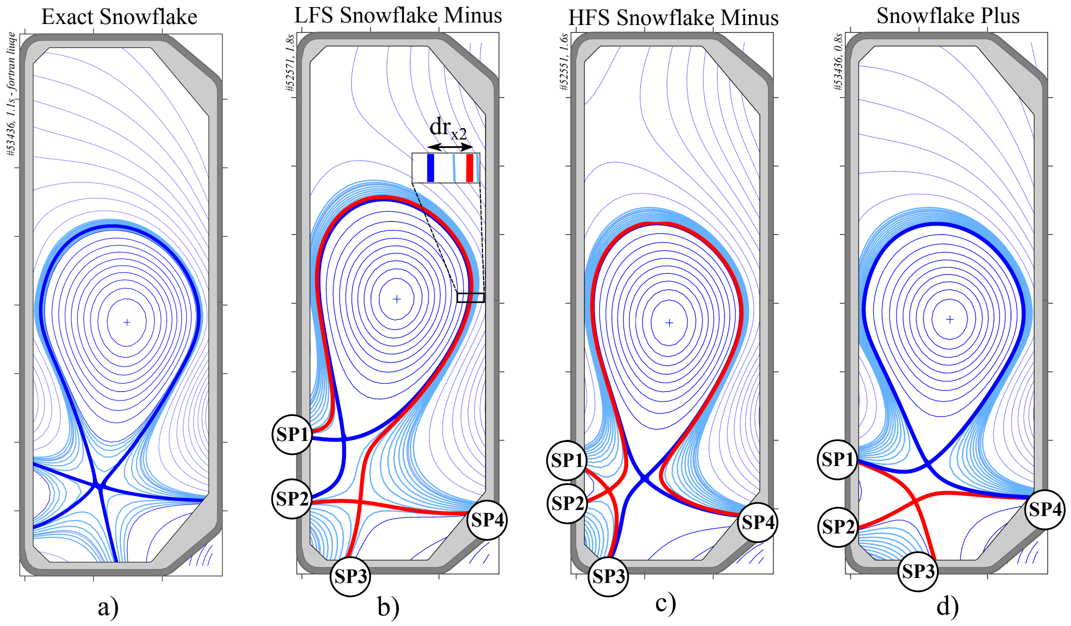

Figure 4.7 – Magnetic equilibria, in a cross-sectional view of TCV, of (a) an exact Snowflake, (b) a LFS Snowflake Minus, (c) a HFS Snowflake Minus and (d) a Snowflake Plus configuration. The convention used in this text in numbering the strike points and the definition for $\mathrm{d}r_{\mathrm{x2}}$ are also indicated. The secondary magnetic separatrix, associated to the secondary x-point, is shown in red.

A SF+ or SF- configuration is uniquely identified by a couplet of geometrical parameters (σ, θ). The σ is the spatial distance, in the poloidal plane, between the two x-points, normalized to the plasma minor radius, and θ is the angle between a line connecting the x-points and a line perpendicular to the segment connecting the magnetic axis and the primary x-point [41]. Many power exhaust properties of the SF- configuration can be described by a single reduced parameter [42], the distance between primary and secondary separatrix computed at the outboard mid-plane $\mathrm{d}r_{\mathrm{x2}}$, see figure 4.7b.

Potential power exhaust benefits The Snowflake divertor is potentially beneficial for power exhaust for several reasons. Firstly, the large volume of weak poloidal field between the two nulls (or, equivalently, that around the second-order null in an exact SF) enhances the SOL field line length $L_{\|}$ and, thus, increases the SOL volume in the vicinity of the separatrix, that is expected to increase volumetric radiative losses. These effects would lower the density threshold for detachment, $n_{e,u}^{\mathrm{det}} \propto (1 - f_{\mathrm{rad}})L_{\|}^{-2/7}$, equation 5.53. Secondly, the region of low poloidal field may enhance the amount of cross-field transport of heat and particles in the SOL, through a churning mode driven by vertical pressure gradient and magnetic field curvature [43] or $\vec{E} \times \vec{B}$ drifts enhanced by the large poloidal gradients [44]. The enhanced transport would cause a broadening of the heat wetted area, at the target, as well as activating strike points that are not connected to the SOL (SP3 in the LFS SF-, SP2 in the HFS SF-, SP2 and SP3 in the SF+, figures 4.7b-c-d). The broader wetted area A_{wet} further reduces the density threshold for divertor detachment, $n_{e,u}^{\mathrm{det}} \propto A_{\mathrm{wet}}^{-1}$, equation 5.53.

In conclusion, this chapter introduced the definitions and nomenclatures used, in the following chapters, to describe the geometry of the SOL and of the magnetic divertor. It also described the methodology adopted to compare target heat loads of different divertor configurations. Using geometric arguments, it is shown that when the field line grazing angle at the target is set equal to its minimum acceptable value (from engineering constraints), the target heat wetted area A_{wet} can be increased exclusively by a larger target radius R_t or by enhancing the SOL heat channel width $\lambda_{\mathrm{int},u}$, that is set by SOL transport physics. This highlights the importance of improving the understanding of the physics that controls $\lambda_{\mathrm{int},u}$ and, in parallel, of exploring any potential link between $\lambda_{\mathrm{int},u}$ and the magnetic divertor geometry. A review of some prominent alternative divertor concepts, evolutions from the standard Single-Null divertor, shows that most of their potential power exhaust benefits result from either the increased SOL field line length or an increased target radius, which can both enhance volumetric radiative losses and broaden the target wetted area. In the Snowflake divertor, additional power exhaust benefits may come from an enhancement of SOL cross-field transport physics associated to the weak poloidal field in proximity of the two x-point and power distribution to additional strike points.

5 The Scrape-Off Layer and divertor physics

This chapter reviews and extends existing models for heat transport in the Scrape-Off Layer, that are used, in chapters 6 and 7, to interpret the experimental measurements. The first part of the chapter, section 5.1, discusses models for SOL heat transport in steady state conditions. The second part of the chapter, section 5.2, discusses models for SOL heat transport during the ELM transients.

5.1 Stationary plasma transport in the SOL

This section discusses models for SOL heat transport in stationary conditions:

- Section 5.1.1 reviews the Eich parameterisation, which introduces two lengths to describe target heat flux profiles, the SOL width $\lambda_{q,u}$, related to asymmetric cross-field SOL transport around the confined plasma, and a spreading factor S_u, related to symmetric cross-field SOL trasport in the divertor region.
- Section 5.1.2 proposes a model of the SOL, where parallel transport is conductive and perpendicular transport is due to temperature gradients. This model does not prescribe a specific cross-field transport mechanism, retaining the cross-field heat diffusivity $\chi_\perp$ as parameter, and yields a prediction for the in-out power sharing and for the SOL width.
- Section 5.1.3 reviews the heuristic drift-based model of the SOL by Goldston where parallel transport is conductive, similarly to section 5.1.2, but perpendicular heat transport is attributed to a specific mechanism, ∇B and curvature B particle drifts. This model also yields an expression for the SOL width.
- Section 5.1.4 proposes a diffusive model for heat transport in the divertor SOL, yielding a prediction for S_u.

- Section 5.1.5 proposes a model for the heat flux splitting at the secondary x-point of the alternative Snowflake Minus magnetic configuration.
- Section 5.1.6 derives, using the basic hypothesis of the conductive model in section 5.1.2, a scaling relation for the minimum plasma density required to achieved divertor detachment in terms of plasma and divertor shape quantities.

5.1.1 The Eich parameterisation

The Eich parameterisation, proposed in [45], interprets the SOL heat flux profile at the divertor target as a result of an exponential heat flux profile undergoing radial (cross-field) heat diffusion in the divertor. Assuming no heat sinks or sources in the divertor, and attached divertor conditions, the SOL heat flux profile at the divertor entrance (near the x-point), parallel to magnetic field lines, is described by

$$q_{\parallel,X}(\bar{x}) = q_{0,X} \exp\left(-\frac{\bar{x}}{\lambda_{q,u} f^*_{x,t}}\right) \quad \text{and} \quad \bar{x} = x - x_0, \qquad x \geq x_0 \tag{5.1}$$

where x is the divertor target coordinate, x_0 the strike line position, $\lambda_{q,u}$ the SOL power decay length and

$$f^*_{x,t} := \frac{dx}{\mathrm{d}r_u} = \frac{f_{x,t}}{\sin \beta_{\mathrm{pol},t}} \tag{5.2}$$

is the effective target flux expansion[1], i.e. the target flux expansion, equation 4.12, corrected for target tilting $\beta_{\mathrm{pol},t}$. Note that the definition of flux expansion in [45] already includes the effect of divertor target tilting. In the divertor region, between x-point and target, the truncated exponential SOL heat flux profile, equation 5.1, diffuses perpendicularly to the magnetic field lines into both the private-flux-region and the common-flux-region of the separatrix. This heat diffusion is parameterised by introducing a Gaussian width S^*_t, named the *divertor spreading factor*, representing the competition between parallel and perpendicular heat transport in the divertor. The target SOL heat flux profile becomes the convolution of the exponential profile, equation 5.1, and a Gaussian function with the width S^*_t,

$$q_{\parallel,t}(\bar{x}) = \frac{q_{0,t}}{2} \exp\left[\left(\frac{S^*_t}{2\lambda_{q,u} f^*_{x,t}}\right)^2 - \frac{\bar{x}}{\lambda_{q,u} f^*_{x,t}}\right] \cdot \operatorname{erfc}\left(\frac{S^*_t}{2\lambda_{q,u} f^*_{x,t}} - \frac{\bar{x}}{S^*_t}\right) + q_{\mathrm{BG}} \tag{5.3}$$

where q_{BG} is added to account for possible offsets in the profile (see section A.2 for a full derivation of the convolution). This function has five free parameters: S^*_t, $\lambda_{q,u}$, $q_{0,t}$, x_0 and q_{BG}. The spreading factor S^*_t can be mapped upstream by using the effective flux

---

[1] Note that, in this thesis work, flux expansion refers to *poloidal* flux expansion unless explicitly stated otherwise.

expansion

$$S_u = S_t^* / f_{x,t}^* \tag{5.4}$$

The function describing the target heat flux, using equation 5.4, becomes

$$\boxed{q_{\parallel,t}(\bar{x}) = \frac{q_{0,t}}{2} \exp\left[\left(\frac{S_u}{2\lambda_{q,u}}\right)^2 - \frac{\bar{x}}{\lambda_{q,u} f_{x,t}^*}\right] \cdot \left[\operatorname{erfc}\left(\frac{S_u}{2\lambda_{q,u}} - \frac{\bar{x}}{S_u f_{x,t}^*}\right)\right] + q_{\mathrm{BG}}} \tag{5.5}$$

Fitting the heat flux profiles measured on the divertor targets with this functional form yields values for the five parameters, see figure 5.1. The two most interesting parameters for SOL heat transport studies, and that will be investigated in this work, are the SOL width $\lambda_{q,u}$ and the spreading factor S_u. They directly relate to the divertor peak heat load and, therefore, determine the extent of the heat exhaust challenge.

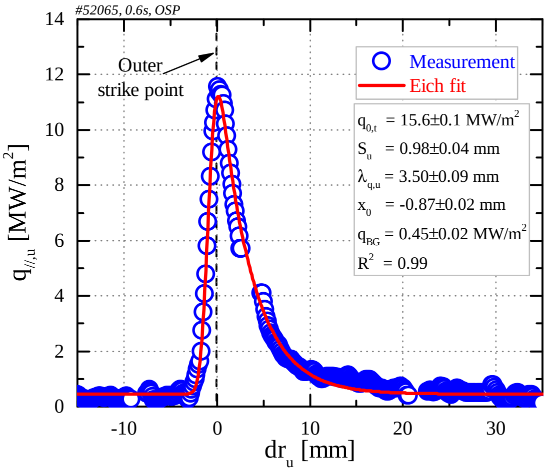

Figure 5.1 – Typical heat flux profile at the outer strike point of an attached Single-Null configuration on TCV, from infrared thermography, projected upstream using equation 4.27 and fitted with the functional form, equation 5.5. Note that the upstream-mapped profile is not the profile upstream, as the projection does not account for SOL power losses and does not remove the divertor spreading. The values of the five fit parameters are indicated, together with the adjusted coefficient of determination R^2. This is a measure of the goodness of the fit, ranging between 0 (the model does not fit the data) and 1 (the model perfectly fits the data).

When the target heat flux profile is parameterised by the Eich function, the integral SOL width $\lambda_{\mathrm{int},u}$ mapped upstream, defined by equation 4.39, can be approximated by $\lambda_{\mathrm{int},u} \approx \lambda_{q,u} + 1.64\ S_u$ [46]. Combining this expression with equations 4.31-4.40 yields a general expression for the peak perpendicular heat flux at the target

$$q_{\perp,t}^{\mathrm{peak}} \approx \frac{c_{\mathrm{div}} P_{\mathrm{SOL}}}{2\pi R_t (\lambda_{q,u} + 1.64 \cdot S_u)} \frac{\sin \beta_{\mathrm{pol},t}}{f_{x,t}} \tag{5.6}$$

where c_{div} is the fraction of power entering the SOL, P_{SOL}, that flows to the divertor.

Since, as explained in section 4.4, engineering constraints impose a lower limit on the ratio $\sin\beta_{\mathrm{pol},t}/f_{x,t}$, the quantity that has to be reduced is the peak parallel heat flux

$$\boxed{q_{\|,t}^{\mathrm{peak}} \approx \frac{c_{\mathrm{div}} P_{\mathrm{SOL}}}{2\pi R_t(\lambda_{q,u} + 1.64 \cdot S_u)} \frac{B_{\mathrm{tot},u}}{B_{p,u}} \propto \frac{c_{\mathrm{div}}}{A_{\mathrm{wet}}}} \tag{5.7}$$

with A_{wet} the heat wetted area, defined by equation 4.40. With the divertor in attached conditions, a reduction in target peak heat loads can be achieved either by increasing the heat wetted area (i.e. a larger R_t, $\lambda_{q,u}$ or S_u) or by reducing the power sharing fraction c_{div} to that divertor (i.e. increasing the power load to the other divertor).

5.1.2 Conductive model of the SOL

This section proposes a conductive model for the SOL, which yields a scaling relation for the SOL power width $\lambda_{q,u}$ and an expression for the divertor power sharing ratio $P_{\mathrm{in}}/P_{\mathrm{out}}$. The model is used to interpret experimental data in sections 6.1.1, 6.1.2, 6.2.3.3 and 7.1.2. The model assumptions are:

- The exhaust power crosses the LCFS and enters the SOL at one poloidal location, the outboard mid-plane, where it separates into a flow towards the inner divertor and another to the outer divertor. Poloidal shifts of this stagnation point with respect to the outboard mid-plane are neglected.
- Parallel heat transport in the SOL, from the outer mid-plane, along field lines, to the targets, is assumed dominated by electron heat conduction, as in the main assumption of the two-point model (2PM) [47]. The model adopts further substantial approximations, such as no sources or sinks of heat and particles in the SOL.
- Cross-field transport in the SOL is assumed to be driven by the temperature gradient, described by an effective perpendicular heat diffusivity $\chi_\perp$, and to occur mostly in the main SOL (surrounding the confined plasma).
- The geometry of SOL magnetic flux tubes is simplified by assuming that the connection length $L_\|$ is constant across the SOL (denoted $L_{\|,\mathrm{in}}$ for the inner SOL, $L_{\|,\mathrm{out}}$ for the outer SOL), and that the major radius is constant along the SOL (i.e. from upstream to target).
- The magnetic field strength is approximated with its toroidal component $B_{\mathrm{tot}} \approx B_\phi$, neglecting the poloidal field, which is typically much weaker than the toroidal field. Due to the absence of sources/sinks of heat in the SOL, and of cross-field transport in the divertor SOL (between x-point and target), this yields

$$q_\|/B_\phi \propto q_\| \cdot R = const. \tag{5.8}$$

i.e. $q_\parallel \cdot R$ is an invariant along each divertor SOL flux tube.

In-out power sharing Using these hypotheses, an expression for the exhaust power repartition between inner and outer divertor is first obtained. Assuming an upstream temperature T_u much larger than the plasma temperature at the target, and since the major radius is constant along the SOL, so that the parallel heat flux is also constant (equation 5.8), the parallel heat flux conducted towards the target

$$q_\parallel(s_\parallel) = -\kappa_0^e \; T(s_\parallel)^{5/2} \; \frac{\mathrm{d}T}{\mathrm{d}s_\parallel} = q_{\parallel,u} \tag{5.9}$$

can be readily integrated along the SOL, from the upstream location (where $s_\parallel = 0$) to the divertor target (where $s_\parallel = L_\parallel$), yielding a well-known expression for T_u that depends only on the parallel heat flux and the connection length,

$$T_u = \left(\frac{7 q_{\parallel,u} L_\parallel}{2\kappa_0^e}\right)^{2/7} \tag{5.10}$$

This integration can be repeated across the inner and outer divertor, yielding $T_{u,\mathrm{in}}$ as a function of $L_{\parallel,\mathrm{in}}$ and $T_{u,\mathrm{out}}$ as a function of $L_{\parallel,\mathrm{out}}$. For the upstream temperatures deduced for the inner and outer divertor to be identical, $T_{u,\mathrm{in}} = T_{u,\mathrm{out}}$, the heat flux distribution to the targets is determined by the ratio of the connection lengths,

$$q_{\parallel,u}^{\mathrm{in}} / q_{\parallel,u}^{\mathrm{out}} = L_{\parallel,\mathrm{out}} / L_{\parallel,\mathrm{in}} \tag{5.11}$$

As the connection length is assumed to be constant across the SOL, integration across the SOL yields an estimate for the divertor power sharing

$$P_{\mathrm{in}} / P_{\mathrm{out}} = L_{\parallel,\mathrm{out}} / L_{\parallel,\mathrm{in}} \qquad \text{Divertor power sharing} \tag{5.12}$$

The power sharing is therefore determined by the divertor geometry.

5.1.2.1 Scaling relation for SOL power width

Here, the model includes perpendicular (cross-field) heat transport, and yields a scaling relation for the SOL heat channel width. The derivation starts with an expression for the power crossing a flux surface, which according to the assumptions occurs predominantly in the upstream SOL

$$P_\perp(\mathrm{d}r_u) = -4\pi^2 R_0 a \sqrt{\frac{1+\kappa^2}{2}} \chi_\perp n_{e,u} \frac{\partial T_u}{\partial r_u} \tag{5.13}$$

where R_0 is the major radius, a the minor radius, κ the elongation, $\chi_\perp$ the perpendicular heat diffusivity, $n_{e,u}$ the upstream density, T_u the upstream temperature and r_u the upstream coordinate (as defined in section 4.2). As the SOL is assumed to be free of sources, the balance between power crossing the flux surface upstream and that deposited to the divertor targets is

$$\frac{\partial P_\perp}{\partial r_u} = -2\pi(R_{t,\text{in}}\ q_{p,t}^{\text{in}}\ f_{x,t}^{\text{in}} + R_{t,\text{out}}\ q_{p,t}^{\text{out}}\ f_{x,t}^{\text{out}}) \tag{5.14}$$

with the target flux expansion defined by equation 4.12 and the poloidal heat flux at the target $q_{p,t}$ by (using equation 4.26)

$$q_{p,t} = \frac{B_{p,t}}{B_{\text{tot},t}} q_{\parallel,t} = \frac{B_{p,t}}{B_{\text{tot},t}} \frac{B_{\text{tot},t}}{B_{\text{tot},u}} q_{\parallel,u} = \frac{B_{p,t}}{B_{\text{tot},u}} q_{\parallel,u} \tag{5.15}$$

with $q_{\parallel,t}$ and $q_{\parallel,u}$ the parallel heat flux at the target and upstream, $B_{p,t}$ and $B_{\text{tot},t}$ poloidal and total field at the target, $B_{p,u}$ and $B_{\text{tot},u}$ poloidal and total field upstream. The rest of the derivation is performed for the outer SOL, but can be repeated for the inner SOL. Differentiating equation 5.10 with respect to r_u, recalling that $L_\parallel$ is assumed to be independent of r_u, yields

$$\frac{\partial T_u}{\partial r_u} = \frac{1}{\kappa_0^e} \left(\frac{7 q_{\parallel,u}^{\text{out}} L_{\parallel,\text{out}}}{2\kappa_0^e} \right)^{-5/7} L_{\parallel,\text{out}} \frac{\partial q_{\parallel,u}^{\text{out}}}{\partial r_u} \tag{5.16}$$

The radial derivative of the temperature is rewritten in terms of $P_\perp$ using equation 5.13. Further differentiation and substitutions using equations 5.14, 4.12 and 5.15, yield a second order partial differential equation for the upstream parallel heat flux to the target,

$$\frac{\partial^2 q_{\parallel,u}^{\text{out}}}{\partial r_u^2} = c_1 (q_{\parallel,u}^{\text{out}})^{12/7} + \frac{5}{7} (q_{\parallel,u}^{\text{out}})^{-1} \left(\frac{\partial q_{\parallel,u}^{\text{out}}}{\partial r_u} \right)^2 \tag{5.17}$$

with

$$c_1 = \frac{B_{p,u}}{B_{\text{tot},u}} \left(1 + \frac{L_{\parallel,\text{out}}}{L_{\parallel,\text{in}}} \right) \frac{\kappa_0^e}{2\pi a \sqrt{\frac{1+\kappa^2}{2}} \chi_\perp n_{e,u} L_{\parallel,\text{out}}} \left(\frac{7 L_{\parallel,\text{out}}}{2\kappa_0^e} \right)^{5/7} \tag{5.18}$$

The profile of the parallel heat flux upstream is assumed to be a decaying exponential,

$$q_{\parallel,u}^{\text{out}} = q_{\parallel,u}^{\text{out,sep}}\ e^{-\mathrm{d}r_u/\lambda_{q,u}} \tag{5.19}$$

with

$$q_{\parallel,u}^{\text{out,sep}} = \frac{P_{\text{SOL}}\ c_{\text{div,out}}}{2\pi R_u \lambda_{q,u}} \frac{B_{\text{tot},u}}{B_{p,u}} \tag{5.20}$$

where P_{SOL} is the exhaust power crossing the magnetic separatrix and entering the SOL, R_u the outboard mid-plane radius, $\lambda_{q,u}$ the SOL power fall-off length and $c_{\text{div,out}}$ the fraction of exhaust power flowing to the outer target, defined as

$$c_{\mathrm{div,out}} = \frac{P_{\mathrm{out}}}{P_{\mathrm{out}} + P_{\mathrm{in}}} = \left(1 + \frac{P_{\mathrm{in}}}{P_{\mathrm{out}}}\right)^{-1} = \left(1 + \frac{L_{\parallel,\mathrm{out}}}{L_{\parallel,\mathrm{in}}}\right)^{-1} \tag{5.21}$$

employing equation 5.12 for the in-out power sharing ratio. Note that the assumption of an exponential profile is supported by the shape of the numerical solution of equation 5.17. Finally, equation 5.19 is substituted in 5.17 and evaluated at the separatrix, where $\mathrm{d}r_u = 0$. With $B_{p,u} \propto I_{\mathrm{P}}/a$, see equation 4.9, one obtains

$$\boxed{\lambda_{q,u} \propto L_{\parallel,\mathrm{out}}^{2/9} \left(1 + \frac{L_{\parallel,\mathrm{out}}}{L_{\parallel,\mathrm{in}}}\right)^{-2/9} \chi_{\perp}^{7/9}\ n_{e,u}^{7/9}\ P_{\mathrm{SOL}}^{-5/9}\ I_{\mathrm{P}}^{-2/9}\ B_{\mathrm{tot},u}^{2/9}\ a\ R_u^{5/9}} \tag{5.22}$$

The thermal diffusivity $\chi_{\perp}$, so far considered as a constant, may depend on the upstream temperature. Two cases are explored:

- Bohm-like diffusivity for drift waves $\chi_{\perp} \propto \rho_s c_s$ [48], where ρ_s is the ion Gyro radius and c_s the ion sound speed. This yields $\chi_{\perp} \propto T_{\mathrm{sep}}/B_{\mathrm{tot},u}$, therefore

$$\boxed{\lambda_{q,u} \propto L_{\parallel,\mathrm{out}}^{4/11} \left(1 + \frac{L_{\parallel,\mathrm{out}}}{L_{\parallel,\mathrm{in}}}\right)^{-4/11} n_{e,u}^{7/11}\ P_{\mathrm{SOL}}^{-3/11}\ I_{\mathrm{P}}^{-4/11}\ B_{\mathrm{tot},u}^{-3/11}\ a\ R_u^{3/11}} \tag{5.23}$$

- Bohm-like diffusivity for ballooning modes $\chi_{\perp} \propto \rho_s c_s q$ [48], using the safety factor $q = (aB_{\mathrm{tot},u})/(R_u B_{p,u})$. This yields $\chi_{\perp} \propto (T_{\mathrm{sep}} a^2)/(R_u I_{\mathrm{P}})$, therefore

$$\boxed{\lambda_{q,u} \propto L_{\parallel,\mathrm{out}}^{4/11} \left(1 + \frac{L_{\parallel,\mathrm{out}}}{L_{\parallel,\mathrm{in}}}\right)^{-4/11} n_{e,u}^{7/11}\ P_{\mathrm{SOL}}^{-3/11}\ I_{\mathrm{P}}^{-1}\ B_{\mathrm{tot},u}^{4/11}\ a^{25/11}\ R_u^{-4/11}} \tag{5.24}$$

These scaling relations for $\lambda_{q,u}$ will be used in section 6.1.2 to interpret the experimentally observed variation of $\lambda_{q,u}$ when varying the plasma current or when changing some characteristics of the outer divertor geometry.

5.1.2.2 Power sharing between inner/outer divertor

This section extends the in-out power sharing prediction, equation 5.12, to the more general case where $L_{\parallel}$ varies across the SOL, $L_{\parallel} = L_{\parallel}(\mathrm{d}r_u)$, and the major radius changes along the SOL, $R = R(s_{\parallel})$. This extension is required to describe power sharing in alternative divertor concepts (e.g. the SF-), where $L_{\parallel}$ can greatly change across the SOL and major radius can greatly vary along the flux tubes.

Following the derivation of the previous section, any location in the SOL at the outer mid-plane is simultaneously connected to both the inner and outer divertors. The exhaust

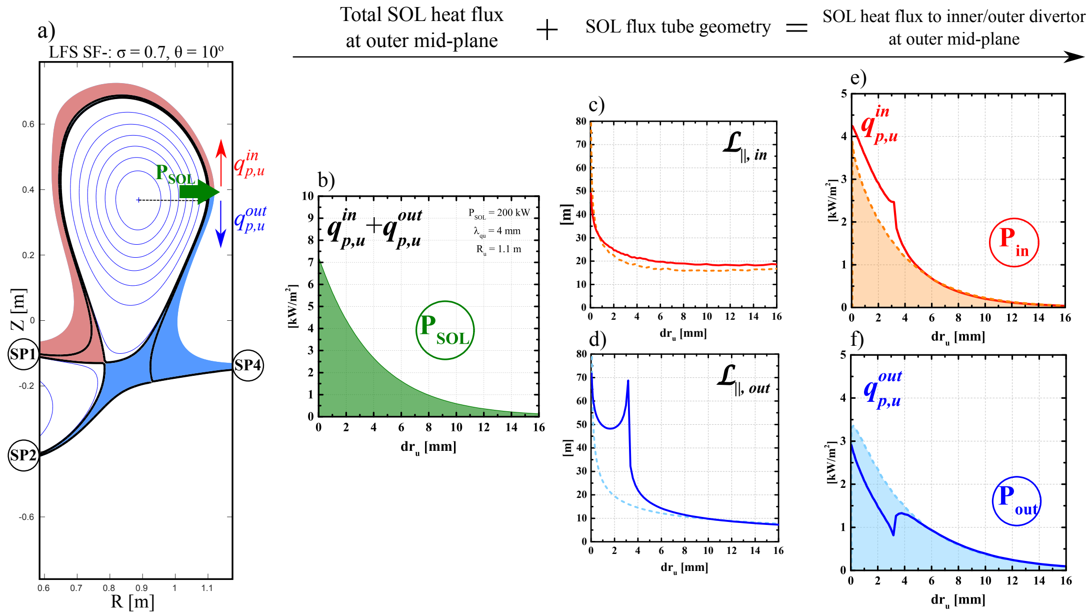

Figure 5.2 – Schematic of the model for the SOL power sharing between inner and outer divertors, illustrated, as an example, for a LFS Snowflake Minus divertor with $(\sigma, \theta) = (0.7, 10°)$ (continuous lines, equilibrium shown in (a)), and one with $(\sigma, \theta) = (0.1, 10°)$ (dashed lines). In the latter configuration, with $\sigma = 0.1$, due to the very small x-point distance, the outer SOL (in blue) connects practically only to SP4. For each SF- configuration, the upstream SOL poloidal heat flux profile (green, fig.(b)) is repartitioned in two profiles, to the inner ($q^{\text{in}}_{p,u}$, red, fig. (e)) and to the outer ($q^{\text{out}}_{p,u}$, blue, fig. (f)) divertor, by considering the flux tubes' effective connection length for the inner, $\mathcal{L}_{\parallel,\text{in}}$ (fig. (c)), and outer, $\mathcal{L}_{\parallel,\text{out}}$ (fig. (d)), divertor.

power P_{SOL} enters the SOL at the outer mid-plane ("upstream"), where it separates into one flow towards the inner divertor (P_{in}) and another to the outer divertor (P_{out}), see figure 5.2. Allowing the major radius to change along the SOL flux tube, the expression for the upstream temperature T_u, equation 5.10, becomes

$$T_u = \left(\frac{7 q_{\parallel,u} \mathcal{L}_{\parallel}}{2\kappa_0^e}\right)^{2/7} \tag{5.25}$$

where

$$\mathcal{L}_{\parallel} = \int_0^{L_{\parallel}} \mathrm{d}s_{\parallel} \, \frac{R_u}{R(s_{\parallel})} \qquad \text{Effective parallel connection length} \tag{5.26}$$

is the parallel connection length of the flux tube, $L_{\parallel}$, weighted by the inverse major radius. In the following, $\mathcal{L}_{\parallel}$ is referred to as the effective parallel connection length. Note that if one neglects the variation of R along the flux tube, $\mathcal{L}_{\parallel} = L_{\parallel}$. Following the derivation of the previous section, the upstream temperatures deduced for the inner and outer divertor with equation 5.25 must be the same, which yields

$$q^{\text{in}}_{\parallel,u} / q^{\text{out}}_{\parallel,u} = \mathcal{L}_{\parallel,\text{out}} / \mathcal{L}_{\parallel,\text{in}} \tag{5.27}$$

Thus the flux tube geometry, alone, determines the sharing of heat flux between the divertors. Long and narrow flux tubes (i.e. with small major radius R, since the cross-sectional area scales as $\propto R$) have a greater $\mathcal{L}_{\|}$ than short and broad flux tubes and therefore conduct less heat to the plates for a given upstream-to-target temperature difference. Equation 5.27 can be formulated in terms of the component of the heat flux in the poloidal plane:

$$q_{p,u}^{\mathrm{in}}/q_{p,u}^{\mathrm{out}} = \mathcal{L}_{\|,\mathrm{out}}/\mathcal{L}_{\|,\mathrm{in}} \tag{5.28}$$

since $q_{p,u} = (B_{p,u}/B_{\mathrm{tot},u})\ q_{\|,u}$, with $B_{p,u}$ and $B_{\mathrm{tot},u}$ the upstream poloidal and total magnetic fields.

To obtain an estimate of the power sharing, the r.h.s. of equation 5.28 must be weighted across the SOL. It is, therefore, assumed that the SOL heat flux perpendicular to flux surfaces is described by an exponential with a characteristic fall-off length $\lambda_{q,u}$. With no heat sources in the SOL, the sum of $q_{p,u}^{\mathrm{in}}$ and $q_{p,u}^{\mathrm{out}}$ is an exponential with the same fall-off length

$$(q_{p,u}^{\mathrm{in}} + q_{p,u}^{\mathrm{out}})(\mathrm{d}r_u) = \frac{P_{\mathrm{SOL}}}{2\pi R_u \lambda_{q,u}} e^{-\mathrm{d}r_u/\lambda_{q,u}} \tag{5.29}$$

with $\mathrm{d}r_u$ the upstream distance from the separatrix and R_u the major radius at the outboard mid-plane (see section A.5 for a full derivation). $\mathcal{L}_{\|,\mathrm{in}}$ and $\mathcal{L}_{\|,\mathrm{out}}$ are then calculated for each SOL magnetic surface using equation 5.26. For each upstream location, using equations 5.28 and 5.29, the poloidal heat flux directed towards the inner divertor, $q_{p,u}^{\mathrm{in}}$, and outer divertor, $q_{p,u}^{\mathrm{out}}$, are computed, see figure 5.2. Finally, integration of these profiles over the entire SOL yields the power flowing to the inner, P_{in}, and outer, P_{out}, divertors.

This estimation of the in-out power sharing will be used in sections 6.1.1 and 6.2.3.3 to interpret the observed variation of $P_{\mathrm{in}}/P_{\mathrm{out}}$ when changing characteristics of the divertor geometry in SN and SF- configurations.

5.1.2.3 Comparison to fluid simulations of the LFS SF-

This section compares the power sharing predicted by the model of section 5.1.2.2 to EMC3-Eirene fluid calculations. As the model, EMC3-Eirene assumes constant cross-field transport coefficients. EMC3-Eirene calculations were performed for TCV-sized LFS SF- configurations with a range of values of σ and θ (defined in section 4.5.2) [42]. Note that, in these fluid simulations, the fraction of input power deposited to the targets is $\approx 60\%$, independently of σ or θ (variations $< 5\%$).

As this SF- database was originally created to investigate the effect of the x-point position on power repartition between strike points, every geometrical parameter of the

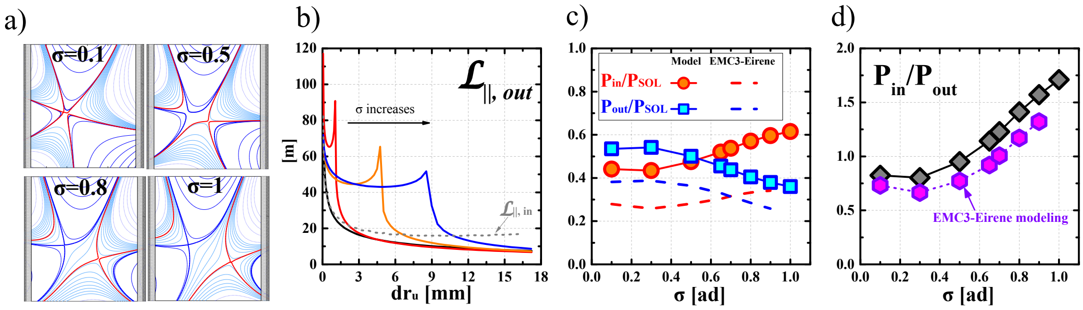

Figure 5.3 – In a LFS SF- configuration, scan of the x-point distance σ at fixed $\theta = 10°$ and $\lambda_{q,u} = 4$ mm. (a) SPIDER magnetic equilibria. (b) Profiles of the effective parallel connection length in the SOL, for $\sigma = 0.1$, 0.5, 0.8, 1. (c) Fraction of exhaust power to each divertor, from the model, as a function of σ. (d) Power sharing ratio, from the model (grey diamonds) and from fluid calculations[42] (purple hexagons), as a function of σ.

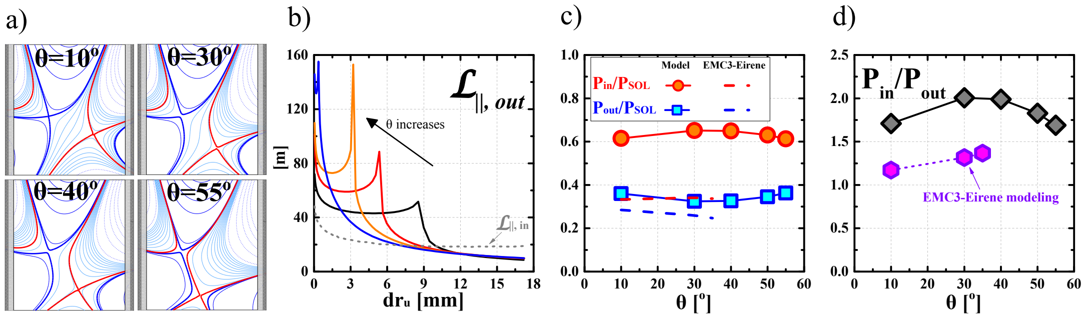

Figure 5.4 – In a LFS SF- configuration, scan of θ at fixed $\sigma = 1$ and $\lambda_{q,u} = 4$ mm. (a) SPIDER magnetic equilibria. (b) Profiles of the effective parallel connection length in the SOL, for $\theta = 10°, 30°, 40°, 55°$. (c) Fraction of exhaust power to each divertor, from the model, as a function of θ. (d) Power sharing ratio, from the model (grey diamonds) and from fluid calculations[42] (purple hexagons), as a function of θ. Note that the fluid calculations use equilibria with slightly increasing $\sigma \approx (0.8; 0.92; 1.15)$.

SF configuration, σ and θ, was varied whilst keeping the other constant.

- **Scan of $\boldsymbol{\sigma}$** The power sharing model reproduces the increase of P_{in} and the decrease of P_{out} from the fluid calculations with increasing σ, figure 5.3c, and the resulting $P_{\text{in}}/P_{\text{out}}$ increase, figure 5.3d. When increasing σ from 0.1 to 0.9, the fluid calculation's $P_{\text{in}}/P_{\text{out}}$ increases from 0.73 to 1.32 and the modelled from 0.82 to 1.57.

- **Scan of $\boldsymbol{\theta}$** The power sharing model reproduces the weak increase of P_{in} and weak decrease of P_{out} from the fluid calculations with increasing θ, figure 5.4c, but there is a systematic offset, with the power sharing model over-predicting P_{in}. Consequently, the model reproduces the weak increase of $P_{\text{in}}/P_{\text{out}}$, figure 5.4d, but overestimates its value. When increasing θ from 10° to 35°, the fluid calculation $P_{\text{in}}/P_{\text{out}}$ increases from 1.17 to 1.37 and the modelled from 1.71 to 2.

In all cases, the total power deposited at the targets in the fluid calculations is lower than the prediction of the power sharing model since charge exchange and elastic collisions with the neutral gas, as well as radiation, are only considered in the fluid calculations.

It is interesting to further investigate how variations of σ and θ in a LFS SF- change the flux tube geometry and thus the power sharing.

- When σ is increased at fixed θ, some flux tubes, formerly connected to SP4, become directed to SP2, figure 5.3a. Their connection lengths increase, due to the low poloidal field in the intra-null region and the higher toroidal field, their major radius, on average, decreases. This enhances $\mathcal{L}_{\|,\mathrm{out}}$, figure 5.3b, which, in turn, limits the heat that can be conducted to SP2, equation 5.27. The flux tubes connecting the same upstream location to SP1 will, in addition, have to exhaust this difference, figure 5.3c.
- When θ is increased at fixed $\sigma = 1$, some flux tubes, formerly intercepting SP2, connect to SP4, figure 5.4a. Their $\mathcal{L}_{\|,\mathrm{out}}$ reduces ($L_{\|}$ decreases and the major radius, on average, increases), so they conduct more heat to the target. In contrast, for the flux tubes connected to SP2, $\mathcal{L}_{\|,\mathrm{out}}$ increases, since the secondary null approaches the divertor leg, figure 5.4a, reducing the poloidal field and, thus, augmenting $L_{\|}$, figure 5.4b. This limits the power that can be conducted to SP2. These two effects approximately balance, and P_{out} does not change significantly with increasing θ, figure 5.4c.

Evaluating the power sharing model, for the LFS SF- geometries of figure 5.3a, for a range of $\lambda_{q,u}$ shows that the ratio $P_{\mathrm{in}}/P_{\mathrm{out}}$ scales as $\propto \mathrm{d}r_{\mathrm{x2}}/\lambda_{q,u}$ and quickly saturates for $\mathrm{d}r_{\mathrm{x2}}/\lambda_{q,u} > 2$. This is explained by the portion of the SOL heat flux profile enclosed between primary and secondary separatricies, which is proportional to $\mathrm{d}r_{\mathrm{x2}}/\lambda_{q,u}$. For $\mathrm{d}r_{\mathrm{x2}}$ larger than $\approx 2\ \lambda_{q,u}$, all the heat in the outer divertor is directed to SP2, so any further increase of $\mathrm{d}r_{\mathrm{x2}}$ can not affect the in-out power balance.

5.1.3 Drift-dominated model of the SOL

This section briefly summarizes the heuristic drift-based model of the SOL power width proposed in [49]. Here, vertical ∇B and curvature B particle drifts in the SOL are balanced with parallel plasma flows, featuring Pfirsch-Schlüter (PS) flows and flows due to the sink effect of the divertor plates. This model is compared to experimental data in sections 6.1.2.4 and 7.2.1.

5.1.3.1 Analytic expression for SOL power width

In the Golston heuristic derivation [49], the time-integrated radial (i.e. perpendicular to flux surfaces) displacement of a particle leaving the plasma at the mid-plane (outer or inner) and flowing, at half of the ion sound speed $c_s/2$, to the bottom of the plasma (i.e. the x-point) is calculated as

$$\lambda_{\mathrm{HD}} = \frac{4T_{\mathrm{sep}}a}{\bar{Z}eB_pRc_s} \qquad \text{ion drift} \tag{5.30}$$

$$\lambda_{\mathrm{HD}} = \frac{4T_{\mathrm{sep}}a}{eB_pRc_s} \qquad \text{electron drift} \tag{5.31}$$

where a is the plasma minor radius, R the major radius, B_p the poloidal field, $\bar{Z}$ the atomic number averaged on the species composing the plasma, and T_{sep} the temperature at the magnetic separatrix. The assumed parallel speed of $c_s/2$ is consistent with the measured parallel flow patterns at the divertor entrance on AUG and TCV [50, 51]. Under the assumption that the ion magnetic drift (∇B and curvature B) determines the net particle transport, the rest of this discussion focuses on equation 5.30. Since the product B_pR varies poloidally, it is natural to take its poloidal average $\langle B_p\rangle \cdot R_{\mathrm{geo}}$, with $\langle B_p\rangle$ computed from the plasma current (equation 4.9),

$$\lambda_{\mathrm{HD}} = \frac{4T_{\mathrm{sep}}a}{\bar{Z}e\langle B_p\rangle R_{\mathrm{geo}}c_s} \tag{5.32}$$

Finally, using the expression of ion sound speed c_s yields

$$\boxed{\lambda_{\mathrm{HD}} = \frac{4a}{\bar{Z}e\langle B_p\rangle R_{\mathrm{geo}}}\left(\frac{\bar{A}m_pT_{\mathrm{sep}}}{(1+\bar{Z})}\right)^{1/2}} \tag{5.33}$$

where $\bar{A}$ is the mass number averaged over the species composing the plasma and m_p the proton mass. The model also assumes that anomalous electron thermal diffusivity fills the particle channel defined by the PS flows, and that the same channel is emptied by Spitzer-Härm electron thermal conductivity. If the power crossing the separatrix into the SOL is uniform along the entire separatrix[2], the temperature at the separatrix upstream is [31]

$$T_{\mathrm{sep}} = \left(\frac{7}{4}\frac{P_{\mathrm{SOL}}L_{\parallel}B_{\mathrm{tot}}}{4\pi\kappa_0^eR_{\mathrm{geo}}\lambda_q\langle B_p\rangle}\right)^{2/7} \tag{5.34}$$

---

[2] In the conductive model of section 5.1.2, in contrast, the exhaust power enters the SOL entirely at the outboard mid-plane. However, the assumption on the spatial distribution of the entering P_{SOL} has almost no effect on T_{sep}, as it leads to a difference of $(1/2)^{2/7} \approx 0.82$ i.e. 18%, as demonstrated in [31] pag. 190.

that, injected into expression 5.33, and using the definition of $\langle B_p \rangle$, yields

$$\boxed{\lambda_{\mathrm{HD}} = 5671\ P_{\mathrm{SOL}}^{1/8} \frac{(1+\kappa^2)^{5/8} a^{17/8} B_{\mathrm{tot}}^{1/4}}{I_P^{9/8} R_{\mathrm{geo}}} \left(\frac{2\bar{A}}{\bar{Z}^2(1+\bar{Z})} \right)^{7/16} \left(\frac{Z_{\mathrm{eff}}+4}{5} \right)^{1/8}} \tag{5.35}$$

Since the model does not allow for spatial profiles of plasma density and temperature in the SOL, this λ_{HD} represents both the width of the SOL particle channel and the SOL heat flux channel, at the bottom of the plasma (i.e. near the x-point).

Mapping to the outboard mid-plane This heuristic estimate, equation 5.35, represents the mean width of the SOL poloidally averaged around the plasma that follows the poloidal flux surfaces. Since experimental estimates for this width always refer to the value at the outer mid-plane, the HD model value should also be mapped to the outer mid-plane,

$$\lambda_{\mathrm{u,HD}} = \lambda_{\mathrm{HD}} \cdot \frac{R_{\mathrm{geo}}}{R_{\mathrm{geo}} + a} \frac{\langle B_p \rangle}{B_{p,u}} \tag{5.36}$$

with $\langle B_p \rangle$ the poloidal average, whereas $B_{p,u}$ is the value at the upstream location, which can be computed from the magnetic reconstruction.

Extension to non-zero plasma triangularity As proposed in [52], equation 5.32 can be generalized to plasma shapes with non-null triangularity by replacing a with $a(1 \pm \delta_x)$, see figure 4.2,

$$\lambda_{\mathrm{HD}} = \frac{4 T_{\mathrm{sep}} a}{\bar{Z} e \langle B_p \rangle R_{\mathrm{geo}} c_s} (1 \pm \delta_x) \tag{5.37}$$

where '+' is used for an ion leaving the plasma at the outboard mid-plane and '-' for an ion leaving the plasma at the in-board mid-plane. The δ_x is the triangularity of the half of the plasma towards which the ion vertical drifts are directed.

5.1.3.2 In-out asymmetry of SOL power width

According to model equation 5.37, an ion leaving the plasma at the outboard mid-plane and another leaving the plasma at the in-board mid-plane can have different values of λ_{HD} when reaching the plasma's x-point. The ratio of their displacements, as already discussed in [52], is

$$\boxed{\frac{\lambda_{\mathrm{u,HD}}^{\mathrm{in}}}{\lambda_{\mathrm{u,HD}}^{\mathrm{out}}} = \frac{\lambda_{\mathrm{HD}}^{\mathrm{in}}}{\lambda_{\mathrm{HD}}^{\mathrm{out}}} = \frac{1-\delta_x}{1+\delta_x}} \tag{5.38}$$

where δ_x is the triangularity of the half of the plasma towards which the vertical drifts of the considered species (ion or electron) are directed. If ions are chosen, δ_x is the lower triangularity in FF ($\delta_x = \delta_{\text{lower}}$, ion drift downwards), the upper triangularity in RF ($\delta_x = \delta_{\text{upper}}$, drift upwards).

In the model, the parallel flow velocity has the same value ($c_s/2$) for both the inner SOL (outboard mid-plane to inner target) and outer SOL (outboard mid-plane to outer target). Relaxing this hypothesis, equation 5.37 becomes [53]

$$\lambda_{\text{HD}} = \frac{2T_{\text{sep}}a}{\bar{Z}eB_pR\nu_{\|}}(1 \pm \delta_x) \tag{5.39}$$

where $\nu_{\|}$ is the SOL flow velocity, and the in-out ratio of λ_{HD} is

$$\frac{\lambda^{\text{in}}_{\text{u,HD}}}{\lambda^{\text{out}}_{\text{u,HD}}} = \frac{1-\delta_x}{1+\delta_x} \cdot \frac{\nu^{\text{out}}_{\|}}{\nu^{\text{in}}_{\|}} \tag{5.40}$$

An in-out asymmetry of the SOL width can, therefore, arise from plasma triangularity or different plasma flow velocities in the inner and outer SOL.

5.1.4 Diffusive model for the divertor spreading factor

This section proposes an analytic model for the cross-field spreading of SOL heat in the divertor region. The model is an extension of that described in [54], considering non-negligible plasma temperatures at the target compared to those upstream. It is similar to those outlined in [53, 55], but assumes fixed perpendicular heat diffusivity and requires pressure conservation along SOL flux tubes. This model is used to interpret experimental data in sections 6.1.3, 7.1.3 and 7.2.2.

The SOL is approximated as a single magnetic flux tube that connects the outer mid-plane ("upstream") to the divertor target, and it is described through the parallel coordinate $s_{\|}$, defined in section 4.2. A value of $s_{\|} = 0$ corresponds to the outboard mid-plane, $s_{\|} = L_{\|,X}$ to the divertor entrance (x-point) and $s_{\|} = L_{\|}$ to the divertor target, where $L_{\|}$ is the connection length. The spreading factor at a position $s_{\|}$ in the divertor is defined as

$$S(s_{\|}) = \int_{L_{\|,X}}^{s_{\|}} \mathrm{d}s_{\|} \sqrt{\frac{\chi_\perp}{\chi_{\|}}} \qquad s_{\|} \in [L_{\|,X}, L_{\|}] \tag{5.41}$$

where $\chi_\perp$ is the SOL perpendicular heat diffusivity, assumed constant in the divertor, and $\chi_{\|} = \kappa_0^e\, T_e^{5/2}/n_e$ is the Spitzer-Härm electron diffusivity. Electron heat conduction is taken to be the dominant mechanism for heat transport from the outer mid-plane along the field lines to the targets. The expression for the parallel heat flux conducted towards the target, equation 5.9 is integrated, along the flux tube, from the x-point ($s_{\|} = L_{\|,X}$)

to a generic position $s_{\parallel}$ between the x-point and the target, neglecting power losses and cross-field conduction, so that $q_{\parallel}$ is a constant. Note that the latter assumption is only justified as long as S_u remains a small perturbation compared to the SOL width. This provides the temperature distribution along the flux tube

$$T(s_{\parallel}) = \left(T_{\mathrm{e,X}}^{7/2} - \frac{7q_{\parallel}}{2\kappa_0^e}(s_{\parallel} - L_{\parallel,X})\right)^{2/7} \tag{5.42}$$

Substituting this expression and that for $\chi_{\parallel}$ in the definition of S, equation 5.41, and requiring pressure conservation along the flux tube, i.e. $n_e(s_{\parallel}) \cdot T_e(s_{\parallel}) = \mathrm{const} = n_{\mathrm{e,X}} T_{\mathrm{e,X}}$, yields

$$\boxed{S(s_{\parallel}) = 2\sqrt{\frac{\chi_{\perp} n_{\mathrm{e,X}}}{\kappa_0^e}} T_{\mathrm{e,X}}^{-5/4} L_{\parallel,\mathrm{div}} \frac{\left[\left(1 + (f_{\mathrm{T}}^{7/2} - 1)\frac{(s_{\parallel} - L_{\parallel,X})}{L_{\parallel,\mathrm{div}}}\right)^{1/2} - 1\right]}{(f_{\mathrm{T}}^{7/2} - 1)}} \tag{5.43}$$

where $L_{\parallel,\mathrm{div}} = L_{\parallel} - L_{\parallel,X}$ is the parallel length of the divertor leg, and $f_{\mathrm{T}} = T_{e,t}/T_{\mathrm{e,X}}$. From this relation, one obtains the spreading factor at the divertor target

$$\boxed{S_t = S(L_{\parallel}) = 2\sqrt{\frac{\chi_{\perp} n_{\mathrm{e,X}}}{\kappa_0^e}} T_{\mathrm{e,X}}^{-5/4} L_{\parallel,\mathrm{div}} \left(\frac{f_{\mathrm{T}}^{7/4} - 1}{f_{\mathrm{T}}^{7/2} - 1}\right)} \tag{5.44}$$

which can be mapped to the outboard mid-plane by dividing by the local flux expansion, $S_u = S_t / f_{x,t}$

$$\boxed{S_u = 2\sqrt{\frac{\chi_{\perp} n_{\mathrm{e,X}}}{\kappa_0^e}} T_{\mathrm{e,X}}^{-5/4} L_{\parallel,\mathrm{div}} \left(\frac{f_{\mathrm{T}}^{7/4} - 1}{f_{\mathrm{T}}^{7/2} - 1}\right) \frac{1}{f_{x,t}}} \tag{5.45}$$

The spreading factor, at the target, is therefore a function of the divertor magnetic geometry (field line length $L_{\parallel,\mathrm{div}}$, target flux expansion $f_{x,t}$) and of the plasma conditions at the divertor entrance (density $n_{\mathrm{e,X}}$ and temperature $T_{\mathrm{e,X}}$).

5.1.5 Model for heat flux splitting at the secondary x-point

This section proposes a model for describing the heat flux splitting at the secondary x-point of a Snowflake Minus configuration, that is a refined version of that published in [56, 57]. This model is compared to experimental data in section 6.2.4, to infer an effective width of the SOL heat flux channel in the low poloidal field region existing between the two x-points.

Using the same set of hypotheses of the conductive model of section 5.1.2.2, this model yields an analytic expression for the power arriving at the two strike-points associated to the secondary null of the SF-. In the following, the LFS SF- configuration is illustrated,

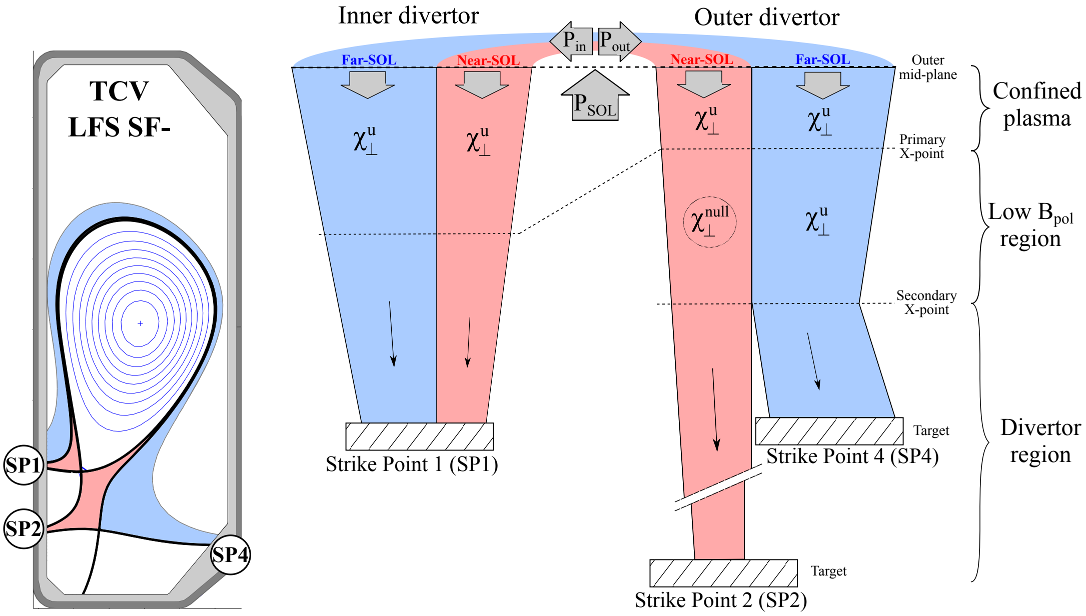

Figure 5.5 – Cartoon explaining the model for the SOL transport. The exhaust power, split at the outer mid-plane in P_{in} and P_{out}, flows along flux tubes, grouped in near-SOL and outer-SOL, towards the divertor targets. The cross-sectional area of these tubes decreases for smaller major radius.

but it also applies to the HFS SF-. As shown in figure 5.5, at the secondary x-point of the LFS SF-, the SOL flux tubes split into two manifolds, with the near-SOL flux tubes connecting to SP2 and the far-SOL flux tubes to SP4. For each SOL magnetic surface, $c_{\text{div}}^{\wedge}$ denotes the heat flux to the divertor which hosts the secondary null, normalized to the sum of that to both divertors ($\wedge = in$ for the HFS SF-, $\wedge = out$ for the LFS SF-), i.e. it describes the in-out power sharing, indicated by $c_{\text{div,near}}^{\wedge}$ and $c_{\text{div,far}}^{\wedge}$ for the near-SOL and far-SOL flux tubes, respectively. In-between the outer mid-plane and the divertor targets, volumetric radiative losses dissipate a fraction of the SOL power, indicated by $f_{r,\text{near}}^{\wedge}$ and by $f_{r,\text{far}}^{\wedge}$ for the near-SOL and far-SOL flux tubes, respectively.

The SOL heat flux profile, in proximity to the secondary x-point, when mapped upstream by following flux surfaces, is approximated by a truncated exponential with decay length $\lambda_{q,u}^{\text{eff},\wedge}$, referred to as the *effective SOL width* near the null. Integration of this profile over the near-SOL ($\mathrm{d}r_u < \mathrm{d}r_{\text{x2}}$) and far-SOL ($\mathrm{d}r_u > \mathrm{d}r_{\text{x2}}$), see the schematic in figure 5.5, yields the power deposited by each manifold at the target

$$P_{\text{near}}^{\wedge} = (1 - f_{r,\text{near}}^{\wedge})\; c_{\text{div,near}}^{\wedge}\; P_{\text{SOL}}\; (1 - e^{-\mathrm{d}r_{\text{x2}}/\lambda_{q,u}^{\text{eff},\wedge}}) \tag{5.46}$$

$$P_{\text{far}}^{\wedge} = (1 - f_{r,\text{far}}^{\wedge})\; c_{\text{div,far}}^{\wedge}\; P_{\text{SOL}}\; e^{-\mathrm{d}r_{\text{x2}}/\lambda_{q,u}^{\text{eff},\wedge}} \tag{5.47}$$

Equation 5.47 can be conveniently written as

$$P_{\text{far}}^{\wedge} = P_{\text{far}}^{\wedge *}\ e^{-\mathrm{d}r_{\text{x2}}/\lambda_{q,u}^{\text{eff},\wedge}} \tag{5.48}$$

with $P_{\text{far}}^{\wedge *} = (1 - f_{r,\text{far}}^{\wedge})\ c_{\text{div,far}}^{\wedge}\ P_{\text{SOL}}$. Equation 5.48 parameterises the power deposited at the divertor target by the far-SOL flux tubes. This corresponds to P_{SP4} of a LFS SF- and to P_{SP1} of a HFS SF-.

5.1.6 Access to the detached divertor regime

This section briefly discusses a useful expression that relates the minimum plasma density required to achieve detachment with plasma and divertor shape quantities. It provides important insights on how to facilitate the access to the detached divertor state through modifications of the divertor and SOL geometry.

Extension of the basic two-point model to include variations of the major radius along SOL flux tubes[58], and radiation losses close to the divertor plates[59], yields a scaling relation for the plasma electron temperature at the divertor target [59],

$$T_{e,t} \propto \frac{(q_{\parallel,u})^{10/7} \cdot (1 - f_{\text{rad}})^2}{n_{e,u}^2 L_{\parallel}^{4/7}} \frac{R_u^2}{R_t^2} \tag{5.49}$$

where $q_{\parallel,u}$, $n_{e,u}$ and R_u are parallel heat flux, plasma density and major radius at the outboard mid-plane, R_t is the target major radius and f_{rad} the exhaust power radiated fraction. A derivation for this expression is presented in section A.6. As the onset of divertor detachment happens at low plasma temperatures, typically $T_{e,t} \leq 5$ eV [31], fixing $T_{e,t}$ to this value, equation 5.49 can be used to obtain the upstream density required for the onset of detachment $n_{e,u}^{\text{det}}$ [60]

$$\boxed{n_{e,u}^{\text{det}} \propto \frac{(q_{\parallel,u})^{5/7} \cdot (1 - f_{\text{rad}})}{L_{\parallel}^{2/7} R_t}} \tag{5.50}$$

With the divertor in the attached regime, $q_{\parallel,u}$ is a truncated exponential with width $\lambda_{q,u}$, given by

$$q_{\parallel,u}(\mathrm{d}r_u) = \frac{c_{\text{div}} P_{\text{SOL}}}{2\pi R_u \lambda_{q,u}} \frac{B_{\text{tot},u}}{B_{p,u}} e^{-\mathrm{d}r_u/\lambda_{q,u}} \tag{5.51}$$

where c_{div} is the fraction of power entering the SOL, P_{SOL}, flowing to that divertor, R_u the major radius at the outboard mid-plane, $B_{\text{tot},u}$ and $B_{p,u}$ are the total and poloidal magnetic field at the outboard mid-plane and $\mathrm{d}r_u$ the upstream SOL coordinate (defined in section 4.2). In the presence of cross-field transport in the divertor, an integral SOL width $\lambda_{\text{int},u}$ is defined that replaces $\lambda_{q,u}$. Now, the expression of $n_{e,u}^{\text{det}}$ evaluated at the separatrix position becomes

$$\boxed{n_{e,u}^{\mathrm{det}} \propto \frac{(c_{\mathrm{div}})^{5/7} \cdot (1 - f_{\mathrm{rad}})}{\lambda_{\mathrm{int},u}^{5/7} L_{\|}^{2/7} R_t}} \tag{5.52}$$

or, in terms of the heat wetted area (equation 4.44),

$$\boxed{n_{e,u}^{\mathrm{det}} \propto \frac{(c_{\mathrm{div}})^{5/7} \cdot (1 - f_{\mathrm{rad}})}{A_{\mathrm{wet}}^{5/7} L_{\|}^{2/7} R_t^{2/7}}} \tag{5.53}$$

The scaling relation for $n_{e,u}^{\mathrm{det}}$ shows that achieving divertor detachment is facilitated by enhanced radiative losses in the SOL (f_{rad}), a broader heat wetted area A_{wet}, a longer parallel connection length $L_{\|}$, larger strike point radius R_t and/or a lower c_{div} (i.e. lower power fraction to the considered divertor).

5.2 Transient plasma transport in the SOL

This section discusses models for SOL heat transport during the ELM transients. The thermal stress induced by the ELM pulse to the divertor plate is analytically related to the ELM pulse characteristics in section 5.2.1. Then, section 5.2.2 summarizes a semi-empirical model for the ELM parallel fluence, a critical ELM power exhaust quantity, and extends the model to magnetic geometries where the target radius differs from that of the outboard mid-plane.

When the plasma is operated in a stationary H-mode configuration, the regime foreseen for ITER [4] and a fusion reactor like DEMO [6], localized edge instabilities can be periodically excited in the plasma, causing a periodic release of hot plasma particles into the SOL. These events are referred to as Edge-Localised-Modes (ELMs), and are described more in detail in chapter 7. Most of the ELM released energy is transported along the SOL field lines to the divertor plates, causing high transient peak heat loads. Section 5.2.1 summarizes an analytic model that relates the target surface thermal fatigue caused by the ELM to the ELM energy pulse characteristics. Then, section 5.2.2 summarizes a semi-empirical model for ELM energy fluence. This is compared to experimental data from TCV in section 7.3.2.

5.2.1 Thermal fatigue of target surface

During an ELM event, heat and plasma particles are expelled from the confined plasma into the SOL. While part of the heat and particles hit the first-wall or are dissipated by volumetric radiation in the SOL, the majority impact the divertor plates. The deposition of the ELM energy onto the target occurs over a very short time scale, typically of the order of 1 ms, and can cause a significant increase of the surface material temperature ΔT_{ELM}, leading to steep thermal gradients and therefore high stress in the material. The thermal stress (fatigue) is, to first order, proportional to the temperature rise ΔT_{ELM}. Depending on the base temperature before the ELM and the ELM deposited energy, plastic deformation, cracking and/or shallow melting can occur [61].

The ELM-induced target surface temperature rise ΔT_{ELM} is, therefore, a crucial quantity for the lifetime of divertor materials. Using a simplified picture, it is possible to express ΔT_{ELM} in terms of the ELM energy pulse characteristic [62]. The ELM energy pulse arriving at the divertor plate is described as a stationary perpendicular heat flux density $q_{\perp,t}$, over a time τ_{ELM}. Since the deposition time τ_{ELM} is short compared to the propagation time of the heat pulse through the target, which is in the order of seconds, the temperature gradient across the target deepness is large compared to its gradient along the target surface. As a result, the heat propagation along the target surface is negligible compared to that across the target depth, and the heat diffusion can be approximated by a one-dimensional process. Solving the 1-D heat diffusion equation for a semi-infinite slab provides the increase of the surface temperature,

$$\Delta T_{\text{ELM}} = \frac{2}{\sqrt{\pi}} \frac{q_{\perp,t}}{\sqrt{k\rho c_p}} \sqrt{\tau_{\text{ELM}}} \tag{5.54}$$

where k is the thermal conductivity, c_p the specific heat capacity and ρ the density. A full derivation for this expression is presented in Appendix A.3. Using the ELM energy pulse fluence,

$$\varepsilon_{\perp,t} = q_{\perp,t}\ \tau_{\text{ELM}} \qquad \text{ELM perpendicular energy fluence} \tag{5.55}$$

the surface temperature excursion becomes

$$\Delta T_{\text{ELM}} = \frac{2}{\sqrt{\pi}} \frac{1}{\sqrt{k\rho c_p}} \frac{\varepsilon_{\perp,t}}{\sqrt{\tau_{\text{ELM}}}} \tag{5.56}$$

Similarly to the heat flux, $\varepsilon_{\perp,t}$ can be projected parallel to the field line by considering the field line grazing angle γ at the target, as $\varepsilon_{\parallel,t} = \varepsilon_{\perp,t}/\sin\gamma$ (see equation 4.25), so that

$$\Delta T_{\text{ELM}} = \frac{2}{\sqrt{\pi}} \frac{1}{\sqrt{k\rho c_p}} \frac{\varepsilon_{\parallel,t}}{\sqrt{\tau_{\text{ELM}}}} \sin\gamma \tag{5.57}$$

The target surface temperature excursion due to the ELM energy pulse, therefore, scales linearly with the pulse fluence $\varepsilon_{\perp,t}$ (or $\varepsilon_{\parallel,t}$) and inversely with the square root of its duration τ_{ELM},

$$\boxed{\Delta T_{\text{ELM}} \propto q_{\perp,t}\sqrt{\tau_{\text{ELM}}} \propto \frac{\varepsilon_{\perp,t}}{\sqrt{\tau_{\text{ELM}}}} \propto \frac{\varepsilon_{\parallel,t}}{\sqrt{\tau_{\text{ELM}}}}} \tag{5.58}$$

Application of this model to locations across the target implies that ΔT_{ELM} varies spatially with $\varepsilon_{\|,t}$. Since the ELM $\varepsilon_{\|,t}$ profile typically is peaked near the strike point, this is the location where ΔT_{ELM} is largest and material damage most likely to occur.

5.2.2 Semi-empirical model for $\varepsilon_{\|,t}^{\mathrm{peak}}$

The model presented in this section is an extension of that proposed in [63] to magnetic divertor geometries where the major radius of the strike point differs significantly from that of the outer mid-plane. In [63], the first assumption is that the energy released during the ELM is that contained in a toroidally-uniform volume V_{ped}, centred at the pedestal top position and with a radial extent at the outboard mid-plane of $\pm(d/2)$,

$$V_{\mathrm{ped}} = 2\pi R_{\mathrm{geo}} \cdot 2\pi a \sqrt{\frac{1+\kappa^2}{2}} \cdot d \cdot \Delta_{\mathrm{equi}} \tag{5.59}$$

where Δ_{equi} is a geometrical factor, computed from the equilibrium reconstruction. For TCV conventional Single-Null plasmas, using d = 1.5 cm gives $\Delta_{\mathrm{equi}} \approx 1.97$. The energy contained in this volume is

$$E_{\mathrm{ped}} = V_{\mathrm{ped}} \cdot 3 n_{e,\mathrm{ped}} T_{e,\mathrm{ped}} \tag{5.60}$$

where $n_{e,\mathrm{ped}}$ and $T_{e,\mathrm{ped}}$ are pedestal (top) plasma electron density and temperature.

The ELM energy pulse flows in the SOL, parallel to field lines, to the divertor targets. No power or particle sink/source in the SOL are considered. Any cross-field heat flux spreading in the divertor is neglected and the ELM energy is assumed to separate equally between inner and outer divertor. V_{ped} is taken to be magnetically connected to the target for the entire duration of the ELM. Under these assumptions, the heat wetted area at the target A_t, where the ELM heat is deposited, is the geometrical projection of d

$$A_t = 2\pi R_t \; d \; \frac{f_{x,t}}{\sin \beta_{\mathrm{pol},t}} \tag{5.61}$$

with $\beta_{\mathrm{pol},t}$ the strike line incidence angle in the poloidal plane and $f_{x,t}$ the target flux expansion.

At the divertor target, the ELM perpendicular fluence is

$$\varepsilon_{\perp,t}^{\mathrm{peak}} = \frac{c_{\mathrm{div}} E_{\mathrm{ped}}}{A_t} = \frac{1}{2} \frac{E_{\mathrm{ped}}}{A_t} \tag{5.62}$$

where $c_{\mathrm{div}} = 1/2$ is the fraction of ELM released energy flowing to that divertor. Note that the ELM perpendicular fluence is assumed to have a constant value across the entire wetted area. The notation "peak" is adopted for the later comparison to experiments where, conversely, the ELM fluence has a spatial profile which peaks near the strike point.

The ELM parallel fluence at the target is

$$\begin{aligned}\varepsilon_{\parallel,t}^{\text{peak}} &= \varepsilon_{p,t}^{\text{peak}}\frac{B_{\text{tot},t}}{B_{p,t}} = \frac{\varepsilon_{\perp,t}^{\text{peak}}}{\sin\beta_{\text{pol},t}}\frac{B_{\text{tot},t}}{B_{p,t}} \approx \frac{\varepsilon_{\perp,t}^{\text{peak}}}{\sin\beta_{\text{pol},t}}\frac{B_{\text{tot},u}}{B_{p,u}}f_{x,t}\\ &\approx \frac{1}{2}\frac{2\pi R_{\text{geo}}\cdot 2\pi a\sqrt{\frac{1+\kappa^2}{2}}\cdot d\cdot\Delta_{\text{equi}}\cdot 3n_{e,\text{ped}}T_{e,\text{ped}}}{2\pi\ R_t\ d\ f_{x,t}/\sin\beta_{\text{pol},t}}\frac{1}{\sin\beta_{\text{pol},t}}\frac{B_{\text{tot},u}}{B_{p,u}}f_{x,t}\end{aligned}$$

leading to

$$\boxed{\varepsilon_{\parallel,t}^{\text{peak}} \approx \Delta_{\text{equi}}\cdot 2\pi a\sqrt{\frac{1+\kappa^2}{2}}\cdot\frac{3}{2}n_{e,\text{ped}}T_{e,\text{ped}}\frac{B_{\text{tot},u}}{B_{p,u}}\cdot\frac{R_{\text{geo}}}{R_t}} \tag{5.63}$$

In case where the strike point has the same major radius of the outboard mid-plane, i.e. $R_{\text{geo}} \approx R_t$, equation 5.63 reduces to

$$\boxed{\varepsilon_{\parallel,t}^{\text{peak}} \approx \Delta_{\text{equi}}\cdot 2\pi a\sqrt{\frac{1+\kappa^2}{2}}\cdot\frac{3}{2}n_{e,\text{ped}}T_{e,\text{ped}}\frac{B_{\text{tot},u}}{B_{p,u}}} \tag{5.64}$$

which is that obtained in the original version of the model [63].

The model prediction 5.64 was compared to measurements from the AUG, JET and MAST tokamaks in [63], where the measurements were found to exceed the prediction by a factor ≈ 3. Section 7.3.2 extends this comparison to the TCV tokamak.

6 Power exhaust of L-mode plasmas in TCV

The topic of the potential variations of the geometry of a standard Single-Null divertor, and their effect on divertor performance, is broad, complex and multi-faceted. This thesis navigates through the multidimensional space of divertor configurations, exploring the power exhaust of innovative divertor concepts and seeking to identify new ways of increasing the heat wetted area to enhance a future fusion reactor's safety margins. The investigation commences, in this chapter, with plasmas in the low-confinement mode (L-mode), as they are easier to diagnose, and extends, in the next chapter, to plasmas in the high-confinement mode (H-mode).

In sections 6.1-6.2, the divertor operational regime is attached/ high-recycling. The plasma line-averaged density is relatively low ($\leq 40\%$ of the Greenwald density[1]), and the plasma is heated exclusively through Ohmic power from the plasma current alone. The fraction of exhaust power that is radiated is typically ≈ 30 to 40%.

- In section 6.1, the magnetic geometries are varied from the standard Single-Null (SN) divertor, but retain a SN topology. The exploration of the SN power exhaust properties spans a six-dimensional space. The varied quantities are four divertor geometry parameters (divertor leg length, target flux expansion, plasma triangularity, target radius) and two core plasma parameters (plasma current and magnetic field direction).
- In section 6.2, the SN topology is modified to create a Snowflake Minus (SF-) divertor. The exploration of its power exhaust properties is taken over a three-dimensional space. The varied quantities are the x-point separation, the relative positioning of primary and secondary nulls and the magnetic field direction.

In section 6.3, the divertor operational regime makes a gradual transition from an attached to a detached regime, by divertor fuelling or nitrogen impurity seeding, while

---

[1] The Greenwald density is defined as $n_{\mathrm{GW}} = I_{\mathrm{P}}/(\pi a^2)$, with n_{GW} in units of $10^{20} m^{-3}$, I_{P} the plasma current in units of MA and a the plasma minor radius in meters [3].

the geometry remains a SN configuration. The SN power exhaust can thus be studied as a function of the divertor operational regime.

6.1 Single-Null divertor

This section investigates the power exhaust of the Single-Null configuration, with a L-mode plasma. The investigative strategy is to gradually modify a feature of the plasma shape or divertor geometry and to measure the resulting changes in the power exhaust. The six scanned quantities are:

1. plasma current I_P, from 130 to 340 kA. The plasma density is varied with I_P to maintain the same plasma Greenwald fraction f_GW[2].
2. outer divertor leg length L_div, from 21 to 64 cm, approximated by the distance between x-point and vessel floor in the poloidal plane, see figure 6.1a.
3. outer target flux expansion $f_{x,t}$, from 2 to 9, see figure 6.1b. Here, $f_{x,t}$ denotes the average of the outer target flux expansion profile (equation 4.12) across the first 2 mm of SOL near the separatrix.
4. plasma upper triangularity δ_upper, from -0.27 to 0.51[3], see figure 6.1c. The triangularity is defined by equation 4.3.
5. outer divertor strike point radius R_t, from 0.62 to 1.02 m, see figure 6.1d. When scanning R_t, the vertical position of the plasma is adjusted to maintain fixed the parallel connection length to the outer plate.
6. magnetic field direction, between
    - Forward field direction (FF): B_ϕ <0, ion ∇B drift downwards (towards active x-point of a Lower Single Null divertor) i.e. favorable for H-mode access.
    - Reversed field direction (RF): B_ϕ >0, ion ∇B drift upwards (away from active x-point of a Lower Single Null divertor) i.e. unfavorable for H-mode access.

    In the sign convention of TCV, the toroidal angle ϕ is positive when counter-clockwise seen from the top. To keep the standard field line helicity ($B_\phi \cdot I_\mathrm{P}$>0, i.e. I_P oriented as B_ϕ), the direction of the plasma current is reversed together with the field, so that I_P <0 for the FF direction, I_P >0 for the RF direction.

---

[2] The Greenwald fraction is defined by $f_\mathrm{GW} = \langle n_e \rangle / n_\mathrm{GW}$, with $\langle n_e \rangle$ the plasma line-averaged density and n_GW the Greenwald density [3].

[3] The measurements at the inner strike point for the highest value of δ_upper are excluded from the analysis, as the secondary null located above the confined plasma diverts a significant fraction of the SOL heat flux from the inner target to the additional strike point on the top of the machine (not monitored in these experiments).

Each parameter scan is repeated with fixed values of the other parameters, together with fixed plasma Greenwald fraction f_{GW}, in an attempt to maintain similar recycling conditions in the divertor.

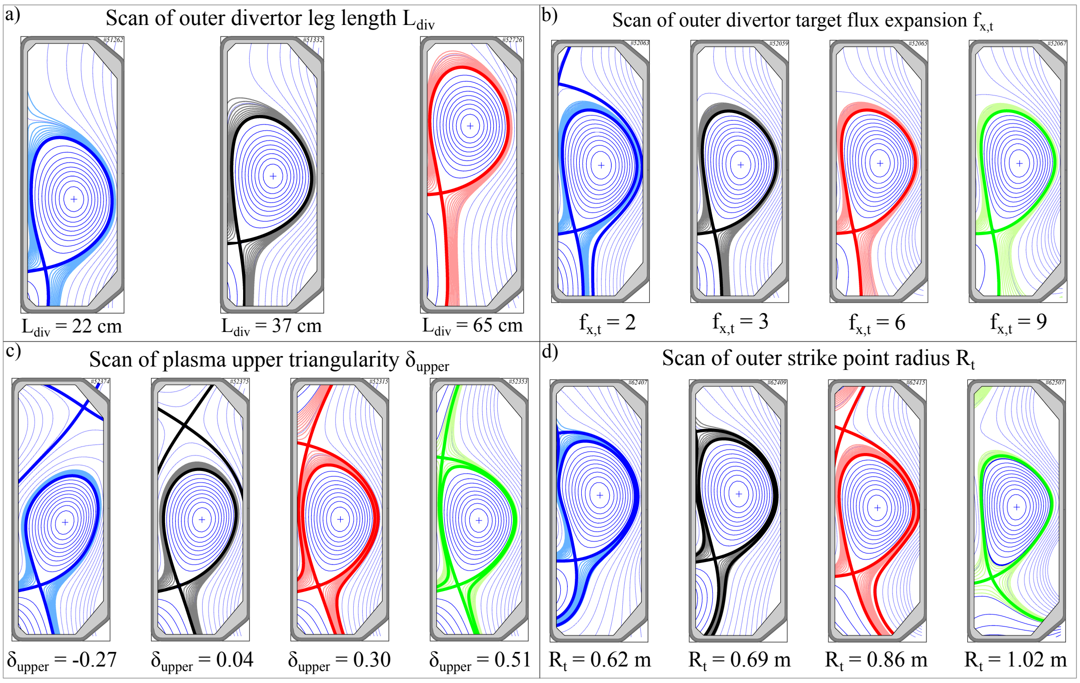

Figure 6.1 – Poloidal cross-section of the TCV vessel, with magnetic equilibria of the four divertor geometry scans, performed with the plasma in L-mode and the divertor in high-recycling/attached regime. The varied quantities are: (a) outer divertor leg length L_{div}, (b) outer divertor target flux expansion, (c) upper plasma triangularity and (d) outer divertor target radius.

Scan	Field	I_{P} [kA]	L_{div} [cm]	$f_{x,t}^{\mathrm{out}}$	δ_{upper}	R_t [m]	$f_{x,t}^{\mathrm{in}}$	f_{GW}	$\langle n_e \rangle$ [$10^{19} m^{-3}$]
I_{P}	FF	$[130, 290]$	36.6	2.4	0.28	0.74	6.1	0.21	$[1.8, 4.2]$
	RF	$[130, 340]$	19.3	3.8	0.29	0.73	4.2	0.21	$[1.5, 4.9]$
L_{div}	FF	212	$[21, 64]$	3.0	0.27	0.74	5.0	0.21	2.8
	RF	206	$[21, 35]$	3.5	0.22	0.72	4.3	0.21	2.7
$f_{x,t}$	RF	338	38.5	$[2, 9]$	0.29	0.77	3.5	0.27	5.9
δ_{upper}	FF	241	29.8	2.3	$[-0.13, 0.45]$	0.85	3.1	0.38	6.0
	RF	239	29.3	2.2	$[-0.27, 0.51]$	0.86	2.8	0.39	6.4
R_t	FF	290	$[38, 47]$	2.3	0.27	$[0.62, 1.02]$	3.3	0.31	5.9
	RF	320	$[38, 47]$	2.5	0.32	$[0.62, 1.02]$	2.8	0.28	5.8

Table 6.1 – Overview of relevant divertor and plasma parameters, for each scan. In the scan of R_t, keeping fixed the flux expansion at the inner and outer targets proved challenging and was not achieved. Therefore, for the R_t scan in FF, $f_{x,t}^{\mathrm{in}} = 6.6$ for the largest R_t, while for the R_t scan in RF, $f_{x,t}^{\mathrm{out}} = 1.5$ and $f_{x,t}^{\mathrm{in}} = 10$ for the largest R_t. Also, for the smallest value of R_t in FF, the current is $I_{\mathrm{P}} = 325$ kA while for larger values of R_t had to be reduced to 290 kA to avoid transition to H-mode.

The actual divertor operational regime is determined by using target Langmuir probes (LPs), described in section 2.2.2, and a fast reciprocating probe (RCP), described in section 2.2.3. For the inner strike point, only the electron temperature profile is presented, since some of the inner wall LPs do not yield a reliable density and, hence, pressure measurements for these discharges. As shown in figures 6.2a and 6.2b, temperature and density gradients are seen along the magnetic field lines, between outboard mid-plane and target. The temperature at both targets, with peak values of ≈ 20 eV, implies that ionization dominates over charge-exchange processes. This is confirmed by the observed conservation of the total pressure (dynamic+static), shown in figure 6.2c. These measurements also confirm that both divertor legs are in the attached/high-recycling regime.

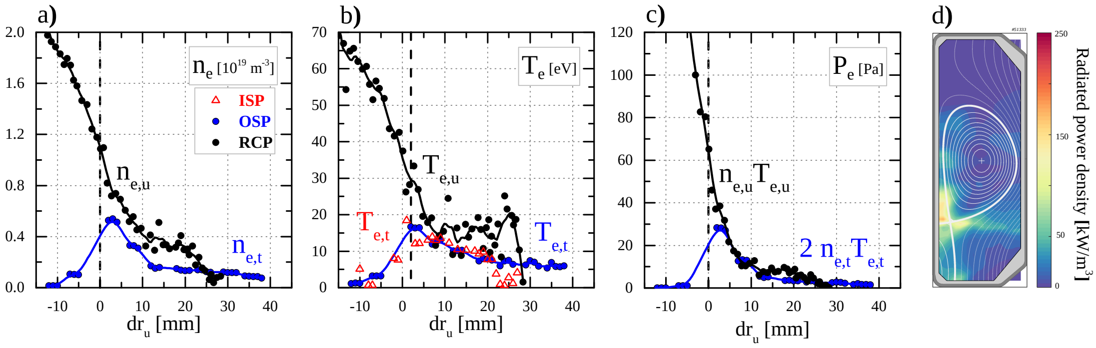

Figure 6.2 – Density (a), temperature (b) and pressure (c) in the SOL, at the target (LPs) and at the mid-plane (RCP), for a typical shot of the database ($I_P = 210\ kA$, $L_{\text{div}} = 36$ cm, $f_{x,t} = 2.5$ at OSP and $f_{x,t} = 6$ at ISP, forward field).(d) For the same shot, radiated power density from a tomographic inversion of bolometric measurements.

The global power balance for these discharges is evaluated using infrared thermography, described in section 2.2.1, and a bolometric system, described in section 2.2.5. The sum of the power measured at the targets with IR thermography $P_{\text{in}} + P_{\text{out}}$ and the total radiated power from bolometric inversions P_{rad} corresponds to 60 to 100% of the Ohmic heating power and is independent of the field direction [54]. This systematic underestimation of the exhaust power can, in part, be ascribed to (1) charged particle losses on the main chamber walls, (2) an incomplete edge coverage by bolometers and (3) reflection by the bolometer foils [64]. An estimate of the power unaccounted for due to effects (1-2) is complicated, and is not investigated here. Accounting for the light reflection on the bolometer foils should increase the measured radiated power by ≈ 5 to 10%.

In this thesis, the power exhaust of the attached SN is characterised by three quantities, all estimated from the infrared system:

- the in-out power sharing ratio $P_{\text{in}}/P_{\text{out}}$, defined as the ratio of the deposited power at the inner and outer strike point
- the SOL power width $\lambda_{q,u}$, introduced in section 5.1.1

- the spreading factor S_u, introduced in section 5.1.1

These quantities are chosen because they directly affect the peak parallel heat flux at the divertor plate, see equation 5.7. Each quantity is discussed in a separate section, first by presenting the experimental measurements and then by proposing interpretations for the observed trends.

6.1.1 In-out divertor power sharing

6.1.1.1 Experimental results

The main observed variations of the in-out divertor power sharing with the varied parameters are shown in figures 6.3-6.4-6.5-6.6-6.7 and here summarized:

- Scan of plasma current, figures 6.3a-6.3b. Increasing I_P increases the power at both targets since the Ohmic heating power directly increases with I_P such that the in-out power ratio is fairly insensitive to I_P, figure 6.3a. The ratio is slightly higher for reversed field direction, figure 6.3b. Note that the I_P scan in reversed field is performed in a different configuration, with a shorter outer divertor leg.
- Scan of divertor leg length, figures 6.4a-6.4b. Increasing L_div increases the power at the inner target and lowers that at the outer target, i.e. the in-out power ratio increases, figure 6.4a. This ratio is slightly higher for the reversed field direction, figure 6.4b.
- Scan of outer target flux expansion, figure 6.5. Increasing the outer $f_{x,t}$ increases the power at the inner target and decreases that at the outer target, i.e. the in-out power ratio increases.
- Scan of plasma upper triangularity, figures 6.6a-6.6b. Increasing δ_upper decreases the power at the inner target but does not affect that at the outer target, i.e. the in-out power ratio decreases, figure 6.6a. This ratio is higher for the reversed field direction, figure 6.6b.
- Scan of outer target radius, figures 6.7a-6.7b. Increasing R_t has an irregular effect on the power at both targets, with the in-out power ratio showing no clear trend. This ratio behaves similarly for the reversed field direction, figure 6.7b.

6.1.1.2 Interpretation using the conductive model

This section proposes an explanation for the observed variations of the in-out power sharing, based on the conductive model discussed in section 5.1.2.2. The value of $\lambda_{q,u}$

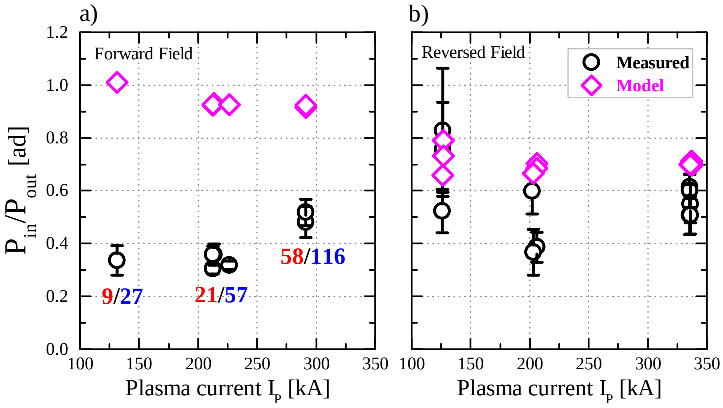

Figure 6.3 – Measured in-out divertor power sharing ratio as a function of plasma current in FF (a) and RF (b), compared to conductive model prediction (purple diamonds) assuming $\lambda_{q,u} = 6$, 5 and 4 mm from the three I_P values respectively. The coloured numbers denote the measured power at the inner (upper in red) and outer (lower in blue) divertor plates, in units of kW.

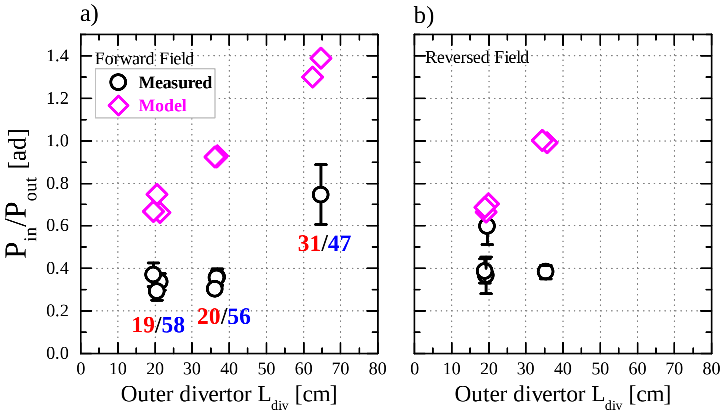

Figure 6.4 – Measured in-out divertor power sharing ratio as a function of outer divertor leg length in FF (a) and RF (b), compared to conductive model prediction (purple diamonds) assuming $\lambda_{q,u} = 5$ mm (typical value at this I_P). The coloured numbers denote the measured power at the inner (upper in red) and outer (lower in blue) divertor plates, in units of kW.

assumed in the model is adjusted for each experimental scan according to the plasma current. However, the model predictions are found to be rather insensitive to the assumed value of $\lambda_{q,u}$, with a factor two change in $\lambda_{q,u}$ resulting in a $< 10\%$ change in $P_\mathrm{in}/P_\mathrm{out}$. The comparison of measured $P_\mathrm{in}/P_\mathrm{out}$ values with predictions from the model is shown in figures 6.3-6.4-6.5-6.6-6.7 and here summarized:

- Scan of plasma current, figures 6.3a-6.3b. In FF, the model reproduces the observed constancy in the power sharing, but it overestimates the values of $P_\mathrm{in}/P_\mathrm{out}$. In RF, the model describes both constancy and absolute value of the measurements.
- Scan of divertor leg length, figures 6.4a-6.4b. In FF, the model reproduces the

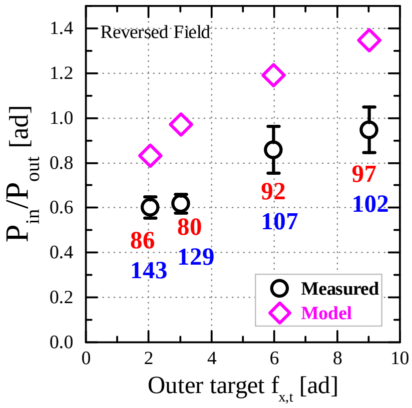

Figure 6.5 – Measured in-out divertor power sharing ratio as a function of outer target flux expansion in RF, compared to conductive model prediction (purple diamonds) assuming $\lambda_{q,u} = 3$ mm (typical value at this I_{P}). The coloured numbers denote the measured power at the inner (upper in red) and outer (lower in blue) divertor plates, in units of kW.

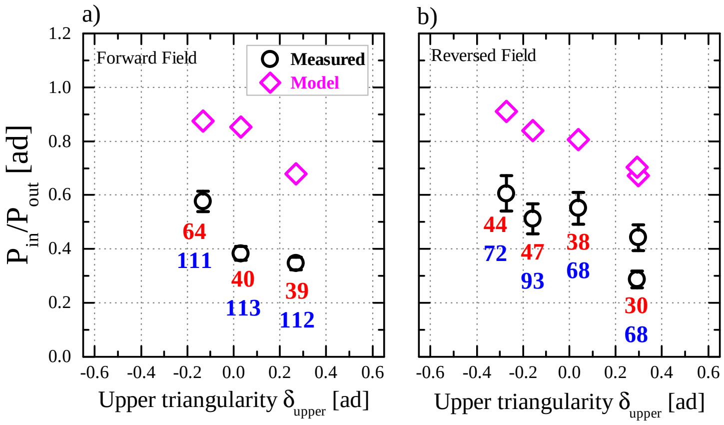

Figure 6.6 – Measured in-out divertor power sharing ratio as a function of plasma upper triangularity in FF (a) and RF (b), compared to conductive model prediction (purple diamonds) assuming $\lambda_{q,u} = 6$ mm (typical value at this I_{P}). The coloured numbers denote the measured power at the inner (upper in red) and outer (lower in blue) divertor plates, in units of kW.

observed change of power sharing with outer divertor leg length L_{div}, although it systematically overestimates the values of $P_{\text{in}}/P_{\text{out}}$. In RF, the comparison is not attempted as only two data points are available.

- Scan of outer target flux expansion, figure 6.5. The model reproduces the observed change of power sharing with the outer target flux expansion, but systematically overestimates the measured values of $P_{\text{in}}/P_{\text{out}}$.

- Scan of plasma upper triangularity, figures 6.6a-6.6b. In both FF and RF, the model reproduces the observed change of power sharing with triangularity, but systematically overestimates the measured values of $P_{\text{in}}/P_{\text{out}}$.

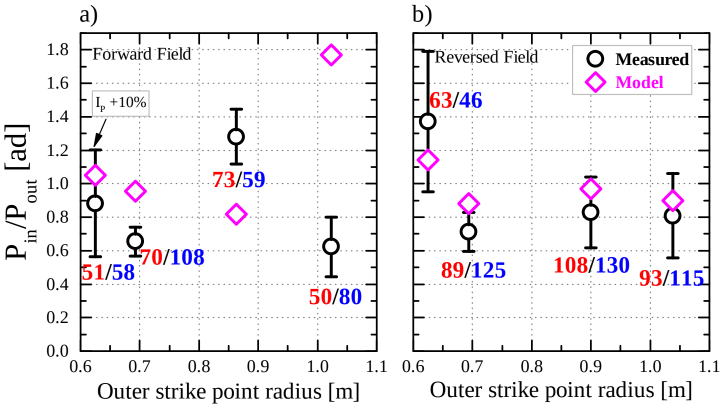

Figure 6.7 – Measured in-out divertor power sharing ratio as a function of outer target radius in FF (a) and RF (b), compared to conductive model prediction (purple diamonds) assuming $\lambda_{q,u} = 4$ mm (typical value at this I_P). The coloured numbers denote the measured power at the inner (upper in red) and outer (lower in blue) divertor plates, in units of kW.

- Scan of outer target radius, figures 6.7a-6.7b. In FF, the model does not reproduces the observed change of power sharing with target radius, while in RF the model well describes the measurements.

Therefore, as also summarized in table 6.2 and figure 6.8, measured and predicted values agree in trend but not in magnitude. An offset between model estimates and data appears, which is systematically smaller in the reversed, compared to forward, field direction. Consequently, it is thought to be a combined effect of in-out asymmetric volumetric radiative losses and classical $\vec{E} \times \vec{B}$ drifts, that are both absent from the model. Volumetric radiative losses are generally observed to be stronger in the inner divertor, compared to the outer, with the FF direction, while they affect similarly the two divertors in the RF direction, as shown in the next section (figure 6.29). This effect reduces the power at the inner strike point, and thus $P_\mathrm{in}/P_\mathrm{out}$, more strongly in FF than in RF, causing a deviation from the initial model prediction stronger in FF than in RF. Enhanced volumetric losses could result from ion drifts in the SOL. In FF, $\vec{E} \times \vec{B}$ drifts in the private flux region of the primary separatrix would transport plasma from the outer divertor strike point (OSP in a SN, SP2 in a LFS SF-) to the inner divertor strike point (ISP in a SN, SP1 in a LFS SF-) [65]. The plasma density at the inner divertor strike point would increase and, furthermore, the sputtered carbon impurity dispersion into the rest of the divertor would be impeded. An increased density of plasma and carbon impurities near the strike point would then enhance volumetric losses, consequently lowering the heat flux to the target.

The target radius scan realized in TCV is not a completely clean assessment of the effect of target radius on in-out power sharing. To measure the effect of target radius on power sharing, the connection lengths to inner and outer divertor targets must also be kept

Scan	$P_{\text{in}}/P_{\text{out}}$ explained by conductive model	Remarks
I_{P}	Yes (independent of I_{P})	Offset w.r.t. model; much smaller in RF
L_{div}	Yes (increases with L_{div})	Offset w.r.t. model; somewhat smaller in RF
$f_{x,t}$	Yes (increases with $f_{x,t}$)	Offset w.r.t. model
δ_{upper}	Yes (decreases with δ_{upper})	Offset w.r.t. model; somewhat smaller in RF
R_t	Yes in RF, No in FF	-

Table 6.2 – Summary of the comparison between measured and modelled in-out power sharing, for the five experimental scanned quantities: I_{P}, L_{div}, $f_{x,t}$, δ_{upper} and R_t. The conductive model can reproduce most of the observations, but an offset between data and model prediction exists, and is typically higher in FF than in RF.

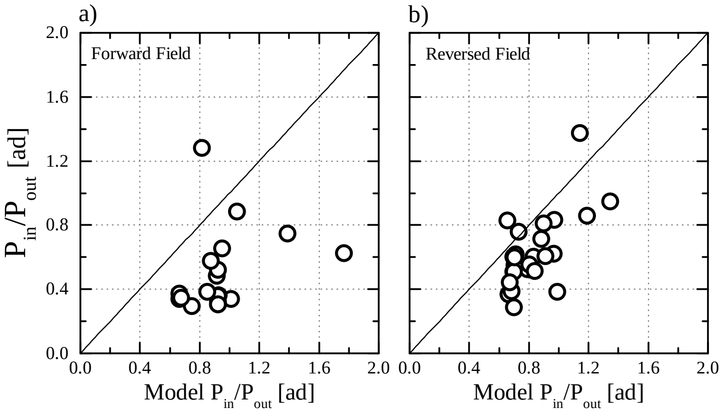

Figure 6.8 – Measured in-out divertor power sharing ratio compared to conductive model prediction in FF (a) and RF (b), using data from all five experimental scans.

constant. This was complicated to achieve experimentally and, despite many attempts, was ultimately abandoned. In the R_t scan, $L_{||,\text{in}}$ increases from $\approx$ 14.7 to $\approx$ 22.3 m (+51%) and $L_{||,\text{out}}$ from $\approx$ 14.1 to $\approx$ 18.9m (+34%). From the changes in the parallel connection length alone, one would expect a decrease of the in-out power ratio from $\approx$ 0.96 to $\approx$ 0.85 (-11%), equation 5.12. From the increased R_t, alone, one would expect an increase of the in-out power ratio, as a larger R_t decreases the effective connection length to the outer target, equation 5.26. The predicted effect of target radius may, thereby, be masked by the changes in parallel connection length.

Conclusion of section 6.1.1

In conclusion, this section has shown that the power sharing between inner and outer divertors of a SN configuration can significantly vary with changes to the plasma or divertor geometry. The observations can mostly be ascribed to the effect of parallel electron heat conduction in the SOL. However, systematic offsets between the measurements and the conductive predictions suggest that a second, additional, mechanism affects power sharing. In-out asymmetric volumetric radiation and particle drifts, both absent in the model, are possible candidates. Potential implications of these findings for the divertor heat handling in a future fusion reactor will be discussed in section 6.4.

6.1.2 SOL power width

6.1.2.1 Experimental results

The SOL power width at each divertor target $\lambda_{q,u}$ is obtained by fitting the heat flux profiles, from the infrared thermography system, with the Eich function, as described in section 5.1.1. In addition, the SOL power width at the outboard mid-plane $\lambda_{q,u}^{\text{Spitzer}}$ is calculated using temperature measurements of the upstream SOL plasma from the Thomson scattering system, described in section 2.2.4, and, when data is available, the outboard mid-plane fast reciprocating probe, described in section 2.2.3. Under the assumption that the SOL is in the conduction limited regime, the SOL power fall-off length is given by

$$\lambda_{q,u}^{\text{Spitzer}} = \frac{2}{7}\lambda_{T,u}^{\text{TS}} \tag{6.1}$$

where $\lambda_{T,u}$ is the SOL electron temperature fall-off length. When the RCP data is not available and the TS measurements are limited to the first few millimetres of SOL, $\lambda_{T,u}$ is extracted by fitting the edge region, i.e. $0.95 \leq \rho_\psi \leq 1.05$.

The main observed variations of the SOL power width with the varied parameters are shown in figures 6.9-6.10-6.11-6.12-6.13 and are summarized here:

- Scan of plasma current, figures 6.9a-b. The power fall-off length $\lambda_{q,u}$ decreases with increasing I_P. In FF direction, exponents of -0.73 and -0.67 for the OSP and the ISP are similar, but $\lambda_{q,u}$ is somewhat larger at the OSP. Changing the magnetic field direction affects the absolute values of target $\lambda_{q,u}$ and their sensitivity to I_P, compare figure 6.9a with 6.9b. In reversed field, $\lambda_{q,u}^{\text{in}}$ is broader and $\lambda_{q,u}^{\text{out}}$ is narrower, such that $\lambda_{q,u}^{\text{in}}/\lambda_{q,u}^{\text{out}} < 1$ in forward field and $\lambda_{q,u}^{\text{in}}/\lambda_{q,u}^{\text{out}} > 1$ in reversed field. This in-out difference decreases with increasing plasma current, vanishing at the highest value of I_P, figure 6.9b.
- Scan of the divertor leg length, figures 6.10a-b. The value of $\lambda_{q,u}$ at both targets increases with a longer outer divertor leg length, figure 6.10a, consistent with the LP data from this experiment [66]. Reversing magnetic field direction from FF to RF causes, similarly to the I_P scan, a larger value of $\lambda_{q,u}^{\text{in}}$ and a narrower value of $\lambda_{q,u}^{\text{out}}$, compare figures 6.10a with 6.10b.
- Scan of flux expansion, figure 6.11. The values of $\lambda_{q,u}$ at both targets, together with that at the outboard mid-plane $\lambda_{q,u}^{\text{Spitzer}}$, are similar and only weakly decrease

for higher $f_{x,t}$.

- Scan of upper triangularity, figures 6.12a-b. For a higher upper triangularity δ_{upper}, $\lambda_{q,u}$ at the outer target and that at the outboard mid-plane, $\lambda_{q,u}^{\text{Spitzer}}$, increase monotonically, while that at the inner target saturates at $\delta_{\text{upper}} \approx 0$, figure 6.12a. The ≈ 3 mm offset between outer target $\lambda_{q,u}$ and upstream $\lambda_{q,u}^{\text{Spitzer}}$ is approximately the same for all triangularity values. The same functional dependence on δ_{upper} is observed when reversing from FF to RF, although the value of $\lambda_{q,u}$ at the outer target is typically smaller, figure 6.12b.
- Scan of strike point radius, figures 6.13a-b. The effect of outer target radius R_t on $\lambda_{q,u}$ depends on the magnetic field direction. In FF, for increasing R_t, the value of $\lambda_{q,u}$ at the outer target decreases, with no clear trend at the inner target, figure 6.13a. In the RF direction, in contrast, with increasing R_t, the value of $\lambda_{q,u}$ at both the inner and outer target increases, figure 6.13b. For both field directions, finally, the value of $\lambda_{q,u}^{\text{Spitzer}}$ at the outboard mid-plane only weakly decreases for higher R_t.

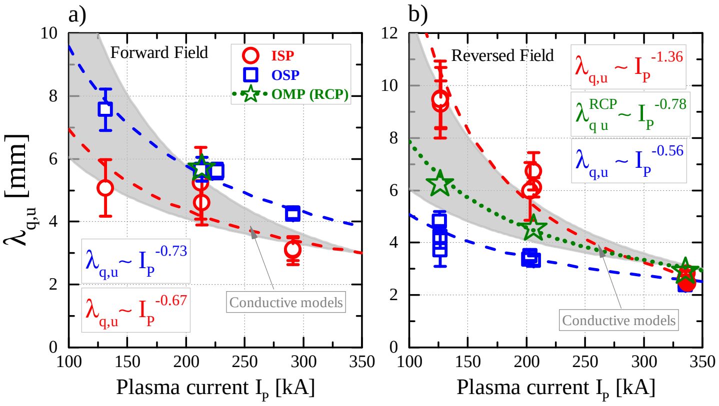

Figure 6.9 – SOL power width as a function of plasma current in FF (a) and RF (b). The inner strike point (ISP) values are red circles, the outer strike point (OSP) values are blue squares, the outboard mid-plane values (from the reciprocating probe, RCP) are green stars. The SOL temperature profile from RCP is fitted for $0 \leq \mathrm{d}r_u \leq 2$ cm. The shaded area is the prediction from the conductive model.

6.1.2.2 Interpretations

This section discusses five physical effects which may explain the observed dependencies of the SOL power width, as measured at the target or at the out-board mid-plane, on the varied parameters. The discussion results are then summarized in table 6.3.

Conductive model of the SOL The conductive model of the SOL discussed in section 5.1.2 yields an expression for the SOL power fall-off length for fixed (temperature

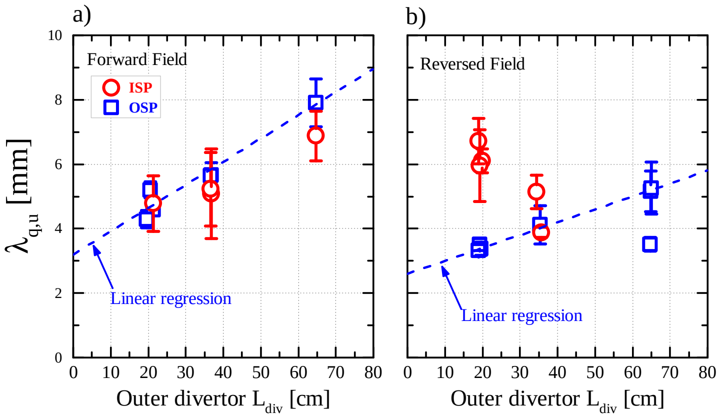

Figure 6.10 – SOL power width as a function of divertor leg length in FF (a) and RF (b). The inner strike point (ISP) values are red circles, the outer strike point (OSP) values are blue squares. The linear regression of OSP values is $\lambda_{q,u}[\text{mm}] = 0.072 \cdot L_{\text{div}}[\text{cm}] + 3.2$ for FF, $\lambda_{q,u}[\text{mm}] = 0.04 \cdot L_{\text{div}}[\text{cm}] + 2.6$ for RF.

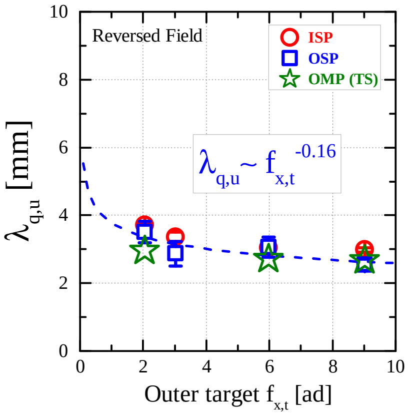

Figure 6.11 – SOL power width as a function of target flux expansion in RF. The inner strike point (ISP) values are red circles, the outer strike point (OSP) values are blue squares, the outboard mid-plane values (from Thomson scattering, TS) are green stars. The SOL temperature profile from TS is fitted for $0.95 \leq \rho_\psi \leq 1.05$.

independent) thermal diffusivity, equation 5.22. This expression can be adjusted by using a Bohm-like diffusivity for drift waves, equation 5.23, or a Bohm-like diffusivity for ballooning modes, equation 5.24. To compare the model to the experiments, a scalar connection length for each target is defined by averaging the connection length profile across the SOL in the vicinity of the separatrix from $\text{d}r_u = [0 \text{ to } 2]$ mm. In the following, this effective connection length is simply referred to as $L_\parallel$ (or $L_{\parallel,\text{out}}$ and $L_{\parallel,\text{in}}$ where required).

- Scaling with plasma current. To adapt model equation 5.22 to the experimental conditions of the I_P scan (fixed Greenwald fraction), the I_P dependencies in the

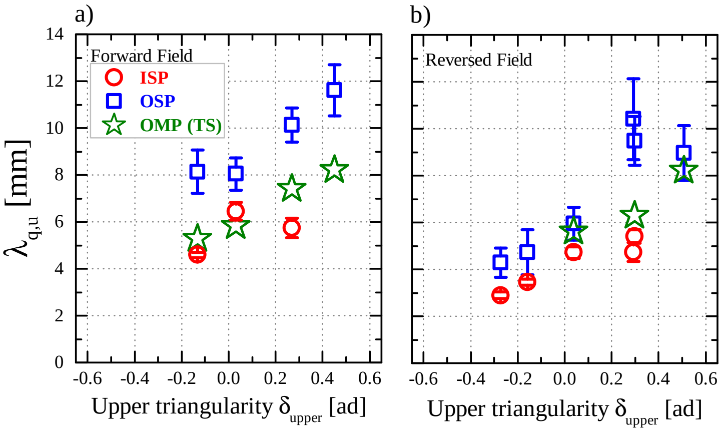

Figure 6.12 – SOL power width as a function of plasma upper triangularity in FF (a) and RF (b). The inner strike point (ISP) values are red circles, the outer strike point (OSP) values are blue squares, the outboard mid-plane values (from Thomson scattering, TS) are green stars. The SOL temperature profile, from Thomson scattering, is fitted for $0.95 \leq \rho_\psi \leq 1.05$.

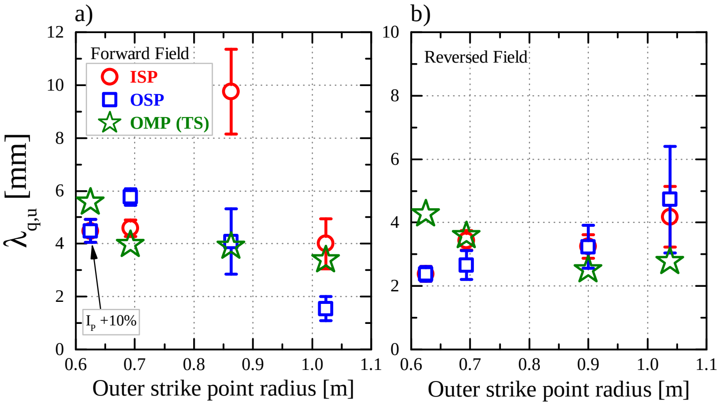

Figure 6.13 – SOL power width as a function of strike point radius in FF (a) and RF (b). The inner strike point (ISP) values are red circles, the outer strike point (OSP) values are blue squares, the outboard mid-plane (OMP) values (from Thomson scattering, TS) are green stars. The SOL temperature profile, from Thomson scattering, is fitted for $0 \leq \mathrm{d}r_u \leq 2$ cm.

other parameters of equation 5.22 are calculated. It is found that $L_{\parallel,\mathrm{out}} \propto I_\mathrm{P}^{-1}$, $L_{\parallel,\mathrm{in}} \propto I_\mathrm{P}^{-1}$, $n_{e,u} \propto I_\mathrm{P}$ (constant Greenwald fraction) and $P_\mathrm{sep} \propto P_\Omega \propto I_\mathrm{P}^{1.6}$ (estimated from TCV database of Ohmic plasmas), so that equation 5.22 yields

$$\lambda_{q,u} \propto I_\mathrm{P}^{-0.56} \qquad (\text{fixed } \chi_\perp) \qquad (6.2)$$

$$\lambda_{q,u} \propto I_\mathrm{P}^{-0.53} \qquad (\text{drift waves}) \qquad (6.3)$$

$$\lambda_{q,u} \propto I_\mathrm{P}^{-1.16} \qquad (\text{ballooning modes}) \qquad (6.4)$$

The model, therefore, predicts a range of scalings for the transport models, with drift waves being the weakest (-0.53) and ballooning modes the strongest (-1.16).

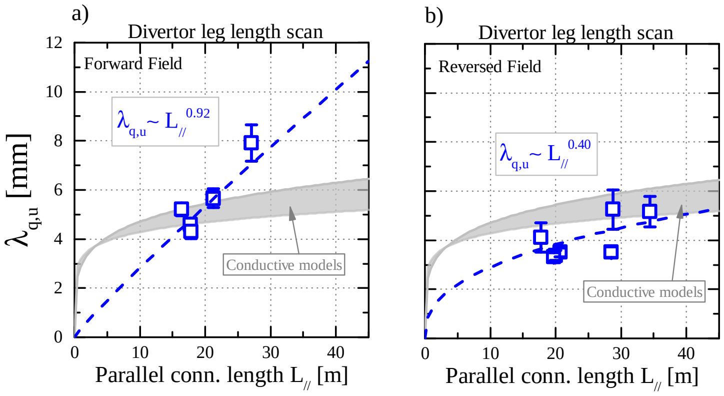

Figure 6.14 – Measured variation of $\lambda_{q,u}$ with parallel connection length, at the outer target, compared to the prediction from the conductive model (shaded area). The dataset includes leg length scans in the FF (a) and RF (b) direction.

As shown in figures 6.9, the predicted range of exponents is quite similar to that observed in the experiment, where the regression exponent ranges between -0.56 and -1.36. However, the model is unable to reproduce the experimental result where the regression exponent changes with the strike point and the magnetic field direction. These effects must, therefore, result from mechanisms not included in the conductive model and no conclusion can be drawn.

- Scaling with divertor leg length. In the divertor leg length scan, all the parameters in the r.h.s. of equation 5.22 are fixed except $L_{\parallel,\mathrm{out}}$ and the expression can be approximated as

$$\lambda_{q,u} \propto L_{\parallel,\mathrm{out}}^{0.13} \qquad \text{(fixed } \chi_\perp\text{)} \tag{6.5}$$

$$\lambda_{q,u} \propto L_{\parallel,\mathrm{out}}^{0.21} \qquad \text{(drift waves or ballooning modes)} \tag{6.6}$$

The model, thus, predicts a weak dependence of $\lambda_{q,u}$ on $L_{\parallel,\mathrm{out}}$, in contrast to the experiment, where the regression exponent was 0.92 for the forward field and 0.40 for the reversed field direction, figures 6.14a-b. This model is, therefore, not sufficient to explain the experimental increase of $\lambda_{q,u}$ with the divertor leg length.

In summary, the relatively strong inverse I_P dependence, observed in the experiments, appears to be a natural part of the conductive model, with details in the cross-field diffusivity affecting its strength. The conductive model does clearly not include enough physics to describe the experimental variation of $\lambda_{q,u}$ with L_div, with SP location (i.e. in-out asymmetry) or with magnetic field direction. Alternatively, the conductive model could make wrong assumptions (e.g. cross-field transport dominantly around the confined plasma). More physics mechanisms, that are possible candidates in explaining these effects, are discussed in the following.

Vertical ∇B and curvature B drifts ∇B and curvature B drifts transfer plasma across the separatrix into the SOL. In forward field, these drifts are directed towards the active x-point, i.e. downwards, whereas in reversed field they are directed away, i.e. upwards. ∇B and curvature B drifts are prime candidates to explain a number of observations:

1. the dependence of the in-out $\lambda_{q,u}$ asymmetry on magnetic field direction. In FF, these drifts are expected to broaden the outer SOL, while narrowing the inner SOL. In RF, their direction reverses, so that they narrow the outer SOL and broaden the inner SOL[49]. As a result, these drifts cause an in-out asymmetry of $\lambda_{q,u}$, with $\lambda_{q,u}^{\text{in}}/\lambda_{q,u}^{\text{out}} < 1$ in forward and $\lambda_{q,u}^{\text{in}}/\lambda_{q,u}^{\text{out}} > 1$ in reversed field. This is consistent with the experiment, where the in-out ratio is smaller than 1 in FF, and becomes larger than 1 in RF (compare figure 6.9a with 6.9b and 6.10a with 6.10b).
2. the reduction of the in-out $\lambda_{q,u}$ asymmetry (towards unity) with increasing current. A higher plasma current reduces the parallel connection length from the OMP to the x-point for both inner and outer SOL. This enhances parallel transport, by increasing the parallel temperature gradient, weakening any effect of drifts on $\lambda_{q,u}$ (i.e. reduces the $\lambda_{q,u}$ in-out asymmetry, towards unity). This is consistent with the experiment, where the in-out ratio converges to unity with increasing I_{P}, figures 6.9a-b.

$\vec{E} \times \vec{B}$ drifts The $\vec{E} \times \vec{B}$ drifts can play an important role in the transport of particles in the divertor region [67, 68]. Simulations with the two dimensional edge plasma transport code UEDGE for two TCV discharges within this study ($I_{\text{P}} = 210$ kA, $L_{\text{div}} = 21$ cm, $f_{x,t} = 4.5$ at ISP and 3.5 at OSP, forward and reversed field) [65] show that, for both forward and reversed field, along most of the outer divertor leg the radial component of the $\vec{E} \times \vec{B}$ drift carries particles from the separatrix towards the far SOL. $\vec{E} \times \vec{B}$ drifts are therefore a candidate to explain:

- the increase of $\lambda_{q,u}$ with increasing L_{div}. For a L_{div} scan, the radial component of the $\vec{E} \times \vec{B}$ drift, along the outer divertor leg, may cause a broadening of the outer SOL $\lambda_{q,u}$, independently of the field direction, increasing the broadening predicted by the analytic model.
- the weak decrease of $\lambda_{q,u}$ with increasing $f_{x,t}$. With a higher $f_{x,t}$, one can expect a higher poloidal component of parallel gradients along field lines of the outer SOL due to the decreasing pitch angle of the field lines. This causes an increase of the radial $\vec{E} \times \vec{B}$ drift velocity in the outer divertor leg that may cancel the effect of the increased distance between flux surfaces. Quantitative studies are required to determine whether the radial drift velocity changes faster than the spacing between flux surfaces. If the latter dominates, the effect of $\vec{E} \times \vec{B}$ drifts on the SOL width

would be smaller for higher flux expansions, consistent with the observed weak decrease of $\lambda_{q,u}$ with $f_{x,t}$ at the OSP, figure 6.11.

Asymmetric turbulent transport in the divertor The distinct dependence of $\lambda_{q,u}$ on L_{div} may be explained by turbulent perpendicular transport in the divertor leg towards the common flux region being stronger than towards the private flux region. Such an asymmetric cross-field transport along the divertor leg would increase $\lambda_{q,u}$ rather than S_u as is observed in TCV experiments. Recent simulations [69] with the 3D fluid turbulent code TOKAM3X [70] of some plasma pulses within this work (L_{div} scan with $I_{\text{P}} = 210$ kA in forward field) support the validity of this hypothesis.
An important observation is that, in the presence of asymmetric transport in the divertor, the classical interpretation of $\lambda_{q,u}$ as a pure main SOL quantity is no longer valid because $\lambda_{q,u}$ captures, by construction (see Eich fitting function, equation 5.5), all asymmetric components of the cross-field transport in the divertor. To decouple these contributions to $\lambda_{q,u}$, of the upstream transport (SOL surrounding the plasma) and that of the divertor transport (SOL between x-point and target), the model suggested by [71] requires extension, for instance, by adding a new divertor contribution to $\lambda_{q,u}$ which could be proportional to the divertor depth L_{div}.

Turbulence in plasma edge/near-SOL The turbulence levels in the plasma edge and the near-SOL are expected to have a strong impact on the SOL power width value at the outboard mid-plane $\lambda_{q,u}^{\text{Spitzer}}$ and, consequently, on its value at the divertor targets $\lambda_{q,u}$. Turbulence in the plasma edge/near-SOL is a candidate mechanism to explain the observed increase of target $\lambda_{q,u}$ and upstream $\lambda_{q,u}^{\text{Spitzer}}$ when increasing the plasma upper triangularity. For increasing δ_{upper}, the edge electron temperature and the plasma stored energy both reduce, consistent with a degradation of plasma confinement inside the separatrix, due to increased turbulent transport in the edge region [72]. The increased SOL width suggests that such an enhanced turbulent transport may propagate across the separatrix into the near-SOL region, thus impacting transport in the SOL. This picture is consistent with GBS [73] simulations of limited plasmas, showing that negative triangularity suppresses turbulence in the SOL [74].

A summary of the transport models, discussed in this section, and of their ability to explain the observations is provided in table 6.3. Each model is able explain some of the observations, but none can explain all.

---

[4] In this basic discussion, vertical drifts do not explain the I_{P} effect on the upstream $\lambda_{q,u}$. However, in the analytic model for the SOL width by Goldston, discussed in section 5.1.3, vertical drifts can explain the I_{P} effect on $\lambda_{q,u}$, with $\lambda_{\text{HD}} \propto I_{\text{P}}^{-9/8}$, equation 5.35.

Scan	Conductive model	Vertical drifts	$\vec{E} \times \vec{B}$ drifts	Divertor asym. turbulence	Edge turbulence
I_{P}	yes	no[4]	no	no	no
L_{div}	partly	no	yes	yes	no
$f_{x,t}$	no	no	yes	no	no
δ_{upper}	no	no	no	no	yes
R_t	no	no	no	no	no
FF/RF	no	yes	no	no	no
in/out	no	yes	no	no	no

Table 6.3 – Summary of the transport models considered to interpret the observed variations of $\lambda_{q,u}$. A qualitative assessment of each model ability to explain the observations is provided: "yes" = the model does or likely can explain the measurement. "partly" = the model explains only part of the measurement. "no" = the model cannot or is unlikely to explain the measurement.

6.1.2.3 Comparison with multi-machine scaling laws

This section compares the $\lambda_{q,u}$ values measured at the outer divertor plate to multi-machine scaling laws. For both the TCV data and the scaling laws, the magnetic field is in the FF direction (ion ∇B drifts towards the active x-point), the magnetic configuration is a Single-Null and the divertor is in the attached regime.

AUG scaling law A recent study in AUG [53] proposes a scaling of the $\lambda_{q,u}$ measured at the outer divertor target of a L-mode SN plasma:

$$\lambda_{q,u}^{\mathrm{AUG}}[\mathrm{mm}] = 0.15\ B_{p,u}[\mathrm{T}]^{-0.62}\ A[\mathrm{m}]^{-0.15}\ n_{\mathrm{edge}}[10^{19}\mathrm{m}^{-3}]^{0.94}\ \mathrm{W_{MHD}}[\mathrm{MJ}]^{-0.99} \quad (6.7)$$

with $B_{p,u}$ the poloidal magnetic field at the outboard mid-plane, A the main ion mass number, n_{edge} the edge electron density and $\mathrm{W_{MHD}}$ the plasma stored energy. As proposed in [72], this scaling may be generalized to other tokamaks by replacing the stored energy term $\mathrm{W_{MHD}}$ with $\mathrm{W_{MHD}} V_{\mathrm{AUG}}/V$, where V is the plasma volume:

$$\begin{aligned}\lambda_{q,u}^{\mathrm{AUG}}[\mathrm{mm}] = 0.15\ B_{p,u}[\mathrm{T}]^{-0.62}\ A[\mathrm{m}]^{-0.15}\ n_{\mathrm{edge}}[10^{19}\mathrm{m}^{-3}]^{0.94} \times \\ \times (\mathrm{W_{MHD}}[\mathrm{MJ}]\ V_{\mathrm{AUG}}/V)^{-0.99}\end{aligned} \quad (6.8)$$

For the TCV plasmas discussed in this work, V $\approx$ 1.35 m^3 and A = 2. n_{edge} is obtained from Thomson Scattering core density profiles evaluated at the normalized poloidal flux coordinate $\rho_\psi = 0.95$. As shown in figure 6.15a, this scaling exceeds the TCV measurements by a factor $\approx$ 2, except for the longest divertor leg.

AUG+JET, MAST scaling laws A scaling law based on AUG+JET data (equation (6) of [75], H_2 and D_2 plasmas) or entirely upon MAST data (equation (4) of [76], with

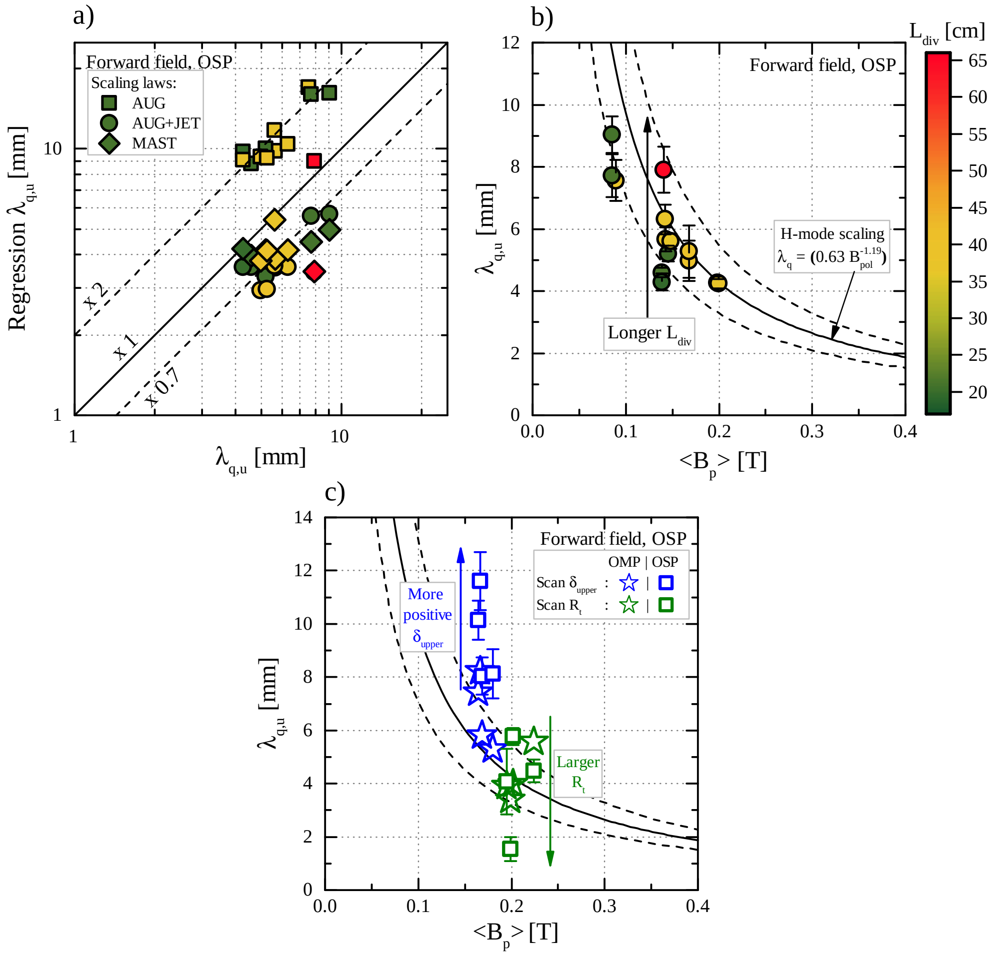

Figure 6.15 – (a) Outer target $\lambda_{q,u}$, for the FF direction, compared to the prediction by the scaling law from AUG [53] (squares, regression modified as in [72]), AUG+JET [75] (circles) and MAST [76] (diamonds). (b) Outer target $\lambda_{q,u}$, for the FF direction, from the L_{div} and I_{P} scans, as a function of the poloidal field $\langle B_p\rangle$, compared to the multi-machine H-mode regression #14 from [71]. (c) Outer target $\lambda_{q,u}$ (squares) and outer mid-plane $\lambda_{q,u}^{\text{Spitzer}}$ (stars), for the FF direction, from the δ_{upper} and R_t scans, as a function of the poloidal field $\langle B_p\rangle$, compared to the same multi-machine H-mode regression.

Double-Null Divertor configuration) are reported below

$$\lambda_{q,u}^{\text{AUG+JET}}[\text{mm}] = 1.44\ B_\phi[\text{T}]^{-0.8}\ q_{95}^{1.14}\ P_{\text{SOL}}[\text{MW}]^{0.22}\ R_{\text{geo}}[\text{m}]^{-0.03} \tag{6.9}$$

$$\begin{aligned}\lambda_{q,u}^{\text{MAST}}[\text{mm}] &= 1.16\cdot 10^{-28}\ \langle n_e\rangle[\text{m}^{-3}]^{1.45}\ B_\phi[\text{T}]^{-0.63}\times\\ &\times q_{95}^{1.45}\ P_{\text{SOL}}[\text{kW}]^{-0.19}\end{aligned} \tag{6.10}$$

As shown in figure 6.15a, both scaling laws underestimate the TCV measurements, up to 30%. A further comparison between these scaling laws and TCV data is performed using only the plasma current scan data. To translate the regressions into a plasma current scaling, the I_{P} dependencies in the other regression parameters are required. As the

Greenwald fraction is fixed, $q_{95} \propto B_{p,u}^{-1} \propto I_{\mathrm{P}}^{-1}$, $P_{\mathrm{SOL}} \propto P_{\Omega} \propto I_{\mathrm{P}}^{1.6}$ and $\langle n_e \rangle \propto I_{\mathrm{P}}$, where $\langle n_e \rangle$ is the line-averaged density and $P_{\mathrm{SOL}} = P_{\Omega} - P_{\mathrm{rad,core}}$ is the power crossing the separatrix. Finally, one obtains

$$\lambda_{q,u}^{\mathrm{AUG+JET}} \propto I_{\mathrm{P}}^{-0.788} \tag{6.11}$$

$$\lambda_{q,u}^{\mathrm{MAST}} \propto I_{\mathrm{P}}^{-0.304} \tag{6.12}$$

Interestingly, the AUG+JET regression predicts a parametric dependence on the plasma current which is very similar to that observed in TCV, see figures 6.9a and 6.9b.

Multi-machine scaling law - H-mode The current multi-machine scaling law for the outer divertor $\lambda_{q,u}$ of H-mode Single Null plasmas, regression # 14 from [71], is

$$\lambda_{q,u}^{\#14}[\mathrm{mm}] = (0.63 \pm 0.08)\ \langle B_p \rangle [\mathrm{T}]^{(-1.19 \pm 0.08)} \tag{6.13}$$

where $\langle B_p \rangle$ is the poloidal magnetic field upstream, computed using the plasma current and equation 4.9. The model predictions are compared to the measurements for the I_{P} and L_{div} scans in figure 6.15b, for the R_t and δ_{upper} scans in figure 6.15c. Some pertinent observations can be made:

- The values of $\lambda_{q,u}$ in TCV L-modes with divertor shape close to other machines, i.e. with short L_{div}, are $\approx 30\%$ smaller than the H-mode scaling, figure 6.15b. This is quite surprising, as in other tokamaks the $\lambda_{q,u}$ in L-mode is ~ 2 times broader than in H-mode [53] for fixed value of $\langle B_p \rangle$.
- The multi-machine scaling seems to describe better the SOL width measured at the outboard mid-plane (from TS, $\lambda_{q,u}^{\mathrm{Spitzer}}$) than that at the outer divertor plate, figure 6.15c. This is particularly clear for the triangularity scan dataset, where there is a ≈ 3 mm offset between target and upstream SOL width, and only the value upstream is compatible with the scaling law. Using the other available dataset (scan of I_{P}, L_{div} and R_t), in contrast, does not allow to confirm or refute this hypothesis, since for them the SOL width value at the target is comparable to that upstream.

6.1.2.4 Comparison with drift-based model of SOL

This section compares the $\lambda_{q,u}$ measured at the outer divertor plate to the prediction from the drift-based model, proposed in [49] and discussed in section 5.1.3. The magnetic field is in the FF direction.

As shown in figure 6.16a, the measured $\lambda_{q,u}$ exceeds the model prediction by a factor ≈ 2 for the L_{div}, I_{P} and R_t scans, by a factor ≈ 4 for the triangularity scan. This large distance

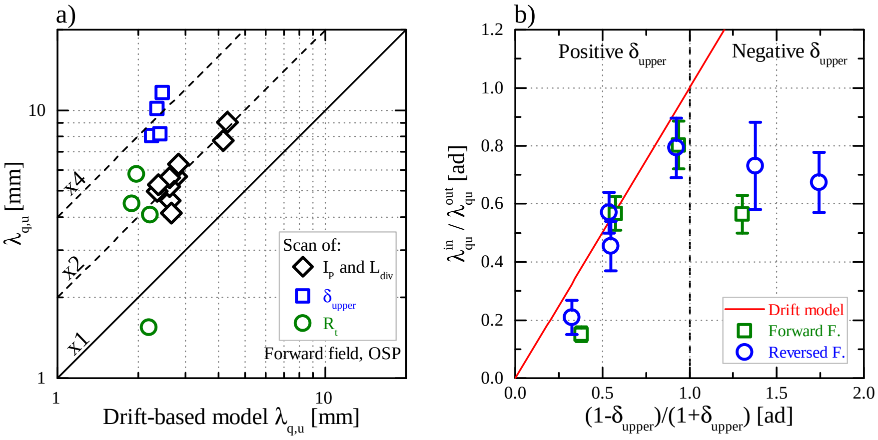

Figure 6.16 – (a) Outer target $\lambda_{q,u}$, in FF conditions, compared to the prediction from the drift-based model, proposed in [49] and summarized in section 5.1.3. (b) In-out $\lambda_{q,u}$ ratio, for FF (green square) and RF (blue circles) conditions, compared to prediction (red line) from drift-based model, equation 5.38 (proposed in [52]).

between measured and drift-based $\lambda_{q,u}$ suggests that additional physical mechanisms, other than vertical ion drifts, contribute to the SOL power width. Turbulence in the SOL and divertor fueling are possible candidates.

The drift-based model predicts that an in-out asymmetry of the target $\lambda_{q,u}$ develops if the plasma has a non-null triangularity, equation 5.38 (proposed in [52]):

$$\frac{\lambda_{q,u}^{\text{in}}}{\lambda_{q,u}^{\text{out}}} = \frac{1-\delta_x}{1+\delta_x} \tag{6.14}$$

where δ_x is the half-triangularity where vertical ion drifts points, i.e. $\delta_x = \delta_{\text{lower}}$ in FF, $\delta_x = \delta_{\text{upper}}$ in RF. For the RF direction, the measured $\lambda_{q,u}^{\text{in}}/\lambda_{q,u}^{\text{out}}$ ratio follows the predicted trend for positive δ_{upper} but disagrees for negative δ_{upper} since it saturates at ~ 0.7, see figure 6.16b. For the FF direction, the measured $\lambda_{q,u}^{\text{in}}/\lambda_{q,u}^{\text{out}}$ matches the values seen in the RF direction, whereas the model would predict a constant value of $(1-\delta_{\text{lower}})/(1+\delta_{\text{lower}}) \approx 0.33$. These disagreements between model and experiment support the hypothesis that additional physical mechanism, other than vertical ion drifts, contribute to the SOL power width for these discharges.

Conclusion of section 6.1.2

In conclusion, this section has shown that the SOL width is sensitive to almost every single scanned parameter, properties of the core plasma (plasma current and magnetic field direction), shape of the plasma (upper triangularity) and shape of the divertor (leg length, target flux expansion, target radius). In addition, poloidal asymmetries of $\lambda_{q,u}$ were found by comparing values at the inner and outer target and outboard mid-plane. Some scanned parameters affect $\lambda_{q,u}$ poloidally everywhere, others the $\lambda_{q,u}$'s

at the targets but have no effect upstream.
This complex series of observations was compared to five interpretative schemes, which cover most of the physical effects that determine heat transport, namely electron heat conduction, particle drifts and turbulence, see table 6.3. Each scheme can explain a subset of observations but not all. Similarly, the drift-based model can neither match the measured $\lambda_{q,u}$ nor explain its dependence on triangularity. This work, therefore, concludes that there is no single, dominant physical mechanism that determines the SOL power width for L-mode, attached plasmas. The actual width is the result of multiple mechanisms, acting with roughly the same order of force. Potential implications of these findings for the divertor heat handling in a future fusion reactor will be discussed in section 6.4.

6.1.3 Divertor spreading factor

6.1.3.1 Experimental results

The spreading factor at each divertor target S_u is obtained by fitting the heat flux profiles, from the infrared thermography system, with the Eich function, as described in section 5.1.1. The main observed variations of the divertor spreading factor with the varied parameters are shown in figures 6.17-6.18-6.19-6.20-6.21 and here summarized:

- Scan of plasma current, figures 6.17a-b. The divertor spreading factor S_u is largely independent of I_P, and systematically smaller at the inner than at the outer target, $S_u^\mathrm{in}/S_u^\mathrm{out} < 1$. Only the value of S_u at the outer target depends on the field direction, with it being smaller for RF than for FF.
- Scan of divertor leg length, figures 6.18a-b. A longer divertor leg L_div does not affect S_u, which is supported by the LP analysis [66]. As seen in the I_P scan, only S_u at the outer target depends on field direction, with its value being smaller for RF than for FF.
- Scan of flux expansion, figure 6.19. While the value of S_u at the inner target is constant, the value at the outer target varies as $S_u \propto f_{x,t}^{-1}$.
- Scan of upper triangularity, figures 6.20a-b. S_u increases with δ_upper at the inner target, for both field directions, whereas there is little change at the outer target. At the inner target, also, S_u is smaller for RF than FF.
- Scan of outer target radius, figures 6.21a-b. Increasing R_t has an irregular effect on S_u at both targets, but S_u is systematically smaller at the inner than at the outer target, $S_u^\mathrm{in}/S_u^\mathrm{out} < 1$. Except for the largest R_t in RF, the spreading factor is smaller for RF than for FF at both targets.

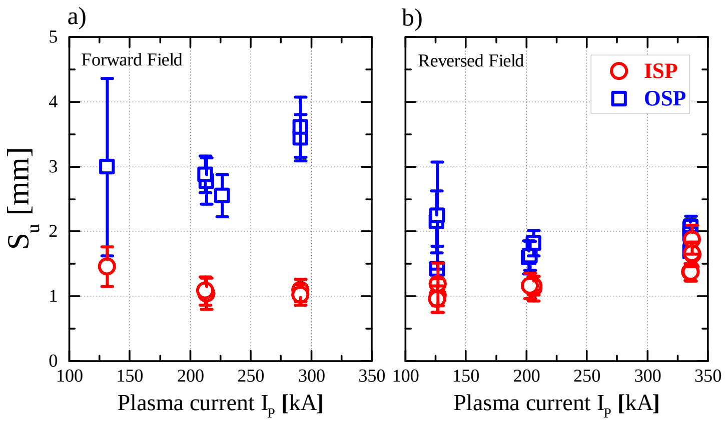

Figure 6.17 – Divertor spreading factor as a function of plasma current in FF (a) and RF (b). The inner strike point (ISP) values are red circles, the outer strike point (OSP) values are blue squares.

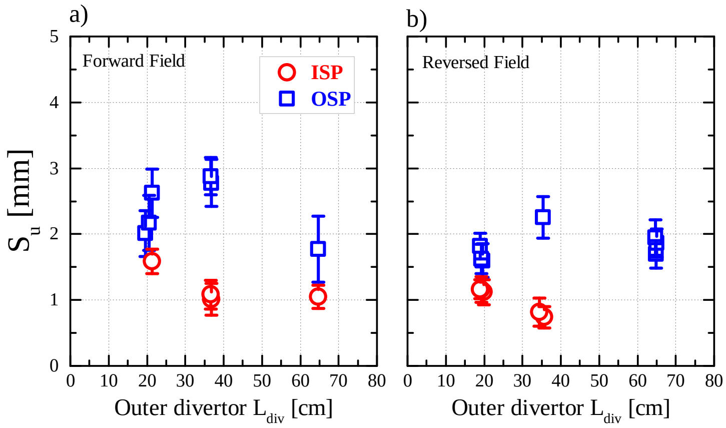

Figure 6.18 – Divertor spreading factor as a function of divertor leg length in F (a) and RF (b). The inner strike point (ISP) values are red circles, the outer strike point (OSP) values are blue squares.

6.1.3.2   Interpretation using diffusive model

This section interprets the observed variations of S_u with the varied parameters, presented in the previous section, using the diffusive model discussed in section 5.1.4, that provided an analytic expression for the spreading factor, equation 5.45. The density and temperature of the SOL plasma at the entrance of the divertor, i.e near the x-point, $n_{\mathrm{e,X}}$ and $T_{\mathrm{e,X}}$, are approximated by the plasma density and temperature at the LCFS, from the Thomson scattering measurements (section 2.2.4). The diffusivity is fixed at $\chi_\perp = 1$ m^2/s, as chosen for recent SOLPS-ITER simulations of TCV [77] to reproduce typical measured upstream density and temperature fall-off lengths. The target temperature is neglected in comparison with the value upstream, $f_T = T_{e,t}/T_{\mathrm{e,X}} = 0$. This is a good approximation since, for the analysed database, the separatrix electron temperature

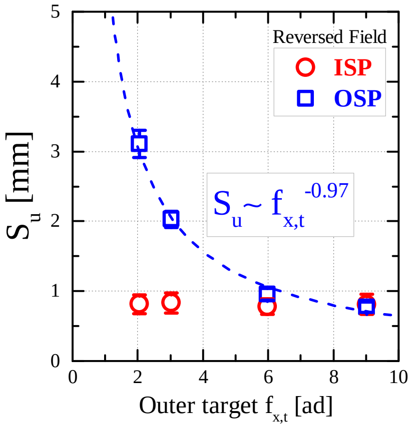

Figure 6.19 – Divertor spreading factor as a function of target flux expansion in RF. The inner strike point (ISP) values are red circles, the outer strike point (OSP) values are blue squares.

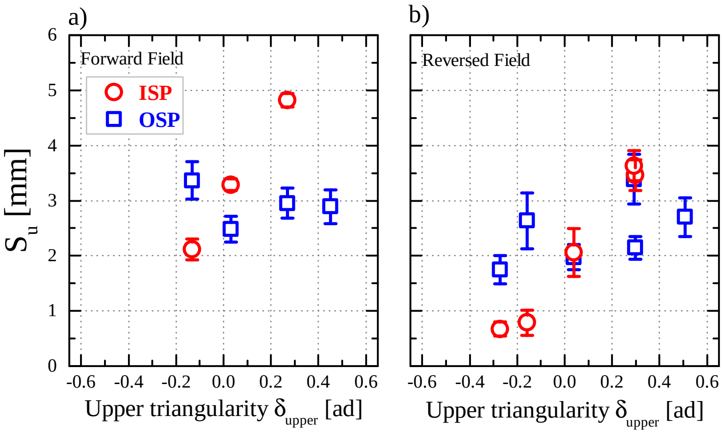

Figure 6.20 – Divertor spreading factor as a function of plasma upper triangularity in FF (a) and RF (b). The inner strike point (ISP) values are red circles, the outer strike point (OSP) values are blue squares.

at the target, yielded by the Langmuir probe system, is a small fraction of the value upstream, $f_T = T_{e,t}/T_{e,X} \approx 0.2 - 0.3$. Taking into account the finite target temperature reduces the estimated S_u by just 5-10%. Only a sub-set of the analysed database has good diagnostic coverage of the plasma edge from the Thomson scattering. This includes the I_P scan in FF, the $f_{x,t}$ scan in RF and the R_t scans in FF and RF directions.

The comparison of measured S_u values with predictions from the diffusive model is shown in figure 6.22 and here summarized:

- Scan of plasma current, figure 6.22a. Although the S_u model underestimates the measurements by a factor ≈ 2, it correctly describes the observed in-out asymmetry, with S_u larger at the outer target than the inner.

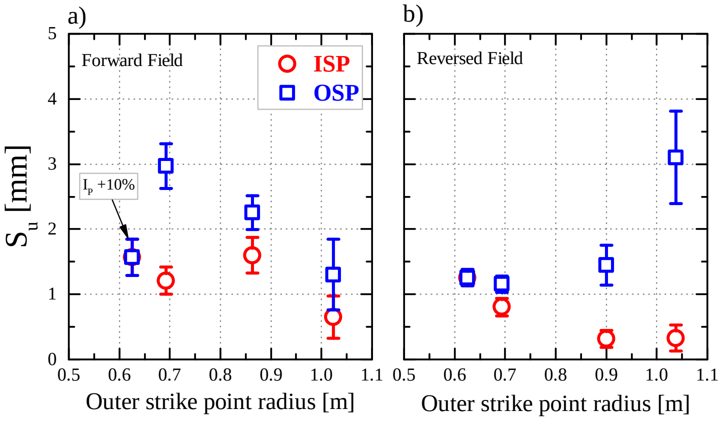

Figure 6.21 – Divertor spreading factor as a function of target radius in FF (a) and RF (b). The inner strike point (ISP) values are red circles, the outer strike point (OSP) values are blue squares.

- Scan of flux expansion, figure 6.22b. The model matches the measurements at the inner target and reproduces the observed decrease of S_u for increasing flux expansion at the outer target. The diffusive model, therefore, provides a possible explanation of the observed reduction of S_u, at the outer target, with increasing flux expansion. In the model, this decrease occurs because the parallel connection length in the divertor $L_{\parallel,\mathrm{div}}$ increases less than linearly with the target flux expansion $f_{x,t}$, so that the ratio $L_{\parallel,\mathrm{div}}/f_{x,t}$, that appears in the expression for S_u, decreases[5], see table 6.4 . Changes in plasma density and temperature, conversely, are much less important and do not impact S_u.

	$f_{x,t} = 2.0$	$f_{x,t} = 5.7$	$f_{x,t} = 8.7$
$n_{\mathrm{e,X}}$ $[10^{19}$ m$^{-3}]$	2.0	1.7	1.5
$T_{\mathrm{e,X}}$ [eV]	39.9	33.2	35.1
f_{T}	0.3	0.2	0.2
$L_{\parallel,\mathrm{div}}$ [m]	6.2	10.4	12.0
$L_{\parallel,\mathrm{div}}/f_{x,t}$	3.1	1.8	1.4

Table 6.4 – Quantities used to compute the model prediction for S_u, equation 5.45, for three values of the outer target flux expansion. Although the parallel connection length increases with increasing $f_{x,t}$, their ratio $L_{\parallel,\mathrm{div}}/f_{x,t}$ decreases.

- Scan of target radius, figures 6.22c-6.22d. The model matches the measurements at the inner target, whereas at the outer target it describes the variation of S_u in RF, but not with FF. The model also reproduces the seen in-out asymmetry $S_u^{\mathrm{in}}/S_u^{\mathrm{out}} < 1$.

---

[5] The $f_{x,t}$ increases faster than $L_{\parallel,\mathrm{div}}$ because in the investigated high-$f_{x,t}$ equilibria the poloidal field is not uniform in the divertor volume, but it decreases towards the target.

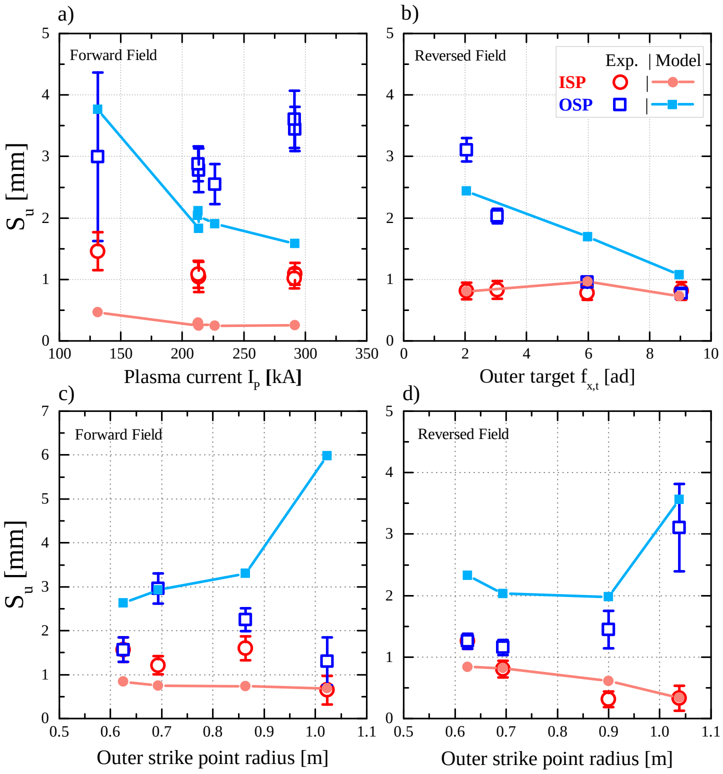

Figure 6.22 – Divertor spreading factor as a function of (a) plasma current in FF, (b) target flux expansion in RF, (c) target radius in FF and (d) target radius in RF. The inner strike point (ISP) values (red circles) and the outer strike point (OSP) values (blue squares) are compared to the predictions from the diffusive model (red and blue lines, for ISP and OSP respectively).

Conclusion of section 6.1.3

In conclusion, this section has shown that the divertor spreading factor is strongly sensitive to the target flux expansion, while remaining insensitive to most of the other scanned parameters. Part of this $f_{x,t}$ dependence can be explained by diffusive transport as, for these experiments, the target $f_{x,t}$ increases faster than the divertor parallel connection length. The $S_u \propto f_{x,t}^{-1}$ dependence implies that the spreading factor at the target and orthogonal to flux surfaces, $S_t = S_u f_x$, has a constant value of $\approx$ 6 mm, which is much larger than the spatial resolution of the infrared system ($\approx$ 2.5 mm). The divertor spreading factor at the inner target is generally lower than at the outer, and less dependent on the field direction. Potential implications of these findings for the divertor heat handling in a future fusion reactor will be discussed in section 6.4.

6.2 Snowflake Minus divertor

This section investigates the power exhaust of the Snowflake Minus (SF-) configuration, for a Ohmic, L-mode deuterium plasma, Ohmic heating power $P_\Omega \approx 250$ kW, elongation $\kappa \approx 1.56$, upper triangularity $\delta_{\text{upper}} \approx 0.12$ and a plasma current of $I_{\text{P}} \approx 240$ kA. The line-averaged electron density is $\langle n_e \rangle \approx 3 \cdot 10^{19}\ m^{-3}$, corresponding to a Greenwald fraction of $f_{\text{GW}} \approx 0.22$ so both the inner and outer divertors are in the attached, high-recycling regime. To evaluate the effect of the SF- on heat exhaust, the SF- is compared to a reference Single-Null configuration, see figures 6.23a-b-c-d. To evaluate the effect of particle drifts on heat exhaust, each of these four configurations is run with the magnetic field with both Forward Field direction (FF) and Reversed Field direction (RF). The strike points of a SF are labelled 1 to 4 starting at the highest (z) strike point on the inner wall and counting counter-clockwise.

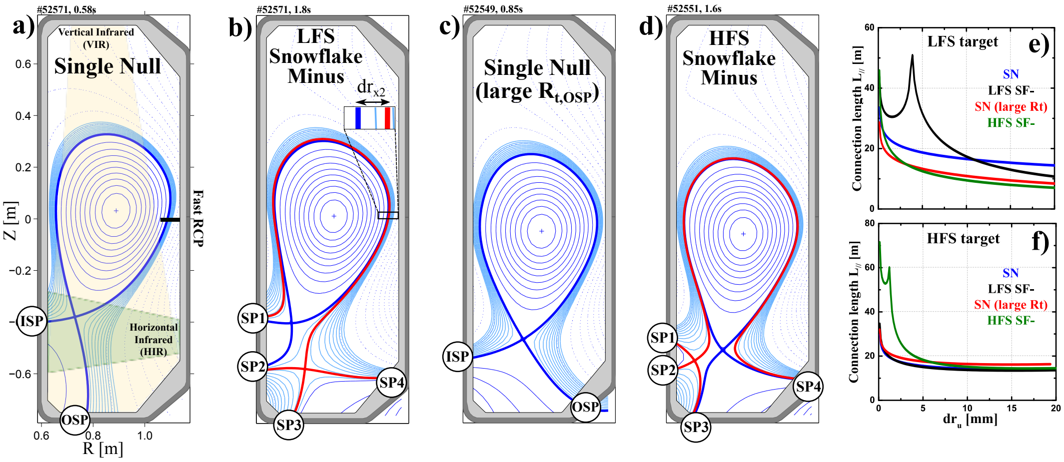

Figure 6.23 – (a-d) Some of the magnetic configurations considered in this study, with the strike point naming convention. In (a), the field-of-view for the horizontal (HIR) and vertical (VIR) infrared system is also shown, together with location and typical depth of the fast reciprocating probe (RCP). (e-f) Profiles of the parallel connection length for the inner (HFS) and outer (LFS) SOL of these configurations.

The global power balance for the discharges of this study shows that the power measured at the strike points, by the IR thermography system (section 2.2.1), and the radiated power, by tomographic inversions of bolometer measurements (section 2.2.5), together account for ≈ 75% (in FF) and ≈ 85% (in RF) of the Ohmic heating power. The deficit in the power balance is independent of the separation of the primary and secondary x-points dr_{x2} and, as a result, does not cast doubt on the analysis described below. The incomplete edge coverage by the bolometers and light reflection on the bolometer foils [64], together with charged particle losses to the main chamber walls can partly account for the missing exhaust power.

6.2.1 Geometrical properties of the Snowflake Minus

This section details the geometrical properties of the SOL in the Snowflake Minus divertor, introducing the terminology used to describe its power exhaust. As described in section 4.5.2, the Snowflake Minus features a secondary x-point, positioned in the common flux region of the primary separatrix. This x-point is associated with a secondary separatrix, shown in red in figures 6.23b and 6.23d, and has a twofold effect on the SOL field line geometry:

- The secondary x-point creates a low poloidal field region, which increases the length of magnetic field lines in the SOL. Consequently, the parallel connection length $L_{||}$ (defined by equation 4.15) in the divertor hosting the secondary x-point is strongly increased for the flux surfaces that pass close to the secondary separatrix, when compared to a similar SN configuration, figure 6.23e and 6.23f. Conversely, the parallel connection length in the other divertor is unaffected.
- The secondary x-point splits SOL magnetic field lines into two manifolds, which lead to two different targets and strike points. These are SP2 and SP4 for the LFS SF- configuration, figure 6.23b, SP1 and SP3 for the HFS SF- configuration, figure 6.23d. The manifold, delimited by primary and secondary separatrix, is here referred to as *near-SOL*, the other as *far-SOL*. The relative size of the manifolds and, therefore, the fractional sharing of SOL heat fluxes are determined by the spatial distance between the separatrices. This distance, $\mathrm{d}r_{\mathrm{x2}}$, is measured at the outboard mid-plane, as shown in figure 6.23b.

The distance $\mathrm{d}r_{\mathrm{x2}}$ controls the power distribution in the divertor hosting the secondary x-point and, for this reason, is the parameter chosen to characterise the exhaust properties of the SF-. In the TCV experiment, $\mathrm{d}r_{\mathrm{x2}}$ is scanned from ≈ 0 mm to ≈ 12 mm for the LFS SF- configuration, up to ≈ 6 mm for the HFS SF-, by moving the secondary x-point away from the primary x-point, whilst keeping the plasma shape as constant as possible, see figure 6.24. A value of $\mathrm{d}r_{\mathrm{x2}} \approx 12$ mm is relatively large since it exceeds by a factor ≈ 3 the typical SOL heat flux width at this plasma current, $\lambda_{q,u}$ between 3 and 5 mm.

Increasing $\mathrm{d}r_{\mathrm{x2}}$ changes both σ and θ, the two geometrical coordinates that are often used to characterise SF configurations, defined in section 4.5.2, see figure 6.24. A value of $\mathrm{d}r_{\mathrm{x2}}$ describes a set of configurations with a range of (σ, θ) values. Thus $\mathrm{d}r_{\mathrm{x2}} \approx 0$ does not necessarily correspond to $\sigma \approx 0$, the "exact" SF. This is demonstrated in figures 6.24a and 6.24e, where $\mathrm{d}r_{\mathrm{x2}} \approx 0$ but the x-points are well separated in space, with $\sigma \approx 0.7$ for the LFS SF- and $\sigma \approx 0.49$ for the HFS SF-.

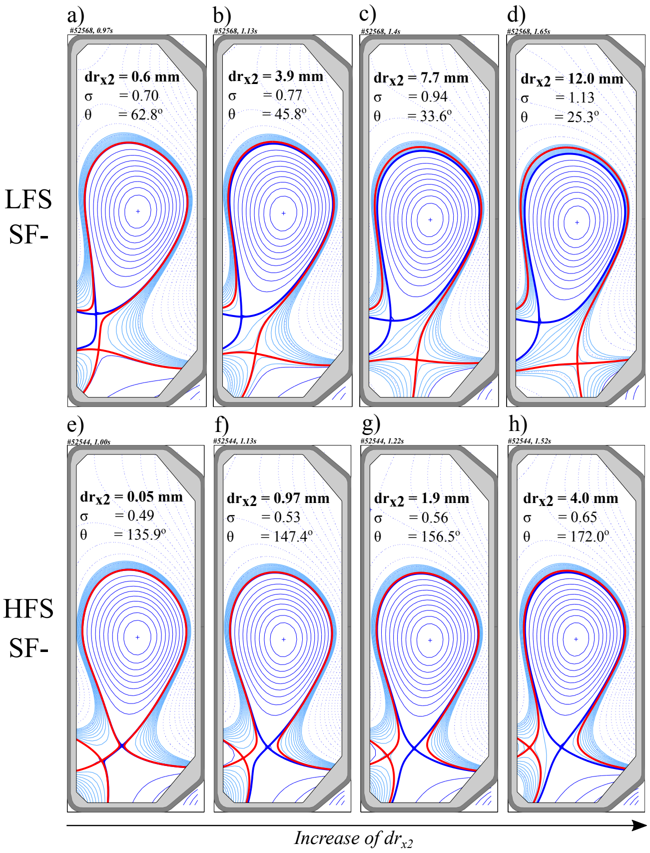

Figure 6.24 – Magnetic equilibria of the realized $\mathrm{d}r_{\mathrm{x2}}$ scan for the LFS SF- (a-d) and the HFS SF- (e-h). The geometrical coordinates (σ, θ) and the separatrix distance $\mathrm{d}r_{\mathrm{x2}}$ at the OMP are indicated.

6.2.2 Target heat flux profiles in the SF-

This section presents the target heat flux profiles of a LFS SF- configuration with $\mathrm{d}r_{\mathrm{x2}} = 3.5$ mm, figure 6.23b and those of a HFS SF- configuration with $\mathrm{d}r_{\mathrm{x2}} = 1.5$ mm, figure 6.23d. Each SF- variant is compared to a reference SN, figure 6.23a and figure 6.23c respectively. The SF- and its SN reference have comparable core shape and parallel connection length to the side of the divertor that does not contain the secondary x-point. The magnetic field is in the forward field (FF) direction.

6.2.2.1 The LFS Snowflake Minus

The target heat flux profiles in the LFS SF- configuration of figure 6.23b are shown in figure 6.25. The main differences from the heat fluxes in the reference SN configuration of figure 6.23a are discussed by strike point.

- SP1. The heat flux resembles the shape of the heat flux at the ISP of the reference

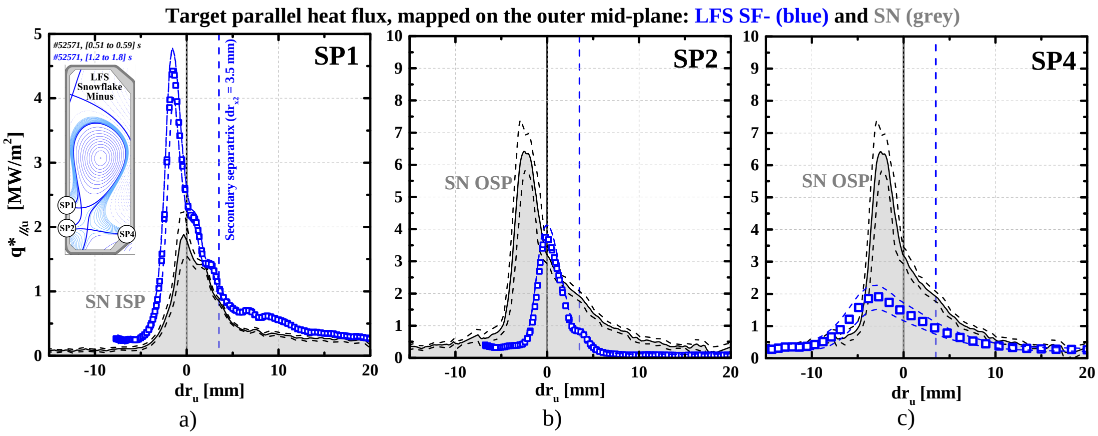

Figure 6.25 – Parallel heat flux measured by IR thermography at the active strike points of the LFS SF- of figure 6.23b (blue squares) and of the reference SN configuration (grey areas) of figure 6.23a, mapped on the outer mid-plane, for the FF direction. dr_u is the outer mid-plane distance of flux surfaces to the separatrix, obtained from the LIUQE equilibrium reconstruction. Dashed blue lines indicate the reconstructed location of the secondary separatrix. Each divertor shape is stationary for [100 to 600] ms, i.e. over many IR acquisition frames.

SN, but with greater associated power.

- SP2. The peak heat flux is lower than at the OSP of the reference SN. The heat flux profile has an approximately symmetric shape.
- SP3. No significant heat flux is detected, as expected from basic geometric considerations as SP3 is not connected by magnetic field lines to the SOL. This observation is consistent with previous observations on TCV [78].
- SP4. The heat flux resembles the shape of the heat flux at the OSP of the reference SN, but with a lower peak heat flux and a lower associated power.
- All strike points, in both the SN and SF-, show a displacement of the peak heat flux from the position of the strike point, towards the private flux region. This may be the effect of errors in the magnetic equilibrium reconstructed with the LIUQE code or of toroidal asymmetries of the magnetic configuration, caused by error fields. The hypothesis of toroidal asymmetries is supported by the relative displacement observed between the target temperature profiles measured at two different toroidal locations by the VIR and TIR systems, at the OSP of a large R_t SN divertor, section 3.3.3. These displacements, however, are not important to the analysis below, which concentrates on the shape of the heat flux profile ($\lambda_{q,u}$ and S_u).

An estimate of the SOL width $\lambda_{q,u}$ and the divertor spreading factor S_u of the LFS SF- is obtained by parametrizing the heat flux profile at SP4 with the same fit function as that used for the SN, where the fit parameter x_0 (see section 5.1.1) now represents a shift of the secondary separatrix position (not of the primary) resulting from uncertainties in the equilibrium reconstruction. Compared to the SN, the LFS SF- SOL width is slightly broader with a divertor spreading factor ≈ 3.5 times larger,

$$\begin{aligned} \lambda_{q,u}^{\mathrm{SP4}} &= (4.6 \pm 0.6)\ \mathrm{mm} & \qquad \lambda_{q,u}^{\mathrm{OSP}} &= (3.8 \pm 0.2)\ \mathrm{mm} \\ S_u^{\mathrm{SP4}} &= (3.2 \pm 0.7)\ \mathrm{mm} & \qquad S_u^{\mathrm{OSP}} &= (0.9 \pm 0.1)\ \mathrm{mm} \end{aligned}$$

6.2.2.2 The HFS Snowflake Minus

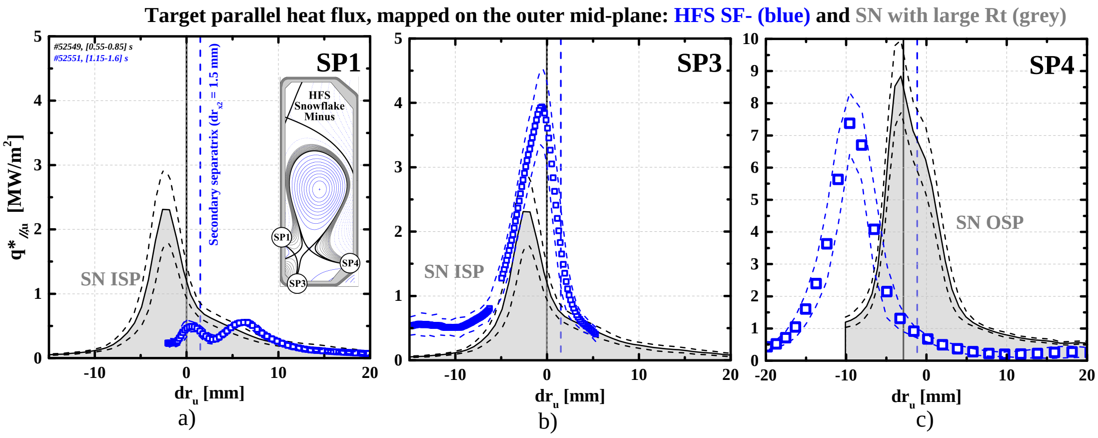

Figure 6.26 – Parallel heat flux measured by IR thermography at the active strike points of the HFS SF- configurations of figure 6.23d (blue squares) and of the reference SN (grey areas) of figure 6.23c, mapped on the outer mid-plane, for the FF direction. dr_u is the outer mid-plane distance of flux surfaces to the separatrix, obtained from the LIUQE equilibrium reconstruction. Dashed blue lines indicate the reconstructed location of the secondary separatrix. Each divertor shape is stationary for [100 to 600] ms, i.e. over many IR acquisition frames.

The target heat flux profiles in the HFS SF- configuration of figure 6.23d are shown in figure 6.26. The main differences from the heat fluxes in the reference SN configuration of figure 6.23c are discussed by strike point.

- SP1. The heat flux profile is hollow ≈ 4 mm from the nominal position of the strike point, here defined by the secondary separatrix, that maps to ≈ 1.6 cm above SP1 at the target. The hollow feature was previously observed on TCV using target Langmuir Probes [78], and may be the effect of ion ∇B, curvature B and $\vec{E} \times \vec{B}$ drifts in the inner SOL [44, 54].
- SP2. No significant heat flux is detected, as expected from basic geometric considerations as SP3 is not connected by magnetic field lines to the SOL. This observation is consistent with previous observations on TCV [78].
- SP3. The heat flux is larger than that at the ISP of the reference SN and has an approximately symmetric shape.

- SP4. The heat flux resembles the heat flux at the OSP of the reference SN, with a similar peak value, with the peak shifted from the expected position of the primary separatrix towards the private flux region.
- All the strike points, in both the SN and SF-, show some displacement of the peak heat flux from the computed strike point position, towards the private flux region. As discussed for the LFS SF- divertor, this displacement could be the effect of errors in the magnetic equilibrium reconstruction or of toroidal asymmetries of the magnetic configuration, due to error fields. These displacements, however, are not important to the analysis below, which concentrates on the shape of the heat flux profile ($\lambda_{q,u}$ and S_u).

The SOL width $\lambda_{q,u}$ and the divertor spreading factor S_u of the LFS SF- is obtained by parametrising the heat flux profile at SP4 with the same fit function as that used for the SN. The hollow feature precludes such an analysis for SP1. Compared to the SN, the SOL width is narrower but the divertor spreading factor is quite similar,

$$\lambda_{q,u}^{\mathrm{SP4}} = (1.6 \pm 0.3)\ \mathrm{mm} \qquad \lambda_{q,u}^{\mathrm{OSP}} = (2.8 \pm 0.7)\ \mathrm{mm}$$
$$S_{u}^{\mathrm{SP4}} = (3.2 \pm 0.4)\ \mathrm{mm} \qquad S_{u}^{\mathrm{OSP}} = (2.8 \pm 0.8)\ \mathrm{mm}$$

6.2.3 In-out divertor power sharing

This section presents the observed variation of the power sharing between inner and outer divertor when increasing the separatrix parameter $\mathrm{d}r_{\mathrm{x2}}$ in the SF- divertor. Then, these observations are interpreted in terms of the conductive power sharing model described in section 5.1.2.2.

6.2.3.1 The LFS Snowflake Minus

With increasing $\mathrm{d}r_{\mathrm{x2}}$, the total power reaching the outer divertor, i.e. $P_{\mathrm{SP2}} + P_{\mathrm{SP4}}$, decreases, figures 6.27b-c, whereas the power reaching the inner divertor, i.e. P_{SP1}, increases by, to within uncertainties, the same amount, figure 6.27a. These dependences are observed for forward and reversed magnetic field direction. Consequently, increasing $\mathrm{d}r_{\mathrm{x2}}$ augments the ratio $P_{\mathrm{in}}/P_{\mathrm{out}}$ in both field directions, figure 6.27d. Note that any power to the unconnected SP3 remains negligible. As the Ohmic heating power and radiated fraction remain largely independent of $\mathrm{d}r_{\mathrm{x2}}$, this is a direct change in the power sharing between divertors. Also, the increased P_{SP1} for larger $\mathrm{d}r_{\mathrm{x2}}$ confirms, qualitatively, predictions from fluid calculations that assumed constant cross-field transport coefficients [42].

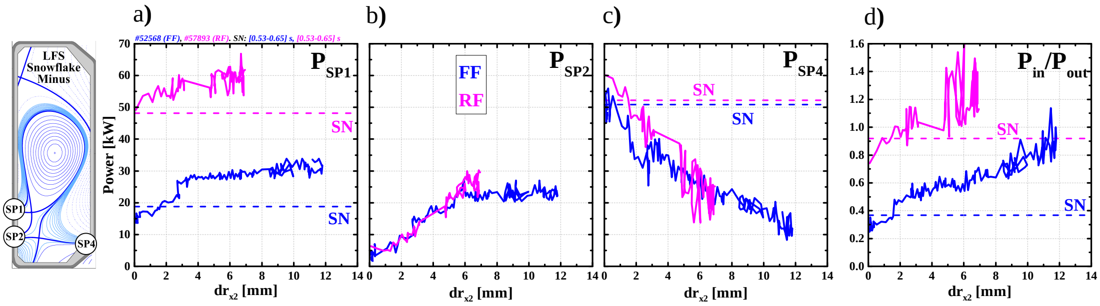

Figure 6.27 – Power measured at the active strike points of the TCV LFS Snowflake Minus configuration, by Infrared thermography, for forward (blue) and reversed (magenta) field direction, as a function of the separatrix distance dr_{x2} at the OMP (a-b-c), and in-out SOL power ratio $P_{\mathrm{in}}/P_{\mathrm{out}} = P_{\mathrm{SP1}}/(P_{\mathrm{SP2}} + P_{\mathrm{SP4}})$ (d). The values for the reference SN of figure 6.23a are also shown.

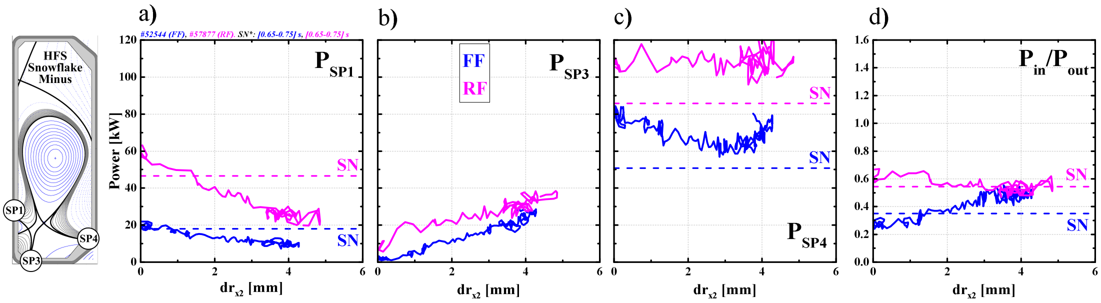

Figure 6.28 – Power measured at the active strike points of the TCV HFS Snowflake Minus configuration, by Infrared thermography, for forward (blue) and reversed (magenta) field direction, as a function of the separatrix distance dr_{x2} at the OMP (a-b-c), and in-out SOL power ratio $P_{\mathrm{in}}/P_{\mathrm{out}} = (P_{\mathrm{SP1}} + P_{\mathrm{SP3}})/P_{\mathrm{SP4}}$ (d). The values for the reference SN of figure 6.23c are also shown.

Effect of field reversal Changing the magnetic field direction from RF to FF appears to create an offset in P_{SP1}, figure 6.27a. The same power variation is observed at the ISP of the SN configuration and can be partially explained by higher radiative losses in the inner divertor, figure 6.29.

6.2.3.2 The HFS Snowflake Minus

With increasing dr_{x2}, the power reaching the outer divertor P_{SP4}, figure 6.28c, shows a weak to negligible dependence on dr_{x2} compared to the P_{SP1} of the LFS SF-, figure 6.27a. The total power reaching the inner divertor, i.e. $P_{\mathrm{SP1}} + P_{\mathrm{SP3}}$, is also largely unchanged. Consequently, the ratio $P_{\mathrm{in}}/P_{\mathrm{out}}$ depends much less on dr_{x2} than for the LFS SF-, figure 6.28d. Note that the power to the unconnected SP2 remains negligible.

Effect of field reversal Changing the magnetic field direction from RF to FF results in an offset of P_{SP1}, figure 6.28a, similarly to that observed for the LFS SF- and for the

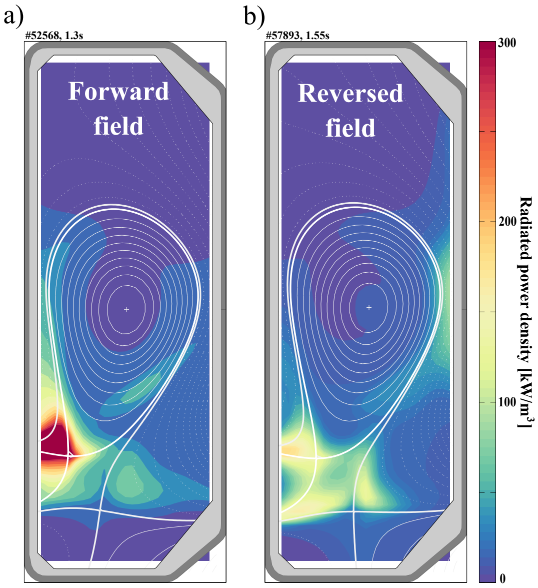

Figure 6.29 – Radiated power density in TCV poloidal plane, from bolometric inversion, of a LFS SF- configuration in FF (a) and (b) RF conditions. The total radiated power is ≈ 102 kW in FF, ≈ 84 kW in RF, with $P_\Omega \approx 250$ kW for both.

SN, which is consistent with increased radiative losses in proximity of SP1. In contrast to the LFS SF-, reversing the magnetic field direction introduces an offset also of P_{SP4}, figure 6.28d.

6.2.3.3 Interpretation using conductive model of SOL

The power sharing model discussed in section 5.1.2.2 is here used to interpret the experimentally observed variation of $P_{\mathrm{in}}/P_{\mathrm{out}}$ when increasing the distance $\mathrm{d}r_{\mathrm{x2}}$ between x-points [79, 80]. The value of $\lambda_{q,u}$ used in the model is 4 mm, which is a typical value for the SOL width at this plasma current (240 kA).

- For the forward field direction, figures 6.30b-e, the power sharing model cannot explain the variation of $P_{\mathrm{in}}/P_{\mathrm{out}}$. In the LFS SF-, figure 6.30b, increasing $\mathrm{d}r_{\mathrm{x2}}$ from 0 to 12 mm increases $P_{\mathrm{in}}/P_{\mathrm{out}}$ from 0.3 to 0.9, whereas the modelled value decreases from 2.1 to 1.5. In the HFS SF-, figure 6.30e, increasing $\mathrm{d}r_{\mathrm{x2}}$ from 0 to 4 mm increases $P_{\mathrm{in}}/P_{\mathrm{out}}$ from 0.25 to 0.5, whereas the modelled value decreases from 0.9 to 0.6.
- For the reversed field direction, figures 6.30c-f, the power sharing model qualitatively reproduces the observed variation of $P_{\mathrm{in}}/P_{\mathrm{out}}$ when increasing $\mathrm{d}r_{\mathrm{x2}}$. In the LFS SF-, figure 6.30c, increasing $\mathrm{d}r_{\mathrm{x2}}$ from 0 to 7 mm increases $P_{\mathrm{in}}/P_{\mathrm{out}}$ from 0.7 to 1.4 (from 1.4 to 1.6 in the model). In the HFS SF-, figure 6.30f, increasing $\mathrm{d}r_{\mathrm{x2}}$ from 0 to 5 mm decreases both the measured and modelled $P_{\mathrm{in}}/P_{\mathrm{out}}$ from 0.7 to 0.55.

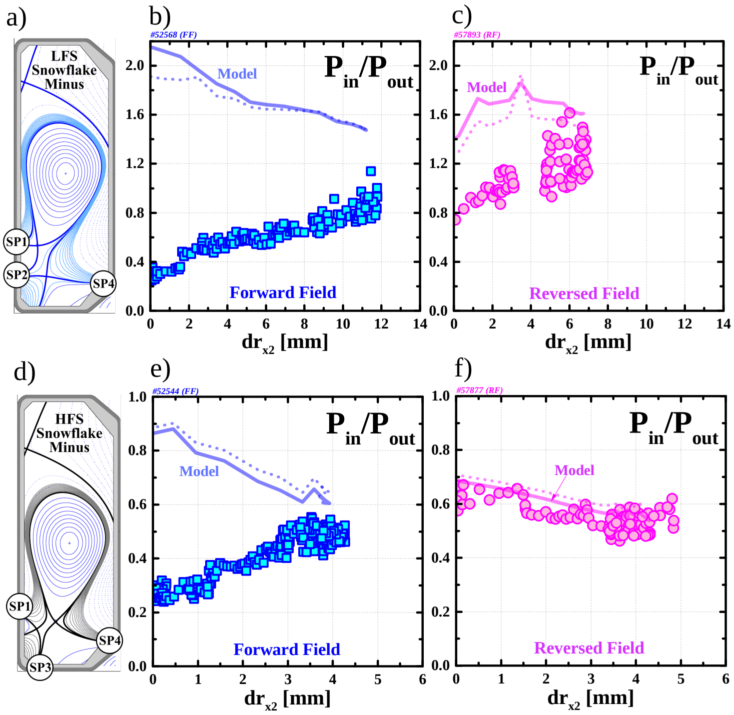

Figure 6.30 – Measured inner/outer divertor power ratio, for the LFS SF- (a-c) and HFS SF- (d-f) configurations, in forward field (blue squares) and reversed field (purple circles) conditions, compared to the predictions from the model for $\lambda_{q,u} = 4$ mm (continuous line) and $\lambda_{q,u} = 6$ mm (dashed line).

A sensitivity study shows that the power sharing predictions are insensitive to the assumed value of $\lambda_{q,u}$, compare dashed ($\lambda_{q,u} = 6$ mm) and continuous lines ($\lambda_{q,u} = 4$ mm) in figure 6.30.

The disagreement between model and data for the forward field direction clearly indicates that the analytical model is missing physics that in the SF- divertor dominate over heat conduction for this field direction. As for the Single Null configurations, discussed in section 6.1.1.2, it is hypothesized that this could be the combined effect of asymmetric divertor radiation and poloidal $\vec{E} \times \vec{B}$ classical drifts [31, 65], which may be stronger in the SF configuration [44].

6.2.4 Power splitting at the secondary x-point

This section focuses on the repartition of SOL power fluxes between the two strike points created by the secondary x-point. As expected from geometrical arguments, increasing dr_{x2} increases the power to the near-SOL strike point (SP2 in the LFS SF-, SP3 in the HFS SF-) while decreasing the power to the far-SOL strike point (SP4 in the LFS SF-, SP1 in the HFS SF-), see figures 6.27 and 6.28. However, contrarily to expectations, a significant power arrives at SP4 of the LFS SF- configuration when $dr_{x2} \approx 12$ mm, figure

Shape	Field	$P_{\text{in}}/P_{\text{out}}$ explained by conductive model	Remarks
LFS SF-	FF	no	Opposite trend
LFS SF-	RF	yes	Small offset w.r.t. model
HFS SF-	FF	no	Opposite trend
HFS SF-	RF	yes	-

Table 6.5 – Qualitative assessment of the conductive model ability to reproduce the observed variation of $P_{\text{in}}/P_{\text{out}}$ with x-point distance $\text{d}r_{\text{x2}}$. The model prediction agrees with data for the RF direction only.

6.27c. As this $\text{d}r_{\text{x2}}$ exceeds the SOL heat flux width $\lambda_{q,u} \approx 4$ mm by a factor ≈ 3, the SOL should be entirely enclosed between primary and secondary separatrix, and the power measured at SP4 negligible.

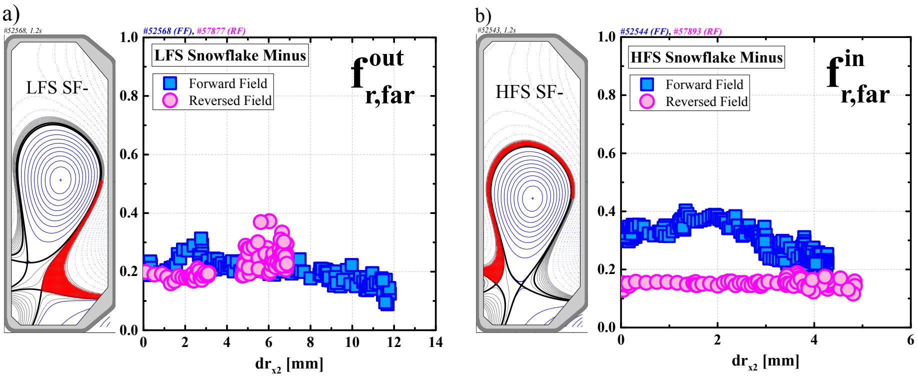

Figure 6.31 – Fraction of SOL power which is radiated in far-SOL manifold created by the secondary x-point for the LFS SF- (a) and HFS SF- (b) configuration, in FF (squares) and RF (circles) conditions.

The power arriving at SP4 when $\text{d}r_{\text{x2}} \approx 12$ mm could result from changed transport properties in the intra-null SOL of the LFS SF-, relative to the rest of the SOL. For instance, radial transport in the intra-null SOL may be comparable to the poloidal projection of parallel transport. To quantitatively characterize this result, the power splitting model discussed in section 5.1.5 is considered. Here, the power deposited by the far-SOL flux tubes at the divertor target is parameterised as (equation 5.48)

$$P^{\wedge}_{\text{far}} = P^{\wedge *}_{\text{far}} \cdot e^{-\text{d}r_{\text{x2}}/\lambda^{\text{eff},\wedge}_{q,u}} \tag{6.15}$$

where $P^{\wedge *}_{\text{far}} = (1 - f^{\wedge}_{r,\text{far}})\ c^{\wedge}_{\text{div,far}}\ P_{\text{SOL}}$, with $f^{\wedge}_{r,\text{far}}$ the radiated power fraction and $c^{\wedge}_{\text{div,far}}$ the power sharing factor. This corresponds to the power arriving to SP4 for the LFS SF- ($\wedge = out$), to SP1 for the HFS SF- ($\wedge = in$). For this experiment, the pre-factor $P^{\wedge *}_{\text{far}}$ is fairly independent of $\text{d}r_{\text{x2}}$, since both $f^{\wedge}_{r,\text{far}}$ and $c^{\wedge}_{\text{div,far}}$ do not correlate with $\text{d}r_{\text{x2}}$, as discussed in the following.

- The radiated fraction $f^{\wedge}_{r,\mathrm{far}}$ does not change with $\mathrm{d}r_{\mathrm{x2}}$. To estimate $f^{\wedge}_{r,\mathrm{far}}$, the radiated power in the far-SOL, $P^{\wedge}_{r,\mathrm{far}}$, is computed by integrating the radiated power density from bolometric inversion over the far-SOL volume, see figure 6.31. Then, $f^{\wedge}_{r,\mathrm{far}}$ is computed, for increasing $\mathrm{d}r_{\mathrm{x2}}$, as

  $$f^{\wedge}_{r,\mathrm{far}} = \begin{cases} f^{\mathrm{out}}_{r,\mathrm{far}} = P^{\mathrm{out}}_{r,\mathrm{far}}/(P^{\mathrm{out}}_{r,\mathrm{far}} + P_{\mathrm{SP4}}) & \text{for the LFS SF-} \\ f^{\mathrm{in}}_{r,\mathrm{far}} = P^{\mathrm{in}}_{r,\mathrm{far}}/(P^{\mathrm{in}}_{r,\mathrm{far}} + P_{\mathrm{SP1}}) & \text{for the HFS SF-} \end{cases}$$

  The results show, figure 6.31, that $f^{\wedge}_{r,\mathrm{far}}$ is relatively small and, most importantly, is independent of $\mathrm{d}r_{\mathrm{x2}}$, which is consistent with the low plasma densities of these experiments.

- The power sharing ratio $c^{\wedge}_{\mathrm{div,far}}$ does not change with $\mathrm{d}r_{\mathrm{x2}}$, under the hypothesis that changes of power sharing between divertors are due to changes of the flux tube geometry, in particular of their length as proposed in [54] and discussed in section 6.1.1.2 (for the SN) and 6.2.3.3 (for the SF-). In the $\mathrm{d}r_{\mathrm{x2}}$ scan, the far-SOL flux tube lengths do not change (little to no effect of the secondary null), and, thereby, the in-out power sharing of each flux tube would be expected to remain independent of $\mathrm{d}r_{\mathrm{x2}}$.

For this experiment, therefore, $P^{\wedge}_{\mathrm{far}} \propto e^{-\mathrm{d}r_{\mathrm{x2}}/\lambda^{\mathrm{eff},\wedge}_{q,u}}$. Fitting with equation 6.15 the measured variation of P_{SP4} with $\mathrm{d}r_{\mathrm{x2}}$ in the LFS SF- yields a value for $\lambda^{\mathrm{eff,out}}_{q,u}$, section 6.2.4.1. Similarly, fitting with equation 6.15 the measured variation of P_{SP1} with $\mathrm{d}r_{\mathrm{x2}}$ in the HFS SF- yields a value for $\lambda^{\mathrm{eff,in}}_{q,u}$, section 6.2.4.2. Some physical interpretations for the unexpectedly high value of $\lambda^{\mathrm{eff,out}}_{q,u}$ in the LFS SF- divertor are discussed in section 6.2.4.3.

6.2.4.1 Effective SOL width for the LFS SF-

In the LFS SF-, the variation of P_{SP4} with $\mathrm{d}r_{\mathrm{x2}}$ is consistent with an effective SOL width of

$$\boxed{\lambda^{\mathrm{eff,out}}_{q,u} = (9 \pm 2)\ \mathrm{mm} \quad \text{LFS SF- (FF and RF)}} \tag{6.16}$$

that is independent of the magnetic field direction, figure 6.32a. This is two times larger than that measured by IR thermography at the OSP of the reference SN,

$$\lambda^{\mathrm{OSP}}_{q,u} = \begin{cases} (3.8 \pm 0.2)\ \mathrm{mm} & \mathrm{FF} \\ (3.8 \pm 0.7)\ \mathrm{mm} & \mathrm{RF} \end{cases} \tag{6.17}$$

The large difference between $\lambda^{\mathrm{eff,out}}_{q,u}$ and $\lambda^{\mathrm{OSP}}_{q,u}$ is indicative of changed transport properties, with respect to SN, at the outer mid-plane and/or in the divertor, i.e. an increase of the

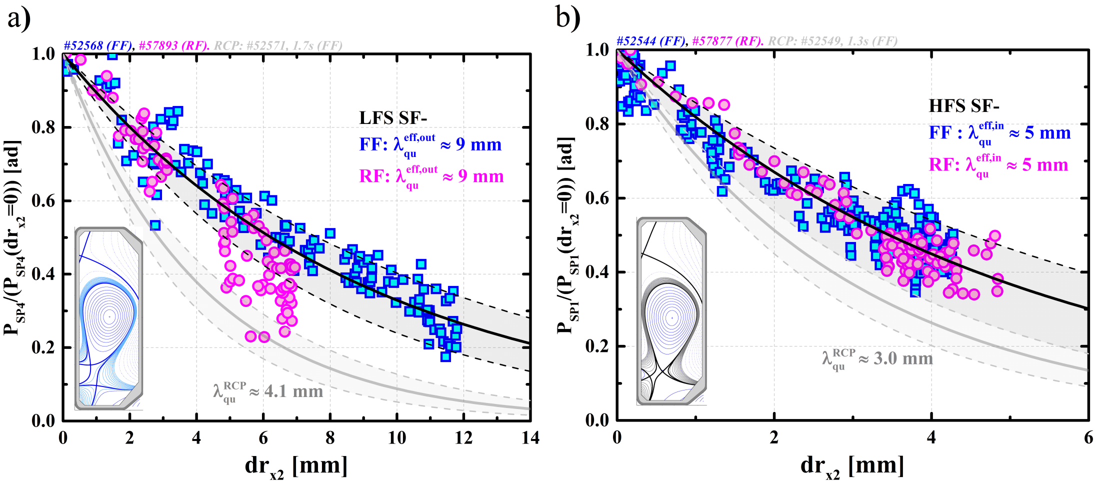

Figure 6.32 – (a) In the LFS SF- configuration, SOL power which is measured at SP4 for increasing distance between the two x-point $\mathrm{d}r_{\mathrm{x2}}$, normalized to the value for $\mathrm{d}r_{\mathrm{x2}} = 0$. (b) In the HFS SF- configuration, SOL power which is measured at SP1 for increasing $\mathrm{d}r_{\mathrm{x2}}$, normalized to the value for $\mathrm{d}r_{\mathrm{x2}} = 0$. Blue squares and purple circles refer to FF and RF respectively. An effective width for the SOL near the secondary null is inferred.

effective cross-field diffusivity $\chi_\perp^u$ and/or $\chi_\perp^{\mathrm{null}}$, according to the scheme of figure 5.5. The transport at the outer mid-plane is investigated with the fast reciprocating probe. The SOL profiles of the LFS SF- are very similar to the SN case with only a small increase in the temperature for the SF- [81], figure 6.33. There is no evidence, thus, for a $\chi_\perp^u$ variation here,

$$\chi_\perp^u(\mathrm{SN}) \approx \chi_\perp^u(\mathrm{LFS\ SF-}) \tag{6.18}$$

Consistently, the SOL width at the outboard mid-plane of the SF-, inferred from the temperature profile,

$$\lambda_{q,u}^{\mathrm{RCP}}(\mathrm{SF-}) = \begin{cases} (4.1 \pm 0.7)\ \mathrm{mm} & \mathrm{FF} \\ (4.3 \pm 0.6)\ \mathrm{mm} & \mathrm{RF} \end{cases} \tag{6.19}$$

grey curve in figure 6.32a, agrees with the target measurement for the SN. The RCP prediction is calculated by assuming a SOL parallel heat transport dominated by electron heat conduction, yielding the simple relation $\lambda_{q,u}^{\mathrm{RCP}} = 2/7 \cdot \lambda_{T,u}$, where $\lambda_{T,u}$ is the decay length of the upstream electron temperature in the SOL, which is measured by the RCP.

As the experiment shows no effect of the secondary null on the upstream transport, the broad $\lambda_{q,u}^{\mathrm{eff,out}}$ is ascribed to an augmented cross-field transport in the outer divertor. This requires that

$$\chi_\perp^{\mathrm{null}}(\mathrm{LFS\ SF-}) \gg \chi_\perp^u \tag{6.20}$$

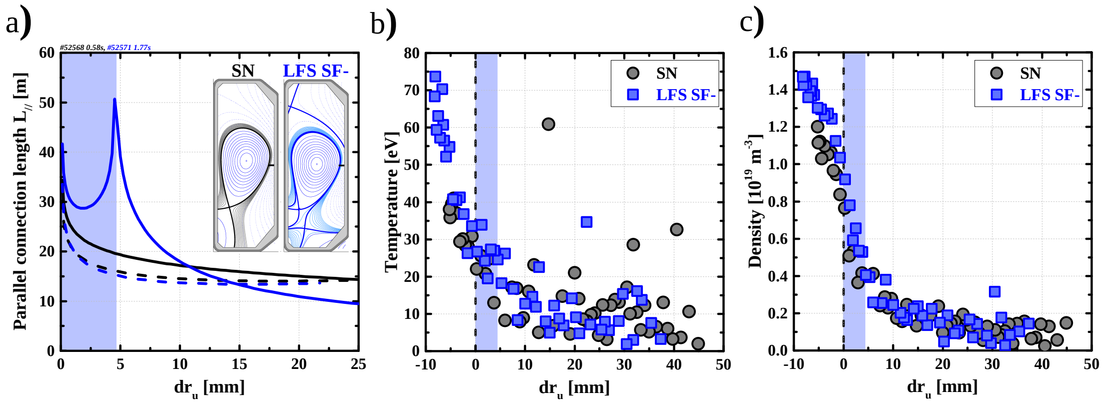

Figure 6.33 – For the SN and LFS SF- configurations: (a) parallel connection length to LFS target (continuous line) and HFS target (dashed line); (b) temperature at outer mid-plane and (c) density at outer mid-plane from the fast reciprocating probe. The shaded area indicates the fraction of SOL enclosed by the primary and secondary separatrices.

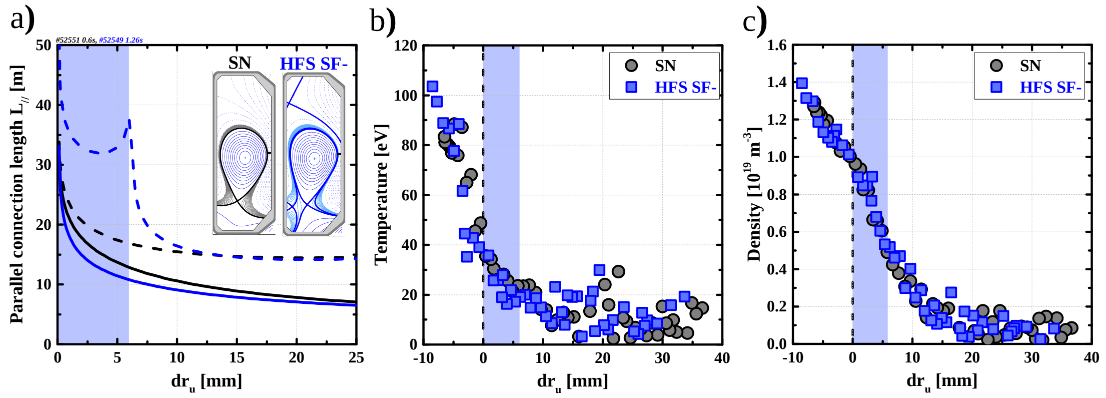

Figure 6.34 – For the SN and HFS SF- configurations: (a) parallel connection length to LFS target (continuous line) and HFS target (dashed line); (b) temperature at outer mid-plane and (c) density at outer mid-plane from the fast reciprocating probe. The shaded area indicates the fraction of SOL enclosed by the primary and secondary separatrices.

i.e. the effective cross-field diffusivity in the null region must be higher than its value in the rest of the SOL, figure 5.5. Since the SOL width measured at SP4 by IR, $\lambda_{q,u}^{\mathrm{SP4}} = (4.6 \pm 0.6)$ mm, matches, within uncertainties, that measured at the outer mid-plane by the RCP, the $\chi_\perp$ enhancement is concluded to be limited to the null region, see figure 5.5.

6.2.4.2 Effective SOL width for the HFS SF-

In the HFS SF-, the variation of P_{SP1} with $\mathrm{d}r_{\mathrm{x2}}$ is consistent with an effective SOL width of

$$\boxed{\lambda_{q,u}^{\mathrm{eff,in}} = (5.0 \pm 1.5)\ \mathrm{mm} \quad \text{HFS SF- (FF and RF)}} \tag{6.21}$$

and is also independent of the magnetic field direction, figure 6.32b. This is unchanged, within uncertainties, from the value measured by the IR thermography at the ISP of the reference SN,

$$\lambda_{q,u}^{\mathrm{ISP}} = \begin{cases} (4.7 \pm 1.1)\ \mathrm{mm} & \mathrm{FF} \\ (3.6 \pm 0.7)\ \mathrm{mm} & \mathrm{RF} \end{cases} \tag{6.22}$$

This suggests that the cross-field transport upstream and in the divertor are not significantly influenced by the secondary null.

The transport upstream is again investigated with the RCP. The SOL profiles at the outer mid-plane are similar for the HFS SF- and its reference SN, figure 6.34. There is thus, again, no evidence for a $\chi_\perp^u$ change,

$$\chi_\perp^u(\mathrm{SN}) \approx \chi_\perp^u(\mathrm{HFS\ SF-}) \tag{6.23}$$

Finally, the SOL width inferred from the RCP temperature profile for the HFS SF-configuration,

$$\lambda_{q,u}^{\mathrm{RCP}}(\mathrm{SF-}) = (3.0 \pm 0.5)\ \mathrm{mm} \quad \mathrm{FF} \tag{6.24}$$

grey curve in figure 6.32b, is again compatible with $\lambda_{q,u}^{\mathrm{eff,in}}$ within uncertainties. This supports the view that transport in the null-region is unaffected by the secondary null,

$$\chi_\perp^{\mathrm{null}}(\mathrm{HFS\ SF-}) \approx \chi_\perp^u \tag{6.25}$$

In conclusion, the HFS SF- does not show the signs of enhanced transport observed for the LFS SF-.

It should be noted that these results are valid for the explored range of $\mathrm{d}r_{\mathrm{x2}}$. When $\mathrm{d}r_{\mathrm{x2}} \to \infty$, the magnetic configuration becomes a SN and it is reasonable to expect that $\lambda_{q,u}^{\mathrm{eff}}$ recovers the $\lambda_{q,u}$ of the SN.

6.2.4.3 Discussion: enhanced transport between nulls

In this section some physical mechanisms that could explain the increased cross-field transport between the two nulls of the LSF SF- divertor are introduced.

Plasma convection near the primary x-point could explain the observed broadening of the SOL heat flux channel in the low poloidal field region of the LFS SF-. Several candidate modes (i.e. instabilities) that could cause the convection have been proposed [43, 41, 82]. Here, the role of the *churning-like mode* and the ballooning mode is discussed. The onset

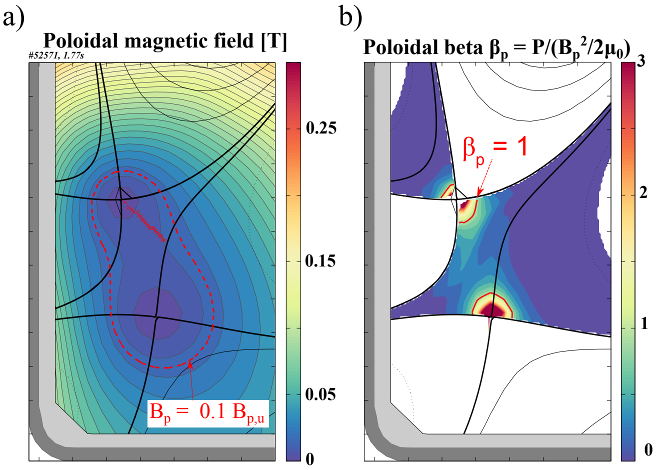

Figure 6.35 – (a) Poloidal magnetic field in the intra-null region of the LFS SF- configuration, from magnetic reconstruction. The dashed red line shows the extent of the low poloidal field region $B_p \leq 0.1\ B_{p,u}$. (b) Poloidal beta in the SOL, computed with the pressure measured by the RCP at the outer mid-plane.

of these modes requires large values of the poloidal beta

$$\beta_p = P/(B_p^2/(2\mu_0)) > 1 \tag{6.26}$$

where P is the plasma pressure and B_p the poloidal field. The onset of these modes depends also on the orientation of the pressure gradient. A vertical pressure gradient maximizes the driving terms of the churning-like mode, while a radial pressure gradient maximizes the driving terms of the ballooning mode.

For a LFS SF- configuration, with relatively small x-point separation in flux surface space ($\mathrm{d}r_{\mathrm{x2}} = 3.5$ mm) but relatively large in real space ($\sigma \approx 0.83$), β_p in the SOL is estimated by using the poloidal field from the magnetic reconstruction, figure 6.35a, and the pressure measured at the outer mid-plane by the RCP (pressure is, as usual, taken to be conserved along field lines). As shown in figure 6.35b, β_p is highest near the two nulls, where the poloidal field vanishes, while it is approximately halved in the intra-null volume. The role of the churning-like mode and the ballooning mode is discussed in the following.

- **Churning-like mode**. In the $\beta_p > 1$ area near the primary x-point, plasma convection could be sustained by a churning-like mode as ∇P is vertical. However, its extent (mapped upstream) would only be

  $$r_u^* \approx 1.1 \text{ mm} \tag{6.27}$$

  which is considerably narrower than the SOL width measured at the outer mid-plane by the RCP $\lambda_{q,u}^{\mathrm{RCP}} \approx 4$ mm. Consequently, any pressure-driven convection near the primary x-point would be expected to be too localized to cause the observed enhanced cross-field transport. Said otherwise, for the SF- configurations of this study, the physical distance between the two x-points is too large to access the high-β_p (low-B_p) effects which are predicted for the exact SF.

- **Interchange ballooning-like turbulence**. The increased diffusivity in the low B_p region of the LFS SF- could be the effect of interchange ballooning-like turbulence. Perpendicular turbulent transport in the outer divertor leg of the SN configuration, being stronger towards the common rather than private flux region, was proposed [69, 54] to explain the increase of $\lambda_{q,u}^{\text{OSP}}$ with increasing outer divertor leg length, presented in section 6.1.2. This idea was also supported by turbulent simulations [69].
  Interchange ballooning-like turbulence, in regions of 'bad curvature', that is locally enhanced by the low poloidal magnetic field between the nulls, is compatible with the data. Such a mechanism would be more effective with the secondary x-point placed in the LFS rather than the HFS SOL, where the magnetic flux surfaces are vertically aligned so the SOL pressure gradient and the magnetic field gradient are in the same direction, maximising the drive terms for several instabilities. This would be compatible with the observations that $\chi_\perp^{\text{null}} \gg \chi_\perp^u$ for the LFS SF- (section 6.2.4.1), while $\chi_\perp^{\text{null}} \approx \chi_\perp^u$ for the HFS SF- (section 6.2.4.2).
  Interestingly, the postulated presence of significant ballooning-like turbulence in the null region of the LFS SF-, but not in that of the HFS SF-, was recently found in GBS [73] simulations of the SF- [83].

6.2.5 Discussion: exhaust performance of the LFS SF-

In this section the power exhaust performance of the LFS SF- configuration is discussed, using, as figure-of-merit, the target peak parallel heat flux $q_{\parallel,t}^{\text{peak}}$. The $q_{\parallel,t}^{\text{peak}}$ is a crucial quantity for power exhaust as, for a fixed grazing angle of magnetic field lines on the target, $q_{\parallel,t}^{\text{peak}} \propto q_{\perp,t}^{\text{peak}}$ (see equation 4.25), where $q_{\perp,t}^{\text{peak}}$ is limited by the heat removal capability of the divertor target.

Considering the outer divertor, the LFS SF- configuration strongly reduces target parallel heat fluxes compared to the SN case, figure 6.36b, for the entire explored range of $\mathrm{d}r_{\text{x2}}$. Increasing $\mathrm{d}r_{\text{x2}}$ reduces its value at SP4 and increases that at SP2, but both remain at least two-times smaller (< 6 MW/m^2) than $q_{\parallel,t}^{\text{peak}}$ at the outer strike point of the reference SN (≈ 12 MW/m^2). Interestingly, the $q_{\parallel,t}^{\text{peak}}$ at SP4 is smaller than at the OSP of the reference SN already for $\mathrm{d}r_{\text{x2}} \approx 0$, when primary and secondary separatrices coincide, SP2 is not active and the low peak value cannot be ascribed to the SOL splitting at the secondary x-point,

$$q_{\parallel,t}^{\text{peak}}(\text{SP4}, \mathrm{d}r_{\text{x2}} = 0)/q_{\parallel,t}^{\text{peak}}(\text{OSP}) \approx 0.38 \tag{6.28}$$

To obtain some physical interpretation, this ratio is computed using the analytic expression for $q_{\parallel,t}^{\text{peak}}$, equation 5.7. This procedure allows a separation of the contributions from the different parameters (changed target radius, power sharing, $\lambda_{q,u}$ and S_u),

$$\frac{q_{\parallel,t}^{\text{peak}}(\text{SP4}, \text{d}r_{\text{x2}} = 0)}{q_{\parallel,t}^{\text{peak}}(\text{OSP})} = \underbrace{\frac{R_t^{\text{OSP}}}{R_t^{\text{SP4}}}}_{0.71} \cdot \underbrace{\frac{c_{\text{div}}^{\text{SP4}}}{c_{\text{div}}^{\text{OSP}}}}_{1.07} \cdot \underbrace{\frac{\lambda_{q,u}^{\text{OSP}} + 1.64\ S_u^{\text{OSP}}}{\lambda_{q,u}^{\text{SP4}} + 1.64\ S_u^{\text{SP4}}}}_{0.53} \approx 0.4$$

Most of the peak reduction ($\approx 50\%$) is the effect of the increased S_u ($S_u^{\text{SP4}}/S_u^{\text{OSP}} \approx 3.5$, see section 6.2.2.1), the increased target radius accounts for a further $\approx 30\%$.

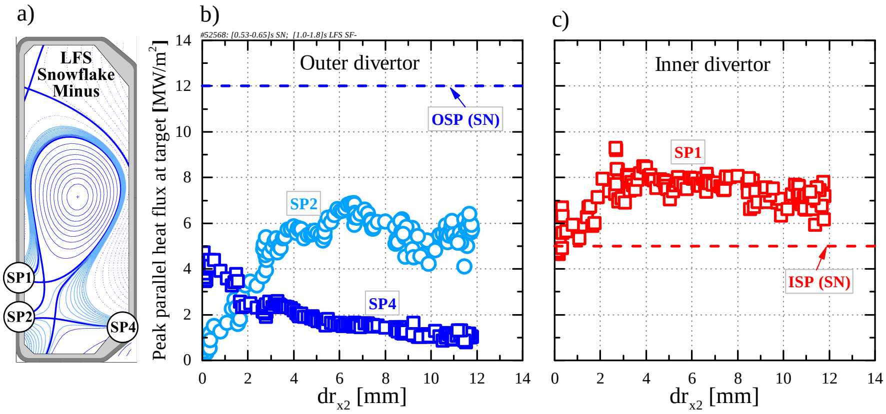

Figure 6.36 – For the LFS SF- configuration in FF conditions (a), peak parallel heat flux at SP2 and SP4 (b) and at SP1 (c) as a function of dr_{x2}. The values for the ISP and OSP of the reference SN, shown in figure 6.23a, are also indicated.

Considering the inner divertor, however, the LFS SF- configuration increases by $\approx 60\%$ the target parallel heat fluxes compared to the SN divertor, figure 6.36c. This results from the changed in-out power sharing, see figure 6.27a, with a larger dr_{x2} causing power to be redistributed from the outer to the inner divertor. A LFS SF-, thereby, complicates the heat handling at the inner divertor compared to the SN.

The enhanced cross-field diffusivity in the low B_p region between the two nulls, section 6.2.4.1, has an additional beneficial effect on the outer divertor power exhaust as it reduces the peak heat flux at SP2, thus increasing the wetted area.

Conclusion of section 6.2

In conclusion, this section presented a unique and thorough study of the power exhaust properties of the alternative SF- configuration, with the plasma in L-mode and the divertors attached/high-recycling. The in-out power sharing varies with the x-point distance dr_{x2}. As summarized in table 6.5, this variation can be explained by electron conduction for the RF direction, while for the FF direction another physical mechanism dominates (e.g. particle drifts). The impact of the secondary x-point on upstream and divertor transport has been assessed. The secondary x-point has no effect on upstream transport, for both LFS and HFS SF-, whereas it enhances cross-field transport in the divertor of the LFS SF-. Such an enhancement in-between the x-points is supported by recent turbulent simulations. Finally, this section demonstrates that, compared to the SN, the LFS SF- reduces peak heat loads at the outer divertor targets, as predicted by fluid calculations [42, 57], but increases the peak heat loads at the inner divertor due to a change in the in-out power sharing.

6.3 Approaching the detached regime

The previous sections investigated the power exhaust of the Single-Null (section 6.1) and Snowflake Minus (section 6.2) configurations, with L-mode plasma and divertors in the attached, high-recycling regime. This section studies the power exhaust of the Single-Null configuration, with L-mode plasma, during the transition from attached to detached divertor regime. The transition is provoked either by seeding nitrogen in the divertor or by strongly increasing the divertor fueling rate. Detachment experiments on TCV are normally performed with the magnetic field in the reversed direction (RF) because it features a higher power threshold value for transition to the high-confinement mode (H-mode, discussed in the next chapter). This section focuses on the shape of target heat flux profiles during the transition to the detached state, i.e. on the heat wetted area A_{wet}, the SOL width $\lambda_{q,u}$ and spreading factor S_u. The analysis shows that the effect of impurity seeding on the heat wetted area is significantly different from that of increasing the core density.

Scan	Field	I_{P} [kA]	L_{div} [cm]	$f_{x,t}^{\text{out}}$	δ_{upper}	R_t [m]	$f_{x,t}^{\text{in}}$	f_{GW}	$\langle n_e \rangle$ $[10^{19} m^{-3}]$
N_2	RF	340	39	4.0	0.32	0.74	3.6	0.41	9
$\langle n_e \rangle$	RF	340	39	6.3	0.32	0.75	3.9	$[0.24, 0.74]$	$[5, 15]$

Table 6.6 – Overview of relevant divertor and plasma parameters, for the nitrogen seeding and divertor fueling experiments.

The detached regime The detached regime is a state achieved at very high SOL plasma collisionality, when the plasma temperature at the target $T_{e,t}$ has dropped below a few eV. In these conditions, friction between recycling neutrals and SOL ions and volume recombination (when $T_{e,t} \leq 1$ eV) become important physical processes compared to ionization, and cause a reduction of SOL pressure and particle flux at the divertor plate. Cooling the divertor to detachment temperatures is achieved either by seeding a low-Z impurity (nitrogen) in the divertor or by strongly increasing the divertor fueling rate. The impurity radiates in the SOL, increasing the SOL radiated power fraction f_{rad} and, thus, reducing the target temperature $T_{e,t} \propto (1 - f_{\text{rad}})^2$ (equation 5.49). The effect of fueling on $T_{e,t}$ is threefold. First, fueling increases the upstream SOL density $n_{e,u}$, which drives down target temperature as $T_{e,t} \propto n_{e,u}^{-2}$ (equation 5.49). Second, fueling can enhance the SOL radiated power fraction, further cooling the plasma as $T_{e,t} \propto (1 - f_{\text{rad}})^2$ (equation 5.49). Third, fueling can change the power entering the SOL upstream P_{SOL}, and, thus, the SOL parallel heat flux upstream $q_{\parallel,u}$, affecting $T_{e,t}$ as $T_{e,t} \propto (q_{\parallel,u})^{10/7}$ (equation 5.49). Fueling, indeed, raises the core plasma density, which results in both increased Ohmic heating power P_Ω and core radiation $P_{\text{rad,core}}$. Whether the net result is a reduction or an increase in $P_{\text{SOL}} = P_\Omega - P_{\text{rad,core}}$ is not immediately clear. For the TCV fueling experiments discussed in this section, fueling increased P_{SOL}.

6.3.1 Effect of nitrogen seeding

The effect of N_2 seeding on target heat flux profiles is investigated in a standard Single-Null configuration, with $I_\mathrm{P} = 340$ kA, $f_{x,t}^{\mathrm{out}} = 4.0$ and in the RF direction. The plasma density is $\langle n_e \rangle = 9 \cdot 10^{19} m^{-3}$, corresponding to $f_\mathrm{GW} = 41\%$, which is slightly below the density value at the onset of outer divertor detachment for this plasma current (from previous TCV experiments [59] and described in the next section 6.3.2). The N_2 is seeded from valve # 3, positioned on the TCV floor at R = 0.646 m i.e. in the private flux region, see figure 6.38d. The injected flux Γ_{N2} commences at 0.8s and is increased linearly in time up to the plasma disruption that occurs at a seeding rate of $\Gamma_{\mathrm{N2}} = 5 \cdot 10^{20}$ molecules/s, figure 6.37a.

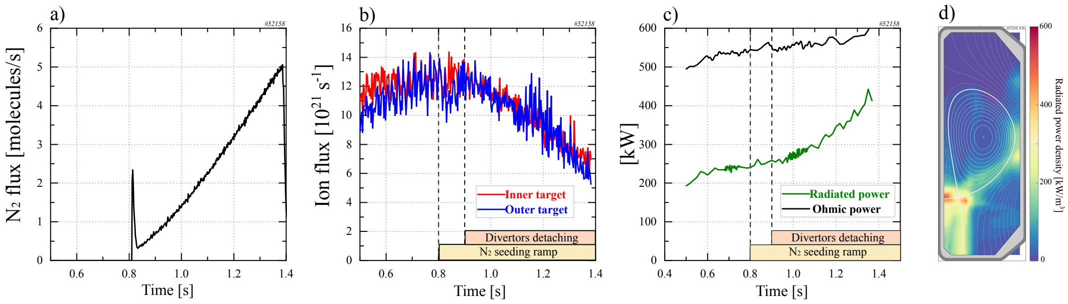

Figure 6.37 – Nitrogen molecule flux (a), ion flux to the divertor targets (b), Ohmic and radiated powers (c), as a function of time during a N_2 injection rate ramp. (d) Poloidal distribution of the radiated power density, at the onset of detachment, shows strong radiation near the x-point and inner target.

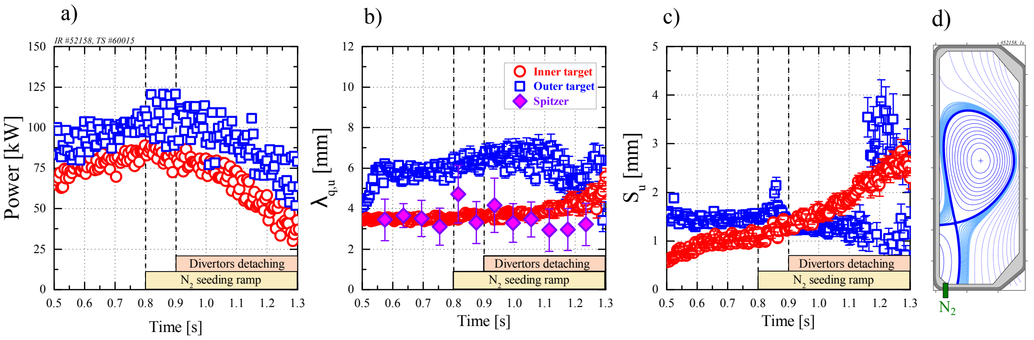

Figure 6.38 – Deposited power (a), SOL width $\lambda_{q,u}$ (b) and divertor spreading factor S_u (c) for the inner (red circles) and outer (blue squares) divertors, as a function of time during a N_2 injection rate ramp. As indicated, the N_2 injection ramp starts at 0.8 s, and both divertors start detaching (ion flux roll-over) at 0.9 s. The upstream SOL temperature profile, from Thomson scattering, is fitted with an exponential in the range dr_u = [0,2] cm, for time dwells of 50 ms, to infer the evolution of $\lambda_{q,u}$. The SN equilibrium and poloidal location of the seeding gas valve are shown in (d).

Shortly after the start of N_2 injection, at t = 0.9 s, the ion flux to the inner and outer targets rolls over, figure 6.37b, which is a signature of the onset of divertor detachment for both divertors [59]. At both divertor targets, the deposited power drops as N_2 is injected, figure 6.38a. This is caused by the increase in radiated power, observed by bolometers, with the Ohmic input power remaining near constant $P_\Omega \approx 550$ kW, figure 6.37c.

For both targets, the heat flux profile shape after the onset of detachment is similar to that in the attached phase, so that a value for $\lambda_{q,u}$ and S_u can be estimated with $R^2 > 0.85$. The target wetted area, however, evolves differently on the inner and outer divertor:

- At the outer target, the heat wetted area is unaffected by the N_2 seeding and the divertor detachment occurs with both $\lambda_{q,u}$ and S_u remaining approximately constant in time, figures 6.38b-c.
- At the inner target, in contrast, the heat wetted area increases with N_2 seeding as S_u steadily rises, figure 6.38c, while $\lambda_{q,u}$ remains constant, figure 6.38b. The increase of S_u appears to be, in particular, independent of the onset of detachment.

After $\approx$ 1.2s, fitting of the heat flux profiles at the outer target becomes unstable, with S_u alternating between 1 and 3 mm, figure 6.38c.

Two possible interpretations for the steady increase of S_u at the inner target are discussed:

- According to the diffusive model of section 5.1.4, the increase of S_u may result from strong radiative cooling of the x-point, as $S_u \propto T_{\mathrm{e,X}}^{-5/4}$, see equation 5.45. This hypothesis is supported by the strong radiation increase observed at the x-point, figure 6.37d, which is stronger during the seeding ramp. However, such an interpretation would also predict an increase of S_u at the outer divertor, which is not seen.
- The increase in S_u may occur as detachment (significant reduction of heat flux and pressure along field lines, between OMP and target) first starts at the strike point and then progresses towards the far-SOL [84]. Such a localised effect would reduce the peak of the target heat flux profile, leading to an increase of S_u. However, as both divertors detach at approximately the same time, figure 6.37, this picture would also predict an increase of S_u at the outer divertor, contrary to the experiment.

6.3.2 Effect of divertor fueling

The effect of divertor fueling on target heat flux profiles is investigated in a standard Single-Null configuration, with $I_{\mathrm{P}} = 340$ kA, $f_{x,t}^{\mathrm{out}} = 6.3$, in the RF direction, without impurity seeding. The fueling valve (#1) is located on the TCV floor at R = 0.880 m i.e. in the common flux region of the outer divertor, see figure 6.40d.

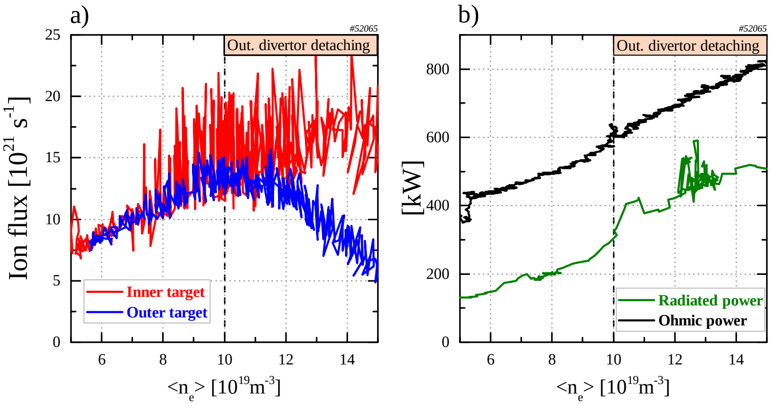

Figure 6.39 – Ion flux to the divertor targets (a), Ohmic and radiated powers (b) as a function of the line-averaged electron density. The roll-over of the ion flux at the outer divertor plate, at $\langle n_e \rangle = 10^{20}$ m^{-3}, is taken as the onset of divertor detachment for the outer divertor [59]. The inner divertor remains attached.

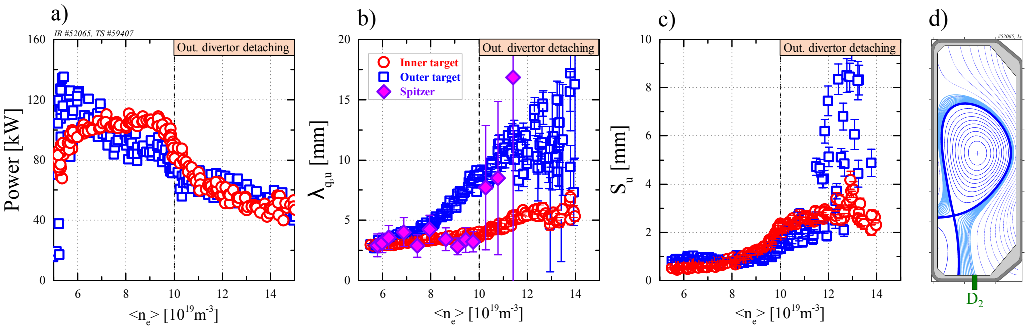

Figure 6.40 – Deposited power (a), SOL width $\lambda_{q,u}$ (b) and divertor spreading factor S_u (c) for the inner (red circles) and outer (blue squares) divertors, as a function of the line-averaged electron density. As indicated, the outer divertor starts detaching (ion flux roll-over) at $\langle n_e \rangle = 10^{20}$ m^{-3}, corresponding to $f_{\mathrm{GW}} = 0.46$ and t = 0.95 s (The density ramp starts at t = 0.55 s). The upstream SOL temperature profile, from Thomson scattering, is fitted with an exponential in the range dr_u =[0,2] cm, for time dwells of 50 ms, to infer a value of $\lambda_{q,u}$. The SN equilibrium and used gas valve are shown in (d).

At $\langle n_e \rangle = 10^{20}$ m^{-3}, corresponding to $f_{\mathrm{GW}} = 0.46$, the ion flux to the outer target rolls over, figure 6.39a, signature of the onset of divertor detachment. Before the onset of detachment, increasing $\langle n_e \rangle$ did not change the power to the inner target, while it did decrease the power to the outer target, figure 6.40a. After the detachment onset, a further increase of $\langle n_e \rangle$ decreases the power at both targets. These measurements correlate well with an increase in the radiated power observed by bolometers, figure 6.39b.

For both targets, the heat flux profile shape after the onset of detachment remains similar to that in the attached phase, so that a value for $\lambda_{q,u}$ and S_u can be extracted with $R^2 > 0.85$. The evolution of the target wetted area, however, is different for inner and outer divertors:

- At the outer target, for increasing $\langle n_e \rangle$, $\lambda_{q,u}$ and S_u increase, figures 6.40b-c. This trend continues after the onset of divertor detachment.
- At the inner target, for increasing $\langle n_e \rangle$, both $\lambda_{q,u}$ and S_u increase, figures 6.40b-c. The increase of $\lambda_{q,u}$ occurs at a much slower rate than for the outer target. At the onset of detachment for the outer plate, the rise of both $\lambda_{q,u}$ and S_u accelerates.

Coupling of inner-outer divertors The sharp change of behaviour of the inner target quantities (power, $\lambda_{q,u}$ and S_u) at the onset of detachment at the outer target (the inner target remains attached) clearly suggests a connection between inner and outer divertors. Particle $\vec{E} \times \vec{B}$ drifts are a candidate mechanism. In RF conditions, $\vec{E} \times \vec{B}$ drifts in the private flux region transport plasma from the inner to the outer divertor [65]. At the onset of detachment, parallel temperature gradients in the outer divertor leg reduce. As discussed in [85], this may reduce the plasma potential in the common SOL right below the x-point that, in turn, reduces the $\vec{E} \times \vec{B}$ poloidal flow. The density at the inner plate will then rise, leading to more radiated power, less deposited power at ISP and a lower target temperature. This picture can qualitatively describe the observed reduction of power at ISP, figure 6.40a, and the rise of S_u which, in the framework of the diffusive model discussed in section 5.1.4, depends inversely on the SOL temperature.

Poloidal asymmetries of the SOL width Before the onset of detachment, the $\lambda_{q,u}$ at the outer target increases with higher $\langle n_e \rangle$, although $\lambda_{q,u}$ upstream is steady, figure 6.40b. This shows that fueling the outer divertor broadens the SOL heat flux channel in the outer divertor volume only, i.e. between x-point and target. The effect is localised in the outer divertor leg since the value of $\lambda_{q,u}$ at the inner plate matches the value upstream, figure 6.40b. After the onset of detachment, however, the upstream $\lambda_{q,u}$ quickly increases, since the SOL temperature profile flattens, and becomes comparable to the value measured at the outer target. This may suggest that the SOL region broadened by the fueling now extends above the x-point, affecting the main SOL.

Conclusion of section 6.3

In conclusion, when seeding nitrogen, both targets detach simultaneously, the deposited power on both targets decreases in a similar way but the wetted area increases solely at the inner target. The increase of the wetted area implies that the peak heat flux drops faster than the total deposited power. Compared to nitrogen seeding, divertor detachment through fueling ramps has a stronger effect on the heat wetted area at the target. The increase of A_{wet} is primarily from an increased $\lambda_{q,u}$, in the outer divertor SOL, leaving the main SOL and inner divertor SOL unaffected. The increased wetted area is beneficial for heat exhaust, since it reduces the threshold density for detachment $n_{e,u}^{\mathrm{det}} \propto A_{\mathrm{wet}}^{-5/7}$, equation 5.53.

6.4 Summary and potential implications for DEMO

This chapter presented an extensive and systematic study of the impact of divertor geometry variations on divertor power exhaust for the Single-Null (section 6.1) and Snowflake Minus (section 6.2) configurations, for plasmas in L-mode and the divertor regime attached (high-recycling). The evolution of target heat loads when transitioning from the attached to the detached divertor regime was analysed, for a fixed Single-Null shape, in section 6.3.

The quantities used to describe the power exhaust are the in-out power sharing ratio $P_{\mathrm{in}}/P_{\mathrm{out}}$, the SOL power width $\lambda_{q,u}$ and the spreading factor S_u. Several interesting, and in large parts unexpected, dependences of these quantities on divertor geometry characteristics were observed:

- **Divertor power sharing**. The power sharing is sensitive to variations of the divertor geometry, in particular to changes of the parallel connection length (through a longer leg length L_{div} or higher target flux expansion $f_{x,t}$). An increased $L_{\parallel}$ to one divertor target (e.g. outer) is found to redistribute exhaust power to the other (e.g. inner). Such a power redistribution can be explained by conduction physics, as a longer $L_{\parallel}$ decreases the parallel temperature gradient (along field lines in the SOL), which, in turn, decreases the heat flux that can be conducted to the plate.
- **SOL power width**. In the SN, this is sensitive to divertor leg length and the plasma upper triangularity, with a longer leg, or a more positive triangularity, leading to an increased $\lambda_{q,u}$. Although the effect on $\lambda_{q,u}$ of L_{div} and δ_{upper} is similar, the dependence on L_{div} is interpreted as a broadening of the SOL in the divertor leg by asymmetric turbulence, while the dependence on δ_{upper} reflects a broadening of the SOL around the plasma, ascribed to increased edge/SOL turbulence levels. In the LFS SF-, the SOL power width increases in the region between the nulls, which is postulated to be the result of strong interchange ballooning-like turbulence in the region of bad curvature. Recent simulations of the SF- with the GBS code support this interpretation.

  These experiments show that the $\lambda_{q,u}$ at the divertor targets is partially a divertor quantity, in contrast to the classical interpretation of $\lambda_{q,u}$ as a pure, main SOL, quantity [45]. The contribution to $\lambda_{q,u}$ by divertor transport can be explained by asymmetric interchange ballooning-like turbulence in both the leg length scan and the LFS SF- experiment.

- **Spreading factor**. In the SN, this scales with the inverse of the target flux expansion, while remaining insensitive to the other varied divertor geometry properties. In the framework of classical parallel diffusivity, most of this dependence is explained by the fact that increasing $f_{x,t}$ increases the parallel connection length in the divertor at a lower pace that $f_{x,t}$.

As regards the study of the transition from attached to detached divertor regime, it is found that approaching detachment with divertor fueling ramps increases the target wetted area A_{wet} more strongly than with nitrogen seeding ramps. The increased A_{wet} with gas fueling is due to an increase in $\lambda_{q,u}$, in the divertor leg, with the SOL around the plasma affected only after the onset of detachment. This is a further indication that $\lambda_{q,u}$ at the divertor target is in part a divertor quantity.

These observations are a unique input for testing models that are required to improve the current understanding of SOL physics and, thus, extrapolate to the divertor of a future nuclear fusion reactor, such as DEMO. Among these observations, there are some crucial divertor geometry effects that may have significant implications in the choice of the magnetic divertor for a reactor:

1. **Divertor geometry affects in-out power sharing.** The analysis of section 6.1.1 shows that divertor geometry can have a large effect on the in-out power distribution. This can, in large part, be explained by a model based on parallel electron heat conduction. This model can be used to predict the divertor power sharing of DEMO-sized conventional and advanced magnetic configurations, figure 6.41. Compared to a SN, figure 6.41a, the advanced configurations, figures 6.41b-c-d, have a higher $P_{\mathrm{in}}/P_{\mathrm{out}}$, i.e. higher P_{in} and lower P_{out}, as a result of an increased parallel connection length to the outer divertor target. This shows that a power exhaust solution at the outer divertor achieved via modifications of the magnetic configuration may come at the expense of harming the inner divertor. For instance, passing from the SN, figure 6.41a, to the X-Divertor, figure 6.41d, reduces the fraction of exhaust power to the outer divertor from $\approx 66\%$ to $\approx 52\%$ but increases that to the inner divertor from $\approx 34\%$ to $\approx 48\%$.
2. **Long-legged divertor increases $\boldsymbol{\lambda_{q,u}}$ and decreases $\boldsymbol{P_{\mathrm{out}}}$.** The measured increase in $\lambda_{q,u}$ at the outer divertor target of a SN for increasing divertor leg length, if experimentally observed for H-mode plasmas too, would imply that a long-legged divertor for a future fusion device would be highly beneficial in terms of power exhaust, since a broader SOL reduces target peak heat fluxes (equation 5.7) and facilitates access to divertor detachment through a broadened wetted area (equation 5.53). Additionally, since a longer L_{div} is observed to increase the power at the inner divertor P_{in} and decrease the power at the outer divertor P_{out}, the divertor leg length may be tuned to balance the heat exhaust between the two divertor plates. Although a long-legged divertor may be a step towards a solution

of the power exhaust issue, it would concomitantly reduce the volume of the vessel available for the confined burning plasma, reducing the fusion power, and would augment power loading at the inner plate, due to the changed in-out power sharing.

3. **Small-$f_{x,t}$ divertor broadens S_u.** The measured broadening of S_u at the outer divertor target of a SN for decreasing target flux expansion, $S_u \propto f_{x,t}^{-1}$, if also observed for H-mode plasmas, would imply that, for a future fusion device, a divertor with low $f_{x,t}$ appears, quite counter-intuitively, as an advantageous choice since it increases the target wetted area $A_{\mathrm{wet}} \propto \lambda_{\mathrm{int},u} \propto S_u$ (at fixed field line grazing angle at the target, equation 4.44), reducing target peak heat fluxes (equation 5.7) and facilitating access to divertor detachment (equation 5.53). Note that the same grazing angle can be realized for different values of $f_{x,t}$ by poloidally tilting the divertor plate, equation 4.24.

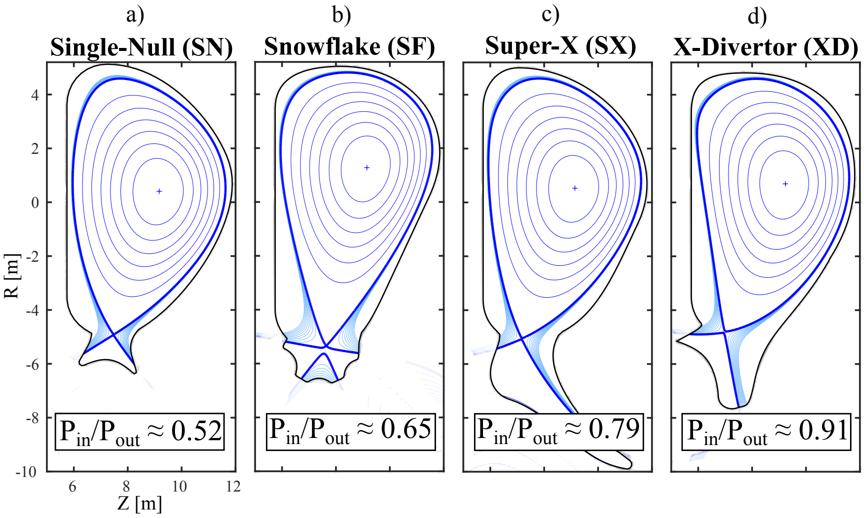

Figure 6.41 – In-out power sharing predicted by the conductive model of section 5.1.2, for some DEMO-sized conventional and advanced magnetic configurations [86], with $\lambda_{q,u}$ = 1 mm and I_{P} = 20.25 MA.

7 Power exhaust of H-mode plasmas in TCV

This chapter presents a general study of the power exhaust properties of TCV plasmas in the high-confinement mode (H-mode). This improved plasma confinement mode, characterised by higher core temperature and density than the L-mode, is observed when the total power deposited in the plasma is raised above a threshold. At the L-H transition, i.e. the transition from L-mode to H-mode, the energy confinement time τ_E of the tokamak plasma, which represents the e-folding relaxation time of the plasma energy, approximately doubles. This improvement is caused by an *edge transport barrier*, which develops at the plasma edge, creating steep gradients of density and temperature near the separatrix [87]. This edge region of strong gradients is also referred to as the *plasma pedestal*. This work distinguishes between two variants of H-mode operation:

- **ELMy H-mode operation.** Here, localised edge instabilities are periodically excited in the plasma, termed Edge-Localised-Modes (ELMs). ELMs can be driven by edge plasma current or pressure gradients, and release energy and hot plasma particles in the SOL. A fraction of the hot plasma particles that are released by the ELM may directly hit the vessel wall, but the majority flow along SOL open field lines to the divertor plates, where they significantly increase the heat load and, thus, their surface temperature. In future fusion reactors, ELM divertor heat loads are predicted to pose a serious threat to the lifetime of the plasma facing components. One usually distinguishes three ELM regimes [31]:
  - Type III ELMs. In this mode of operation there is an almost continuous excitation of ELMs, and the pedestal pressure saturates at a relatively low level. The ELM frequency decreases with higher heating power. These ELMs each eject typically only a few percent of the main plasma stored energy.
  - Type II ELMs. In this mode of operation, bursts of ELMs are clearly separated in time and are of higher amplitude, so that the pedestal pressure reaches higher levels.
  - Type I ELMs. Here, bursts of ELM are larger in amplitude and narrower

in time than for Type II ELMs. The pedestal pressure saturates at a level similar to that of the Type II ELMs case, but the larger-amplitude ELMs result in higher pulsed heat loads on the divertor targets. The ELM frequency increases with higher heating power. These ELMs can each eject up to 10-15% of the main plasma stored energy.

- **ELM-free H-mode operation.** Here, the main plasma conditions are not stationary as there is an uncontrolled (which on TCV is often linear in time) rise of core and edge density. The density rise encounters a disruptive limit at a density well below the Greenwald density [3]. This ELM-free H-mode operation is, therefore, not a reactor-relevant scenario but it can be used in present day machines to investigate aspects of SOL transport and power exhaust physics with H-mode like pedestal profiles[1].

In section 7.1, the study investigates the effect of the transition from L- to ELM-free H-mode on target heat loads, in a standard Single-Null configuration. This is then extended to ELMy H-mode plasmas, discussing separately target heat loads in-between ELMs, section 7.2, and during the ELM event, section 7.3. The analysed TCV database includes both standard and innovative divertor shapes, such as an X-Divertor (figure 4.6c).

H-mode	Field	I_{P} [kA]	L_{div} [cm]	$f_{x,t}^{\mathrm{out}}$	δ_{upper}	R_t [m]	$f_{x,t}^{\mathrm{in}}$	f_{GW}	$\langle n_e \rangle$ [$10^{19}m^{-3}$]
ELM-free	FF	320	35	2.9	0.11	0.76	3.1	$[0.40, 0.76]$	$[8.3, 17.0]$
ELMy	FF	$[170, 380]$	$[21, 65]$	$[2, 9]$	0.15	0.75	$[3, 6]$	$[0.25, 0.43]$	$[4.0, 6.2]$

Table 7.1 – Overview of relevant divertor and plasma parameters, for the H-mode experiments. For the ELM-free scenario, the density variation is obtained within the same plasma shot. For the ELMy scenario, in contrast, the variations in the divertor and plasma parameters are obtained from shot to shot.

7.1 ELM-free (non-stationary) power exhaust

This section investigates the changes in SOL power exhaust at the plasma transition from L- to ELM-free H-mode. These changes are inferred from the variations in the shape of target heat flux profiles, measured by Infrared thermography (section 2.2.1), and of the edge plasma temperature profiles, measured by Thomson scattering (section 2.2.4). The magnetic configuration is a standard Single-Null, with $I_{\mathrm{P}} = 320$ kA, $L_{\mathrm{div}} =$ 35 cm and target flux expansion of $f_{x,t}^{\mathrm{in}} = 3.1$ and $f_{x,t}^{\mathrm{out}} = 2.9$.

The transition of the plasma from L- to ELM-free H-mode is induced by injecting 200 kW of Neutral Beam power, figure 7.1c. The time of the transition, t $\approx$ 1.2 s, is identified by a sharp drop of D_α intensity, figure 7.1b, and an initial rise in the plasma line-averaged

---

[1] Although there are several ELM-free H-mode scenarios, this thesis only considers that featuring an uncontrolled rise of core and edge density.

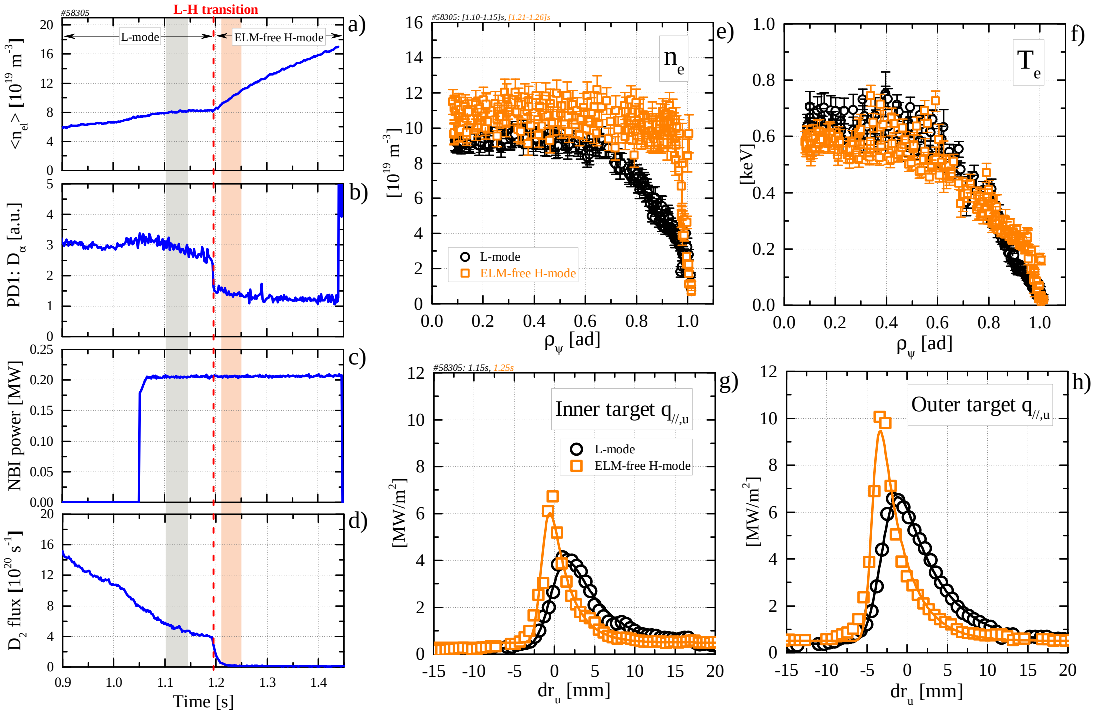

Figure 7.1 – Time evolution of plasma line-averaged density (a), D_α line intensity (b), neutral beam power (c) and D_2 flux (d). Plasma density (e) and temperature (f) profiles, from Thomson scattering, before (black circles, from black-shaded time interval in fig. (a-d)) and after (orange squares, from orange-shaded time interval in fig. (a-d)) the L-H transition, showing a profile steepening in the edge region ($\rho_\psi > 0.9$). Parallel heat flux profile measured at the inner (g) and outer (h) divertor plate, before (black circles) and after (orange squares) the L-H transition, superimposed with the corresponding Eich-fits (continuous line).

density, 7.1a. At the plasma transition to ELM-free H-mode, the feedback gas valve stops deuterium injection, figure 7.1d. This indicates that recycling from the chamber walls is sufficient to fuel the plasma.

At the transition from L- to ELM-free H-mode, plasma density and temperature profiles in the edge region steepen, figures 7.1e-f, reflecting the existence of an edge transport barrier. Simultaneously, target heat flux profiles become narrower, figures 7.1g-h, suggesting a change in the balance between parallel and perpendicular heat transport in the SOL. The following sections investigate the SOL heat exhaust before and after the L-H transition in more detail, using, similarly to the L-mode study (chapter 6), the in-out power sharing ratio $P_{\text{in}}/P_{\text{out}}$, the SOL width $\lambda_{q,u}$ and the spreading factor S_u, with $\lambda_{q,u}$ and S_u inferred from fitting the target heat flux profiles with the function discussed in section 5.1.1.

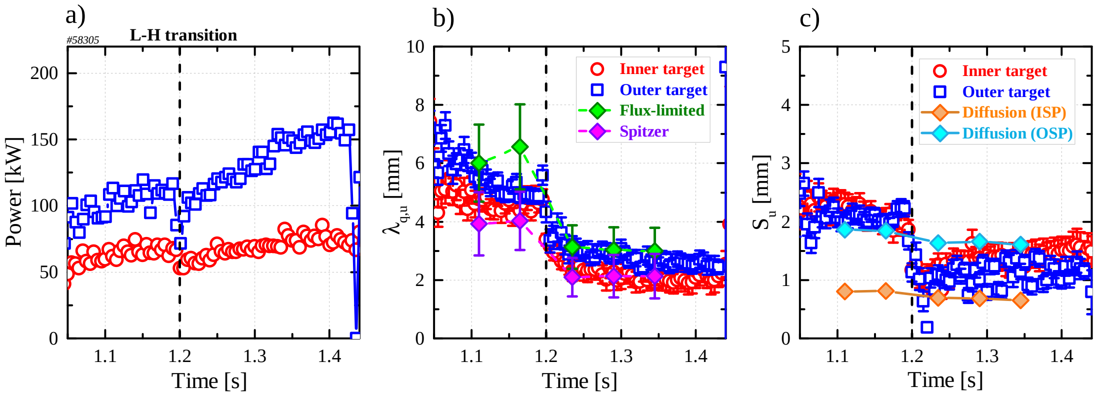

Figure 7.2 – Time evolution of deposited power (a), SOL width $\lambda_{q,u}$ (b) and spreading factor S_u (c), around the transition from L-mode to ELM-free H-mode. In (b), the SOL width values inferred using the upstream edge temperature profile, under the flux-limited or the conduction-limited (Spitzer) approximation, are shown. In (c), the S_u computed with the diffusive model of section 5.1.4 is shown. The density and temperature profiles are fitted in the edge region ($0.95 \leq \rho_\psi \leq 1.05$), for time dwells of 50 ms. The model prediction for S_u uses $f_T = 0.15$ for the OSP, while $f_T = 0$ for the ISP as the $T_{e,t}$ measurements were not available for the inner plate.

7.1.1 In-out divertor power sharing

At the transition from L- to ELM-free H-mode, the integrated power to the targets initially drops, before recovering the L-mode value, figure 7.2a. This transient reflects an increase in the plasma stored energy. As the power deposited at each target, immediately following the transient, matches the L-mode value, the in-out power sharing ratio remains the same for L- and ELM-free H-mode. This is consistent with the conductive model for power sharing between divertors proposed in section 5.1.2.2, as the SOL geometry (parallel connection length and target radius) is unaffected by the L-H transition.

7.1.2 SOL power width

At the transition from L- to ELM-free H-mode, the SOL width $\lambda_{q,u}$ at both divertor targets decreases by a factor ≈ 2, figure 7.2b, but remains constant during the following core density rise. The decrease in target $\lambda_{q,u}$ agrees with observations from the JET tokamak, where the outer divertor $\lambda_{q,u}$ also decreases by a factor ≈ 2 at the transition from L- to ELM-free H-mode [75]. Another estimate of the SOL power width can be obtained using the edge temperature and density profiles at the outboard mid-plane, measured by Thomson scattering. Under the assumption of a SOL in the conduction limited regime, the SOL power fall-off length is given by

$$\lambda_{q,u}^{\text{Spitzer}} = \frac{2}{7}\lambda_{T,u}^{\text{TS}} \tag{7.1}$$

where $\lambda_{T,u}^{\mathrm{TS}}$ is the electron temperature fall-off length. Alternatively, under the assumption of a SOL in the flux-limited regime (i.e. low collisionality), the SOL power fall-off length is given by

$$\lambda_{q,u}^{\text{flux-limited}} = \left(\frac{3}{2} \frac{1}{\lambda_{T,u}^{\mathrm{TS}}} + \frac{1}{\lambda_{n,u}^{\mathrm{TS}}} \right)^{-1} \tag{7.2}$$

where $\lambda_{n,u}^{\mathrm{TS}}$ is the electron density fall-off length. As shown in figure 7.2b, the SOL width at the outboard mid-plane, derived with either assumption ($\lambda_{q,u}^{\text{Spitzer}}$ or $\lambda_{q,u}^{\text{flux-limited}}$), decreases by a factor ≈ 2 at the L-H transition, similarly to the target $\lambda_{q,u}$. This suggests that the observed decrease of $\lambda_{q,u}$ at the targets can be entirely attributed to the decrease of $\lambda_{q,u}$ upstream. The decrease of $\lambda_{q,u}$ upstream, i.e. the narrowing of the SOL heat channel around the plasma, indicates that the balance between parallel and perpendicular transport in the main SOL changes between L- and H-mode.

Interpretation of $\lambda_{q,u}$ reduction with conductive model The reduction of $\lambda_{q,u}$ at the L-H transition can be interpreted using the conductive SOL model proposed in section 5.1.2. Combining equation 5.19 and 5.17, evaluating the result at the separatrix and using the separatrix temperature expression from the 2PM, yields an expression for the perpendicular heat diffusivity

$$\chi_\perp = \frac{2}{7} \lambda_T^2 T_{\mathrm{sep}}^{5/2} \frac{B_{p,u}}{B_{\mathrm{tot},u}} \left(1 + \frac{L_{\|,\mathrm{out}}}{L_{\|,\mathrm{in}}} \right) \frac{\kappa_0^e}{2\pi a \sqrt{\frac{1+\kappa^2}{2}} n_e L_{\|,\mathrm{out}}} \tag{7.3}$$

(for the symbol definition, see section 5.1.2). Since, at the transition from L- to ELM-free H-mode, plasma current, plasma shape and divertor geometry do not change, the expression for $\chi_\perp$ simplifies to

$$\chi_\perp \propto \lambda_T^2 \; T_{\mathrm{sep}}^{5/2} \; n_e^{-1} \tag{7.4}$$

Note that using a single flux tube model for the SOL, as in [88], reduces to the same expression. For the plasma shot described here, evaluating relation 7.4 before and after the L-H transition[2] yields

$$\frac{\chi_\perp^{\mathrm{H}}}{\chi_\perp^{\mathrm{L}}} = \underbrace{\left(\frac{\lambda_T^H}{\lambda_T^L} \right)^2}_{0.2950} \cdot \underbrace{\left(\frac{T_{\mathrm{sep}}^H}{T_{\mathrm{sep}}^L} \right)^{5/2} \left(\frac{n_{\mathrm{sep}}^H}{n_{\mathrm{sep}}^L} \right)^{-1}}_{1.2148} = 0.3584 \tag{7.5}$$

implying

$$\boxed{\chi_\perp^{\mathrm{L}} / \chi_\perp^{\mathrm{H}} \approx 2.8} \tag{7.6}$$

---

[2] The considered time dwell before the transition is [1.085, 1.135]s, that after the transition is [1.265, 1.315]s.

In the framework of the conductive model, the observed reduction of $\lambda_{q,u}$ at the L-H transition is explained by a factor ~ 3 reduction of the SOL perpendicular heat diffusivity. Interestingly, the ratio $\chi_\perp^{\mathrm{L}}/\chi_\perp^{\mathrm{H}}$ found for this TCV discharge is similar to that found, using the same procedure, on the AUG tokamak, $\chi_\perp^{\mathrm{L}}/\chi_\perp^{\mathrm{H}} \approx 2$ [88].
The transition to ELM-free H-mode comes, therefore, with a significant suppression of perpendicular heat transport in the SOL. A possible interpretation is that the edge transport barrier extends into the near-SOL.

7.1.3 Divertor spreading factor

At the transition from L- to ELM-free H-mode, the divertor spreading factor S_u at both divertor targets also decreases by a factor ≈ 2, figure 7.2c.

Interpretation of S_u reduction with diffusive model The reduction of S_u at the L-H transition can be interpreted using the diffusive model proposed in section 5.1.4. With a fixed $\chi_\perp = 1$ m^2/s (the perpendicular heat diffusivity in the divertor SOL), the model prediction for S_u is the same before and after the L-H transition, in contradiction with the experiment, see figure 7.2c. In particular, the increase of the SOL temperature in H-mode ($T_{\mathrm{e,X}}$ increases from 44 eV to 54 eV and $T_{e,t}$ from 5.8 eV to 6.6 eV) is not sufficient to explain the observed reduction of S_u. With $\chi_\perp$ assumed unknown, the model expression for S_u, equation 5.45, can be inverted to yield a relation for $\chi_\perp$

$$\chi_\perp = \frac{\kappa_0^e}{4} S_u^2 \frac{T_{\mathrm{e,X}}^{5/2}\, f_{x,t}^2}{n_{\mathrm{e,X}}\, L_{\parallel,\mathrm{div}}^2} \left(\frac{f_{\mathrm{T}}^{7/4}-1}{f_{\mathrm{T}}^{7/2}-1} \right)^{-2} \tag{7.7}$$

Since, at the transition from L- to ELM-free H-mode, divertor geometry ($L_{\parallel,\mathrm{div}}$ and $f_{x,t}$) does not change, the expression for $\chi_\perp$ simplifies to

$$\chi_\perp \propto S_u^2 \frac{T_{\mathrm{e,X}}^{5/2}}{n_{\mathrm{e,X}}} \left(\frac{f_{\mathrm{T}}^{7/4}-1}{f_{\mathrm{T}}^{7/2}-1} \right)^{-2} \tag{7.8}$$

The scaling evaluated before and after the L-H transition[3] for the plasma shot considered here yields

$$\begin{aligned} \frac{\chi_\perp^{\mathrm{H}}}{\chi_\perp^{\mathrm{L}}} &= \underbrace{\left(\frac{S_u^{\mathrm{H}}}{S_u^{\mathrm{L}}} \right)^2}_{0.262} \cdot \underbrace{\left(\frac{T_{\mathrm{e,X}}^{\mathrm{H}}}{T_{\mathrm{e,X}}^{\mathrm{L}}} \right)^{5/2} \left(\frac{n_{\mathrm{e,X}}^{\mathrm{H}}}{n_{\mathrm{e,X}}^{\mathrm{L}}} \right)^{-1} \left(\frac{\left[(f_{\mathrm{T}}^{7/4}-1)/(f_{\mathrm{T}}^{7/2}-1) \right]_{\mathrm{H}}}{\left[(f_{\mathrm{T}}^{7/4}-1)/(f_{\mathrm{T}}^{7/2}-1) \right]_{\mathrm{L}}} \right)^{-2}}_{1.219} \\ &= 0.319 \end{aligned} \tag{7.9}$$

---

[3] The considered time dwells before/after the transition are the ones adopted in the previous section.

implying

$$\boxed{\chi_\perp^{\mathrm{L}}/\chi_\perp^{\mathrm{H}} \approx 3.1} \tag{7.10}$$

As some of the model assumptions constitute a significant simplification of the transport in the TCV divertor (e.g. convection is expected to contribute to the heat transport parallel to field lines and the divertor spreading leads to a reduction of $q_\parallel$ along the flux tube), the obtained change in perpendicular heat diffusivity may have a large uncertainty. A consistency check using Thomson scattering and Langmuir probes measurements shows that, at the transition from L- to ELM-free H-mode, the change in target and x-point electron temperatures ($T_{e,t}$ increases by $\approx 15\%$ and $T_{\mathrm{e,X}}$ by $\approx 25\%$) is entirely consistent with the factor ≈ 2 reduction of the SOL width. Substituting $T_{\mathrm{e,X}}$ and $T_{e,t}$ in equation 5.42 yields $q_\parallel^{\mathrm{H}}/q_\parallel^{\mathrm{L}} \approx 2.13$. Similarly, assuming that the upstream SOL heat flux is exponential and using the measured $\lambda_{T,u}$ yields $q_\parallel^{\mathrm{H}}/q_\parallel^{\mathrm{L}} \approx 1.84$. This indicates that the 2PM constitutes a good approximation of the temperature distribution and, hence, balance between parallel and cross-field transport in the TCV divertor both before and after the L-H transition.

In the framework of the diffusive model, therefore, the observed reduction of S_u at the L-H transition is explained by a factor ~ 3 reduction of the perpendicular heat diffusivity in the divertor SOL. Interestingly, in the previous section, a similar reduction was inferred for the perpendicular heat diffusivity in the main SOL (i.e. around the confined plasma). Here again, a possible interpretation is that the edge transport barrier extends into the near-SOL, and the transport suppression propagates along SOL open field lines into the divertor.

Conclusion of section 7.1

In conclusion, this section showed that, at the transition from L- to ELM-free H-mode, both the SOL heat channel width (at targets and outboard mid-plane) and the spreading factor S_u narrow by a factor ≈ 2. This corresponds to a decrease of the heat wetted area by the same factor, equivalent to a factor ≈ 2 increase of the peak parallel heat flux $q_{\parallel,t}^{\mathrm{peak}}$, see equation 5.7.

Interpreting the change of $\lambda_{q,u}$ with a conductive model for the SOL and the change of S_u with a diffusive model for the divertor SOL leads to the conclusion that the perpendicular heat diffusivity $\chi_\perp$, both in the main SOL (around the plasma) and in the divertor SOL, significantly decreases at the L-H transition. This suggests that the edge transport barrier extends into the SOL and propagates, along open field lines, into the divertor. This hypothesis is practically equivalent to that formulated in section 6.1.2 to explain the observed simultaneous reduction of plasma stored energy and SOL width (upstream and targets) when decreasing the plasma triangularity.

7.2 Inter-ELM power exhaust

This section and the following investigate SOL power exhaust for Type-I ELMy H-mode plasmas in the Single Null magnetic configuration. The analysis starts with the stationary phase in-between ELMs, referred to as the *inter-ELM* phase, and then extends, in the next section, to the transient ELM phase.

The analysed database features 22 TCV plasma discharges in a lower Single Null configuration for a range of plasma currents (170 to 380 kA), outer divertor leg lengths (21 to 65 cm) and outer target flux expansions (≈ 2 to ≈ 9). The plasma uses an auxiliary neutral beam injector (NBI), with P_{NBI} between 0.2 and 1.1 MW, except the case with the longest outer divertor leg length, which uses Ohmic heating alone. The plasma shape is fixed, with elongation $\kappa \approx 1.6$, upper triangularity $\delta_{\mathrm{upper}} \approx 0.15$ and lower triangularity $\delta_{\mathrm{lower}} \approx 0.6$. The magnetic field is in the forward field direction (i.e. with the vertical ion ∇B drifts towards the active x-point), the plasma line-averaged density ranges from 25% to 43% of the Greenwald density, with both divertors in the attached, high-recycling, regime. The ELMs are detected from their characteristic spike in the D_α emission, as described in section 7.3.

For each ELM cycle, the inter-ELM target heat load at $\approx 90\%$ of the ELM cycle, measured with Infrared Thermography, is mapped to the out-board midplane. The profiles from all ELM cycles of a discharge are averaged, yielding a canonical inter-ELM heat flux profile for each discharge. The average profile is then parameterised with equation 5.5 to infer a value for the SOL width $\lambda_{q,u}$ and the divertor spreading factor S_u.
For each plasma discharge, inter-ELM plasma electron temperature profiles from 60 to 99% of the ELM cycles, measured by Thomson Scattering, are grouped together. The resulting profile is fitted with an exponential in the edge region ($0.95 \leq \rho_\psi \leq 1.05$) to estimate the temperature fall-off length $\lambda_{T,u}^{\mathrm{TS}}$. Then, under the assumption that the SOL is in the conduction limited regime, a value for the SOL width at the outboard mid-plane $\lambda_{q,u}^{\mathrm{Spitzer}}$ is calculated using equation 6.1.

Infrared camera setup for ELMy plasmas To resolve divertor heat fluxes in-between ELMs, whose frequency typically ranges from 100 Hz to 200 Hz, the acquisition rate of the Infrared cameras is increased from 200 Hz, which is the value used for L-mode and ELM-free plasmas, to ≈ 6 to 9 kHz. To reach this acquisition frequency, the frame acquisition time, equation 3.1, must be reduced. This is achieved by operating the camera detector in the sub-frame mode, reducing the number of pixels and thus the read-out time. The sub-window is positioned to cover the location of the strike points, as shown in figure 7.3 for the outer strike point of a SN configuration.

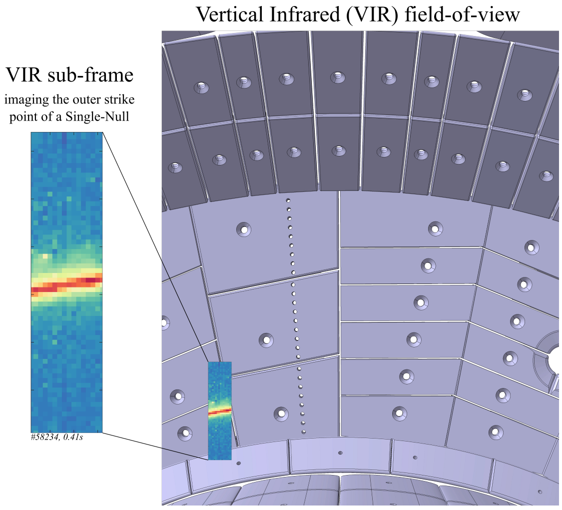

Figure 7.3 – Reduced field-of-view of the VIR system, with a 64 × 16 pixels sub-window, for an ELMy H-mode plasma in the lower Single-Null configuration (insert), compared to the full field-of-view (320 × 256 pixels). The sub-window position is adjusted to cover the position of the SN outer strike point.

7.2.1 Inter-ELM power width

Similarly to the study of L-mode (section 6.1.2) and ELM-free H-mode (section 7.1.2) plasmas, the inter-ELM $\lambda_{q,u}$ measured at the targets is compared to the value measured at the outboard mid-plane. Then, it is related to some prominent multi-machine scaling laws and to the prediction from the heuristic drift-based model (section 5.1.3).

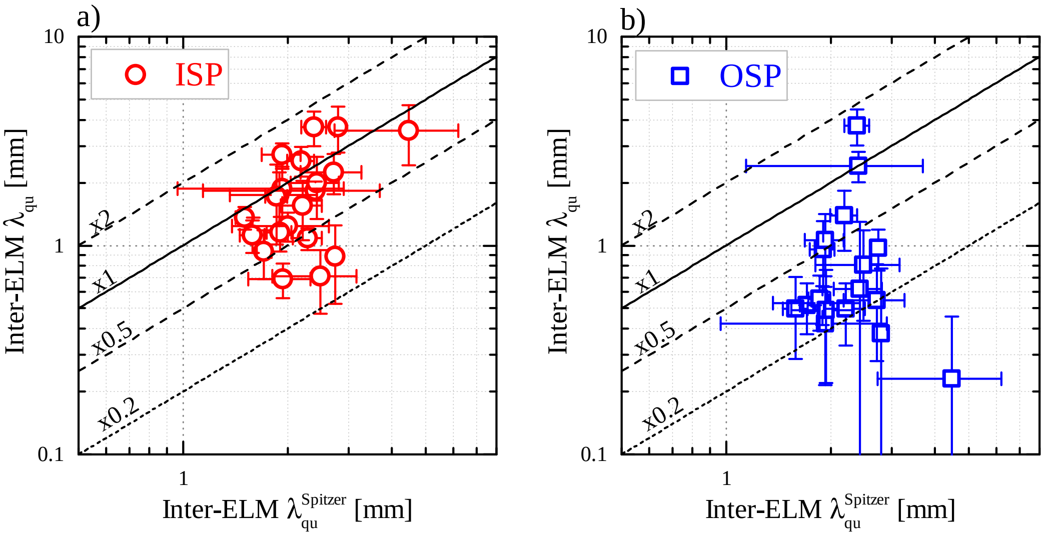

Figure 7.4 – Inter-ELM SOL width measured at the inner (a) and outer (b) strike point of a Single-Null configuration, shown as a function of the inter-ELM SOL width measured at the outboard mid-plane.

Comparison between target and upstream At the inner target, the value of $\lambda_{q,u}$ is comparable to that at the outboard midplane, figure 7.4a, with $\lambda_{q,u}^{\text{in}}/\lambda_{q,u}^{\text{Spitzer}} = (0.81\pm0.34)$. At the outer target, in contrast, the $\lambda_{q,u}$ is ≈ 2.3 times lower than upstream, figure 7.4b, with $\lambda_{q,u}^{\text{out}}/\lambda_{q,u}^{\text{Spitzer}} = (0.42 \pm 0.36)$.

Comparison with multi-machine scaling laws To compare TCV data to multi-machine scaling laws, the upstream $\lambda_{q,u}^{\text{Spitzer}}$, from Thomson scattering, is chosen instead of the target $\lambda_{q,u}$, from IR, as $\lambda_{q,u}$ is sensitive to the divertor geometry, as shown in section 6.1.2 for L-mode plasmas, and displays in-out asymmetries. In the analysed database, three discharges have a divertor shape close to other machines, with $L_{\text{div}} = 23$ cm and outer target $f_{x,t}$ between 4 and 6, see figure 4.6a. These cases are indicated by filled data symbols in the figures.
First, the SOL temperature fall-off length $\lambda_{T,u}^{\text{TS}}$ is related to a recent AUG regression, then the SOL width $\lambda_{q,u}^{\text{Spitzer}}$ is compared to three prominent multi-machine scaling laws, not featuring TCV data.

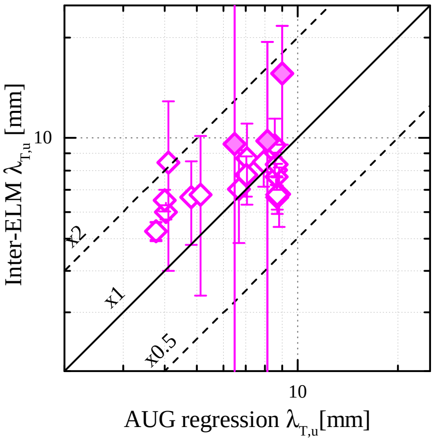

Figure 7.5 – Inter-ELM plasma edge temperature fall-off length, compared to the prediction from the AUG regression of [89]. Filled symbols correspond to discharges with a standard SN shape (short L_{div} and moderate $f_{x,t}$).

- A study in AUG [89] proposes a scaling for the edge plasma temperature fall-off length $\lambda_{T,u}$ (measured by TS) for attached, ELMy lower SN plasmas,

$$\lambda_{T,u}[\text{mm}] = 2.63\ B_\phi[T]^{-0.50}\ q_{\text{cyl}}^{0.974}\ P_{\text{SOL}}[\text{MW}]^{0.05} \qquad \text{AUG [89]} \tag{7.11}$$

  with B_ϕ the toroidal magnetic field at R_{geo}, q_{cyl} the cylindrical safety factor

$$q_{\text{cyl}} = \frac{2\pi B_\phi a\epsilon}{\mu_0 I_P}\frac{1+\kappa^2}{2} \tag{7.12}$$

  and $\epsilon = a/R_{\text{geo}}$ the inverse aspect ratio. This scaling well describes the average value

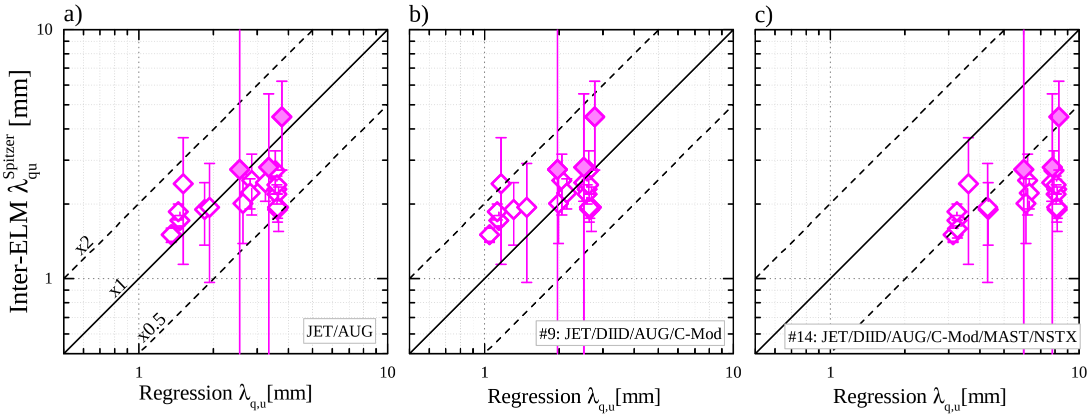

Figure 7.6 – Inter-ELM SOL power fall-off length, measured upstream, compared to the prediction from (a) a JET/AUG regression (equation 7.13, [90]), (b) a JET/DIII-D/AUG/C-Mod regression (equation 7.14, [71]) and (c) a JET/DIII-D/AUG/C-Mod /MAST/NSTX regression (equation 7.15, [71]). Filled symbols correspond to discharges with a standard SN shape (short L_{div} and moderate $f_{x,t}$).

on TCV, $\lambda_{T,u}^{\mathrm{TCV}}/\lambda_{T,u}^{\mathrm{scaling}} = (1.23 \pm 0.34)$, figure 7.5, despite the different machine size. The observed dependence on the plasma current is, however, somewhat weaker than the scaling equation 7.11 at constant B_ϕ, $\lambda_{T,u}^{\mathrm{AUG}} \propto I_{\mathrm{P}}^{-0.974}$. Note that the other regression parameters (i.e. B_ϕ and P_{SOL}) are not significantly varied in this study.

- Studies using data from multiple tokamaks [71, 90] propose several scaling laws for $\lambda_{q,u}$, depending on the devices included in the regression,

$$\lambda_{q,u}[\mathrm{mm}] = 0.90\ B_\phi[\mathrm{T}]^{-0.73}\ q_{\mathrm{cyl}}^{1.16}\ P_{\mathrm{SOL}}[\mathrm{MW}]^{0.04}\ R_{\mathrm{geo}}[\mathrm{m}]^{-0.11} \quad \text{JET/AUG [90]} \tag{7.13}$$

$$\lambda_{q,u}[\mathrm{mm}] = 0.70\ B_\phi[\mathrm{T}]^{-0.77}\ q_{95}^{1.05}\ P_{\mathrm{SOL}}[\mathrm{MW}]^{0.09}\ R_{\mathrm{geo}}[\mathrm{m}]^{0.00} \quad \text{JET/DIII-D/AUG/C-Mod , \#9 [71]} \tag{7.14}$$

$$\lambda_{q,u}[\mathrm{mm}] = 0.63\ \langle B_p\rangle[\mathrm{T}]^{-1.19} \quad \text{JET/DIII-D/AUG/C-Mod /MAST/NSTX, \#14 [71]} \tag{7.15}$$

For all the tested regressions, the range in TCV data is smaller than that in the regressions because of a weaker functional dependence on I_{P}, as discussed above. Scaling laws 7.13 and 7.14, which include both toroidal and poloidal magnetic field as regression parameters, well describe the upstream $\lambda_{q,u}$ of TCV plasmas, figures 7.6a-b, with $\lambda_{q,u}^{\mathrm{Spitzer}}/\lambda_{q,u}^{\mathrm{scaling}} = (0.90 \pm 0.29)$ and $\lambda_{q,u}^{\mathrm{Spitzer}}/\lambda_{q,u}^{\mathrm{scaling}} = (1.19 \pm 0.36)$ respectively. In contrast, scaling law 7.15, which includes only the poloidal field as regression parameter, overestimates TCV measurements by a factor ≈ 2.5, figure 7.6c, with $\lambda_{q,u}^{\mathrm{Spitzer}}/\lambda_{q,u}^{\mathrm{scaling}} = (0.40 \pm 0.12)$.

Comparing TCV data with other conventional aspect ratio devices, therefore, clearly indicates that the SOL width has a dependence on the toroidal field B_ϕ. The inclusion of unconventional (low) aspect ratio tokamaks (MAST and NSTX) in the multi-machine regression, however, removed the B_ϕ dependence and increased the $\langle B_p \rangle$ dependence. TCV data suggests that the B_ϕ dependence is vital, and the low aspect ratio devices would be better parameterised using an explicit aspect ratio dependence, i.e. adding ϵ as an additional regression parameter.

Comparison with drift-dominated model of SOL The SOL width measured at the outboard mid-plane $\lambda_{q,u}^{\mathrm{Spitzer}}$ is compared to the prediction from the heuristic drift-dominated model of the SOL, proposed in [49] and summarized in section 5.1.3, mapped to the outboard mid-plane, equation 5.36. The model prediction well fits the TCV measurements, figure 7.7, with $\lambda_{q,u}^{\mathrm{Spitzer}}/\lambda_{\mathrm{u,HD}} = (0.83 \pm 0.23)$. Considering only the discharges with a standard divertor shape leads to an even better agreement of $\lambda_{q,u}^{\mathrm{Spitzer}}/\lambda_{\mathrm{u,HD}} = (0.98 \pm 0.19)$.

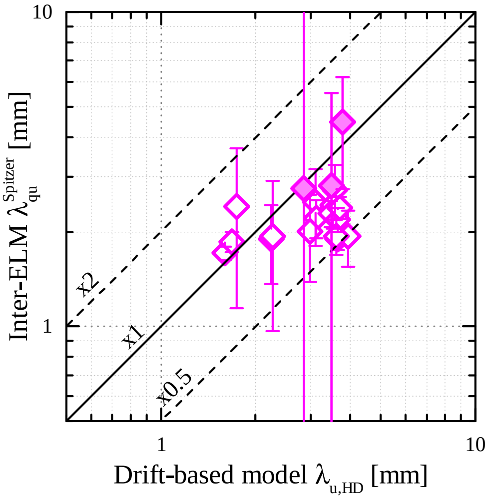

Figure 7.7 – Inter-ELM SOL power fall-off length, measured upstream, compared to the prediction from the drift-based model, proposed in [49] and summarized in section 5.1.3. Filled symbols correspond to discharges with a standard SN shape (short L_{div} and moderate $f_{x,t}$).

7.2.2 Inter-ELM spreading factor

Similarly to the study of L-mode (section 6.1.2) and ELM-free H-mode (section 7.1.2) plasmas, the inter-ELM S_u, measured at the targets, is compared to the prediction from the diffusive model discussed in section 5.1.4, equation 5.45. The target temperature may be neglected compared to the upstream value, and the SOL perpendicular heat diffusivity is set to $\chi_\perp = 1\ \mathrm{m}^2/\mathrm{s}$.

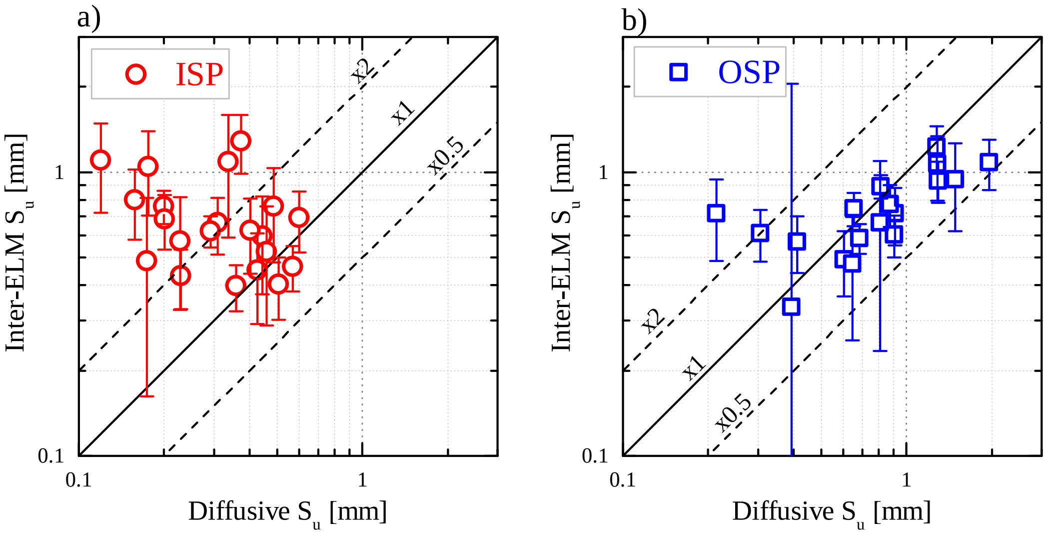

Figure 7.8 – Inter-ELM divertor spreading factor, for the inner (a) and outer (b) target, compared to the prediction from the diffusive transport model proposed in section 5.1.4, equation 5.45.

At the inner target, the values of S_u only partly agree with the model, which tends to underestimate the measurements, figure 7.8a. At the outer target, however, the values of S_u show better agreement, with the model capable of reproducing the measured increase from $\approx$ 0.3 to $\approx$ 2 mm, figure 7.8b. According to the model, this increase is due to the increase of the ratio between divertor connection length and target flux expansion $L_{\|,\mathrm{div}}/f_{x,t}$. A higher $L_{\|,\mathrm{div}}/f_{x,t}$ ratio can be obtained through a longer divertor leg length, higher target flux expansion or lower plasma current.

Conclusion of section 7.2

In conclusion, this section investigated the target heat loads in-between ELMs for Type-I ELMy H-mode plasmas in the Single Null configuration on TCV. The SOL power widths measured at the outboard mid-plane, by Thomson scattering, are found to be in quantitative agreement with the prediction from multi-machine scaling laws where the toroidal magnetic field B_ϕ is included as a regression parameters. This indicates that the B_ϕ dependence is vital, i.e. the toroidal field plays a role into the physics setting the SOL power width. As a result, the inclusion of unconventional aspect ratio devices in the multi-machine regressions should be reworked by adding an explicit aspect ratio dependence and specifically not by removing the B_ϕ dependence thereby increasing the $\langle B_p \rangle$ dependence. The drift-based prediction for the SOL power width is quantitatively compatible with the measurements. Note that the drift-based model includes a B_ϕ dependence, that seems to be important in the comparison of TCV with other devices. The trend in TCV data is somewhat weaker than the regressions and the drift-based model, indicating a weaker functional dependence on the plasma current. The divertor spreading factor is found to be in good agreement with the prediction from a diffusive model for the outer target only, where the scatter in experimental measurements is ascribed to changes in the ratio of divertor connection length and target flux expansion $L_{\|,\mathrm{div}}/f_{x,t}$.

7.3 ELM power exhaust

This section presents a study of the Type-I ELM power exhaust in TCV. The magnetic configuration is the Single-Null, and the experimental database is the same as used in section 7.2.

The ELMs are detected using the characteristic spikes in the D_α emission, figure 7.9d. The ELM size, defined using the change in stored plasma energy as

$$\Delta E_{\mathrm{ELM}}\ [\%] = 100 \cdot \Delta \mathrm{W}_{\mathrm{MHD}}/\mathrm{W}_{\mathrm{MHD}} \tag{7.16}$$

where $\mathrm{W}_{\mathrm{MHD}}$ is the plasma stored energy before the ELM and $\Delta\mathrm{W}_{\mathrm{MHD}}$ its decrease by the ELM, is between 6 and 15%. The stored energy variation is computed as

$$\Delta \mathrm{W}_{\mathrm{MHD}} = \frac{3\pi}{\mu_0} R_{\mathrm{geo}}\ B_{\phi,v}\ \Delta\phi_{\mathrm{dia}} \tag{7.17}$$

with μ_0 the permeability of free space, $B_{\phi,v}$ the vacuum toroidal field at the geometrical major radius R_{geo} and ϕ_{dia} the plasma toroidal flux, also known as the diamagnetic flux, measured by the diamagnetic loop, defined as

$$\phi_{\mathrm{dia}} = \int_{S_{pl}} (B_\phi - B_{\phi,v}) \cdot d\mathrm{S} \tag{7.18}$$

with B_ϕ the total toroidal magnetic field in presence of plasma, $B_{\phi,v}$ the vacuum toroidal magnetic field (i.e. with no plasma) and S_{pl} the plasma poloidal cross-section.

During the ELM cycle, the target surface temperature evolution in proximity of the strike point is provided by the infrared thermography system, figures 7.9b-c, and is used to compute the heat flux. Infrared measurements are recorded every 0.17 ms for the outer target (acquisition frequency of 5.8 kHz, integration time of 0.1 ms) and every 0.11 ms for the inner target (acquisition frequency of 9 kHz, integration time of 0.05 ms). With a typical ELM duration of ≈ 1 ms, this setup can well resolve the ELM heat load transient, described by ≈ 6 samples for the outer target and ≈ 10 for the inner target. For each plasma discharge, inter-ELM edge plasma profiles of temperature and density from 60% to 99% of the ELM cycles, measured by Thomson scattering, are grouped together, figures 7.9e-f. The resulting profiles are then fitted with a modified hyperbolic tangent function [91] to obtain pedestal plasma properties ($T_{e,\mathrm{ped}}$, $n_{e,\mathrm{ped}}$).

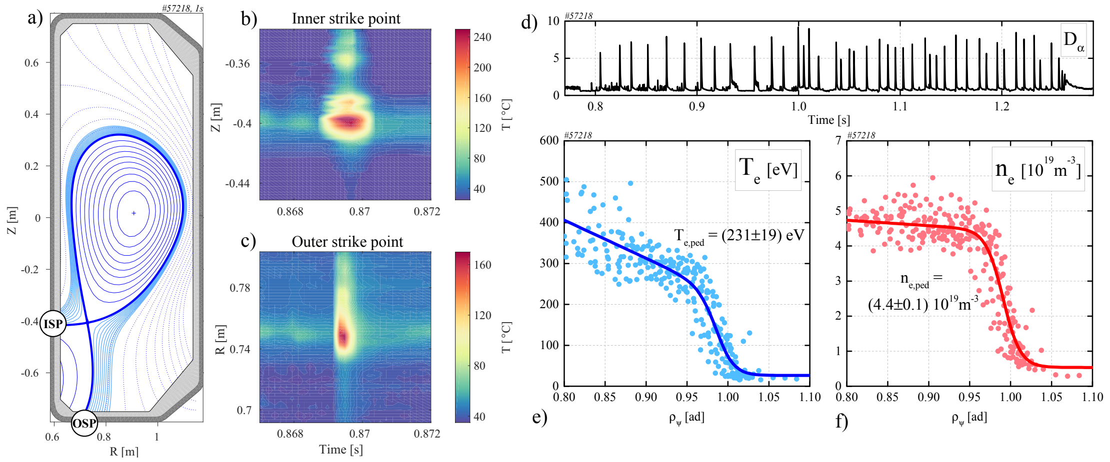

Figure 7.9 – (a) Poloidal cross-section of TCV showing a Single-Null magnetic configuration of the analysed database, showing the inner (ISP) and outer (OSP) strike point. (b-c) Target temperature evolution, near the inner and outer strike points, around one ELM event. (d) D-α signal time trace, featuring a spike at each ELM. (e-f) Inter-ELM plasma temperature and density profiles, in the edge / pedestal region, are fitted with a modified hyperbolic tangent function, yielding the pedestal temperature and density.

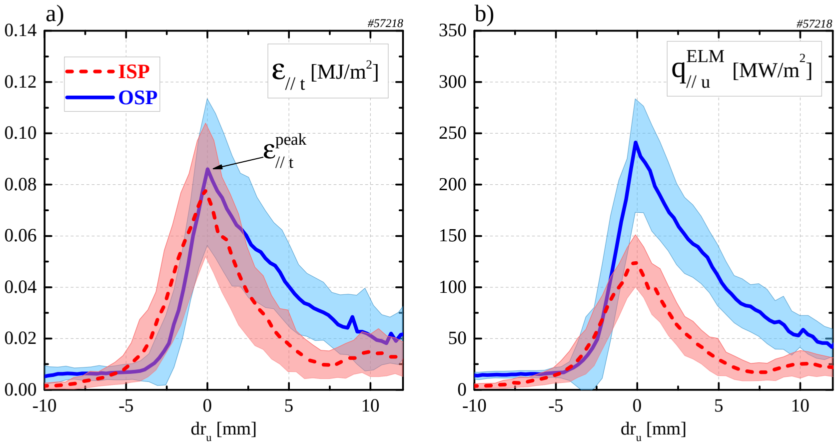

Figure 7.10 – (a) ELM parallel energy fluence profile, at the target, for the inner (red) and outer (blue) strike point. The peak fluence $\varepsilon_{\parallel,t}^{\text{peak}}$ is also indicated. (b) ELM parallel heat flux profile, mapped to the outboard mid-plane, at the moment of maximum heat load, for the inner (red, continuous line) and outer (blue, dashed line) strike point. Each profile is conditionally averaged over several ELM events.

As discussed in section 5.2.1, the two critical power exhaust quantities of the ELM event are (1) the energy deposition time τ_{ELM} and (2) the peak parallel energy fluence $\varepsilon_{\parallel,t}^{\text{peak}}$, as they directly relate to the ELM-induced target surface temperature rise. A third important quantity is the integral power width $\lambda_{\text{int},u}^{\text{ELM}}$, as it affects the ELM heat wetted area and, thus, the target peak heat flux. Note that $\varepsilon_{\parallel,t}^{\text{peak}}$ and $\lambda_{\text{int},u}^{\text{ELM}}$ are inversely correlated as they are deduced from the same fluence profile (see description below).

However, since the in-out ELM energy repartition may change with plasma conditions and divertor shape, $\varepsilon_{\|,t}^{\mathrm{peak}}$ and $\lambda_{\mathrm{int},u}^{\mathrm{ELM}}$ can be independent, which motivates discussing both separately.

Consequently, τ_{ELM}, $\varepsilon_{\|,t}^{\mathrm{peak}}$ and $\lambda_{\mathrm{int},u}^{\mathrm{ELM}}$ are chosen to characterise the ELM divertor heat loads in sections 7.3.1, 7.3.2 and 7.3.3, respectively, and are computed as described below:

1. The duration of the ELM power deposition, $\tau_{\mathrm{ELM}}^{\mathrm{IR}}$, defined as the time over which the power to the divertor plate, estimated by IR thermography, exceeds $(1/e)$-times the peak of the ELM power load [92].

2. The peak of the ELM parallel energy fluence profile at the target, $\varepsilon_{\|,t}^{\mathrm{peak}}$,

$$\varepsilon_{\|,t}^{\mathrm{peak}} = \max(\varepsilon_{\|,t}) \tag{7.19}$$

$$\varepsilon_{\|,t} = \int_{\tau_{\mathrm{ELM}}^{\mathrm{IR}}} q_{\|,t}\ \mathrm{d}t \tag{7.20}$$

   where $q_{\|,t}$ is the parallel heat flux profile at the target, computed with equation 4.25. For the considered database, the $\varepsilon_{\|,t}$ profile peaks in the proximity of the strike point, figure 7.10a.

3. The integral width $\lambda_{\mathrm{int},u}^{\mathrm{ELM}}$ of the ELM parallel heat flux profile mapped upstream (equation 4.43), evaluated at the moment of peak ELM heat load,

$$\lambda_{\mathrm{int},u}^{\mathrm{ELM}} = \left[\frac{\int q_{\|,u}\ \mathrm{d}r_u}{q_{\|,u}^{\mathrm{peak}}}\right]_{t=t^*} \qquad \text{with } P(t^*) = P_{\max} \tag{7.21}$$

   where $q_{\|,u}$ is the parallel heat flux profile mapped upstream, computed with equation 4.27. For the considered database, the profile of $q_{\|,u}^{\mathrm{ELM}}$ peaks in the proximity of the strike point, figure 7.10b, similarly to $\varepsilon_{\|,t}$.

7.3.1 ELM energy flux duration

The ELM power deposition time $\tau_{\mathrm{ELM}}^{\mathrm{IR}}$ at the TCV divertor targets varies between ≈ 0.4 and 1.0 ms, and is slightly longer at the inner than the outer target. Most of this change is the effect of plasma current, with higher I_{P} leading to smaller $\tau_{\mathrm{ELM}}^{\mathrm{IR}}$. To gain a better insight into the ELM energy transport process, $\tau_{\mathrm{ELM}}^{\mathrm{IR}}$ is compared to two characteristic times for the ELM event, the duration of the D_α light transient and the ion parallel transit time in the SOL $\tau_{\|,\mathrm{ion}}$. Then, $\tau_{\mathrm{ELM}}^{\mathrm{IR}}$ is compared with a recent scaling law based on JET data.

- **Comparison with D_α spike duration** The duration of the ELM power deposition $\tau_{\mathrm{ELM}}^{\mathrm{IR}}$ matches the duration of the D_α light intensity spike $\tau_{\mathrm{ELM}}^{\mathrm{D}\alpha}$, figure 7.11a,

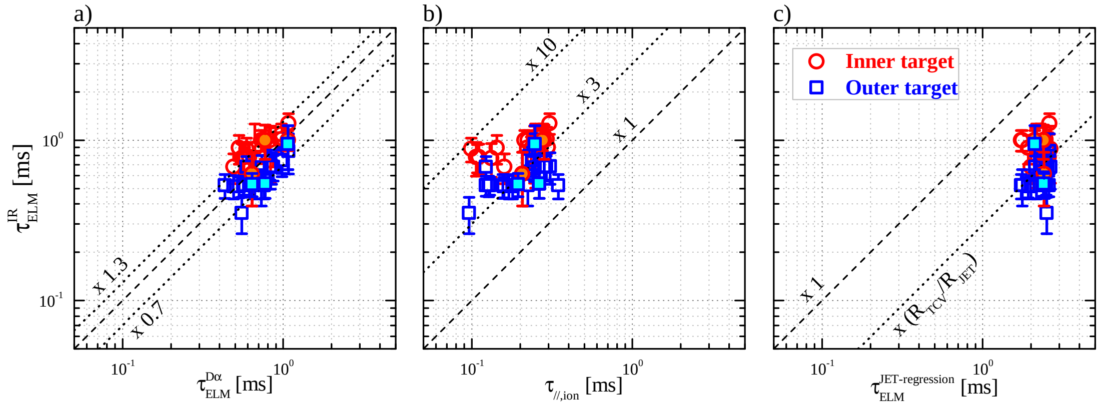

Figure 7.11 – For inner (red circles) and outer (blue squares) targets, ELM power deposition duration $\tau^{\mathrm{IR}}_{\mathrm{ELM}}$, compared to (a) D_α spike duration $\tau^{\mathrm{D}\alpha}_{\mathrm{ELM}}$, (b) pedestal ion parallel transit time $\tau_{\|,\mathrm{ion}}$ and (c) a JET-regression from [93]. In (c), TCV measurements are a factor $\approx (R_{\mathrm{TCV}}/R_{\mathrm{JET}})$ smaller than the JET-regression prediction. Filled symbols correspond to discharges with a standard SN shape (short L_{div} and moderate $f_{x,t}$).

measured with a photodiode whose line-of-sight crosses the plasma horizontally at the height of the magnetic axis. The transient in the D_α line emission is indicative of enhanced divertor recycling levels, compared to the inter-ELM phase. The $\tau^{\mathrm{D}\alpha}_{\mathrm{ELM}}$ is computed similarly to $\tau^{\mathrm{IR}}_{\mathrm{ELM}}$. This correlation between $\tau^{\mathrm{IR}}_{\mathrm{ELM}}$ and $\tau^{\mathrm{D}\alpha}_{\mathrm{ELM}}$ is consistent with a simple picture where the ELM plasma heat and particles enter the SOL and, whilst travelling along field lines towards the targets, perturb the recycling levels in the divertor volume, until they are absorbed by the divertor plate.

- **Comparison with ion parallel transit time** The duration of the ELM power deposition $\tau^{\mathrm{IR}}_{\mathrm{ELM}}$ is ≈ 3 times longer than, but correlates with, the transient time of pedestal plasma ions flowing along the field line from the pedestal to the divertor plate, $\tau_{\|,\mathrm{ion}}$, see figure 7.11b. This time is computed as

$$\tau_{\|,\mathrm{ion}} = L_\| / c_{s,\mathrm{ped}} \tag{7.22}$$

where $c_{s,\mathrm{ped}}$ is the sound speed calculated from the pedestal plasma parameters and $L_\|$ is the parallel connection length, between outer mid-plane and target, obtained from the magnetic reconstruction. The ion sound speed is taken as

$$c_s[\mathrm{cm/s}] = 9.79 \times 10^5 \; (\gamma_a \; Z \; T_e[\mathrm{eV}]/\mu)^{1/2} \tag{7.23}$$

with $\gamma_a = 1$ the assumed adiabatic index, $Z = 1$ the deuterium charge state and $\mu = m_i/m_p = 2$ (m_i is the mass of deuterium ion, m_p of the proton). TCV's results are consistent with observations from larger tokamaks (JET, AUG and JT-60U) [94, 95] in that the ELM deposition time scales almost linearly with the ion parallel transit time and is, in average, ≈ 2 to 3 times longer. For this TCV database, the variations in $\tau_{\parallel,\mathrm{ion}}$ are mostly caused by variations in the $L_{\parallel}$.

- **Comparison with JET scaling law** The duration of the ELM power deposition $\tau^{\mathrm{IR}}_{\mathrm{ELM}}$ in TCV is compared to a recent scaling law based on IR thermography data from the JET tokamak [93],

$$\tau^{\mathrm{IR}}_{\mathrm{ELM}}[\mathrm{ms}] = 43.06\ (n_{e,\mathrm{ped}}[10^{19}m^{-3}])^{0.61}\ (T_{e,\mathrm{ped}}[\mathrm{eV}])^{-0.69} \tag{7.24}$$

  where $n_{e,\mathrm{ped}}$ and $T_{e,\mathrm{ped}}$ are the pedestal plasma density and temperature. Note that pedestal plasma properties are the sole regression parameters in this parameterisation, i.e. no machine size parameters. The ELM power flux duration at the outer target in TCV is ≈ 3.5 times shorter than JET-based predictions, figure 7.11c. This difference well correlates with the different parallel connection length between the two machines, dominated by their major radii,

$$L^{\mathrm{JET}}_{\parallel}/L^{\mathrm{TCV}}_{\parallel} \propto R^{\mathrm{JET}}_{\mathrm{geo}}/R^{\mathrm{TCV}}_{\mathrm{geo}} = 2.96/0.88 = 3.36 \tag{7.25}$$

  This suggests that $\tau^{\mathrm{IR}}_{\mathrm{ELM}}$ may scale linearly with the device size, $\tau^{\mathrm{IR}}_{\mathrm{ELM}} \propto R_{\mathrm{geo}}$. Such a conclusion is consistent with previous multi-machine studies that, as discussed above, highlighted an almost linearly scaling of the ELM power flux duration with the ion transit time $\tau_{\parallel,\mathrm{ion}}$ and, therefore, with the machine major radius, since $\tau_{\parallel,\mathrm{ion}} \propto L_{\parallel} \propto R_{\mathrm{geo}}$.

The observed correlation of $\tau^{\mathrm{IR}}_{\mathrm{ELM}}$ with parallel transit time and machine size suggests a nearly linear dependence of $\tau^{\mathrm{IR}}_{\mathrm{ELM}}$ on the parallel connection length, which is favourable for an extrapolation to a nuclear fusion reactor. Due to an increased size over present-day tokamaks, a fusion reactor would benefit of a longer τ_{ELM}, reducing the ELM-induced divertor target surface temperature rise $\Delta T_{\mathrm{ELM}} \propto (\tau_{\mathrm{ELM}})^{-1/2}$, equation 5.58. At fixed device size, a further increase in τ_{ELM} could be achieved by using alternative magnetic configurations, that enhance the parallel connection length.

7.3.2 ELM peak parallel energy fluence

The ELM peak parallel energy fluence $\varepsilon^{\mathrm{peak}}_{\parallel,t}$ varies between ≈ 0.07 and ≈ 0.21 MJ/m^2 at the inner target, between ≈ 0.05 and ≈ 0.16 MJ/m^2 at the outer target. In this section, the ELM peak parallel energy fluence measured at the inner and outer divertor targets of TCV is compared to a recent multi-machine scaling law, and the prediction from the semi-empirical model described in section 5.2.2.

- **Comparison with multi-machine scaling law.** A recent study [63] yields a scaling law for the peak fluence measured at the outer divertor plate of JET, MAST

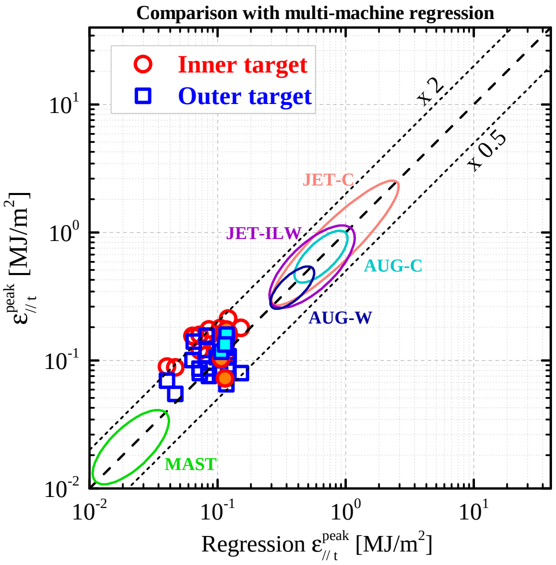

Figure 7.12 – ELM peak parallel energy fluence $\varepsilon^{\text{peak}}_{\parallel,t}$ measured at the inner (red circles) and outer (blue squares) divertor target, compared to the prediction from a multi-machine regression, equation 7.26 (proposed in [63]). The location of data points from other machines is also indicated (compare to figure 2 of [63]). Filled symbols correspond to discharges with a standard SN shape (short L_{div} and moderate $f_{x,t}$).

and AUG tokamaks,

$$\varepsilon^{\text{peak}}_{\parallel,t} = (0.28 \pm 0.14) \times n_{e,\text{ped}}^{(0.75\pm0.15)} \times T_{e,\text{ped}}^{(0.98\pm0.10)} \Delta E_{\text{ELM}}^{(0.52\pm0.16)} \times R_{\text{geo}}^{(1.0\pm0.4)} \quad (7.26)$$

with $\varepsilon^{\text{peak}}_{\parallel,t}$ in units of [MJ/m^2], $n_{e,\text{ped}}$ the plasma pedestal density (in units of [10^{20} m^{-3}]), $T_{e,\text{ped}}$ the plasma pedestal temperature (in [keV]), ΔE_{ELM} the ELM size (in [%], equation 7.16) and R_{geo} the machine major radius (in [m]). For the analysed TCV database, the peak fluence measured at the outer target quantitatively agrees with the regression, figure 7.12, occupying the gap left between MAST and AUG data points and adding a small major radius device for a conventional aspect ratio.

- **Comparison with semi-empirical model.** Similarly to MAST, JET and AUG, the peak parallel fluence measured at the outer divertor plate of TCV exceeds by a factor 3.0 ± 1.3 the semi-empirical model prediction of equation 5.64 (proposed in [63]), see figures 7.13a-b. This increases, at the inner target, to a factor 4.1 ± 1.6. When major radius change between outer mid-plane and target is accounted for, equation 5.63, the model prediction increases by $\approx 40\%$ for the inner target ($R_{\text{geo}}/R_t^{\text{ISP}} = 1.4$) and $\approx 17\%$ for the outer ($R_{\text{geo}}/R_t^{\text{OSP}} = 1.17$). This causes the difference between measurements and prediction to reduce only slightly, with the fluence exceeding the prediction by a factor 2.6 ± 1.0 at the outer target and 2.9 ± 1.1 at the inner target, figure 7.13c.

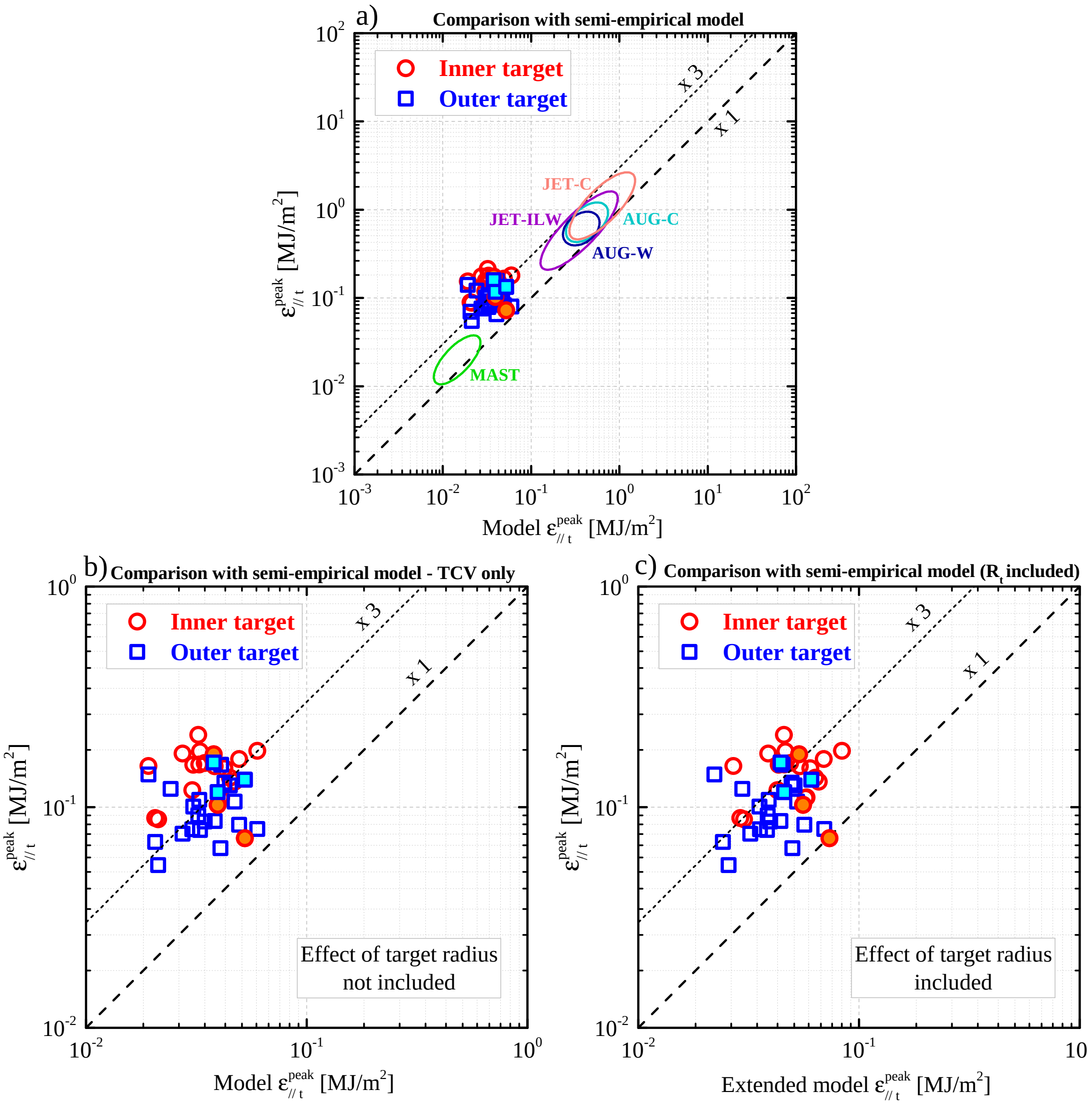

Figure 7.13 – ELM peak parallel energy fluence $\varepsilon^{\text{peak}}_{\parallel,t}$ measured at the inner (red circles) and outer (blue squares) divertor target, compared to the prediction (a-b) from a semi-empirical model (equation 5.64, proposed in [63]) and (c) from the same model, extended to account for target radius (equation 5.63). The location of data points from other machines is also indicated in figure a (compare to figure 3 of [63]). Filled symbols correspond to discharges with a standard SN shape (short L_{div} and moderate $f_{x,t}$).

7.3.3 ELM integral power width dependence on flux expansion

In this section, the ELM integral power width $\lambda^{\text{ELM}}_{\text{int},u}$ (defined by equation 7.21) is studied as a function of the outer target flux expansion $f_{x,t}$, at fixed plasma shape, plasma current and divertor leg length[4]. This corresponds to a sub-set of 3 plasma discharges

---

[4] Note that, within the available database, it is not possible to perform a similar study for the effect of plasma current or of divertor leg length, because scanning one of these two quantities at fixed $f_{x,t}$ turned

from the database. The outer target flux expansion is varied from 2 to 9 at fixed I_P = 169 kA, L_div = 43 cm, Greenwald fraction $f_\mathrm{GW} \approx 0.4$ and cylindrical safety factor $q_\mathrm{cyl} = 4$. Increasing the $f_{x,t}^\mathrm{out}$ increases $f_{x,t}^\mathrm{in}$ weakly from 3 to 5, and decreases the ELM size ΔE_ELM from 15% to 10%.

Quite unexpectedly, the ELM integral power width at the outer target strongly scales approximately with the inverse of the flux expansion,

$$\lambda_{\mathrm{int},u}^\mathrm{ELM} \propto f_{x,t}^{-1.17} \tag{7.27}$$

see figure 7.14a. The profile is fitted with equation 5.5 to infer a value for the SOL width $\lambda_{q,u}^\mathrm{ELM}$ and the divertor spreading factor S_u^ELM. The fit reveals that the decrease of $\lambda_{\mathrm{int},u}^\mathrm{ELM}$ with increasing flux expansion is the consequence of a corresponding decrease of $\lambda_{q,u}^\mathrm{ELM}$, figure 7.14b, whereas S_u^ELM remains independent of $f_{x,t}$, figure 7.14c.

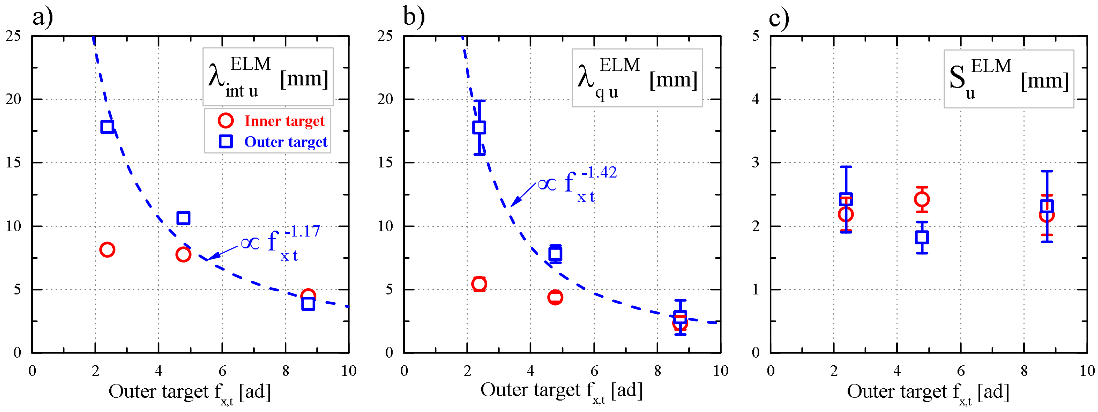

Figure 7.14 – For inner (red circles) and outer (blue squares) target, (a) ELM integral power width $\lambda_{\mathrm{int},u}^\mathrm{ELM}$, (b) ELM power width $\lambda_{q,u}^\mathrm{ELM}$ and (c) ELM spreading factor S_u^ELM, as a function of the outer target flux expansion.

Similarly to the outer target, an increase of the flux expansion at the inner target decreases the ELM integral power width, figure 7.14a. This is, again, the result of a decrease in $\lambda_{q,u}^\mathrm{ELM}$, figure 7.14b, at constant S_u^ELM, figure 7.14c.

The effect of flux expansion on ELM heat loads is quite different from that observed in L-mode, sections 6.1.2 and 6.1.3, where increasing the flux expansion has no effect on $\lambda_{q,u}$ but greatly reduces $S_u \propto f_{x,t}^{-0.97}$. A possible interpretation is that SOL heat transport during the ELM transient is dominated by a different mechanism (e.g. convection instead of electron heat conduction).

---

out to be much more challenging and was, ultimately, not achieved.

7.3.4 ELM energy repartition between targets

In this section, the ELM energy repartition between the two targets is discussed, and related to observations from other tokamaks. For the analysed database of TCV discharges, the ELM energy on average predominantly flows to the outer divertor with

$$E_{\mathrm{ELM}}^{\mathrm{ISP}}/E_{\mathrm{ELM}}^{\mathrm{OSP}} = (0.85 \pm 0.26) \tag{7.28}$$

but there is a significant scatter in the data, see figures 7.15a-b. Although more power is distributed to the outer divertor, the $\lambda_{\mathrm{int},u}^{\mathrm{ELM}}$ at the inner target is systematically lower (section 7.3.3), causing a higher energy fluence peak at the inner target (section 7.3.2).

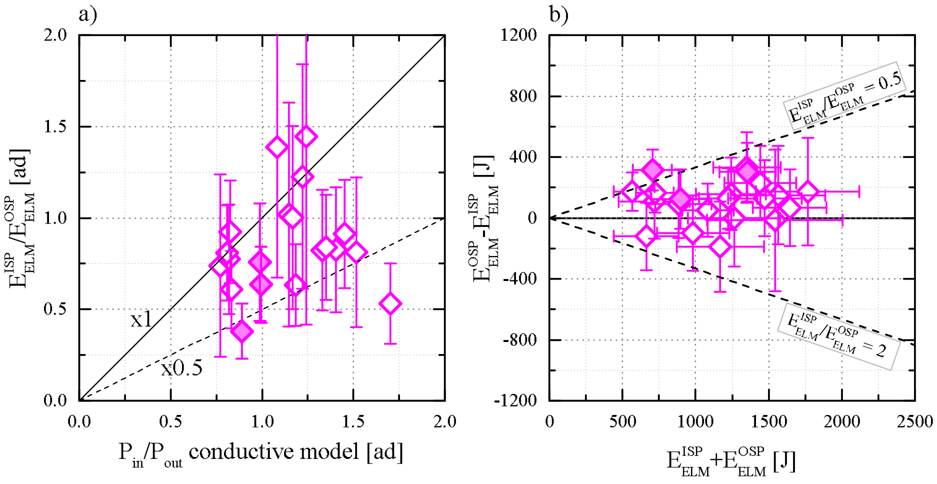

Figure 7.15 – (a) Measured in-out ELM energy ratio, compared to the prediction from the conductive power sharing model described in section 5.1.2.2. (b) Difference between the ELM energy deposited to the outer and inner target $E_{\mathrm{ELM}}^{\mathrm{OSP}}$-$E_{\mathrm{ELM}}^{\mathrm{ISP}}$, as a function of their sum $E_{\mathrm{ELM}}^{\mathrm{ISP}}$ +$E_{\mathrm{ELM}}^{\mathrm{OSP}}$. This way of presenting the ELM in-out asymmetry follows figure 2 of [96]. Filled symbols correspond to discharges with a standard SN shape (short L_{div} and moderate $f_{x,t}$).

The observed in-out ELM energy ratio is compared to the in-out power sharing ratio predicted by the conductive model described in section 5.1.2, using the inter-ELM $\lambda_{q,u}^{\mathrm{Spitzer}}$ as the SOL width value input to the model. As shown in figure 7.15a, the in-out ELM energy ratio is on average lower than the conductive prediction. This is similar to the observations in stationary L-mode discharges, section 6.1.1, where the measured $P_{\mathrm{in}}/P_{\mathrm{out}}$ is systematically lower than the conductive prediction. As discussed for the L-mode discharges, it could be the combined effect of in-out asymmetric volumetric radiation and particle drifts. In addition, the in-out ELM energy ratio does not correlate with the prediction, figure 7.15a. This could indicate that the ELM energy transport, along field lines in the SOL, is not completely dominated by electron heat conduction, there being an important contribution from convection.

The observed in-out ELM energy ratio is also qualitatively consistent with previous TCV investigations [97] but in contrast to measurements at JET [96, 98], where the Type-I ELM energy deposition at the inner divertor is approximately twice of that at the outer divertor, $E^{\mathrm{ISP}}_{\mathrm{ELM}}/E^{\mathrm{OSP}}_{\mathrm{ELM}} \approx 2$ (see figure 2 of [96]).

Conclusion of section 7.3

In conclusion, this section studied the power exhaust of Type-I ELMs in TCV, with a SN magnetic configuration. The study focusses on the ELM energy deposition time τ_{ELM}, ELM parallel energy fluence peak $\varepsilon^{\mathrm{peak}}_{\|,t}$ and ELM integral power width $\lambda^{\mathrm{ELM}}_{\mathrm{int},u}$. The duration of the ELM power deposition $\tau^{\mathrm{IR}}_{\mathrm{ELM}}$ measured in TCV is consistent with that published from larger tokamaks. The comparison of $\tau^{\mathrm{IR}}_{\mathrm{ELM}}$ in TCV and JET supports the observation, from other tokamaks, that this duration increases approximately linearly with the parallel connection length $L_{\|}$ and, therefore, with the major radius R_{geo}. The dependence of $\tau^{\mathrm{IR}}_{\mathrm{ELM}}$ on $L_{\|}$ is, therefore, favourable for the extrapolation to a nuclear fusion reactor. It also suggests that a further increase in $\tau^{\mathrm{IR}}_{\mathrm{ELM}}$ could be achieved, at fixed reactor size, by using alternative magnetic configurations that increase $L_{\|}$. The ELM peak parallel energy fluence $\varepsilon^{\mathrm{peak}}_{\|,t}$ measured in TCV is consistent with a recent multi-machine scaling law and semi-empirical model, supporting current extrapolations of this quantity to ITER. The ELM integral power width at the outer target is observed to scale with the inverse of the target flux expansion, which is due to a decreased SOL width $\lambda^{\mathrm{ELM}}_{q,u}$ at fixed spreading factor S^{ELM}_{u}. This effect of $f_{x,t}$ is rather different from that observed in L-mode, possibly indicating that SOL heat transport during the ELM transient is strongly affected by a different mechanism (e.g. convection instead of conduction). The ELM energy is observed to flow predominantly to the outer divertor, and the in-out energy ratio is, on average, lower than the prediction of a conductive power sharing model. As for the L-mode discharges, this could result from in-out asymmetric volumetric radiation and particle drifts. In addition, the ELM energy in-out ratio does not correlate with the conductive prediction, suggesting that parallel SOL heat transport during the ELM is affected by another transport mechanism (e.g. convection).

7.4 Summary and potential implications for DEMO

This chapter presented a general study of the power exhaust properties of TCV plasmas in the high-confinement mode, with the Single-Null magnetic configuration and attached, high-recycling divertors. Operation in ELM-free H-mode (section 7.1) and ELMy H-mode (sections 7.2-7.3) was discussed.

The quantities used to describe the power exhaust in stationary conditions are the SOL power width $\lambda_{q,u}$ and the spreading factor S_u. The quantities used to describe the power exhaust during ELM transients are the power flux duration $\tau^{\mathrm{IR}}_{\mathrm{ELM}}$, peak parallel energy fluence $\varepsilon^{\mathrm{peak}}_{\|,t}$ and integral power width $\lambda^{\mathrm{ELM}}_{\mathrm{int},u}$. Several interesting effects of H-mode confinement and ELM transients on SOL heat transport were observed:

- **SOL power width.** At the transition from L- to ELM-free H-mode, $\lambda_{q,u}$ substantially reduces both at the divertor targets (from IR) and at the outboard mid-plane (from Thomson scattering). This reduction is associated with a steepening of the plasma edge profiles upstream, caused by an edge transport barrier. Interpreting the change of $\lambda_{q,u}$ with the conductive model of section 5.1.2 leads to a conclusion that the cross-field heat diffusivity of the main SOL in H-mode is halved compared with L-mode. This can be interpreted as the H-mode edge transport barrier extending, across the separatrix, into the main SOL (the SOL around the confined plasma).
  For Type-I ELMy plasmas, the inter-ELM $\lambda_{q,u}$ at the inner/outer targets (from IR) is larger/smaller compared to the value at the outboard midplane (from Thomson scattering). The value at the outboard mid-plane, also, quantitatively agrees with predictions from multi-machine scaling laws as long as the toroidal magnetic field B_ϕ is used as a regression parameters. This indicates that such a B_ϕ dependence is vital and that, thus, the inclusion of unconventional aspect ratio devices in multi-machine regression should be reworked by adding an explicit aspect ratio dependence and not by simply neglecting any B_ϕ dependence.
  During the ELM transient, the ELM power width $\lambda_{q,u}^{\mathrm{ELM}}$ is found to strongly scale with the inverse of $f_{x,t}$. This effect of $f_{x,t}$ is rather different from that observed in L-mode, possibly indicating that SOL heat transport during ELM transients is dominated by a different mechanism (e.g. convection instead of conduction).

- **Spreading factor.** At the transition from L- to ELM-free H-mode, S_u substantially reduces at both divertor targets. Interpreting the change of S_u with the diffusive model of section 5.1.4, implies that the cross-field heat diffusivity of the divertor SOL in H-mode is more than halved compared to L-mode. This means that the H-mode edge transport barrier effectively extends, across the separatrix, to the divertor SOL (the SOL between x-point and targets).
  For Type-I ELMy plasmas, the inter-ELM S_u is in quantitative agreement with the prediction from the diffusive model at the outer target only, with most of the scatter in the data ascribable to the change in the ratio between divertor connection length and target flux expansion.
  During the ELM transient, the ELM spreading factor S_u^{ELM} is independent of $f_{x,t}$ at both divertor targets.

- **ELM duration and peak fluence.** The duration of the ELM power deposition at the divertor targets $\tau_{\mathrm{ELM}}^{\mathrm{IR}}$ is consistent with previously published ELM data [94, 95], supporting the observation that $\tau_{\mathrm{ELM}}^{\mathrm{IR}}$ scales near linearly with the SOL parallel connection length and, thus, the machine size. The ELM peak parallel energy fluence agrees with a recent multi-machine scaling law (equation 7.26) and with a semi-empirical model (discussed in section 5.2.2), both proposed in [63], supporting current extrapolations of this quantity to ITER, in the range of 10 to 30 MJ/m^2 for Q=10 operation (15 MA/5.3T).

The expected ELM peak *perpendicular* energy fluence at the outer ITER target, in the range of 0.6 to 1.9 MJ/m^2 [63, 99], would exceed the fatigue damage threshold of 0.1 MJ/m^2 for the ITER tungsten mono-block divertor [99, 100]. ELMs in ITER and, most likely, in DEMO must, thus, be mitigated or suppressed. However, even if such an ELM suppression/mitigation method was developed, accidental failures of the control system might occur, resulting into ELM heat loads to the divertor targets. The ELM heat load handling capability should, therefore, be an additional criteria when choosing the magnetic divertor for a fusion reactor. Among the observations of this chapter, there are some crucial divertor geometry effects on ELM heat load that may impact the choice of the magnetic divertor for a reactor:

1. **Small-$\boldsymbol{f_{x,t}}$ divertor broadens $\boldsymbol{\lambda^{\mathrm{ELM}}_{\mathrm{int},u}}$.** The measured broadening of the ELM $\lambda^{\mathrm{ELM}}_{\mathrm{int},u}$ at the outer divertor target of a SN for decreasing target flux expansion, $\lambda^{\mathrm{ELM}}_{\mathrm{int},u} \propto f_{x,t}^{-1.17}$, implies that, for a future fusion device, a small flux expansion divertor appears, quite counter-intuitively, as an advantageous choice as it increases the ELM target wetted area $A^{\mathrm{ELM}}_{\mathrm{wet}} \propto \lambda^{\mathrm{ELM}}_{\mathrm{int},u}$ (at fixed field line grazing angle at the target, equation 4.44), reducing target peak heat fluxes, peak energy fluence and, thus, the ELM-induced target surface thermal stress. Furthermore, a low $f_{x,t}$ divertor also has attractive power exhaust properties in steady-state, as chapter 6 shows that, in L-mode, the spreading factor scales as $S_u \propto f_{x,t}^{-0.97}$, implying that a small $f_{x,t}$ divertor increases the heat wetted area also in stationary conditions.
2. **Alternative magnetic configurations increase $\boldsymbol{\tau^{\mathrm{IR}}_{\mathrm{ELM}}}$.** The TCV data supports the observation that $\tau^{\mathrm{IR}}_{\mathrm{ELM}}$, the ELM power deposition time measured at the targets by IR, scales almost linearly with the SOL parallel connection length $L_{\parallel}$. As a result, alternative magnetic configurations, that increase $L_{\parallel}$, would have a beneficial effect on ELM heat exhaust, increasing $\tau^{\mathrm{IR}}_{\mathrm{ELM}}$ and, thus, reducing the ELM-induced divertor target surface temperature rise $\Delta T_{\mathrm{ELM}} \propto (\tau^{\mathrm{IR}}_{\mathrm{ELM}})^{-1/2}$, equation 5.58.

8 Conclusions

This doctoral thesis contributes to the fusion research efforts by experimentally assessing the power exhaust properties of an unprecedented range of alternative magnetic configurations, generated in a single device, the TCV tokamak. It, more specifically, identifies ways to reduce the power exhaust challenge, envisaged for next-step fusion devices, by experimentally identifying modifications to the magnetic divertor geometry that increase the target heat deposition area. This work also improves our understanding of Scrape-Off Layer (SOL) heat and particle physics, by testing existing models and empirical regressions over a wide range of operational scenarios and divertor shapes, thus increasing the confidence in current extrapolations for a future fusion reactor.

The power exhaust of attached magnetic configurations is characterized by three key quantities, all estimated using TCV's infrared (IR) thermography systems. These are the power sharing between the inner and outer divertor targets, $P_{\text{in}}/P_{\text{out}}$, the SOL power width $\lambda_{q,u}$ and the divertor spreading factor S_u. In addition, a value for the SOL power width upstream is estimated from Thomson scattering and/or an outboard mid-plane fast reciprocating probe. To be able to collect data for this wide range of regimes and divertor geometries, major improvements to the IR system were performed as part of the thesis. These include a new control software for the IR cameras and its integration in the TCV shot cycle, upgrades to the routines that process IR data and the commissioning of a third infrared system, to observe divertor leg heat deposition on the outside wall.

The experimental investigation commences with plasmas in the low-confinement mode (L-mode), as they are simpler to diagnose. The magnetic geometries are first varied from the standard Single-Null (SN) divertor, retaining a SN topology, see section 6.1. The four divertor geometry parameters divertor leg length, target flux expansion, plasma triangularity, target radius, and the two core parameters plasma current and magnetic field direction are varied. It is found that:

- The power sharing between the inner and outer divertor targets can significantly vary with changes to the plasma and/or divertor geometry. Many of these observations can be ascribed to the effect of parallel electron heat conduction in the SOL. Systematic offsets between the measurements and the conductive predictions that, in particular, vary with magnetic field direction suggest that one, or more, additional mechanisms affect power sharing. In-out asymmetries in volumetric radiation losses clearly introduce such offsets. Since these offsets depend on the field direction, particles drifts must also be important, either directly by adding convective components to the heat exhaust or by affecting the radiation pattern, which also varies with field direction.

- The SOL width $\lambda_{q,u}$ is sensitive to almost every scanned parameter. In addition, poloidal asymmetries of $\lambda_{q,u}$ were observed when comparing values at the inner and outer target and outboard mid-plane. Some scanned parameters affect $\lambda_{q,u}$ poloidally everywhere, whereas others the $\lambda_{q,u}$'s at the targets with no effect upstream. The $\lambda_{q,u}$'s at the targets and upstream decrease with increasing plasma current I_P, and a conductive model of the SOL transport with some assumptions on the cross-field heat diffusivity can yield an I_P dependence in the observed range. The $\lambda_{q,u}$ at the outer target increases with increased outer divertor leg length more strongly than predicted by the conductive model. Turbulent simulations support the hypothesis that this L_div dependence may be due to a stronger turbulent perpendicular transport in the divertor leg towards the common flux region than towards the private flux region. The $\lambda_{q,u}$ at the outer target and upstream increase for a higher upper triangularity. Concomitantly, the edge electron temperature and the plasma stored energy both reduce, consistent with a degradation of plasma confinement inside the separatrix due to increased turbulent transport in the edge region. The increased $\lambda_{q,u}$, therefore, suggests that such an enhanced turbulent transport may propagate across the separatrix into the SOL. The $\lambda_{q,u}$ at the outer target is compared with multi-machine scaling laws, finding a good agreement with the AUG-JET and MAST scalings (within 30%). The H-mode scaling law, with $\langle B_p \rangle$ as unique regression parameter, however, overestimates TCV's L-mode data. This is quite surprising, as in other tokamaks the $\lambda_{q,u}$ in L-mode is ~ 2 times broader than in H-mode for fixed value of $\langle B_p \rangle$.
- The divertor spreading factor S_u scales as the inverse of the target flux expansion, whilst remaining insensitive to most other parameters. Part of this $f_{x,t}$ dependence can be explained by diffusive transport as the target $f_{x,t}$ increases faster than the divertor parallel connection length. The resulting spreading factor at the target and orthogonal to flux surfaces, $S_t = S_u f_x$, has, therefore, a constant value (≈ 6 mm).

The SN topology is then modified to create a Snowflake Minus (SF-) divertor, see section 6.2. The varied quantities are the x-point separation, the relative positioning of primary and secondary nulls and the magnetic field direction. The secondary x-point has no effect on upstream transport, for both LFS and HFS SF-, whereas it enhances cross-field transport in the divertor of the LFS SF-. Such an enhancement between the x-points is supported by recent turbulent simulations. The in-out power sharing varies with the x-point distance $\mathrm{d}r_{\mathrm{x}2}$. Similarly to the SN configuration, this power sharing variation can be explained by electron conduction for the RF direction, but not for the FF direction where another physical mechanism dominates (e.g. particle drifts). Adding an x-point on one side of the SOL is found to divert exhaust power to the other, and the LFS SF- configuration increases the peak heat loads at the inner divertor, complicating the heat handling compared to the standard SN.

The divertor operational regime is then made to make a gradual transition from an attached to a detached regime, by divertor fuelling or nitrogen impurity seeding, while the geometry remains a SN configuration, see section 6.3. When seeding nitrogen, both targets detach simultaneously, with the deposited power on both targets decreasing in a similar way but the wetted area increasing solely at the inner target. Divertor detachment through fueling ramps has a stronger effect on the heat wetted area at the target. This increase of A_{wet} is primarily from an increased $\lambda_{q,u}$, in the outer divertor SOL, leaving the main SOL and inner divertor SOL unaffected.

When overviewing these observations, some crucial divertor geometry effects, that may have significant implications in the choice of the magnetic divertor for a reactor, can be identified:

- The effect of divertor geometry on the in-out power sharing implies that alternative configurations have a higher $P_{\mathrm{in}}/P_{\mathrm{out}}$, compared to the SN, as a result of an increased parallel connection length to the outer divertor target. A power exhaust solution at the outer divertor achieved via modifications of the magnetic configuration may, thus, come at the expense of increasing the exhaust challenge at the inner divertor.
- The increase of $\lambda_{q,u}$ and decrease of P_{out} associated to a long-legged divertor imply that such a configuration is highly beneficial for the power exhaust of the outer target, reducing target peak heat fluxes and facilitating access to divertor detachment, at the expense of increased heat to the inner target.
- The increase in S_u for a decreased flux expansion implies that a small $f_{x,t}$ configuration appears, quite counter-intuitively, beneficial to the power exhaust of the outer target, reducing target peak heat fluxes and facilitating access to divertor detachment (assuming a fixed field line grazing angle at the target).

The investigation extends, in chapter 7, to plasmas in the high-confinement mode (H-mode), considering two variants of H-mode operation, the ELMy H-mode and ELM-free H-mode:

- The study first investigates the effect of the transition from L- to ELM-free H-mode on target heat loads, in a standard Single-Null configuration, see section 7.1. At the transition from L- to ELM-free H-mode, both the SOL heat channel width (at targets and outboard mid-plane) and the spreading factor S_u narrow by a factor ≈ 2. The simultaneous reduction indicates not only a reduction of the effective cross-field diffusivity in the main SOL, but also in the divertor. This suggests that the edge transport barrier extends into the SOL and propagates, along open field lines, into the divertor.

- The study then investigates target heat loads in-between ELMs for Type-I ELMy H-mode plasmas in the Single Null configuration, see section 7.2. The SOL power widths measured at the outboard mid-plane, by Thomson scattering, are found to be in quantitative agreement with predictions from multi-machine scaling laws where the toroidal magnetic field B_ϕ is included as a regression parameter, but not with the $\langle B_p \rangle$ scaling alone. This indicates that the B_ϕ dependence is vital, i.e. the toroidal field plays a role into the physics setting the SOL power width. The inclusion of unconventional aspect ratio devices in the multi-machine regressions should, thus, be reworked by adding an explicit aspect ratio dependence rather than by simply removing the B_ϕ dependence thereby increasing the strength of the $\langle B_p \rangle$ dependence. The drift-based prediction for the SOL power width is quantitatively compatible with the measurements. Note that the drift-based model requires a similar B_ϕ dependence, that seems necessary to align TCV with other devices. The divertor spreading factor is found to be in good agreement with the prediction from a diffusive model for the outer target alone.

- Finally, target heat loads during ELMs for Type-I ELMy H-mode plasmas in the Single Null configuration are investigated, see section 7.3. This study focusses on the ELM energy deposition time τ_{ELM}, ELM parallel energy fluence peak $\varepsilon_{\parallel,t}^{\mathrm{peak}}$ and ELM integral power width $\lambda_{\mathrm{int},u}^{\mathrm{ELM}}$. The duration of the ELM power deposition $\tau_{\mathrm{ELM}}^{\mathrm{IR}}$ is consistent with that from larger tokamaks. The comparison of $\tau_{\mathrm{ELM}}^{\mathrm{IR}}$ in TCV and JET supports the observation, from other tokamaks, that this duration increases approximately linearly with the parallel connection length $L_\parallel$ and, therefore, with the major radius R_{geo}. The ELM peak parallel energy fluence $\varepsilon_{\parallel,t}^{\mathrm{peak}}$ is consistent with a recent multi-machine scaling law and semi-empirical model, supporting current extrapolations to ITER. The ELM integral power width at the outer target is observed to scale with the inverse of the target flux expansion, observed as a decreased SOL width $\lambda_{q,u}^{\mathrm{ELM}}$ at fixed spreading factor S_u^{ELM}. This effect of $f_{x,t}$ is different from that observed in L-mode, possibly indicating that SOL heat transport during the ELM transient is also determined by a different mechanism (e.g. convection instead of conduction). The ELM energy is observed to flow predominantly to the outer divertor, with the in-out energy ratio being, on average, lower than that predicted by a conductive power sharing model. As for the L-mode measurements, this could result from in-out asymmetric volumetric radiation and particle drifts. In addition, the ELM energy in-out ratio does not correlate with the conductive prediction, suggesting that parallel SOL heat transport during the ELM requires an additional transport mechanism (e.g. convection).

Although ELMs in ITER, and most likely DEMO, must be mitigated or suppressed, accidental failures of the ELM-mitigation/suppression system might occur, resulting into dangerous ELM heat loads to the divertor targets. The ELM heat load handling capability must, therefore, be an additional criteria when choosing the magnetic divertor for a fusion reactor. Some observations of this chapter are crucial divertor geometry effects on ELM heat load that may impact this choice:

- The increase of $\lambda_{q,u}^{\mathrm{ELM}}$ with decreased flux expansion implies that a small $f_{x,t}$ divertor reduces ELM target peak heat loads, ELM peak fluence and, thus, the ELM-induced target surface thermal stress. Furthermore, a low $f_{x,t}$ divertor also has attractive power exhaust properties in steady-state, as the L-mode analysis showed that $S_u \propto f_{x,t}^{-0.97}$, implying that a small $f_{x,t}$ divertor increases the heat wetted area also in stationary conditions.
- TCV data supports the observation that $\tau_{\mathrm{ELM}}^{\mathrm{IR}}$, the ELM power deposition time measured at the targets by IR, scales almost linearly with the SOL parallel connection length $L_{\parallel}$. Thus alternative magnetic configurations that increase $L_{\parallel}$ would have a beneficial effect on ELM heat exhaust, increasing $\tau_{\mathrm{ELM}}^{\mathrm{IR}}$ and reducing the ELM-induced divertor target surface thermal stress.

In conclusion, the results presented in this thesis show that geometrical modifications to the magnetic divertor have some potential to increase the target heat wetted area in attached regimes, therefore decreasing the challenge to provide sufficient protection of the divertor in a future nuclear fusion reactor. As such modifications would be expected to increase the engineering effort and overall costs, an optimal trade-off between improved exhaust performance and higher device costs must be found.

A Appendix

A.1 Extrapolation of calibration curve using Planck's Law

The IR cameras of TCV, described in detail in sections 2.2.1.1-2.2.1.2-2.2.1.3, are temperature calibrated in-situ, using thermocouples and heating elements embedded into dedicated carbon tiles in the field-of-view of each camera. These elements heat the tiles to a maximum of $\sim$ 200-250°C, a value that is large compared to the typical tile temperatures measured during experiments. However, during thermal transients such as Edge-Localised-Modes (ELMs) and plasma disruptions, target temperatures can exceed 250°C and, therefore, the IR cameras need to be calibrated for higher temperatures. This section describes the method that was developed to extrapolate the calibration curve beyond this limit, using Planck's Law and the Black Body theory.

Planck's Law describes the radiation spectrum emitted by a Black Body (BB) through the spectral radiance I_{BB}

$$I_{\mathrm{BB}}(\lambda, T) = \frac{2hc^2}{\lambda^5}\frac{1}{\exp\left(\frac{hc}{\lambda k_B T}\right) - 1} \qquad \left[\frac{W}{sr \cdot m^3}\right] \tag{A.1}$$

where h is the Planck constant and k_B the Boltzmann constant.
When the IR camera images a BB source, the BB power flux in the camera detector (and filter, when present) spectral range $[\lambda_1 : \lambda_2]$, per unit of solid angle and of emitting surface, is given by

$$\Gamma_{\mathrm{BB}}(T; \lambda_1, \lambda_2) = \int_{\lambda_1}^{\lambda_2} I_{\mathrm{BB}}(\lambda, T)\ d\lambda \qquad \left[\frac{W}{sr \cdot m^2}\right] \tag{A.2}$$

which yields the photon flux

$$\Phi_{\mathrm{BB}}(T; \lambda_1, \lambda_2) = \int_{\lambda_1}^{\lambda_2} \frac{I_{\mathrm{BB}}(\lambda, T)}{E(\lambda)}\ d\lambda = \int_{\lambda_1}^{\lambda_2} \frac{\lambda}{hc} I_{\mathrm{BB}}(\lambda, T)\ d\lambda \qquad \left[\frac{1}{s \cdot sr \cdot m^2}\right] \tag{A.3}$$

The number of BB photons that are measured by the IR camera during the integration time Δt_{int} is

$$N_{\text{BB}}(T; \lambda_1, \lambda_2) = \Phi_{\text{BB}}(T; \lambda_1, \lambda_2)\ \Delta t_{\text{int}}\ A_{\text{BB}}\ \Delta\Omega \tag{A.4}$$

with A_{BB} the emitting area of the BB, $\Delta\Omega$ the solid angle associated to the IR camera sensor.

When, instead, the IR camera images an object that is not a Black Body, i.e. its emissivity ε is smaller than unity, such as a carbon tile, the number of photons measured during the integration time is

$$N(T; \lambda_1, \lambda_2) = \varepsilon\ N_{\text{BB}}(T; \lambda_1, \lambda_2) = \varepsilon\ \Phi_{\text{BB}}(T; \lambda_1, \lambda_2)\ \Delta t_{\text{int}}\ A_{\text{BB}}\ \Delta\Omega \tag{A.5}$$

This shows that, at a fixed integration time of the detector, the measured number of photons $N(T)$ is linearly proportional to the photon flux $\Phi_{\text{BB}}(T)$ that would be measured for a BB source:

$$N(T) = c(\Delta t_{\text{int}})\ \Phi_{\text{BB}}(T) \tag{A.6}$$

where $c(\Delta t_{\text{int}}) = \varepsilon\ \Delta t_{\text{int}}\ A_{\text{BB}}\ \Delta\Omega$ is the constant of proportionality. The constant of proportionality $c(\Delta t_{\text{int}})$ is estimated by comparing, at fixed integration time and for a range of temperature (up to $\sim$250 °C), the IR camera signal $N(T)$ with the BB photon flux $\Phi_{\text{BB}}(T)$, which is computed using equations A.3 and A.1. For the HIR system, one finds $c = 2 \cdot 10^{-18} s\ sr\ m^2$ for $\Delta t_{\text{int}} = 0.05$ ms, while $c = 4 \cdot 10^{-18} s\ sr\ m^2$ for $\Delta t_{\text{int}} = 0.1$ ms. Once c is known, equation A.6 is used to compute $N(T)$ for temperatures beyond the in-site calibration limit (250°C).

A.2 Derivation of the Eich function

This section presents the analytic derivation of the Eich function, equation 5.5. The function, proposed first in [45], is defined as the convolution of a truncated exponential with decay length λ,

$$f(\bar{x}) = \begin{cases} q_0 \exp\left(-\frac{\bar{x}}{\lambda}\right) & \bar{x} > 0 \\ 0 & \bar{x} < 0 \end{cases} \qquad \text{and} \qquad \bar{x} = x - x_0 \tag{A.7}$$

where x is the divertor target coordinate and x_0 the strike line position, with a normalized Gaussian of width d

$$g(\bar{x}) = \frac{1}{\sqrt{\pi d}} \exp\left(-\frac{\bar{x}^2}{d}\right) \tag{A.8}$$

The convolution of $f(\bar{x})$ with $g(\bar{x})$ is

$$\begin{aligned}
h(\bar{x}) &= \int_{-\infty}^{\infty} \mathrm{dt}\ f(\bar{x}-t)\cdot g(t) \\
&= \int_{-\infty}^{\infty} \mathrm{dt}\ \begin{cases} q_0 \exp\left(-\frac{\bar{x}-t}{\lambda}\right) & \bar{x}-t>0 \\ 0 & \bar{x}-t<0 \end{cases} \quad \cdot \quad \frac{1}{\sqrt{\pi d}} \exp\left(-\frac{t^2}{d}\right) \\
&= \int_{-\infty}^{\bar{x}} \mathrm{dt} \frac{q_0}{\sqrt{\pi d}} \exp\left(-\frac{\bar{x}-t}{\lambda}\right) \exp\left(-\frac{t^2}{d}\right) \\
&= \int_{-\infty}^{\bar{x}} \mathrm{dt} \frac{q_0}{\sqrt{\pi d}} \exp\left(-\frac{d(\bar{x}-t)+\lambda t^2}{\lambda d}\right) \\
&= \int_{-\infty}^{\bar{x}} \mathrm{dt} \frac{q_0}{\sqrt{\pi d}} \exp\left(-\frac{1}{d}\left(t-\frac{d}{2\lambda}\right)^2\right) \exp\left(\frac{d}{4\lambda^2}-\frac{\bar{x}}{\lambda}\right)
\end{aligned}$$

which, after a change of variable $y = \frac{1}{\sqrt{d}}\left(t-\frac{d}{2\lambda}\right)$, becomes

$$= \frac{q_0}{\sqrt{\pi}} \exp\left(\frac{d}{4\lambda^2}-\frac{\bar{x}}{\lambda}\right) \int_{-\infty}^{\frac{1}{\sqrt{d}}\left(\bar{x}-\frac{d}{2\lambda}\right)} \mathrm{dy} \exp(-y^2)$$

using $\frac{d}{dz}\mathrm{erf}(z) = \frac{2}{\sqrt{\pi}}\exp(-z^2)$ yields

$$\begin{aligned}
&= \frac{q_0}{2} \exp\left(\frac{d}{4\lambda^2}-\frac{\bar{x}}{\lambda}\right) \left(\mathrm{erf}(y)\right]_{-\infty}^{\frac{1}{\sqrt{d}}\left(\bar{x}-\frac{d}{2\lambda}\right)} \\
&= \frac{q_0}{2} \exp\left(\frac{d}{4\lambda^2}-\frac{\bar{x}}{\lambda}\right) \left[1+\mathrm{erf}\left(\frac{1}{\sqrt{d}}\left(\bar{x}-\frac{d}{2\lambda}\right)\right)\right]
\end{aligned}$$

using the identity $1+\mathrm{erf}(-z) = \mathrm{erfc}(z)$ yields

$$= \frac{q_0}{2} \exp\left(\frac{d}{4\lambda^2}-\frac{\bar{x}}{\lambda}\right) \mathrm{erfc}\left(\frac{\sqrt{d}}{2\lambda}-\frac{\bar{x}}{\sqrt{d}}\right)$$

Finally, writing the gaussian width as $\sqrt{d} = S_t^* = S_u f_{x,t}^*$ and the fall-off length as $\lambda = \lambda_{q,u} f_{x,t}^*$, one obtains

$$\boxed{h(\bar{x}) = \frac{q_0}{2} \exp\left[\left(\frac{S_u}{2\lambda_{q,u}}\right)^2 - \frac{\bar{x}}{\lambda_{q,u} f_{x,t}^*}\right] \mathrm{erfc}\left(\frac{S_u}{2\lambda_{q,u}} - \frac{\bar{x}}{S_u f_{x,t}^*}\right)} \tag{A.9}$$

that corresponds to the Eich function, equation 5.5.

A.3 1-D heat diffusion in a semi-infinite slab

This section presents the derivation of equation 5.54, which is the analytical solution of the heat diffusion equation for the special case of a semi-infinite slab, exposed to a spatially uniform and time constant heat flux density q_s [1]. The heat equation is

$$\frac{\partial T(y,t)}{\partial t} = D\frac{\partial^2 T(y,t)}{\partial y^2} \tag{A.10}$$

where y is the coordinate perpendicular to the slab surface and D the thermal diffusivity of the material, whose dependence on T is neglected, defined as

$$D = \frac{k}{\rho c_p} \tag{A.11}$$

with ρ the density, c_p the specific heat capacity. At $t = 0$, the temperature of the slab is T_i and a constant (in time and space) heat flux density q_s impinges on the slab surface. The boundary conditions, therefore, are

- $T(y,0) = T_i$
- $\lim_{y\to\infty} T(y,t) = T_i$
- $-k\frac{\partial T}{\partial y}|_{y=0} = q_s$

After a change of variable to $\theta(y,t) = T(y,t) - T_i$, the heat equation becomes

$$\frac{\partial \theta(y,t)}{\partial t} = D\frac{\partial^2 \theta(y,t)}{\partial y^2} \tag{A.12}$$

and the boundary conditions translate to

- $\theta(y,0) = 0$
- $\lim_{y\to\infty} \theta(y,t) = 0$
- $-k\frac{\partial \theta}{\partial y}|_{y=0} = q_s$

Application of the Laplace transform to both sides of equation A.12 yields

$$s\;\bar{\theta}(y,s) - \theta(y,0) = D\frac{\partial^2 \bar{\theta}(y,t)}{\partial y^2} \tag{A.13}$$

---

[1] The derivation follows the lecture 12 "Heat Conduction in Semi-infinite Slab with Constant Flux density at the wall", module 2 "Diffusive heat and mass transfer" of Prof. Saikat Chakraborty (Department of Chemical Engineering, IIT Kharagpur), available as on-line course in the Nptel (National Programme on Technology Enhanced Learning, https://nptel.ac.in/course.html).

where $\bar{\theta}(s) = \mathscr{L}(\theta(t))$ is the Laplace transform of $\theta(t)$. Since $\theta(y,0) = 0$, one obtains a second order differential equation in y,

$$\frac{\partial^2 \bar{\theta}(y,s)}{\partial y^2} - \frac{s}{D}\bar{\theta}(y,s) = 0 \tag{A.14}$$

whose general solution is of the form

$$\bar{\theta}(y,s) = C_1 \exp\left(y\sqrt{\frac{s}{D}}\right) + C_2 \exp\left(-y\sqrt{\frac{s}{D}}\right) \tag{A.15}$$

The boundary condition at $y = \infty$ implies that $C_1 = 0$, that at the slab surface determines the value of C_2,

$$\mathscr{L}\left(-k\frac{\partial\theta}{\partial y}|_{y=0}\right) = -k\frac{\partial\bar{\theta}}{\partial y}|_{y=0} = \mathscr{L}(q_s) = s\ q_s \quad \rightarrow \quad C_2 = \frac{q_s}{s\ k}\sqrt{\frac{D}{s}} \tag{A.16}$$

so that the solution becomes

$$\bar{\theta}(y,s) = \frac{q_s}{s\ k}\sqrt{\frac{D}{s}} \exp\left(-y\sqrt{\frac{s}{D}}\right) \tag{A.17}$$

To perform the Laplace anti-transform of equation A.17, one can use the property that, for any given function $f(t)$, with Laplace transform $\bar{f}(s)$, it holds the relation

$$\mathscr{L}\left(\int_0^t f(t')dt'\right) = \frac{\bar{f}(s)}{s} \tag{A.18}$$

and the tabled inversion[2]

$$\mathscr{L}^{-1}\left(\frac{1}{\sqrt{s}}\exp\left(-y\sqrt{\frac{s}{D}}\right)\right) = \frac{1}{\sqrt{\pi t}}\exp\left(-\frac{y^2}{4Dt}\right) \tag{A.19}$$

Recognising that the r.h.s. of equation A.17 can be written as the r.h.s. of equation A.18 with

$$\bar{f}(s) = \frac{q_s}{k}\sqrt{\frac{D}{s}} \exp\left(-y\sqrt{\frac{s}{D}}\right) \tag{A.20}$$

and then performing the Laplace anti-transform, yields

$$\mathscr{L}^{-1}(\bar{\theta}) = \frac{q_s}{k}\sqrt{\frac{D}{\pi}}\int_0^t dt'\frac{1}{\sqrt{t'}}\exp\left(-\frac{y^2}{4Dt}\right) = \theta(y,t) \tag{A.21}$$

---

[2] [H.S. Mickley, T.S. Sherwood, and C.E. Reed, Applied Mathematics in Chemical Engineering., McGraw-Hill, 1979]

which is the solution of the heat equation in the time domain. To perform the integration, it is convenient to use the similarity variable $\eta = y/\sqrt{4Dt}$, and then integrate by parts,

$$
\begin{aligned}
\theta(y,t) &= \frac{q_s y}{k\sqrt{\pi}} \int_{\frac{y}{\sqrt{4Dt}}}^{\infty} d\eta \frac{1}{\eta^2} e^{-\eta^2} = \\
&= \frac{q_s}{k}\left[\sqrt{\frac{4Dt}{\pi}} \exp\left(-\frac{y^2}{4Dt}\right) - y \operatorname{erfc}\left(\frac{y}{\sqrt{4Dt}}\right)\right]
\end{aligned}
$$

where $\operatorname{erfc}(z) = \frac{2}{\pi}\int_z^\infty e^{-q^2} dq$. Finally, the temperature in the slab is

$$T(y,t) = T_i + \frac{q_s}{k}\left[\sqrt{\frac{4Dt}{\pi}} \exp\left(-\frac{y^2}{4Dt}\right) - y \operatorname{erfc}\left(\frac{y}{\sqrt{4Dt}}\right)\right] \tag{A.22}$$

and the increase of the surface temperature, relative to the initial value T_i, is

$$\boxed{\Delta T_s(t) = T(0,t) - T_i = \frac{q_s}{k}\sqrt{\frac{4Dt}{\pi}} = \frac{2}{\sqrt{\pi}} \frac{q_s}{\sqrt{k\rho c_p}} \sqrt{t}} \tag{A.23}$$

which corresponds to equation 5.54.

A.4 The THEODOR code

This section briefly summarizes the principles and the functioning of the THEODOR code[25, 93] (THermal Energy Onto DivertOR). In a tokamak, the problem of heat diffusion in the divertor plate can be treated as a 2-D problem. The heat impinging on the divertor plate diffuses perpendicularly to the target surface (y coordinate), along the target surface in the radial direction (x coordinate) but not along the toroidal direction because, due to the toroidal symmetry of the tokamak, toroidal temperature gradients are very weak compared to radial gradients or gradients across the plate. The THEODOR code, therefore, solves the heat diffusion equation along the x and y directions, using the measured target temperature as a boundary condition. Once the temperature in the divertor plate is known, the code compute the heat flux perpendicular to the target surface.

2-D heat diffusion equation The 2-D heat diffusion equation implemented in THEODOR is

$$\rho c_p \frac{\partial T}{\partial t} = \nabla(k\ \nabla T) \qquad \text{with } T = T(x,y;t) \tag{A.24}$$

where ρ is the target density, c_p the specific heat capacity, k is the thermal conductivity. Both c_p and k have a dependence on the temperature T. A heat flux potential U is introduced [101]

$$U(T) = \int_0^T k(T')\mathrm{d}T' \tag{A.25}$$

to write the heat diffusion equation in a simpler form

$$\boxed{\frac{\partial U}{\partial t} = \frac{k}{\rho c_p}\frac{\partial^2 U}{\partial t^2} = D\frac{\partial^2 U}{\partial t^2}} \tag{A.26}$$

where D the thermal diffusivity of the target material. The temperature dependence of k and c_p is approximated by the analytic function

$$f(T) = a + b\left(1 + \frac{T}{T_0}\right)^{-2} \tag{A.27}$$

where the coefficients a, b, and T_0 are estimated using the values of k and c_p at three reference temperatures, typically 0°C, 500°C and 1000°C.

Numerical solution of heat equation In THEODOR, the partial differential equation A.26 is solved numerically using the explicit (i.e. forward) Euler method. Note that an implicit solving method also exists, but was not used for the data analysis of this thesis. The poloidal cut of the divertor plate is modelled by a grid, with spatial resolution Δx and Δy in the x and y directions respectively. To have the numerical stability of the method, the time step Δt must fulfill the Courant-Friedrichs-Lewy condition,

$$\frac{D\ \Delta t}{\min(\Delta x^2, \Delta y^2)} < 0.5 \tag{A.28}$$

The solution $U(x, y; t)$ is calculated for each time step, prescribing the following conditions at the physical boundaries of the slab

$$\frac{\partial T}{\partial x} = 0 \qquad \text{slab lateral sides} \tag{A.29}$$

$$T(x, y_b) = T_b \qquad \text{slab rear side} \tag{A.30}$$

with T_b the prescribed temperature at the back of the slab (typically room temperature). Also, another boundary condition is needed for the slab surface, to account for the presence of a deposited layer of composite material. Because of this layer, the temperature measured on the surface of the layer $T_s(x)$ is different from that on the top of the slab (i.e. below the layer) $T(x, 0)$. Using Fourier's law for the heat flux impinging onto the surface layer

$$q_s(x) = -k_{\text{layer}}\frac{\partial T}{\partial y} \tag{A.31}$$

it is possible to extract the temperature below the layer, i.e. on the top of the slab

$$T(x, 0) = T_s(x) - q_s \frac{d_{\text{layer}}}{k_{\text{layer}}} = T_s(x) - q_s \frac{1}{\alpha} \qquad \text{slab front side} \tag{A.32}$$

where

$$\boxed{\alpha = \frac{k_{\text{layer}}}{d_{\text{layer}}}} \tag{A.33}$$

is known as the surface layer heat transmission factor, measured in [W m^{-2} K^{-1}]. Equation A.32 is the last boundary condition to the heat equation A.26 in the slab. Since the composition of the surface layer is unknown, a value for α needs to be estimated from the experiment, as explained in section 3.2.3. Note that, unlike the k of the bulk material, the surface layer α does not depend on the temperature.

Estimation of target heat flux After solving the heat equation for $U(x, y; t)$, using the measured surface temperature evolution $T_s(x, t)$ and the boundary conditions described above, the heat flux profile at the surface is calculated using again Fourier's law,

$$q_s(y) = -k \frac{\partial T}{\partial x} = -\frac{\partial U}{\partial x} \tag{A.34}$$

where the spatial gradient of U is computed using the three top most grid points in the x direction.

A.5 SOL poloidal heat flux profile upstream

This section presents the derivation of equation 5.29, the SOL poloidal heat flux profile at the outboard mid-plane. Consistently with the hypotheses of the conductive model of section 5.1.2, the exhaust power is assumed to cross the LCFS and enter the SOL at the outboard mid-plane, through a finite toroidally-symmetric surface of small vertical extent Δz. The heat flux perpendicular to flux surfaces is assumed to be described by an exponential profile with characteristic fall-off length $\lambda_{q,u}$,

$$q_\perp(r_u) = q_{\perp,0}\; e^{-(r_u - R_u)/\lambda_{q,u}} \tag{A.35}$$

where r_u is the radial coordinate, at the outboard midplane. With no heat sinks or sources in the SOL, the divergence of the heat flux is null, $\nabla \cdot \vec{q} = 0$. This implies that, for a toroidally-symmetric volume with small radial extent Δr and vertical extent Δz, located at the outboard mid-plane, it holds the power balance relation

$$(q_{p,u}^{\text{in}} + q_{p,u}^{\text{out}}) \cdot 2\pi r_u \Delta r = q_\perp(r_u) \cdot 2\pi r_u \Delta z - q_\perp(r_u + \Delta r) \cdot 2\pi(r_u + \Delta r)\Delta z \tag{A.36}$$

which becomes, in the limit of $\Delta r \to 0$,

$$(q_{p,u}^{\mathrm{in}} + q_{p,u}^{\mathrm{out}}) = -\frac{\nabla_r (q_\perp r_u)}{r_u} \Delta z \tag{A.37}$$

Using equation A.35 for $q_\perp$ yields

$$(q_{p,u}^{\mathrm{in}} + q_{p,u}^{\mathrm{out}}) = -\frac{\Delta z}{r_u} \nabla_r \left(q_{\perp,0}\ r\ e^{-(r_u - R_u)/\lambda_{q,u}} \right) \tag{A.38}$$

$$= -\frac{\Delta z\ q_{\perp,0}}{r_u}\ e^{-(r_u - R_u)/\lambda_{q,u}} \left(1 - \frac{r_u}{\lambda_{q,u}} \right) \tag{A.39}$$

where the constant $q_{\perp,0}$ can be expressed in terms of the power entering the SOL,

$$P_{\mathrm{SOL}} = \int_{R_u}^{\infty} 2\pi r_u (q_{p,u}^{\mathrm{in}} + q_{p,u}^{\mathrm{out}}) \mathrm{d}r_u = 2\pi R_u \Delta z q_{\perp,0} \tag{A.40}$$

which yields

$$(q_{p,u}^{\mathrm{in}} + q_{p,u}^{\mathrm{out}}) = \frac{P_{\mathrm{SOL}}}{2\pi R_u \lambda_{q,u}}\ e^{-(r_u - R_u)/\lambda_{q,u}} \left(1 - \frac{r_u}{\lambda_{q,u}} \right) \tag{A.41}$$

Since $\lambda_{q,u}$ is much smaller than r_u, and defining $\mathrm{d}r_u = r_u - R_u$, one finally obtains

$$(q_{p,u}^{\mathrm{in}} + q_{p,u}^{\mathrm{out}}) = \frac{P_{\mathrm{SOL}}}{2\pi R_u \lambda_{q,u}}\ e^{-\mathrm{d}r_u/\lambda_{q,u}} \tag{A.42}$$

which corresponds to equation 5.29.

A.6 Scaling relation for the target temperature

This section presents the derivation of equation 5.49, which is a scaling relation for the divertor target temperature in terms of upstream quantities and divertor geometry parameters. Following the hypotheses of the two-point model [47], included also in the conductive model of section 5.1.2, the divertor is in the attached, high-recycling regime and electron heat conduction is the dominant heat transport mechanism along the SOL. As the flux tube cross-sectional area changes with the major radius, the parallel heat flux varies as

$$q_\parallel(s_\parallel) \approx q_{\parallel,u} \cdot \frac{R_u}{R(s_\parallel)} \tag{A.43}$$

where $q_{\parallel,u}$ and R_u are parallel heat flux and major radius at the outboard mid-plane, and $s_\parallel$ the parallel distance along the flux tube from the outboard mid-plane. For simplicity, the major radius is assumed to change linearly with the distance $s_\parallel$ [58], from R_u (at the outboard mid-plane, where $s_\parallel = 0$) to R_t (at the target, where $s_\parallel = L_\parallel$),

$$R(s_\parallel) = R_u + \frac{R_t - R_u}{L_\parallel} s_\parallel = R_u + \frac{R_u}{L_\parallel}(f_R - 1)s_\parallel \tag{A.44}$$

with $f_R = R_t/R_u$. Combining equations 5.9-A.43-A.44, and integrating the resulting equation along the SOL flux tube, from the outboard mid-plane to the divertor target, yields an expression for the upstream temperature $T_{e,u}$,

$$T_{e,u}^{7/2} = T_{e,t}^{7/2} + \frac{7}{2}\frac{q_{\parallel,u}L_\parallel}{\kappa_0^e}\frac{\ln f_R}{f_R - 1} \approx \frac{7}{2}\frac{q_{\parallel,u}L_\parallel}{\kappa_0^e}\frac{\ln f_R}{f_R - 1} \tag{A.45}$$

assuming that $T_{e,t} \ll T_{e,u}$, which is normally the case in high-recycling conditions. At the divertor target, the parallel heat flux scales as [31]

$$q_{\parallel,t} \propto \gamma_s k_B T_{e,t} n_{e,t} c_{s,t} \tag{A.46}$$

with γ_s the total sheath heat transmission coefficient, k_B the Boltzmann constant, $n_{e,t}$ the electron density and $c_{s,t} \propto T_{e,t}^{1/2}$ the ion sound speed at the target. Note that this expression for $q_{\parallel,t}$ neglects the contribution of the electron-ion recombination energy. Using equation A.43 and assuming that, near the divertor plate, a fraction f_rad of the SOL power is dissipated via volumetric radiation, $q_{\parallel,t}$ can also be written as

$$q_{\parallel,t} = q_{\parallel,u} \cdot \frac{R_u}{R_t} \cdot (1 - f_\text{rad}) \tag{A.47}$$

Combining these two expressions for $q_{\parallel,t}$, assuming pressure conservation between outer mid-plane and target ($n_{e,u}T_{e,u} = 2n_{e,t}T_{e,t}$) and using equation A.45 for $T_{e,u}$, yields

$$q_{\parallel,u} \cdot \frac{R_u}{R_t} \cdot (1 - f_\text{rad}) \propto n_{e,u}\; q_{\parallel,u}^{2/7}\; L_\parallel^{2/7}\; T_{e,t}^{1/2} \left(\frac{\ln f_R}{f_R - 1}\right)^{2/7} \tag{A.48}$$

where, for realistic values of f_R (between ≈ 0.5 and ≈ 1), the factor $\left(\frac{\ln f_R}{f_R - 1}\right)^{2/7} \approx 1$ can be neglected. This leads to

$$\boxed{T_{e,t} \propto \frac{(q_{\parallel,u})^{10/7} \cdot (1 - f_\text{rad})^2}{n_{e,u}^2 L_\parallel^{4/7}} \frac{R_u^2}{R_t^2}} \tag{A.49}$$

which is equation 5.49.

B Curriculum Vitae

Roberto Maurizio

robertomaurizio91@gmail.com

EDUCATION

École Polytechnique Fédérale de Lausanne (EPFL) Lausanne, CH
Ph.D. in Plasma Physics November 2019

Padua University, Department of Physics and Astronomy Padua, IT
- Master degree in Physics, *magna cum laude* Fall 2015
- Bachelor degree in Physics Fall 2013

RESEARCH EXPERIENCE

EPFL Swiss Plasma Center (SPC) Lausanne, CH
Ph.D. candidate with Dr. H. Reimerdes and Dr. B.P. Duval Oct. 2015 - Nov. 2019

Doctoral project: "Investigating Scrape-Off Layer transport in alternative divertor geometries on the TCV tokamak"

- Responsible for the infrared (IR) thermography system on the TCV tokamak
- Structured and automatized IR acquisition and data analysis routines
- Explored plasma power exhaust of innovative magnetic divertor concepts on TCV
- Discovered strong impact of divertor geometry on SOL exhaust heat physics
- Developed new transport models explaining the link between divertor geometry and power exhaust
- Discovered new Snowflake Minus exhaust features, selected as highlight of 2017 TCV boundary research
- Investigated ELM-induced target heat load properties, selected as a highlight of 2018 TCV research

Max-Planck Institute Für Plasma Physik (IPP) Munich, DE

Master Student with Dr. G. Serianni March-August 2015

Master thesis project: "Beam property characterization by means of three beam diagnostics at BATMAN".

- Explored negative ion beam properties in a very large range of operational scenarios
- Discovered unfavorable up-down asymmetries in the beam, explained by asymmetric Cesium distribution in the beam source and local magnetic field strength

RFX laboratories Padua, IT

Bachelor Student with Dr. G. Serianni Summer 2013

Bachelor thesis project: "Analysis of the diagnostic calorimeter measurements and characterisation of the particle beam of the BATMAN experiment"

TEACHING EXPERIENCE

École Polytechnique Fédérale de Lausanne (EPFL) Lausanne, CH

Teaching Assistant 2015-2019

- Awarded distinction for excellent teaching quality from the EPFL Physics Department in 2018
- Selected as teaching assistant for General Physics I (Prof. M.Q. Tran, Prof. C. Theiler)
- Selected as teaching assistant for General Physics II (Dr. J.-P. Hogge)
- Designed and led weekly exercise session with 1-3 student assistants for 20-50 students
- Designed exercise problems and exams
- Graded problem sets and exams

Undergraduate supervisor

- Ms. Danxuan Chen, "Test of the standard infrared thermography analysis using 3D heat flux simulations in the TCV protection tiles", EPFL semester project.
- Mr. Joeri Lenaerts, "Experimental test of simple diffusive models for the Scrape-off layer heat flux spreading in the divertor of the TCV Single Null configuration", EPFL semester project.
- Ms. Claire Blaga, "Plasma isotope effect on Scrape-Off Layer transport physics in the TCV Single-Null divertor", EPFL semester project.

PEER-REVIEWED PUBLICATIONS

First author

- Maurizio R., et al, "Conduction-based model of the Scrape-Off Layer power sharing between inner and outer divertor in diverted low-density tokamak plasmas", Nucl. Materials and Energy 19 (2019)
- Maurizio R., et al, "The effect of the secondary x-point on the Scrape-Off Layer transport in the TCV Snowflake Minus divertor", Nucl. Fusion 59 (2019) 016014
- Maurizio R., et al, "Divertor power load studies for attached L-mode single-null plasmas in TCV", Nucl. Fusion 58 (2018) 016052
- Maurizio R., et al, "Characterisation of the properties of a negative hydrogen ion beam

by several beam diagnostic techniques", Nucl. Fusion 56 (2016) 066012

Co-author ** = leading contribution*

- *Faitsch M. et al, "Dependence of the L-Mode scrape-off layer power fall-off length on the upper triangularity in TCV", Plasma Phys. Control. Fusion 60 (2018) 045010
- *Gallo A., et al, "Impact of the plasma geometry on divertor power exhaust: experimental evidence from TCV and simulations with SolEdge2D and TOKAM3X", Plasma Phys. Control. Fusion 60 (2018) 014007
- *Gallo A., et al, "Effect of plasma geometry on divertor heat flux spreading: MONALISA simulations and experimental results from TCV", Nuclear Materials and Energy 12 (2017) 893-898
- Anand H., et al, "Real time magnetic control of the snowflake plasma configuration in the TCV tokamak", Nucl. Fusion 59 (2019) 126032
- Christen N., et al, "Exploring drift effects in TCV single-null plasmas with the UEDGE code", Plasma Phys. Control. Fusion 59 (2017) 105004
- Harrison J., et al, "Progress toward divertor detachment on TCV within H-mode operating parameters", Plasma Phys. Control. Fusion 61 (2019) 065024
- Labit B., et al, "Dependence on plasma shape and plasma fueling for small edge-localized mode regimes in TCV and ASDEX Upgrade", Nucl. Fusion 59 (2019) 086020
- Nespoli F., et al, "Understanding and suppressing the near scrape-off layer heat flux feature in inboard-limited plasmas in TCV", Nucl. Fusion 57 (2017) 126029
- Nespoli F., et al, "Application of a two-fluid two-point model to SolEdge2D-EIRENE simulations of TCV H-mode plasma", Nucl. Materials and Energy 18 (2019) 29-34
- Reimerdes H., et al, "TCV experiments towards the development of a plasma exhaust solution", Nucl. Fusion 57 (2017) 126007
- Theiler C., et al, "Results from recent detachment experiments in alternative divertor configurations on TCV", Nucl. Fusion 57 (2017) 072008
- Tsui C.K., et al, "Filamentary velocity scaling validation in the TCV tokamak", Phys. of Plasmas 25 (2018) 072506
- Vallar M., et al, "Status, scientific results and technical improvements of the NBH on TCV tokamak", Fusion Engineering and Design 146 (2018) 773-777
- Verhaegh K., et al, "An improved understanding of the roles of atomic processes and power balance in divertor target ion current loss during detachment", Nucl. Fusion 59 (2019) 126038
- Verhaegh K., et al, "Spectroscopic investigations of divertor detachment in TCV", Nuclear Materials and Energy 12 (2017) 1112–1117
- Vianello N., et al, "Scrape-Off Layer (SOL) transport and filamentary characteristics in high density tokamak regimes", Nucl. Fusion 60 (2020) 016001

Reviewer

Reviewed journal papers for *Nuclear Fusion* (3) and *Plasma Science and Technology* (1).

CONFERENCE PRESENTATIONS

- Maurizio R., et al, "Challenging current alternative divertor concepts", oral presentation, 61st APS Conference on Plasma Physics (October 21-25, 2019), Ft. Lauderdale, USA
- Maurizio R., et al, "The effect of the secondary x-point on the Scrape-Off Layer transport in the TCV Snowflake Minus divertor", poster presentation, 23rd International Conference on Plasma Surface Interactions in Controlled Fusion Devices (June 17-22, 2018), Princeton, USA
- Maurizio R., et al, "Divertor heat flux characterisation during detachment experiments in TCV", poster presentation, 44th EPS Conference on Plasma Physics (June 26-30, 2017), Belfast, UK
- Maurizio R., et al, "Infrared measurements of the heat flux spreading under variable divertor geometries in TCV", poster presentation, 43rd EPS Conference on Plasma Physics (July 4-8, 2016), Leuven, BE

SKILLS

Young, self-motivated and hard-working scientist with strong communications skills developed from undergraduate teaching experience and ability to work independently or as a part of a team. Special skills in the following areas:

- **Teaching and mentoring**
- **Communication**: proficient in oral speaking and scientific writing.
- **Data analysis**: structured large amount of experimental data, developed critical analysis strategies
- **Software**: proficient in Matlab, IDL, C++, Latex, Origin, MS Office, Python.
- **Languages**: English (Proficient, C2), French (Fluent, B2), Italian (Mother tongue), German (Basic, A2).

REFERENCES

Holger Reimerdes, Ph.D.
Senior researcher
Swiss Plasma Center
École Polytechnique Fédérale de Lausanne
EPFL SB SPC, Station 13
CH-1015 Lausanne, Switzerland
holger.reimerdes@epfl.ch

Ursel Fantz, Ph.D.
Head of ITER Technology & Diagnostics Division
Max-Planck Institute Für Plasma Physik (IPP)
Boltzmannstrasse 2
D-85748 Garching, Germany
ursel.fantz@ipp.mpg.de

Gianluigi Serianni, Ph.D.
Senior researcher
Consorzio RFX
University of Padua
Corso Stati Uniti 4
I-35127 Padua, Italy
gianluigi.serianni@igi.cnr.it

Bibliography

[1] International Energy Agency. *World Energy Outlook 2018.* 2018. https://www.iea.org/weo2018/.

[2] J. Stangeby. *Plasma Physics and Fusion Energy.* Cambridge University Press, 2007.

[3] J. Wesson. *Tokamaks.* Oxford University Press, 2004.

[4] A. Loarte et al. Chapter 4: Power and particle control. *Nucl. Fusion*, 47(6):203–263, 2007. doi: 10.1088/0029-5515/47/6/S04.

[5] R.A. Pitts et al. Physics conclusions in support of ITER W divertor monoblock shaping. *Nucl. Mater. Energy*, 12:60–74, 2017. doi: 10.1016/j.nme.2017.03.005.

[6] G. Federici et al. Overview of EU DEMO design and R&D activities. *Fusion Engineering and Design*, 89(7-8):882–889, 2014. doi: 10.1016/j.fusengdes.2014.01.070.

[7] H. Reimerdes et al. Assessment of Alternative Divertor Configurations for a European DEMO. *46th EPS Plasma Physics Conference (Milan, Italy, July 8-12 2019)*, 2019.

[8] F. Hofmann et al. Creation and control of variably shaped plasmas in TCV. *Plasma Phys. Control. Fusion*, 36(12B):B277–B287, 1994. doi: 10.1088/0741-3335/36/12B/023.

[9] F. Hofmann. FBT - a free-boundary tokamak equilibrium code for highly elongated and shaped plasmas. *Computer Phys. Communic.*, 48(2):207–221, 1988. doi: 10.1016/0010-4655(88)90041-0.

[10] J.-M. Moret et al. Tokamak equilibrium reconstruction code LIUQE and its real time implementation. *Fusion Engineering and Design*, 91:1–15, 2015. doi: 10.1016/j.fusengdes.2014.09.019.

[11] J.-M. Moret. Magnetic measurements on the TCV Tokamak. *Rev. Sci. Instrum.*, 69(6):2333–2348, 1998. doi: 10.1063/1.1148940.

[12] R.A. Pitts et al. The design of central column protection tiles for the TCV tokamak. *Nucl. Fusion*, 39(10):1433, 1999. doi: 10.1088/0029-5515/39/10/306.

[13] H. Reimerdes et al. TCV divertor upgrade for alternative magnetic configurations. *Nucl. Mater. Energy*, 12:1106–1111, 2017. doi: 10.1016/j.nme.2017.02.013.

[14] M. Planck. *The theory of heat radiation.* P. Blakiston's Son & CO., 1914.

[15] O. Février et al. Analysis of wall-embedded Langmuir probe signals in different conditions on the Tokamak à Configuration Variable. *Rev. Sci. Instrum.*, 89(5):053502, 2018. doi: 10.1063/1.5022459.

[16] J.A. Boedo et al. Fast scanning probe for the NSTX spherical tokamak. *Rev. Sci. Instrum.*, 80(12):123506, 2009. doi: 10.1063/1.3266065.

[17] C. K. Tsui et al. Poloidal asymmetry in the narrow heat flux feature in the TCV scrape-off layer. *Phys. Plasmas*, 24(6):062508, 2017. doi: 10.1063/1.4985075.

[18] C. K. Tsui et al. Accounting for Debye sheath expansion for proud Langmuir probes in magnetic confinement fusion plasmas. *Rev. Sci. Instrum.*, 89(1):013505, 2018. doi: 10.1063/1.4995353.

[19] I.H. Hutchinson. *Principles of Plasma Diagnostics.* Cambridge University Press, 2005.

[20] S. Franke. Application of Thomson Scattering at 1.06 μm as a diagnostic for spatial profile measurements of electron temperature and density on the TCV tokamak, 1997. École Polytechnique Fédérale de Lausanne (EPFL).

[21] A. Pitzschke. Pedestal Characteristics and MHD Stability of H-Mode Plasmas in TCV, 2011. École Polytechnique Fédérale de Lausanne (EPFL), doi: 10.5075/epfl-thesis-4917.

[22] J. Fuchs et al. Radiation distribution and energy balance during type-I ELMs in ASDEX Upgrade. *J. Nucl. Mater.*, 337-339(1-3 SPEC. ISS.):756–760, 2005. doi: 10.1016/j.jnucmat.2004.09.054.

[23] G. Matthews et al. Divertor energy distribution in JET H-modes. *J. Nucl. Mater.*, 290-293:668–672, 2001. doi: 10.1016/S0022-3115(00)00482-7.

[24] J. Márki et al. Sheath heat transmission factors on TCV. *J. Nucl. Mater.*, 363-365(1-3):382–388, 2007. doi: 10.1016/j.jnucmat.2007.01.197.

[25] A. Herrmann et al. Limitations for divertor heat flux calculations of fast events in tokamaks. *28th EPS Conf. on Controlled Fusion and Plasma Physics (Funchal, Portugal, 18–22 June 2001)*, pages 2109–2112, 2001. www.cfn.ist.utl.pt/EPS2001/fin/authors/nav/AutH02fr.html.

[26] C.D. Kuglin and D.C. Hines. The phase correlation image alignment method. *Proc. of IEEE Int. Conf. on Cybernetics and Society, New York, NY, USA*, pages 163–165, 1975.

[27] H. Foroosh et al. Extension of phase correlation to subpixel registration. *IEEE Transactions on Image Processing*, 11(3):188–199, 2002. doi: 10.1109/83.988953.

[28] C. Marini. Poloidal CX visible light plasma rotation diagnostics in TCV, 2017. École Polytechnique Fédérale de Lausanne (EPFL), doi: 10.5075/epfl-thesis-8031.

[29] G. Paganini Canal. Sawtooth generated magnetic islands and the properties of the snowflake divertor, 2014. École Polytechnique Fédérale de Lausanne (EPFL), doi: 10.5075/epfl-thesis-6272.

[30] F. Piras et al. Measurement of the magnetic field errors on TCV. *Fusion Engineering and Design*, 85(5):739–744, 2010. doi: 10.1016/j.fusengdes.2010.04.049.

[31] P.C. Stangeby. *The Plasma Boundary of Magnetic Fusion Devices.* Institute of Physics Publishing Bristol and Philadelphia, 2000.

[32] F. Nespoli. Scrape-Off Layer physics in limited plasmas in TCV, 2017. École Polytechnique Fédérale de Lausanne (EPFL), doi: 10.5075/epfl-thesis-7475.

[33] A. Loarte et al. Multi-machine scaling of the divertor peak heat flux and width for L-mode and H-mode discharges. *J. Nucl. Mater.*, 266:587–592, 1999. doi: 10.1016/S0022-3115(98)00590-X.

[34] M. Kotschenreuther et al. On heat loading, novel divertors, and fusion reactors. *Phys. Plasmas*, 14(7):072502, 2007. doi: 10.1063/1.2739422.

[35] H. Takase. Guidance of Divertor Channel by Cusp-Like Magnetic Field for Tokamak Devices. *J. Phys. Soc. Japan*, 70(3):609–612, 2015. doi: 10.1143/JPSJ.70.609.

[36] M. Kotschenreuther et al. Magnetic geometry and physics of advanced divertors: The X-divertor and the snowflake. *Phys. Plasmas*, 20(10):102507, 2013. doi: 10.1063/1.4824735.

[37] P.M. Valanju et al. Super-X divertors and high power density fusion devices. *Phys. Plasmas*, 16(5):056110, 2009. doi: 10.1063/1.3110984.

[38] I.H. Hutchinson et al. Thermal front analysis of detached divertors and MARFEs. *Nucl. Fusion*, 34(10):1337, 1994. doi: 10.1088/0029-5515/34/10/I04.

[39] B. Lipschultz et al. Sensitivity of detachment extent to magnetic configuration and external parameters. *Nucl. Fusion*, 56(5):056007, 2016. doi: 10.1088/0029-5515/56/5/056007.

[40] D.D. Ryutov et al. Geometrical properties of a "snowflake" divertor. *Phys. Plasmas*, 14(6):064502, 2007. doi: 10.1063/1.2738399.

[41] D.D. Ryutov et al. The snowflake divertor. *Phys. Plasmas*, 22(11):110911, 2015. doi: 10.1063/1.4935115.

[42] T. Lunt et al. Numerical study of potential heat flux mitigation effects in the TCV snowflake divertor. *Plasma Phys. Control. Fusion*, 58(4):045027, 2016. doi: 10.1088/0741-3335/58/4/045027.

[43] D.D. Ryutov et al. The 'churning mode' of plasma convection in the tokamak divertor region. *Physica Scripta*, 89(8):088002, 2014. doi: 10.1088/0031-8949/89/8/088002.

[44] G.P. Canal et al. Enhanced $\vec{E} \times \vec{B}$ drift effects in the TCV snowflake divertor. *Nucl. Fusion*, 55(12):123023, 2015. doi: 10.1088/0029-5515/55/12/123023.

[45] T. Eich et al. Inter-ELM Power Decay Length for JET and ASDEX Upgrade: Measurement and Comparison with Heuristic Drift-Based Model. *Phys. Rev. Lett.*, 107(21):215001, 2011. doi: 10.1103/PhysRevLett.107.215001.

[46] M.A. Makowski et al. Analysis of a multi-machine database on divertor heat fluxes. *Phys. Plasmas*, 19(5):056122, 2012. doi: 10.1063/1.4710517.

[47] P. C. Stangeby. A tutorial on some basic aspects of divertor physics. *Plasma Phys. Control. Fusion*, 42(12B):B271–B291, 2000. doi: 10.1088/0741-3335/42/12B/321.

[48] P. Ricci et al. Plasma turbulence in the scrape-off layer of tokamak devices. *Phys. Plasmas*, 20(1):010702, 2013. doi: 10.1063/1.4789551.

[49] R.J. Goldston. Heuristic drift-based model of the power scrape-off width in low-gas-puff H-mode tokamaks. *Nucl. Fusion*, 52(1):013009, 2012. doi: 10.1088/0029-5515/52/1/013009.

[50] H.W. Müller et al. Deuterium plasma flow in the scrape-off layer of ASDEX Upgrade. *J. Nucl. Mater.*, 363-365(1-3):605–610, 2007. doi: 10.1016/j.jnucmat.2006.12.054.

[51] R.A. Pitts et al. Parallel SOL flow on TCV. *J. Nucl. Mater.*, 363-365(1-3):505–510, 2007. doi: 10.1016/j.jnucmat.2006.12.065.

[52] M. Faitsch et al. Change of the scrape-off layer power width with the toroidal B-field direction in ASDEX upgrade. *Plasma Phys. Control. Fusion*, 57(075005), 2015. doi: 10.1088/0741-3335/57/7/075005.

[53] B. Sieglin et al. Investigation of scrape-off layer and divertor heat transport in ASDEX Upgrade L-mode. *Plasma Phys. Control. Fusion*, 58(5):055015, 2016. doi: 10.1088/0741-3335/58/5/055015.

[54] R. Maurizio et al. Divertor power load studies for attached L-mode single-null plasmas in TCV. *Nucl. Fusion*, 58(1):016052, 2018. doi: 10.1088/1741-4326/aa986b.

[55] D. Nille et al. Analytic 1d Approximation of the Divertor Broadening S in the Divertor Region for Conductive Heat Transport. *Plasma Phys. Control. Fusion*, 61:085016, 2019. doi: 10.1088/1361-6587/ab240f.

[56] B. Labit et al. Experimental studies of the snowflake divertor in TCV. *Nucl. Mater. Energy*, 12(1):1015–1019, 2017. doi: 10.1016/j.nme.2017.03.013.

[57] T. Lunt et al. Proposal of an alternative upper divertor in ASDEX upgrade supported by EMC3-EIRENE simulations. *Nucl. Mater. Energy*, 12(1):1037–1042, 2017. doi: 10.1016/j.nme.2016.12.035.

[58] T.W. Petrie et al. Effect of changes in separatrix magnetic geometry on divertor behaviour in DIII-D. *Nucl. Fusion*, 53(11):113024, 2013. doi: 10.1088/0029-5515/53/11/113024.

[59] C. Theiler et al. Results from recent detachment experiments in alternative divertor configurations on TCV. *Nucl. Fusion*, 57(7):072008, 2017. doi: 10.1088/1741-4326/aa5fb7.

[60] H. Reimerdes et al. TCV experiments towards the development of a plasma exhaust solution. *Nucl. Fusion*, 57(12):126007, 2017. doi: 10.1088/1741-4326/aa82c2.

[61] G. De Temmerman et al. The influence of plasma-surface interaction on the performance of tungsten at the ITER divertor vertical targets. *Plasma Phys. Control. Fusion*, 60(4):044018, 2018. doi: 10.1088/1361-6587/aaaf62.

[62] A. Herrmann et al. Overview on stationary and transient divertor heat loads. *Plasma Phys. Control. Fusion*, 44:897–917, 2002. doi: 10.1088/0741-3335/44/6/319.

[63] T. Eich et al. ELM divertor peak energy fluence scaling to ITER with data from JET, MAST and ASDEX upgrade. *Nucl. Mater. Energy*, 12:84–90, 2017. doi: 10.1016/j.nme.2017.04.014.

[64] U.A. Sheikh et al. A novel carbon coating technique for foil bolometers. *Rev. Sci. Instrum.*, 87(11):11D431, 2016. doi: 10.1063/1.4961271.

[65] N. Christen et al. Exploring drift effects in TCV Single-Null plasmas with the UEDGE code. *Plasma Phys. Control. Fusion*, 59(10):105004, 2017. doi: 10.1088/1361-6587/aa7c8e.

[66] A. Gallo et al. Effect of plasma geometry on divertor heat load spreading: MONALISA simulations and experimental results from TCV. *Nucl. Mater. Energy*, 2016. doi: 10.1016/j.nme.2016.10.003.

[67] A.V. Chankin et al. Toroidal field reversal effects on divertor asymmetries in JET. *Plasma Phys. Control. Fusion*, 38:1579–1592, 1996. doi: 10.1088/0741-3335/38/9/004.

[68] I.H. Hutchinson et al. The effects of field reversal on the alcator c-mod divertor. *Plasma Phys. Control. Fusion*, 37(12):1389, 1995. doi: 10.1088/0741-3335/37/12/004.

[69] A. Gallo et al. Impact of the plasma geometry on divertor power exhaust: experimental evidence from TCV and simulations with SolEdge2d and TOKAM3X. *Plasma Phys. Control. Fusion*, 60(014007), 2018. doi: 10.1088/1361-6587/aa857b.

[70] P. Tamain et al. The TOKAM3X code for edge turbulence fluid simulations of tokamak plasmas in versatile magnetic geometries. *J. Comp. Phys.*, 321(Supplement C):606–623, 2016. doi: 10.1016/j.jcp.2016.05.038.

[71] T. Eich et al. Scaling of the tokamak near the scrape-off layer H-mode power width and implications for ITER. *Nucl. Fusion*, 53(9):093031, 2013. doi: 10.1088/0029-5515/53/9/093031.

[72] M. Faitsch et al. Dependence of the L-mode scrape-off layer power fall-off length on the upper triangularity in TCV. *Plasma Phys. Control. Fusion*, 60:045010, 2018. doi: 10.1088/1361-6587/aaaef7.

[73] P. Ricci et al. Simulation of plasma turbulence in scrape-off layer conditions: The GBS code, simulation results and code validation. *Plasma Phys. Control. Fusion*, 54(12):124047, 2012. doi: 10.1088/0741-3335/54/12/124047.

[74] F. Riva et al. Plasma shaping effects on tokamak scrape-off layer turbulence. *Plasma Phys. Control. Fusion*, 59(3):035001, 2017. doi: 10.1088/1361-6587/aa5322.

[75] A. Scarabosio et al. Outer target heat fluxes and power decay length scaling in L-mode plasmas at JET and AUG. *J. Nucl. Mater.*, 438(SUPPL):S426–S430, 2013. doi: 10.1016/j.jnucmat.2013.01.086.

[76] J-W. Ahn et al. L-mode SOL width scaling in the MAST spherical tokamak. *Plasma Phys. Control. Fusion*, 48(8):1077, 2006. doi: 10.1088/0741-3335/48/8/003.

[77] M. Wensing et al. SOLPS-ITER simulations of the TCV divertor upgrade. *Plasma Phys. Control. Fusion*, 61(8):085029, 2019. doi: 10.1088/1361-6587/ab2b1f.

[78] H. Reimerdes et al. Power distribution in the snowflake divertor in TCV. *Plasma Phys. Control. Fusion*, 55(12):124027, 2013. doi: 10.1088/0741-3335/55/12/124027.

[79] R. Maurizio et al. The effect of the secondary x-point on the Scrape-Off Layer transport in the TCV Snowflake Minus divertor. *Nucl. Fusion*, 59(1):016014, 2019. doi: 10.1088/1741-4326/aaee1b.

[80] R. Maurizio et al. Conduction-based model of the Scrape-Off layer power sharing between inner and outer divertor in diverted low-density tokamak plasmas. *Nucl. Mater. Energy*, 19:372–377, 2019. doi: 10.1016/j.nme.2019.03.020.

[81] C.K. Tsui et al. The effects of the Snowflake Divertor on upstream SOL profiles. *58th Annual Meeting of the APS Division of Plasma Physics (San Jose, California, USA, October 31– November 4 2016)*, 2016. doi: 10.13140/RG.2.2.23468.77441.

[82] M.V. Umansky and D.D. Ryutov. Toroidally symmetric plasma vortex at tokamak divertor null point. *Phys. Plasmas*, 23(3):030701, 2016. doi: 10.1063/1.4943101.

[83] M. Giacomin et al. Turbulence and flows in the plasma boundary of snowflake magnetic configurations. *To be submitted to Nucl. Fusion*, 2020.

[84] A. Kallenbach et al. Partial detachment of high power discharges in ASDEX upgrade. *Nucl. Fusion*, 55(5):053026, 2015. doi: 10.1088/0029-5515/55/5/053026.

[85] A.E. Jaervinen et al. $\vec{E}\times\vec{B}$ Flux Driven Detachment Bifurcation in the DIII-D Tokamak. *Phys. Rev. Lett.*, 121(7):75001, 2018. doi: 10.1103/PhysRevLett.121.075001.

[86] R. Ambrosino et al. Evaluation of feasibility and costs of alternative magnetic divertor configurations for DEMO. *Fusion Engineering and Design*, 146:2717–2720, 2019. doi: 10.1016/j.fusengdes.2019.04.095.

[87] F. Wagner et al. Development of an Edge Transport Barrier at the H-Mode Transition of ASDEX. *Phys. Rev. Lett.*, 53(15):1453–1456, 1984. doi: 10.1103/PhysRevLett.53.1453.

[88] H.J. Sun et al. Relating the near SOL transport with plasma properties of the confined edge region in ASDEX Upgrade. *Plasma Phys. Control. Fusion*, 61(1):014005, 2019. doi: 10.1088/1361-6587/aae33c.

[89] H.J. Sun et al. Study of near scrape-off layer (SOL) temperature and density gradient lengths with Thomson scattering. *Plasma Phys. Control. Fusion*, 57(12), 2015. doi: 10.1088/0741-3335/57/12/125011.

[90] T. Eich et al. Empirical scaling of inter-ELM power widths in ASDEX Upgrade and JET. *J. Nucl. Mater.*, 438:S72–S77, 2013. doi: 10.1016/j.jnucmat.2013.01.011.

[91] R. Groebner et al. Progress in quantifying the edge physics of the H mode regime in DIII-D. *Nucl. Fusion*, 41(12):1789–1802, 2001. doi: 10.1088/0029-5515/41/12/306.

[92] B. Sieglin et al. Power load studies in JET and ASDEX-Upgrade with full-W divertors. *Plasma Phys. Contr. Fusion*, 55(12):124039, 2013. doi: 10.1088/0741-3335/55/12/124039.

[93] B. Sieglin. Experimental Investigation of Heat Transport and Divertor Loads of Fusion Plasma in All Metal ASDEX Upgrade and JET, 2014. Physik Department - Technische Universität München.

[94] A. Loarte et al. Characteristics of type I ELM energy and particle losses in existing devices and their extrapolation to ITER. *Plasma Phys. Control. Fusion*, 45(9):1549–1569, 2003. doi: 10.1088/0741-3335/45/9/302.

[95] K. Kamiya et al. Edge localized modes: recent experimental findings and related issues. *Plasma Phys. Control. Fusion*, 49(7):43–62, 2007. doi: 10.1088/0741-3335/49/7/S03.

[96] R.A. Pitts et al. ELM transport in the JET scrape-off layer. *Nucl. Fusion*, 47(11):1437–1448, 2007. doi: 10.1088/0029-5515/47/11/005.

[97] J. Márki. Infrared Thermography of Divertor ELM Heat Loads on TCV, 2012. École Polytechnique Fédérale de Lausanne (EPFL), doi: 10.5075/epfl-thesis-5021.

[98] T. Eich et al. ELM resolved energy distribution studies in the JET MKII Gas-Box divertor using infra-red thermography. *Plasma Phys. Control. Fusion*, 49(5):573–604, 2007. doi: 10.1088/0741-3335/49/5/002.

[99] R.A. Pitts et al. Physics basis for the first ITER tungsten divertor. *Nucl. Mater. Energy*, 20(June):100696, 2019. doi: 10.1016/j.nme.2019.100696.

[100] T. Loewenhoff et al. Tungsten and CFC degradation under combined high cycle transient and steady state heat loads. *Fusion Engineering and Design*, 87(7-8):1201–1205, 2024. doi: 10.1016/j.fusengdes.2012.02.106.

[101] B. Sieglin et al. Real time capable infrared thermography for ASDEX Upgrade. *Rev. Sci. Instrum.*, 86(11):113502, 2015. doi: 10.1063/1.4935580.